UNIVERSITY OF BIRMINGHAM

LASER POWDER BED FUSION OF HIGH-STRENGTH NICKEL-BASED METAL MATRIX COMPOSITES: MICROSTRUCTURE CHARACTERISATION, MECHANICAL TESTING AND NUMERICAL MODELLING

By:

CHANG SHU

A thesis submitted to the University of Birmingham for the degree of

DOCTOR OF PHILOSOPHY

Department of Mechanical Engineering

School of Engineering

University of Birmingham

January 2025

ABSTRACT

The development of high-performance nickel-based composites for aerospace and energy applications is hindered by the high crack sensitivity of IN738LC alloy, despite its excellent high-temperature durability, corrosion resistance, and fatigue resistance. To address this challenge, this study investigates the incorporation of Titanium Carbide (TiC) nanoparticles to enhance the mechanical properties and crack resistance of IN738LC fabricated via laser powder bed fusion (L-PBF). Two nanoparticle integration methods, mechanical mixing and wet chemical processing—were investigated, with the latter exhibiting superior powder morphology, nanoparticle distribution, and enhanced mechanical performance. The effects of processing parameters on porosity, microstructure, and mechanical properties were systematically analysed through a full-factorial experimental design. The optimal processing parameters were identified. The results demonstrated that TiC reinforcement significantly enhances the mechanical properties of IN738LC. Microstructural analysis confirmed that the chemically processed powders resulted in a more uniform and equiaxed grain structure, mitigating microstructural defects and improving mechanical performance. Morphological analysis of fractured samples revealed the presence of dimples, highlighting enhanced ductility. The primary strengthening mechanisms responsible for the observed improvements include fine grain strengthening, load-bearing strengthening, and Orowan strengthening. Additionally, high-fidelity Computational Fluid Dynamics (CFD) modelling was employed to investigate the influence of powder morphology on melt pool dynamics, validating the role of powder sphericity in microstructural integrity and mechanical performance. This study provides critical insights into the fabrication of high-strength, crack-resistant nickel-based composites through L-PBF, offering an experimental reference for optimizing processing parameters and nanoparticle addition methods for aerospace and energy applications.

ACKNOWLEDGEMENTS

Well, I think this chapter is the only place where I can step a bit outside the research focus. There are so many stories and adventures I want to acknowledge.

First and most importantly, **Professor Essa**, you are my greatest role model for my future career. Your quick responses, sharp mind, honesty, and integrity make you the kind of professor I aspire to become. A huge thanks also to **Professor Abdel-Wahab**—your passion and patience with me and my work have meant so much. Your encouragement and guidance in revising my manuscripts have been invaluable.

The two most important people in my life are my father and mother, **Dr. Xuedao Shu** and **Mrs. Yinmei Liu**. Thank you for supporting me unconditionally and for bringing me into this world.

I also want to highlight my deep gratitude to the soon-to-be **Dr. Peiran Lei**. You are a shining gem, and I cannot thank you enough for everything you have done for me. Your support during my PhD has been unwavering—you are my lifelong friend and my best friend in the UK. I cannot imagine my journey without you, for all the words of encouragement you have given me and for the times you lit the way through my darkest moments.

A special thanks to **Ms. Rancy Li**—you are the one who fights me the hardest, but I couldn't even imagine losing you, like losing the air I breathe. You have protected my weak side when I lost control. Thank you for your companionship; all the video calls we made were my elixir, and you are the diamond in my universe.

Then, it must come to my **three cats—Mother Meow, Daughter Black,** and **Tuxedo Milky**. I miss you all so much; you are the best companions I could ever have. I feel incredibly lucky to have had you in my life. Finally, I want to thank all the **team members in my group** and **all the friends** I have made along the way. To end this chapter and confess my bit of cliché, a special thanks to **Dr. Fangjian Chen, Mr. Xiaotong Ding,** and **Dr. Siyu Lei**. It's been good knowing you all over these years.

TABLE OF CONTENTS

LIST OF FIGURES

LIST OF TABLES

LIST OF ABBREVIATIONS AND NOMENCLATURE

AM	Additive Manufacturing
ANOVA	Analysis Of Variance
AP&C	Advanced Powders and Coatings Company
ASTM	American Society for Testing and Materials
ATI	Allegheny Technologies Incorporated
CAD	Computer Aided Design
CFD	Computational Fluid Dynamics
DED	Directed Energy Deposition
DEM	Discrete Element Method
DOE	Design Of Experiment
EBM	Electron Beam Melting
EBSD	Electron Backscatter Diffraction
EDS	Energy Dispersive Spectroscopy
EIGA	Electrode Induction Melting Gas Atomization
GA	Gas Atomization
GND	Geometrically Necessary Dislocations
GZ	Grain Size Distribution
HAGBs	High-Angle Grain Boundaries
HIP	Hot Isotopic Pressing
IPF	Inverse Pole Figure
KAM	Kernel Average Misorientation
LAGBs	Low-Angle Grain Boundaries
L-PBF	Laser Powder Bed Fusion
MA	Misorientation Angle
MC	Metastable Carbides

MMC	Metal Matrix Composite
OM	Optical Microscope
PA	Plasma Atomization
PBF	Powder Bed Fusion
PF	Pole Figure
PREP	Plasma Rotating Electrode Process
SAC	Strain-Age Cracking
SAED	Selected Area Electron Diffraction
SEM	Scanning Electron Microscope
SLS	Selective Laser Sintering
TEM	Transmission Electron Microscopy
TiB_2	Titanium Diboride
TiC	Titanium Carbide
TIMET	Titanium Metals Corporation
VED	Volumetric Energy Density
VIGA	Vacuum Induction Melting Gas Atomization
VOF	Volume Of Fluid
WA	Water Atomization
WAAM	Wire And Arc Additive Manufacturing
WC	Tungsten Carbide
$\overrightarrow{f_B}$	Buoyancy Force
h_c	Convective Heat Transfer Coefficient
E_l	Laser Linear Energy Density
F_s	Solid Fraction
L_v	Latent Heat of Evaporation
P_0	Atmospheric Pressure
R_{ESOR}	Energy Term
R_b	Radius Of the Laser Beam

T_0	Ambient Temperature
T_b	Boiling Temperature
T_{ref}	Reference Temperature
V_F	Volume Fraction of Metal Within a Cell
$\frac{d\gamma}{dT}$	Temperature Coefficient of Surface Tension
$\vec{g}$	Gravitational Acceleration
k_y	Constant Term Called the Hall-Petch Slope
q_{evap}	Heat Loss Due to Evaporation
r_p	Particle Radius
$\vec{v}$	Velocity Of the Melt Pool
v_P	Solidification Velocity of The Particle
γ_0	Surface Tension at The Melting Temperature
μ_T	Viscosity Of the Liquid
ρ_{p}	Density Of the Reinforcing Particles
ρ_ι	Density Of the Liquid Metal
σ_0	Intrinsic Strength of Material
σ_0	Stefan-Boltzmann Constant
σ_y	Yield Strength of The Material
ω_0	Evaporation Rate
d	Average Grain Size
G	Temperature Gradient
h	Hatch Spacing
h	Enthalpy
P	Laser Power
R	Solidification Growth Rate
t	Layer Thickness

ν	Scanning Speed
A	Laser Absorptivity of The Powder Bed
B	Small Constant Introduced to Prevent Division by Zero
C	Constant Characterizing the Morphology of The Mushy Zone
R	Gas Constant
T	Fluid Temperature
a	Gravitational Acceleration
k	Thermal Conductivity
p	Pressure
t	Time
β	Coefficient Of Thermal Expansion
γ	Surface Tension
ε	Emissivity
η	Viscosity Of the Liquid Metal
ρ	Density

LIST OF PUBLICATIONS

The following publications result from the research conducted during the period of this thesis.

Journal articles as the first author:

- **Shu, C.,** Chen, S., Zheng, Z., Lu, X., Li, W., De Lisi, M., ... & Essa, K. (2023). Fabrication and strengthening mechanism of crack-free nano-TiC reinforced IN738LC with enhanced mechanical properties by laser powder bed fusion. *Journal of Materials Research and Technology*, *27*, 3835-3848.
- **Shu, C.,** Chen, S., Shu, X., Abdel-Wahab, A., & Essa, K. (2024). Enhanced high-temperature mechanical properties and strengthening mechanisms of chemically prepared nano-TiC reinforced IN738LC via laser powder bed fusion. *Materials Characterization*, *217*, 114434.
- **Shu, C.,** Zheng, Z., Lei, P., Xu, H., Shu, X., & Essa, K. (2024). Optimization of process parameters for TC11 alloy via tailoring scanning strategy in laser powder bed fusion. *Frontiers of Materials Science*, 18(4), 1-15.
- **Shu, C.,** Chen, S., Lei, P., Shu, X., Abdel-Wahab, A., & Essa, K. (2025). Effect and mechanism of powder morphology on mechanical properties of nickel-based metal matrix composites TiC-IN738LC in laser powder bed fusion. *Progress in Additive Manufacturing*, 1-19.

Journal article as the collaborating author:

- Li, W., **Shu, C.,** Hassan, A., Attallah, M. M., & Essa, K. (2022). Application of machine learning on tool path optimisation and cooling lubricant in induction heating-assisted single point incremental sheet forming of Ti-6Al-4V sheets. *The International Journal of Advanced Manufacturing Technology*, *123*(3), 821-838.

- Lu, X., **Shu, C.,** Zheng, Z., Shu, X., Chen, S., Essa, K., ... & Xu, H. (2023). Effects of L-PBF Scanning Strategy and Sloping Angle on the Process Properties of TC11 Titanium Alloy. *Metals*, *13*(5), 983.
- De Lisi, M., **Shu, C.,** Attia, U. M., & Essa, K. (2023). DLP of translucent alumina: in-depth investigation on slurry development and debinding regimes. *Machines*, *11*(3), 321.
- Guner, A., Bidare, P., Jiménez, A., **Shu, C.,** Kovacev, N., & Essa, K. (2024). A numerical model for predicting powder characteristics in LMD considering particle interaction. *Advanced Powder Technology*, *35*(3), 104348.

CHAPTER 1 INTRODUCTION

Additive manufacturing is an advanced technology that builds three-dimensional structures by sequentially adding material layers based on CAD models. Compared to conventional subtractive manufacturing methods (e.g., milling, turning, drilling, etc.) and formative manufacturing (such as casting, forging, rolling, drawing, etc.), additive manufacturing uniquely excels in producing complex structural components. Additive manufacturing has experienced significant economic growth, expanding from $3.07 billion in 2013 to $10.8 billion in 2021, and its market size is expected to continue growing substantially over the next decade [1]. Its impact on modern economic development is substantial, acting as a transformative technology for the real economy and a driver of sustainable economic growth. A prominent technique in metal additive manufacturing is Laser Powder Bed Fusion (L-PBF), which uses high-energy lasers to melt metal powder layer by layer, facilitating the production of parts with intricate geometries, particularly advantageous in aerospace applications. For instance, the IN738LC alloy, a γ' phase precipitation-strengthened nickel-based superalloy, contains diverse phases and alloying elements, demonstrating high-temperature durability and strong resistance to corrosion and fatigue [2]. It is used for components in marine vessels, industrial gas turbines, and aircraft engines below 900°C [3]. However, IN738LC still presents numerous challenges, such as its susceptibility to crack formation during the additive manufacturing process, the anisotropy caused by large columnar grains oriented along the building direction, and the deterioration of high-temperature performance in components produced by L-PBF compared to those fabricated through conventional casting methods.

Therefore, this chapter aims to present the advantages of L-PBF and its application, focusing on key research topics such as the major issue of hot cracking in IN738LC and the degradation of its high-temperature performance after L-PBF processing. The academic motivation of this study lies in addressing these challenges by exploring the mechanisms of microstructural strengthening in L-PBF-fabricated components. The ultimate research objective is to tailor the microstructure to enable precise control over

the mechanical properties of IN738LC, thereby advancing the understanding and optimization of its performance in L-PBF applications.

1.1 Background

1.1.1 Overview of Bottlenecks in L-PBF Processing of High Percent Al-Ti Nickel-Based Superalloys

IN738LC alloy is a precipitation-strengthened nickel-based superalloy with a γ-Ni-Cr-Co (face-centered cubic) matrix phase. Its primary strengthening phase is γ′-Ni3(Al, Ti), with an L12 face-centered cubic structure that is coherent with the γ matrix [4]. Due to its high aluminum and titanium content (Al + Ti > 6 wt%), the alloy forms a high-volume fraction of the γ′ strengthening phase, giving it excellent high-temperature creep resistance, strength, corrosion resistance, and structural stability, making it a critical material for turbine blades in aircraft engines. Traditional casting and machining methods for turbine blades face challenges due to complex geometries and long processing times, while L-PBF technology provides a high-precision, rapid manufacturing solution for complex structures, particularly suited for producing small to medium-sized overhung structures and intricate internal cavities, thereby improving turbine blade production efficiency [5]. Figure 1.1 shows the overall classification and specific branches of additive manufacturing [6].

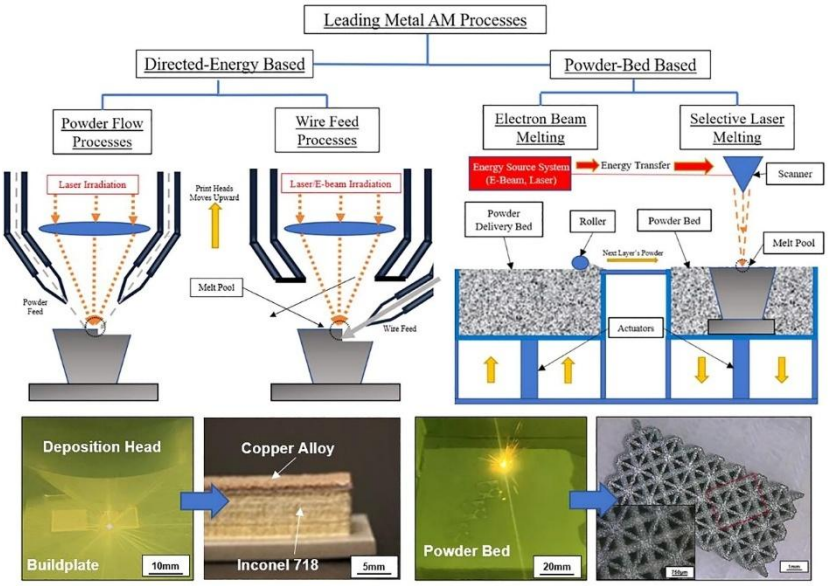

Figure 1.1 Schematic diagram of main additive manufacturing routes [6].

However, due to the multi-elemental composition of IN738LC alloy—particularly its high aluminum and titanium content, which increases its susceptibility to cracking—and considering the extreme thermal gradients ($\geq 10^5$ K/cm), rapid cooling rates ($\geq$0.01 K/s), and cyclic thermal effects inherent to the L-PBF process, cracks and other defects are even more easily formed during L-PBF processing and heat treatment. This mismatch between the alloy's printability and mechanical performance significantly limits the application and development of high Al- and Ti-content nickel-based superalloy components for hot-end applications via L-PBF [7]. Figure 1.2 shows how research is distributed across various nickel-based alloys in the L-PBF process [4]. It is obvious that the research on high Al- and Ti-content nickel alloys like IN738LC and CM247LC is limited compared to IN718 and IN625 yet offers significant potential. Due to their high-temperature capabilities, advancing these alloys for aerospace and other high-end applications is essential. Consequently, achieving crack-free, high-temperature mechanical performance L-PBF-fabricated IN738LC alloy components is the main focus of current research.

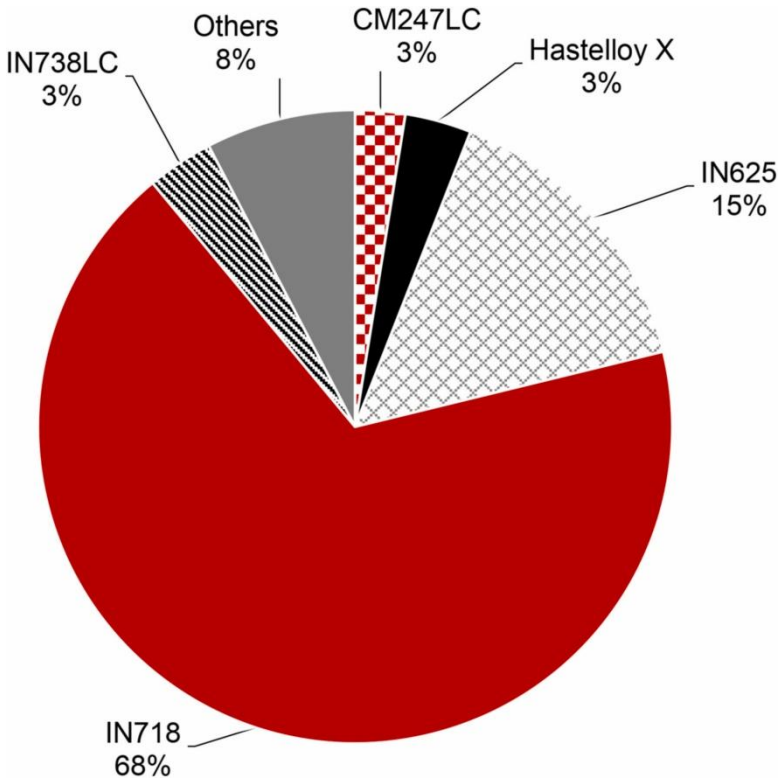

Figure 1.2. Proportion of the most common nickel superalloy used in L-PBF [4].

Due to the complex metallurgical transformations that metals undergo in L-PBF processing—from solid to liquid and back to solid—combined with high temperature gradients, rapid cooling rates, and complex cyclic thermal effects, thermal and/or phase transformation stresses are likely to develop, leading to metallurgical defects during L-PBF processing [8]. Additionally, nickel superalloys contain a variety of alloying elements and exhibit a wide solidification temperature range. The high percentages of aluminum and titanium make it likely for low-melting phases to form at the final stage of solidification, while the substantial precipitation of the γ' phase during heat treatment further increases crack sensitivity in L-PBF processing. Furthermore, since the rapid heat dissipation during L-PBF typically occurs along the direction of the highest temperature gradient, crystals tend to grow preferentially in this direction, resulting in anisotropy in the alloy's microstructure and properties [9]. The presence of crack defects further reduces the high-temperature mechanical performance of hard-to-weld nickel superalloys, particularly affecting the ductility. Consequently, the difficulty in aligning printability and high-temperature mechanical performance is a bottleneck for the application of these alloys in L-PBF processing.

1.1.2 High Crack Sensitivity

Unlike traditional casting processes, the L-PBF process features high temperature gradients and rapid cooling rates within the melt pool. The Ni-alloy powder undergoes extreme metallurgical processes involving intense, unstable, and cyclic heating and cooling from a high-energy-density heat source. This easily induces thermal and phase transformation stresses, leading to a high susceptibility to crack defects in L-PBF-processed parts, such as liquation cracks, solidification cracks, strain-age cracks, high-temperature embrittlement cracks, and cold cracks [10]. The first two types are liquid-state cracks, which require the presence of a liquid film, while the latter three are solid-state cracks. The presence of a liquid film can help differentiate liquation and solidification cracks (liquid-state cracks) from strain-age, high-temperature embrittlement, and cold cracks (solid-state cracks). However, distinguishing between solidification cracks and liquation cracks is challenging due to the complex thermal

history of the L-PBF process and the diverse alloying elements in nickel-based superalloys. These alloys contain solid-solution strengthening elements (W, Co, Mo, Nb, etc.), precipitation-strengthening elements (Al, Ti, Ta, Nb, etc.), and grain boundary strengthening elements (C, B, Zr, Si, etc.), all of which can contribute to various types of cracking. Figure 1.3 shows several common crack patterns observed during the L-PBF process [11].

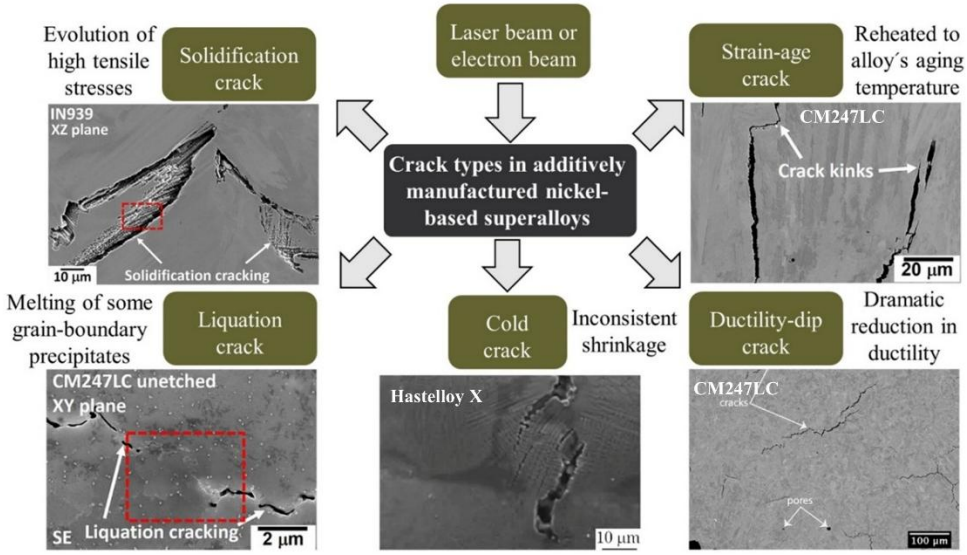

Figure 1.3. Classification and examples of common types of cracks in AM processed nickel-based superalloys [11].

In high Al- and Ti-content nickel superalloys, a low-melting-point γ+γ′ eutectic phase is preferably formed, which can lead to liquation cracks under thermal stress [12]. Additionally, due to high residual stress and micro-segregation, L-PBF-processed high Al- and Ti-content alloys are also prone to strain-age cracking (SAC) during post-processing [13]. The sensitivity to SAC is closely related to the aluminum and titanium content; the higher the total content and Al/Ti ratio, the greater the crack sensitivity. For example, Inconel 625 and Inconel 718 have low SAC sensitivity due to their lower Al+Ti content, whereas alloys like IN939 and IN738LC exhibit higher crack sensitivity because of their high Al+Ti content. Therefore, L-PBF-processed high Al- and Ti-content nickel superalloys exhibit high crack sensitivity, which presents a key challenge in the L-PBF process.

1.1.3 Anisotropy in Microstructure and Mechanical Properties

In L-PBF-processed nickel superalloys, columnar grain structures typically form with grains extending across multiple melt layers. This is due to the directional nature of heat dissipation and preferential crystal growth during rapid solidification, resulting in grain growth along the epitaxial direction. The grain orientation in L-PBF-processed IN718 alloy aligns parallel to the build direction (BD), displaying a <100> direction, and this anisotropic grain structure leads to anisotropy in the alloy's mechanical properties [14]. Similarly, L-PBF-processed Hastelloy alloys exhibit a comparable result, with significant differences in mechanical properties between build direction and scan direction samples at room temperature. Although traditional heat treatment and hot isostatic pressing (HIP) can reduce the mechanical anisotropy to some extent, it still persists [15]. Additionally, the L-PBF-processed K418 alloy has also identified anisotropy in grain structure and mechanical properties. Horizontal specimens exhibit slightly higher yield strength than vertical specimens, but their tensile strength and elongation are significantly lower. This is because the stress direction in vertical specimens is parallel to the columnar grains, resulting in better ductility, whereas in horizontal specimens, the applied stress is perpendicular to the columnar grains, causing grain layer separation and thus poorer ductility [16]. However, it is noteworthy that crack defects in L-PBF-processed nickel-based superalloys may cause abnormal mechanical anisotropy, impacting the overall performance of the material. Therefore, mechanical anisotropy is closely related to grain structure, texture, and defects, and its manifestation varies among different nickel-based superalloys. Nonetheless, grain structure anisotropy is not always detrimental. By properly controlling the heterostructures, specific mechanical properties can be achieved, similar to the benefits of directionally solidified or single-crystal structures [17].

Although it is relatively difficult to achieve a fully columnar grain structure in nickel superalloys using L-PBF technology, a mixed grain structure dominated by columnar grains is usually formed. However, by adjusting the L-PBF process parameters, equiaxed grain structures can be produced, thereby reducing the anisotropy in

mechanical properties. Therefore, this represents an important research direction and a significant challenge for L-PBF-processed nickel-based superalloys: to adjust the microstructural properties by inducing or transforming columnar grains into equiaxed grains. This approach aims to overcome the presence of large columnar grains oriented along the building direction and thereby lowering this negative anisotropic effect.

1.1.4 Poor High-Temperature Mechanical Properties

Compared to cast and forged nickel-based superalloys, L-PBF-processed samples exhibit reduced high-temperature creep and tensile properties. Even after heat treatment, their performance often falls short of the levels achieved by cast and forged counterparts. This is primarily due to unique microstructural characteristics inherent to the L-PBF process, such as precipitation phases, initial defect rates, and grain structures. For example, in L-PBF-processed Inconel 718 alloy, the δ phase precipitates perpendicular to the stress axis, resulting in reduced ductility and shorter creep life [18]. Additionally, the formation of creep voids and microcracks around the δ phase at grain boundaries and the laves phase further exacerbates intergranular fracture [19]. The metallurgical defects that are difficult to avoid during the L-PBF process also significantly impact creep performance. These initial defects may serve as nucleation sites for voids or grow on their own during creep, leading to increased connectivity between voids as the number of defects rises, resulting in poorer creep behavior. L-PBF-processed Inconel 718 alloy, with a higher initial porosity, has a higher creep rate and shorter creep life compared to traditional forged alloys [20].

This disadvantage in high-temperature mechanical properties is especially pronounced in high Al- and Ti-content nickel-based superalloys. For instance, L-PBF-processed CM247LC alloy has a maximum creep life of only 9.6 hours at 1050°C/100 MPa, which is far below the 236 hours predicted by the Larson-Miller parameter, mainly due to the presence of crack defects [21]. Furthermore, grain structure plays a significant role in creep performance. In L-PBF-processed IN738LC alloy, vertical samples exhibit creep strength close to that of cast samples, whereas horizontal samples show reduced creep

performance. This difference arises because the long columnar grains in vertical samples are aligned parallel to the loading direction, while the grain orientation in horizontal samples is perpendicular to the loading direction [4].

In summary, due to the complex composition of nickel superalloys and the specific characteristics of the L-PBF process, existing high Al- and Ti-content nickel superalloys are highly prone to crack defects during L-PBF, resulting in a severe "printability-performance" mismatch bottleneck.

1.2 Motivation

With the growing demand for high-performance materials in advanced fields like aerospace, nickel-based superalloys-key structural material for high-temperature applications – are subject to increasingly stringent operating conditions. The application of additive manufacturing (L-PBF) technology offers a new approach to addressing the challenges of complex structures and high costs that traditional manufacturing methods struggle to overcome. However, existing research indicates that high Al- and Ti-content nickel-based superalloys are susceptible to cracks and other metallurgical defects during L-PBF processing. This creates a critical mismatch between printability and mechanical performance that needs to be urgently addressed. Therefore, this study aims to systematically investigate the behavior of nickel-based composite materials during L-PBF processing by incorporating nano-ceramic particles, optimizing L-PBF process parameters, and designing alloy compositions. The objective is to uncover the mechanisms behind crack formation and identify suppression methods, ultimately enhancing the formability and high-temperature performance of IN738LC alloy.

The motivation for this research stems from the ever-increasing demands for new materials in the aerospace field. By thoroughly exploring L-PBF technology and its impact on nickel-based superalloys, this study will provide theoretical support for developing crack-free, high-performance additive manufacturing materials and promote the widespread application and advancement of additive manufacturing

technology in high-temperature applications. This not only addresses the current manufacturing challenges associated with the IN738LC alloy but also lays a solid foundation for the future design and application of high-temperature alloy materials. In conclusion, to realize the aforementioned motivations, it is essential to investigate strategies for optimizing material properties, mitigating L-PBF induced defects, and overcoming the limitations of conventional alloys through innovative alloy design.

1.3 Aims and Objectives

The main objective of this research is to enhance the nickel-based IN738LC alloy mechanical properties by incorporating nano-ceramic TiC particles to suppress thermal cracking during the L-PBF process and improve its mechanical properties, thereby meeting the high-strength requirements for aerospace components. Specifically, this study aims to increase the crack resistance of IN738LC alloy during the L-PBF process and enhance its strength at high temperatures through the incorporation of nanomaterials. To achieve this, two approaches —mechanical preparation and wet chemical preparation—will be employed to produce composite powder, ensuring excellent wettability and sphericity to satisfy the requirements of the L-PBF process.

To achieve the above aim, the following objectives will be completed:

1. Investigate the Ball Milling preparation route of TiC and IN738LC composite powder on structure integrity of TiC-IN738 MMC produced by L-PBF.

2. Enhance powder wettability and printability by using wet chemical method and optimize L-PBF process parameters for producing crack-free, high-strength nickel-based MMC.

3. Study the nano-particle reinforcement mechanism. This will be done by investigating the effect of the Orowan looping mechanism and coefficient of thermal expansion (CTE) mismatch strengthening, induced by incorporating nano-ceramic particles, on material properties.

4. Numerical modelling and simulation of powder morphology and mechanical performance using computational fluid dynamics (CFD). This will help to understand and verify how the sphericity and wettability of the powder prepared by the two methods affect the quality of L-PBF printed samples.

1.4 Thesis Structures

Chapter 1 introduces the motivation, background, and significance of this research, and provides a brief overview of the overall structure of the thesis. By analyzing the challenges and opportunities of nickel-based superalloys in L-PBF additive manufacturing, the practical application value of this study is highlighted.

Chapter 2 reviews the latest literature related to this research, covering recent advancements in L-PBF processes, the latest research findings on nickel-based composites in L-PBF, the advantages and disadvantages of various preparation methods, and the current gaps and challenges in nickel-based composite materials research.

Chapter 3 discusses the preparation of TiC-IN738LC composites using the ball milling method, employing experimental design to optimize process parameters and exploring the reinforcement mechanism of nano TiC during L-PBF processing, resulting in the fabrication of crack-free composites.

Chapter 4 presents a wet chemical method for preparing TiC-IN738LC composites, where experimental design is used to determine the optimal process parameters. Through alloy microstructure analysis, the reinforcement mechanisms of nanoparticles are thoroughly explained, achieving higher strength at both room and high temperatures compared to traditional IN738LC.

Chapter 5 compares the powder morphology and build quality of TiC-IN738LC composites prepared by ball milling and wet chemical methods, providing a detailed analysis of the advantages of the wet chemical method. A CFD model is established to simulate the behavior of different powder morphologies during the L-PBF process,

analyzing the thermal history and printing quality, and validating the results against experimental data.

Chapter 6 summarizes the main conclusions of this research and provides an outlook on future research directions for additive manufacturing technology of nickel-based metal matrix composites.

References

1. Thiesse F, Wirth M, Kemper H-G, Moisa M, Morar D, Lasi H, et al. Economic implications of additive manufacturing and the contribution of MIS. Business & Information Systems Engineering. 2015;57:139-48.
2. Wang H, Zhang X, Wang G, Shen J, Zhang G, Li Y, et al. Selective laser melting of the hard-to-weld IN738LC superalloy: Efforts to mitigate defects and the resultant microstructural and mechanical properties. Journal of Alloys and Compounds. 2019;807:151662.
3. Golezani A, Bageri M, Samadi R. Microstructural change and impact toughness property of Inconel 738LC after 12years of service. Engineering Failure Analysis. 2016;59:624-9.
4. Sanchez S, Smith P, Xu Z, Gaspard G, Hyde CJ, Wits WW, et al. Powder Bed Fusion of nickel-based superalloys: A review. International Journal of Machine Tools and Manufacture. 2021;165:103729.
5. Chowdhury S, Yadaiah N, Prakash C, Ramakrishna S, Dixit S, Gupta LR, et al. Laser powder bed fusion: a state-of-the-art review of the technology, materials, properties & defects, and numerical modelling. Journal of Materials Research and Technology. 2022;20:2109-72.
6. Bandyopadhyay A, Traxel KD, Lang M, Juhasz M, Eliaz N, Bose S. Alloy design via additive manufacturing: Advantages, challenges, applications and perspectives. Materials Today. 2022;52:207-24.
7. Shu C, Chen S, Zheng Z, Lu X, Li W, De Lisi M, et al. Fabrication and strengthening mechanism of crack-free nano-TiC reinforced IN738LC with enhanced mechanical properties by laser powder bed fusion. Journal of Materials Research and Technology. 2023;27:3835-48.
8. Mostafaei A, Ghiaasiaan R, Ho I-T, Strayer S, Chang K-C, Shamsaei N, et al. Additive manufacturing of nickel-based superalloys: A state-of-the-art review on process-structure-defect-property relationship. Progress in Materials Science. 2023;136:101108.
9. Lim B, Chen H, Chen Z, Haghdadi N, Liao X, Primig S, et al. Microstructure-property gradients in Ni-based superalloy (Inconel 738) additively manufactured via electron beam powder bed fusion. Additive Manufacturing. 2021;46:102121.
10. Tan Q, Liu K, Li J, Geng S, Sun L, Skuratov V. A review on cracking mechanism and suppression strategy of nickel-based superalloys during laser cladding. Journal of Alloys and Compounds. 2024:175164.
11. Wei Q, Xie Y, Teng Q, Shen M, Sun S, Cai C. Crack types, mechanisms, and suppression methods during high-energy beam additive manufacturing of nickel-based superalloys: a review. Chinese Journal of Mechanical Engineering: Additive

Manufacturing Frontiers. 2022;1(4):100055.
12. Zhang X, Chen H, Xu L, Xu J, Ren X, Chen X. Cracking mechanism and susceptibility of laser melting deposited Inconel 738 superalloy. Materials & Design. 2019;183:108105.
13. Griffiths S, Tabasi HG, Ivas T, Maeder X, De Luca A, Zweiacker K, et al. Combining alloy and process modification for micro-crack mitigation in an additively manufactured Ni-base superalloy. Additive Manufacturing. 2020;36:101443.
14. Enrique PD, Keshavarzkermani A, Esmaeilizadeh R, Peterkin S, Jahed H, Toyserkani E, et al. Enhancing fatigue life of additive manufactured parts with electrospark deposition post-processing. Additive Manufacturing. 2020;36:101526.
15. Sanchez-Mata O, Muñiz-Lerma J, Wang X, Atabay S, Shandiz MA, Brochu M. Microstructure and mechanical properties at room and elevated temperature of crack-free Hastelloy X fabricated by laser powder bed fusion. Materials Science and Engineering: A. 2020;780:139177.
16. Chen Z, Li Y, Zhang S, Wei P, Dang X, Jiang X, et al. Hierarchical architecture and mechanical behavior of K418 Ni-based superalloys manufactured by laser powder bed fusion. Materials Science and Engineering: A. 2022;851:143630.
17. Li Y, Yu Y-F, Wang Z-B, Liang X-Y, Kan W-B, Lin F. Additive manufacturing of nickel-based superalloy single crystals with IN-738 alloy. Acta Metallurgica Sinica (English Letters). 2022:1-6.
18. Ma T, Zhang G-P, Tan P, Zhang B. Effects of homogenization temperature on creep performance of laser powder bed fusion-fabricated Inconel 718 at 650° C. Materials Science and Engineering: A. 2022;853:143794.
19. Wu S, Peng H, Gao X, Hodgson P, Song H, Zhu Y, et al. Improving creep property of additively manufactured Inconel 718 through specifically-designed post heat treatments. Materials Science and Engineering: A. 2022;857:144047.
20. Teixeira Ó, Silva FJ, Atzeni E. Residual stresses and heat treatments of Inconel 718 parts manufactured via metal laser beam powder bed fusion: an overview. The International Journal of Advanced Manufacturing Technology. 2021;113(11):3139-62.
21. Carter LN. Selective laser melting of nickel superalloys for high temperature applications: University of Birmingham; 2013.

CHAPTER 2 LITERATURE REVIEW

This chapter provides a comprehensive review of the state-of-the-art techniques involved in typical additive manufacturing processes, emphasizing the advantages and challenges of L-PBF and analyzing the effects of key processing parameters on the quality of fabrication. Based on the L-PBF framework, the chapter highlights the current research trends on the incorporation of ceramic-reinforced phases in metal matrix composites, examines the integrity of powders and evaluates the impact of various powder preparation techniques on the quality of the L-PBF process. Additionally, it offers a systematic review of simulation and modeling efforts related to L-PBF, concluding with insights into the future prospects and developmental pathways for nickel-based composites.

2.1 Overview of AM Technologies

2.1.1 AM Categories and Features

Additive Manufacturing (AM), commonly referred to as 3D Printing, is an advanced manufacturing technique that constructs physical objects directly from digital models [1]. This innovative technology exemplifies the seamless integration of information network systems, advanced materials science, and digital manufacturing techniques, encompassing key domains such as Computer-Aided Design (CAD), Computer-Aided Manufacturing (CAM), and Computer Numerical Control (CNC), additive manufacturing stands as a cornerstone of modern advanced manufacturing technologies [2]. As a novel manufacturing technique, additive manufacturing plays a pivotal role in driving technological innovation and advancing manufacturing processes.

In contrast to traditional "subtractive manufacturing" techniques (e.g., cutting, planning) and "formative manufacturing" methods (e.g., casting, forging), additive manufacturing adopts a "bottom-up" approach, where materials are accumulated layer by layer to fabricate components [3]. As illustrated in Figure 2.1, this distinction underscores the advantages of additive manufacturing in terms of product complexity and production cost [4]. Metal additive manufacturing represents a pivotal division within this field.

By utilizing energy sources such as lasers, electron beams, or electric arcs, metal materials—whether in powder, wire, or sheet form—are deposited layer by layer to create dense, fully functional metal components [2]. This approach offers unparalleled advantages for fabricating complex geometries, high-value components, and small-batch customized products. Today, metal additive manufacturing finds extensive application in sectors such as aerospace, automotive, healthcare and defence [2, 3]. However, the high hardness, strength, and melting point of metallic materials make metal additive manufacturing a complex problem involving multi-scale and multi-physics coupling phenomena. These include heat and mass transfer, phase transitions, and microstructural evolution [2]. These complexities not only elevate the difficulty of process optimization and technological implementation but also stimulate considerable interest in driving innovations within the field.

As classified by the ISO/ASTM international standards, metal additive manufacturing is divided into two main categories: Directed Energy Deposition (DED) and Powder Bed Fusion (PBF) [5]. DED employs high-energy beams—such as lasers, electron beams, or plasma arcs—to directly feed metal powder or wire into the energy focal point, creating a molten pool for material deposition [6]. Powder-based DED technology is particularly well-suited for fabricating highly complex components and repairing existing assemblies. To prevent oxidation during the process, operations are typically conducted in an inert gas environment. The resulting surface roughness ranges from 20 to 100 μm [6]. The workflow includes slicing CAD models into layered thickness files, configuring printing parameters, and sequentially depositing metal powder to form a molten pool, ultimately completing the component [7]. Conversely, Wire and Arc Additive Manufacturing (WAAM) utilizes arc welding techniques to melt and deposit wire material layer by layer [8]. This technology is optimal for manufacturing medium to large components with lower geometric complexity. WAAM is characterized by its low equipment costs and economical raw materials (wire costs considerably less than powder). Furthermore, WAAM offers a high deposition rate (4–9 kg/h). However, the process produces parts with a surface roughness of approximately

0.5 mm, necessitating additional post-processing to achieve the final desired dimensions and surface quality [8].

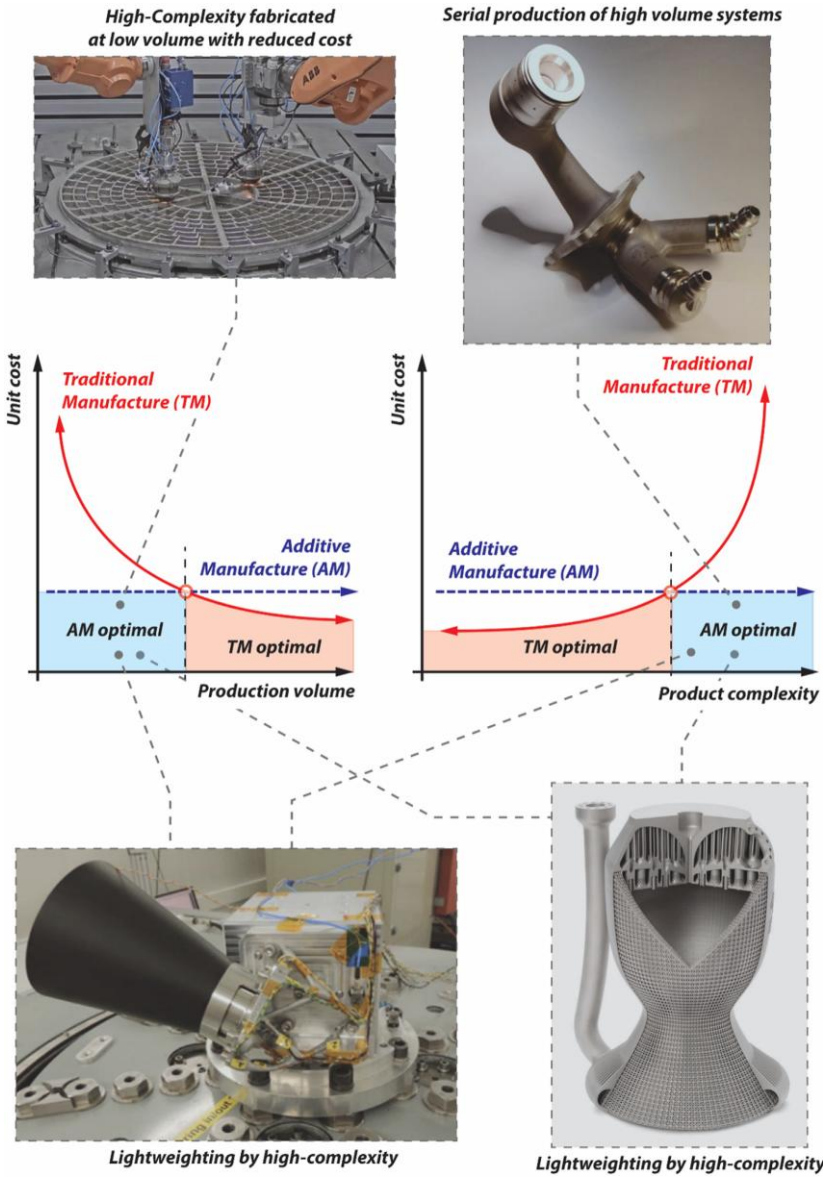

Figure 2.1 Relationship between unit cost, production volume, and product complexity. Applications with high complexity and low production volume show potential for commercial additive manufacturing [4].

PBF technology fabricates components by selectively melting metal powders layer by layer within a powder bed. This category includes several processes, such as Selective Laser Sintering (SLS), Direct Metal Laser Sintering (DMLS), Laser Powder Bed Fusion (L-PBF), and Electron Beam Melting (EBM) [9]. Among these, L-PBF is

particularly advantageous for producing small parts with intricate geometries, offering superior mechanical properties and a surface roughness of less than 20 μm [10]. The manufacturing process begins with slicing a CAD model and importing it into the printer. A recoater spreads a thin layer of metal powder, which is then selectively melted using a laser or electron beam. After each layer is completed, the build platform lowers by one layer thickness, and the process repeats until the component is fully built [2]. The rapid cooling and solidification inherent to this process (with cooling rates ranging from 10^3 to 10^6 K/s) result in components with refined microstructures and exceptional mechanical performance [10]. The fundamental principles of L-PBF are depicted in Figure 2.2 [11].

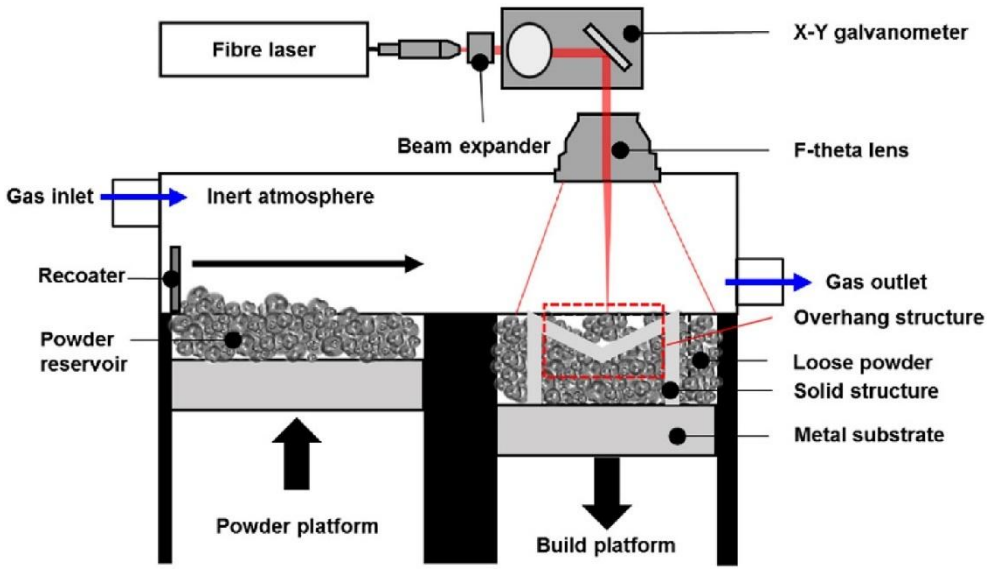

Figure 2.2 Schematic illustration of the building mechanism in L-PBF [11].

In conclusion, metal additive manufacturing offers innovative solutions for fabricating complex metal components and meeting the demands of customized production. Figure 2.3 illustrates the classification system of all additive manufacturing categories as defined by ASTM standards [12]. Among these, L-PBF stands out for its ability to utilize finer powder scales, enabling the production of high-quality components with exceptional surface finish and dimensional accuracy. This makes L-PBF particularly suitable for alloy design and performance optimization. However, significant gaps remain in understanding and mitigating issues specific to high-crack-sensitivity alloys

and complex geometries. Challenges such as controlling microstructural evolution, managing residual stress, and optimizing powder properties require further research to realize L-PBF's potential.

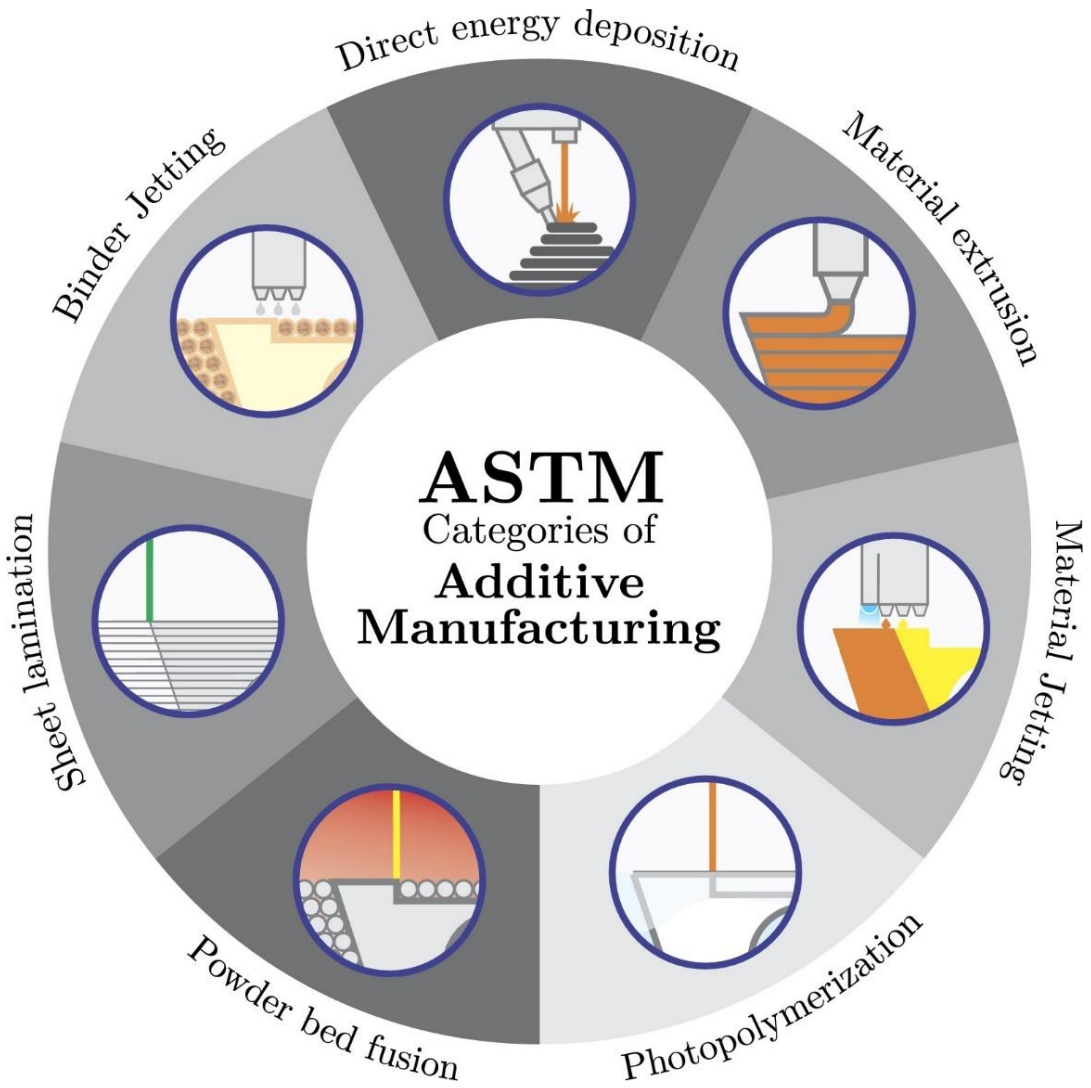

Figure 2.3 Overview of the classification of additive manufacturing technologies [12].

2.1.2 L-PBF Technology: Advantages and Challenges

L-PBF technology has emerged as a leading approach in the field of additive manufacturing, offering distinct advantages and demonstrating exceptional application potential in metal material processing. Firstly, L-PBF technology is compatible with a wide range of metal materials, including nickel-based superalloys, stainless steel, titanium alloys, aluminum alloys, and cobalt-chromium alloys. This extensive material adaptability meets the needs of various industries, such as aerospace, healthcare, and

automotive manufacturing [3, 13]. Moreover, the L-PBF offers relatively low surface roughness [14]**:** the as-built surface roughness typically ranges from Ra ≈ 5–25 μm, depending on orientation and scan strategy. This corresponds to ISO 1302 roughness grades N9 to N11, with up-skin surfaces generally smoother (Ra ≈ 5–10 μm, ~N9) and down-skin or side surfaces rougher (Ra up to 25 μm, ~N11). Additionally, the process eliminates the need for molds, significantly reducing manufacturing time and costs [10].

In terms of material density, L-PBF technology achieves densities exceeding 99% under optimized process parameters, closely approaching the standards of traditional manufacturing techniques [15]. The synergy of high density and refined microstructure grants L-PBF components exceptional mechanical properties, often comparable to those of forged parts [13]. However, the realization of these high-performance characteristics is not without technical challenges. The rapid cooling of the molten pool generates steep temperature gradients and significant shrinkage effects, which can induce substantial residual stress within the fabricated parts. These stresses may lead to deformation, warping, or even microcracks [16]. If unaddressed, such defects can compromise the reliability and performance of the components. To mitigate these issues, post-process treatments are essential to ensure the quality and functionality of the final parts.

In recent years, L-PBF technology has achieved remarkable breakthroughs in the aerospace sector. Leading global companies, including Pratt & Whitney, Airbus, and Boeing, have utilized this technology to develop a range of complex metal components, such as combustion chambers and turbine blades for aircraft engines [17]. Meanwhile, nations such as France, Germany, the United Kingdom, the United States, and Sweden have been actively advancing the development of L-PBF additive manufacturing equipment across various scales while conducting foundational process research. These initiatives have substantially accelerated the adoption of L-PBF technology for manufacturing high-performance metal components, further driving innovation in the field [18].

Therefore, despite the ongoing challenges associated with L-PBF, its distinctive advantages have garnered widespread attention from nations and industries alike. Its flexibility in alloy design and the superior microstructural properties give L-PBF tremendous potential for research and development. Consequently, despite the numerous obstacles, the academic community continues to strive to overcome these challenges, driving ongoing efforts to unlock its full application potential.

2.2 L-PBF of Nickel Superalloy

2.2.1 Typical Defects in Nickel Superalloys

Metal additive manufacturing technologies, particularly L-PBF, have made significant strides in the fabrication of nickel-based superalloys [19]. Extensive research has delved into the correlations between microstructure, mechanical properties, and process parameters. For instance, Tao et al. [20] investigated the L-PBF processing of IN718 alloy, revealing that the molten pool solidifies from its boundary and grows along the epitaxial direction at a solidification rate of 0.1–1.0 m/s. The resulting grains form parallel or 90° rotated dendritic structures, extending across the deposition layers. Further findings demonstrated that process parameters play a crucial role in the densification of nickel-based superalloys. Optimizing these parameters significantly reduces cracking while enhancing the density and mechanical properties of the samples. Figure 2.4 depicts common cracks in L-PBF and their underlying mechanisms, offering valuable insights into the relationship between cracking and residual stress [21].

Choi et al., in their investigation of IN718 alloy fabricated via L-PBF, examined the influence of scanning speed on density and Vickers hardness [22]. Their findings revealed that increasing the scanning speed to 800 mm/s resulted in a sample density exceeding 99% and an increase in hardness to 320 HV, While the laser power of 90 W, layer thickness of 25 μm, hatch spacing of 80 μm keep unchanged. Furthermore, the grain size of the samples ranged from a few microns to several hundred microns, with small grains embedded within larger grain structures. Similarly, Chlebus et al. [23]

identified that the rapid heating and cooling cycles inherent to the L-PBF process induced the formation of nanoscale inter-dendritic regions in IN718 alloy. These regions exhibited elemental segregation (e.g., Nb, Mo, C), which facilitated the precipitation of NbC carbides and Laves phases.

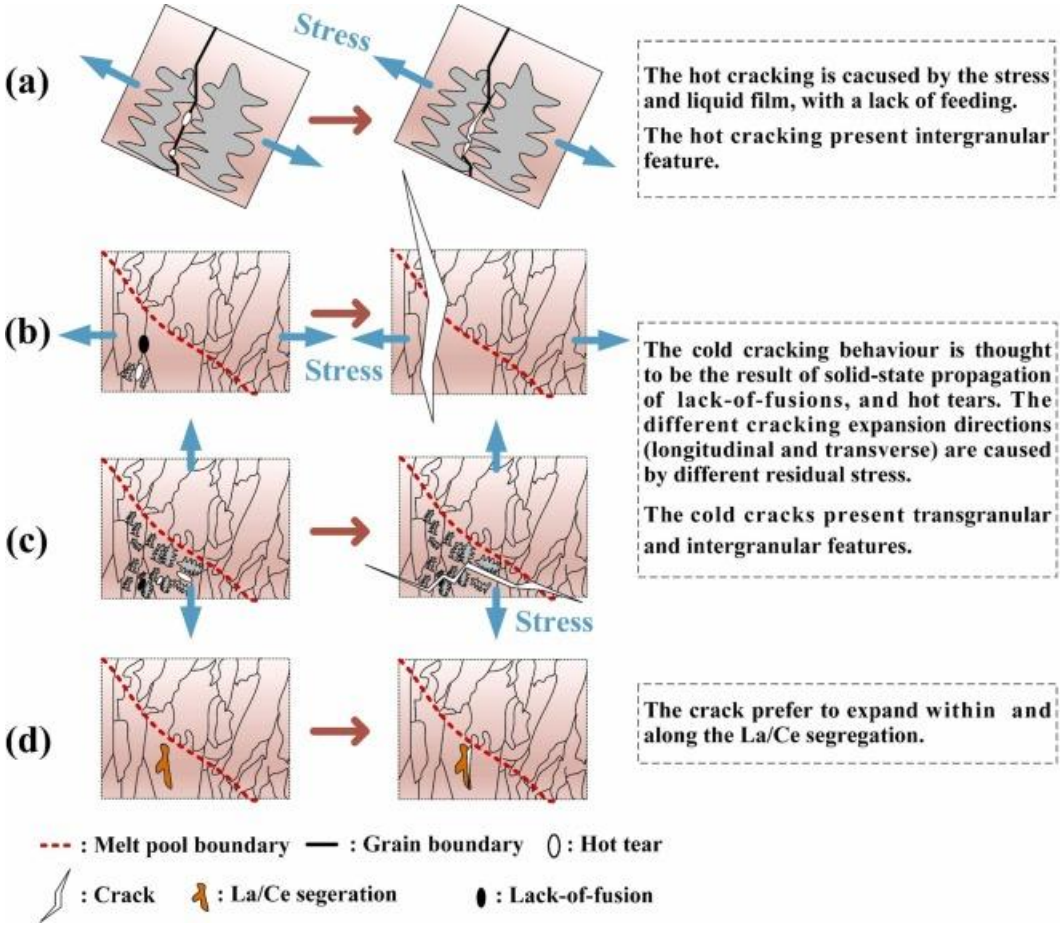

Figure 2.4 Summary of different crack types and their mechanisms: (a) Hot cracking, (b) Longitudinal cold cracking, (c) Transverse cold cracking, and (d) Segregation cracking [21].

In the L-PBF fabrication of K418 nickel alloy, Lu et al. [24] observed that increasing the laser power from 160 W to 240 W significantly reduced surface defects and induced a microstructural transition from columnar dendrites to cellular crystals, While the others processing parameters keep unchanged: the Scanning speed is 1200 mm/s, layer thickness is 0.03 mm and the hatch spacing is 0.07 mm. Optimal mechanical properties were achieved when the grain size was minimized, and the fraction of low-angle grain

boundaries was elevated. However, the rapid melting and solidification characteristic of L-PBF may cause stress concentration, leading to cracking and performance degradation. Tang et al. [25] reported the occurrence of thermal cracking during the L-PBF fabrication of IN939 alloy, while Griffiths et al. [26] identified the presence of liquefaction and solidification cracks in the L-PBF processing of CM247LC alloy. Similarly, Han et al. [27] demonstrated that in the L-PBF fabrication of Hastelloy X, thermal cracks typically nucleate at grain boundaries. They further noted that reducing trace elements in the alloy composition can effectively mitigate crack sensitivity.

Although L-PBF offers many advantages in the processing of nickel-based superalloys, such as microstructural control, the mechanisms underlying defect formation and suppression have attracted significant attention. Due to the exceptional properties of nickel-based superalloys, the defect mechanisms in L-PBF vary depending on the alloy composition. Consequently, understanding the mechanisms of defect suppression and improving performance remains a critical research gap. Systematic studies are required to fully comprehend these mechanisms and optimize the performance of nickel-based superalloys in L-PBF processes.

2.2.2 Strategies to Mitigate Defects and Enhance Properties

Heat treatments and Hot Isostatic Pressing (HIP) as post-processing techniques have been highly effective in addressing cracking issues in L-PBF-fabricated samples. Boswell et al. [28] investigated the effect of post-heat treatment on CM247LC alloy and observed that at temperatures exceeding 750°C, the precipitation of the γ' phase and the growth of grain boundary carbides contributed to reduced crack propagation. Han et al. [27] highlighted the benefits of HIP on Hastelloy X, demonstrating that the process effectively closed internal cracks and pores, resulting in a significant enhancement of fatigue life. Wang et al. [29] evaluated the combined effects of HIP and dual aging treatment on IN738LC nickel-based superalloy. Their findings revealed a reduction in the number of cracks, more uniform γ-phase precipitation, and remarkable improvements in both ductility and strength of the fabricated samples.

Additionally, Li et al. [30] investigated the effects of laser power and scanning speed on the molten pool characteristics during the L-PBF fabrication of IN625 alloy. Their findings revealed that the width and depth of the molten pool are significantly influenced by these parameters, with high-power conditions leading to an increase in the occurrence of gas pores. Samuel et al. [31] examined the friction behavior of L-PBF-fabricated IN718 alloy and observed that as temperature increases, the wear mechanism transitions from abrasive wear to delamination and oxidative wear, resulting in increased wear loss and altered debris morphology.

L-PBF exhibits notable process dependency in the fabrication of nickel-based superalloys. By optimizing process parameters and post-processing techniques, the mechanical performance and microstructural properties of L-PBF-fabricated samples can be significantly improved. Specifically, the refinement of dendritic substructures and precipitate phases contributes to the superior mechanical performance [16]. For low (Al + Ti) content nickel-based superalloys, such as IN718 and IN625, the performance of L-PBF-fabricated samples is even comparable to that of traditionally forged components [32, 33]. This proves the feasibility of L-PBF and has sparked interest in its application to high (Al + Ti) content nickel-based superalloys, such as IN738LC.

Inconel 738LC (IN738LC) alloy is a precipitation-strengthened nickel-based superalloy developed by the ‘Licensees of International Nickel’ company in the United States [34]. It contains refractory elements such as W, Mo, Nb, and Ta. The alloy exhibits excellent creep resistance, oxidation resistance, and corrosion resistance through a combination of strengthening mechanisms, including precipitation strengthening by Ni_3(Al, Ti), solid solution strengthening by the dissolution of elements like W and Mo into the matrix, and grain boundary strengthening by carbides such as (Ti, Ta, Nb)C [35]. Therefore, IN738LC is widely used in the manufacture of heat- and corrosion-resistant turbine components in the aerospace and petrochemical industries.

In the L-PBF fabrication of IN738LC alloy, Rickenbacher et al. [36] observed that the grains exhibit a columnar structure along the axial direction, with a size smaller than that of traditional castings (<100 μm). The mechanical properties, including tensile strength and creep performance, were found to vary depending on the build direction. Samples parallel to the XOY plane exhibited higher tensile strength but poorer creep performance, while those parallel to the XOZ plane demonstrated superior creep performance. This effect is attributed to build-induced anisotropy, where XOY-oriented samples show higher tensile strength due to finer grains, while XOZ-oriented samples exhibit improved creep resistance as columnar grains aligned with the load direction suppress grain boundary sliding and dislocation climb. Xu Jianjun et al. [37] reported that high Al + Ti content in IN738LC alloy makes it prone to heat-affected zone liquefaction cracking during the L-PBF process, which is closely associated with the uneven distribution of residual stress. Cloots et al. [38], using atomic probe tomography, discovered that the enrichment of Zr at grain boundaries is a primary cause of crack formation. They also found that crack density is inversely proportional to porosity. Perevoshchikova et al. [39] utilized the Doehlert method to optimize process parameters and successfully fabricated IN738LC samples with a density of 99.5% and no microcracks. Engeli et al. [40] demonstrated that as the Si content increases, the crack density of L-PBFed IN738LC significantly rises, suggesting that Si has a notable impact on crack sensitivity.

In conclusion, the findings on microstructure evolution, crack formation mechanisms, and process optimization in L-PBF-fabricated IN738LC alloy provide valuable theoretical insights and experimental evidence for advancing its printability and mechanical performance. However, for IN738LC-based composites, the mechanisms for defect suppression and performance enhancement remain underexplored and undeveloped. Further research is necessary to validate and advance these aspects.

2.2.3 Effects of Process Parameters on Structural Integrity and Microstructure Evolution

L-PBF is a complex, non-equilibrium, rapid-time metallurgical process characterized by intense thermal and mass interactions [1, 2]. In the fabrication of nickel-based superalloys, transient temperature fields, flow fields, mass fields, and stress fields are closely influenced by specific process parameters. Crucial parameters, including laser power (P), scanning speed (v), hatch spacing (h), and powder layer thickness (t), directly impact the depth, width, and shape of the molten pool through the control of energy density. Additionally, the scanning strategy alters the relative overlap positions of trajectories and interlayer connections, significantly affecting the thermal history of the materials, which ultimately determines its microstructure and mechanical properties [19]. Therefore, by optimizing laser energy density and scanning strategies, the mechanical properties of L-PBF-fabricated nickel-based superalloys can be significantly enhanced.

In L-PBF, process parameters such as laser power, scan speed, hatch spacing, and layer thickness are commonly used in design of experiments (DoE) to explore and optimize build quality and performance. The most widely adopted DoE methods include full factorial design, response surface methodology (RSM), and orthogonal array design [41]. When categorized based on the number of experimental runs required, orthogonal design typically requires the fewest experiments, followed by RSM, while full factorial design demands the most extensive testing. Orthogonal experimental design is particularly suitable during the early stages of process development, where time and material costs are limited. It enables the prediction of optimal parameter combinations with minimal trials, which can then be validated through follow-up testing. However, its main limitations include a limited capacity to capture interactions among parameters and a lower resolution of response trends, which may affect its predictive accuracy in complex systems [42]. Response Surface Methodology, which requires a moderate number of experiments, allows for more detailed analysis of parameter effects and their interactions. Nonetheless, RSM still requires validation experiments, and its

performance is highly sensitive to the accuracy of the initial parameter range. This makes it less suitable when the parameter bounds are not well established and requires prior knowledge from the literature or pre-screening studies [43]. Full factorial design, despite requiring the highest number of experimental runs, offers the most comprehensive dataset. It is particularly useful for new material or under-researched alloys, where limited prior knowledge exists. This method provides high-resolution insight into both individual effects and interactions, helping to establish a more complete understanding of the process–property relationship [44].

Laser energy density is a pivotal parameter in L-PBF, expressed as laser linear energy density (E_l) and laser volumetric energy density (VED) [45]. E_l is defined as the ratio of laser power (P) to scanning speed (ν) and VED incorporates laser power (P), scanning speed (ν), hatch spacing (h), and layer thickness (t) [45, 46]. The corresponding equations for these metrics are represented as Equations (2.1) and (2.2):

$$E_l = \frac{P}{v} \tag{2.1}$$

$$VED = \frac{P}{(v \cdot h \cdot t)} \tag{2.2}$$

In these equations, P denotes laser power (W), ν represents scanning speed (mm/s), h is the hatch spacing (mm), and t refers to the layer thickness (mm). Laser energy density significantly influences the microstructural solidification of nickel-based superalloys during L-PBF [17, 19]. Table 2.1 outlines several commonly used L-PBF process parameters and their corresponding effects on melt track characteristics [19]. Studies [47, 48] have shown that the cellular crystal diameter in L-PBF-fabricated nickel-based superalloys is inversely proportional to the VED. This relationship arises because the morphology and size of the microstructure are determined by the temperature gradient (**G**) and solidification growth rate (**R**):

- **G/R** governs dendric morphology.
- **G** × **R** controls the dendritic size.

By adjusting L-PBF process parameters, it is possible to manipulate **G** and **R**, thereby fine-tuning the microstructure and optimizing the mechanical properties[47].

Table 2.1 Process parameters and their effects on L-PBF process [19].

Category	Parameter	Range	Impact
Laser parameters	Laser power	10–110 W	Primarily used to melt the powder. Higher laser power is suitable for high-melting-point powder materials.
	Pulse duration	10 ns–200 μs	Determines energy input; longer pulse durations increase melt pool depth and diameter.
Scanning parameters	Scanning speed	100–600 mm/s	Affects residual stress accumulation. Changes in scanning speed can lead to deformation or poor issues.
	Hatch spacing	-	Determines overlap between laser paths, influencing structural uniformity and strength.
	Scanning strategy	-	Impacts residual stress and printability; inconsistent scanning strategies can cause failure on printing.
Powder parameters	Particle size	15–50 μm	Influences laser energy absorption, powder density, and thermal conductivity.
	Particle shape	Spherical	Spherical powders offer better flowability, ensuring uniform distribution on the powder bed.
	Particle size distribution width	Around 1.38 μm	Narrower distribution increases surface area, enhancing laser

Category	Parameter	Range	Impact
			energy absorption efficiency.
	Layer thickness	20–100 μm	Determines the uniformity of the microstructure.
	Packing density	Typically, 50%–60% (as low as 30% for irregular powders)	Higher packing density improves thermal conductivity, resulting in better mechanical properties of samples.
	Material characteristics	-	Mechanical properties are determined by the combined effects of process parameters.
Temperature parameters	Powder bed temperature	Material-dependent	Affects laser absorption and thermal conductivity.
	Powder feeder temperature	-	Helps maintain consistent powder flowability and enhances energy absorption efficiency.

Figure 2.5 depicts the relationship between **G** and **R** [49]. The dendritic morphology within a molten pool varies significantly depending on location, as follows:

- **Top of the molten pool:** Characterized by low **G/R** and high **G × R**, leading to the formation of equiaxed dendrites with fine grains.
- **Bottom of the molten pool:** Dominated by high **G/R**, resulting in planar dendritic structures.
- **Center of the molten pool:** Features predominantly columnar dendrites.

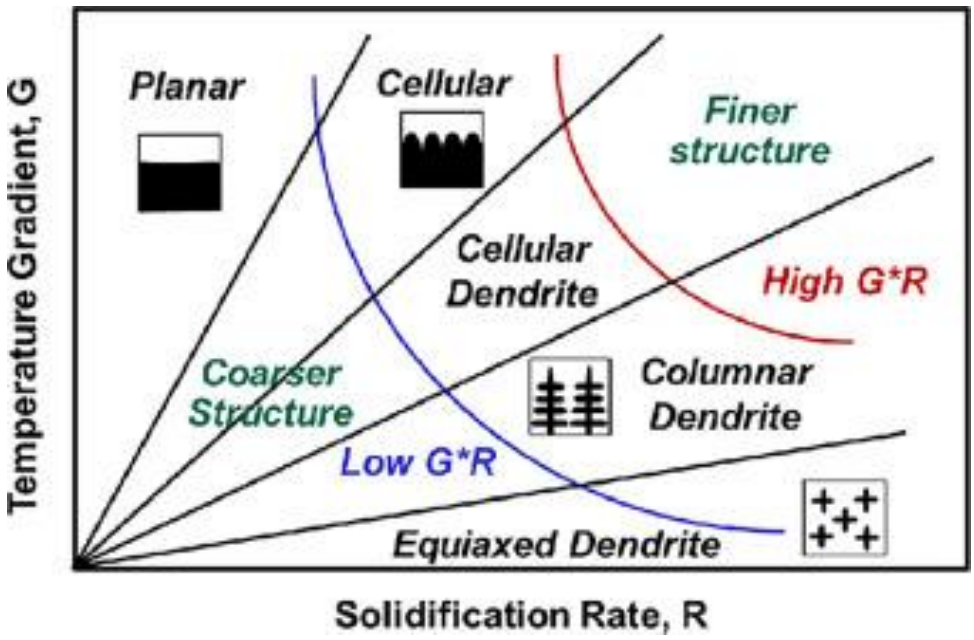

Figure 2.5 Influence of temperature gradient (**G**) and solidification rate (**R**) on microstructures [49].

As the temperature gradient to growth rate ratio (**G/R**) increases from the bottom to the top of the molten pool, the solidification morphology transitions from equiaxed dendrites to columnar dendrites and ultimately to planar dendrites. Within the appropriate process window of L-PBF, tailored process parameter combinations can modify the molten pool morphology, thereby enabling control the microstructure. For instance, Jian et al. [50] investigated the L-PBF fabrication of René88DT alloy and found that increasing the laser energy density causes a transition from equiaxed grains to columnar dendrites. This behavior is attributed to dendrite competition under low energy density conditions, where growth in multiple orientations leads to a near-equiaxed microstructure. Similarly, Watring et al. [51], in their study on Inconel 718, observed that low laser energy densities result in smaller grain sizes and a more uniform near-equiaxed microstructure.

The density of L-PBF-fabricated nickel-based superalloys is predominantly governed by laser energy density [51]. Low energy density: Insufficient powder melting results in the formation of irregular pores; high energy density: Excessive energy input leads to gas entrapment in the molten pool, causing spherical pores [52]. Furthermore, laser

energy density has a notable impact on cracking in nickel-based superalloys [53]. For low-crack-sensitivity alloys (e.g., Inconel 718 and Inconel 625), improper process parameters can cause cracking, but the overall process window is relatively broad [54]. In contrast, for high-crack-sensitivity alloys (e.g., CM247LC and Inconel 738), inappropriate laser energy densities further elevate the risk of cracking, resulting in a narrower process window [55, 56]. Table 2.2 summarizes common defects, their causes, and typical solutions in the L-PBF process [19].

Table 2.2 Defects, causes, and solutions in L-PBF [19].

Defect	Cause	Solution
Balling	The loose powder in the powder bed	Increase laser power and reduce scanning speed; apply remelting or secondary heat treatment.
Porosity	Insufficient laser energy density leading to low penetration depth	Lower laser power; increase laser scanning speed; apply remelting or secondary heat treatment.
High surface roughness	Oxidation in the atmosphere and partial molten powder adhering to the surface	Optimize process parameters; apply post-processing techniques such as sandblasting or chemical etching.
Residual stress, deformation, and cracking	Uneven local heating; rapid heating and cooling	Reduce scanning vector length; use a heated substrate or chamber; reduce laser scanning speed.
Composition vaporization / Alloy element loss	Overheating leading to material evaporation	Decrease laser power and energy; increase hatch spacing; increase layer thickness.
Oxide inclusion	High oxygen affinity of the powder leading to oxide inclusions	Provide protective gas; use a vacuum environment.

Under high-energy-density conditions, cracking issues become increasingly noticeable [40, 57]. Cater et al. [57] investigated the cracking behavior of CM247LC alloy during L-PBF processing and observed that high laser energy density promotes the formation of solidification cracks and large-sized pores. They identified the optimal process parameters for minimizing cracks as: scanning speed: 1500 mm/s, laser power: 150 W

and hatch spacing: 0.2 mm. Similarly, Mumtaz et al. [58] , in their study on Waspaloy alloy, reported that although high laser energy density achieves high densification, it also increases crack density. On the other hand, Perevoshchikova et al. [39], by optimizing L-PBF process parameters, achieved a density of 99.5% for IN738LC with no microcracks. These studies indicate that optimizing laser energy density and process parameters can balance high density with low defect rates in L-PBF process.

Additionally, the regulation of laser energy density has a significant impact on the mechanical properties and fatigue life of L-PBFed samples [59, 60]. Suitable laser energy density can optimize both the room-temperature mechanical performance and fatigue resistance, achieving a good match between structure integrity and performance. This is particularly crucial for low-crack-sensitivity nickel-based superalloys, while for high-crack-sensitivity alloys, optimizing the thermal history distribution through scanning strategy adjustments is necessary to reduce stress concentration and minimize crack formation [61]. Figure 2.6 illustrates changes in porosity, demonstrating that optimizing process parameters effectively reduces porosity, thereby improving fabrication quality [62]. Cater et al. [61] showed that by adjusting energy input and scanning strategies, it is possible to significantly reduce stress concentration regions within the molten pool, thereby enhancing the overall performance of fabricated samples.

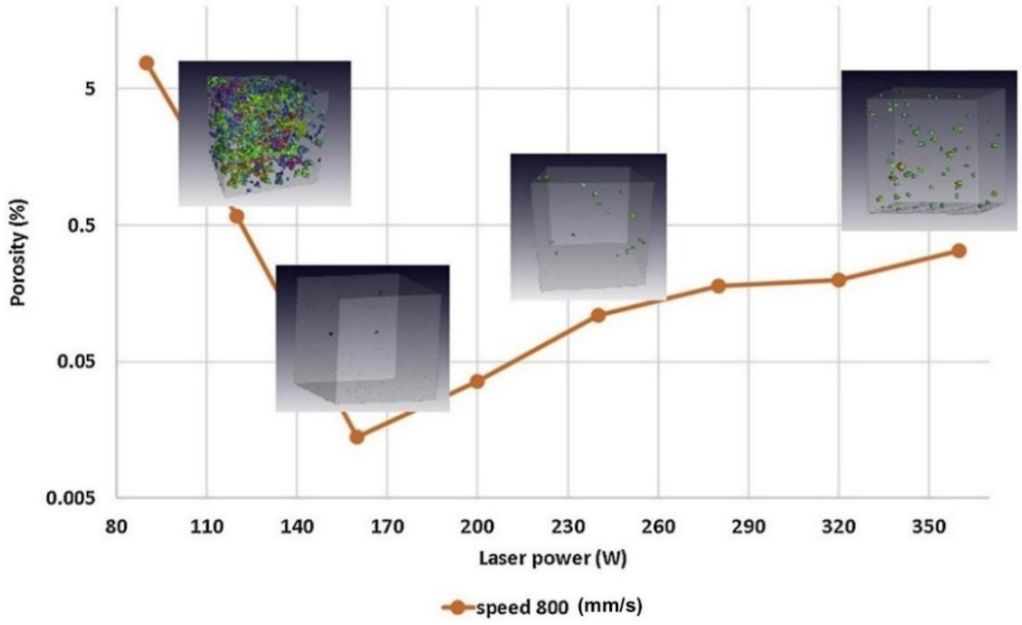

Figure 2.6 Effects of laser power on porosity in L-PBF, as revealed by X-ray computed tomography [62]

In summary, the microstructure and performance of L-PBF-fabricated nickel-based superalloys are strongly influenced by laser energy density. Optimized laser energy density promotes microstructure refinement, achieves high densification, and effectively mitigates the formation of cracks and pores. This optimization is a practical strategy for improving the performance of low-crack-sensitivity alloys (e.g., Inconel 718 and Inconel 625). Although for high-crack-sensitivity alloys (e.g., Inconel 738LC and CM247LC), findings from low-crack-sensitivity alloys offer theoretical support and practical guidance for fabrication. However, further exploration and validation are required to better understand the phases in their microstructure and their high-temperature performance. Additional research is particularly necessary for composite materials based on high-crack-sensitivity alloys.

2.2.4 Effect of Scanning Strategy on Structure Integrity

The scanning strategy, as a key parameter in L-PBF, plays a vital role in enhancing the structure integrity of materials [61]. Figure 2.7 illustrates several common scanning strategies used in L-PBF [63]. Scanning strategy refers to the combination of laser scanning direction and length within a single layer and the interlayer rotation angle. It is typically classified into four main categories [63]:

1) **Linear continuous scanning:** Combined with interlayer rotation angles such as 0°, 45°, 67°, and 90°.
2) **Fractal scanning:** Includes Hilbert and Peano-Gosper filling patterns.
3) **Spiral scanning:** Subdivided into in-plane spiral and outward spiral patterns.
4) **Island scanning:** Further categorized into block-shaped and stripe-shaped island geometries.

These scanning strategies represent an important research direction, as they influence the thermal field and molten pool dynamics by altering the direction and distribution of heat dissipation during L-PBF process. This modification influences the solidification behavior, thereby affecting grain growth orientation and size, which ultimately determines the mechanical properties of the fabricated nickel-based superalloys. The influence of scanning strategies on these alloys primarily focuses on defect control, grain morphology and texture regulation, and mechanical property enhancement [64]. An optimized scanning strategy not only reduces porosity and cracking but also controls grain growth direction and size, mitigates anisotropy, improves tensile strength and ductility, and reduces residual stress [61, 64]. Therefore, selecting and optimizing scanning strategies is crucial for improving the microstructural quality and mechanical properties of L-PBF-fabricated nickel-based superalloys.

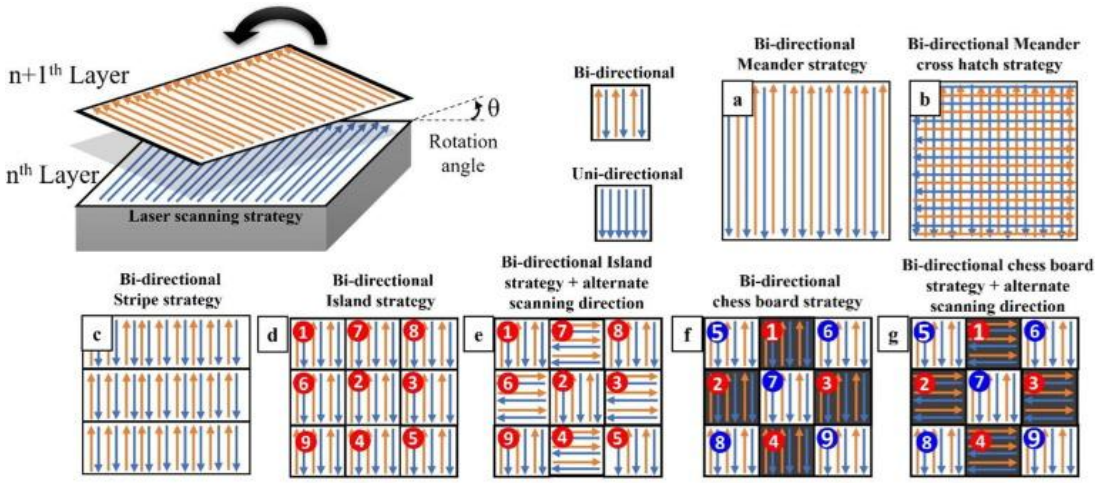

Figure 2.7 Schematic of common scanning strategies for L-PBF. Scanning strategies are classified as bidirectional or unidirectional. (a–g) illustrate examples of bidirectional scanning strategies, with numbers in (d–g) indicating the printing sequence. For instance, in the island strategy and the chess board strategy, the white or black squares are printed first, followed by the remaining sections [63].

The scanning strategy plays a pivotal role in influencing the densification and defect formation in L-PBF-fabricated nickel-based superalloys [61, 65, 66]. Catchpole et al. [65] investigated the impact of scanning strategies on the cracking behavior of CM247LC alloy and observed that the fractal scanning strategy resulted in a significant reduction in crack density and a 2 ± 0.7% improvement in density compared to the island scanning strategy. This underscores the potential of fractal scanning strategies for applications in hard-to-weld nickel-based superalloys. Lu et al. [66] reported that in the L-PBF fabrication of Inconel 718, reducing the block size of the island scanning strategy to less than 3 × 3 mm² led to a notable increase in crack rate, attributed to thermal stress concentration at weld track overlaps, which induced metallurgical defects. Carter et al. demonstrated that an intra-layer bidirectional continuous scanning strategy produced a more uniform grain structure compared to the island scanning strategy, thereby significantly reducing crack density [61]. These findings highlight the critical importance of scanning strategy optimization in controlling crack formation and porosity defects, thereby achieving higher densification and improving the overall quality of L-PBF-fabricated nickel-based superalloys.

In addition to defect control, scanning strategies can effectively regulate the grain morphology and texture of L-PBF-fabricated nickel-based superalloys [67, 68]. Wan et al. investigated the effects of two scanning strategies on the grain structure and texture of L-PBF-fabricated Inconel 718 alloy, revealing that a bidirectional non-rotational scanning strategy (X) and a 90° interlayer rotational scanning strategy (XY) produced bimodal grain structures and oriented columnar grain structures, respectively [68]. Sun et al. reported that in Ni-25at. %Mo alloy, scanning strategies significantly influenced texture formation and can be concluded as below: (1) bidirectional non-rotational and 90° rotational scanning resulted in single-crystal-like textures; (2) 67° rotational scanning produced a fiber-like texture [67]. By controlling scanning strategies, the thermal flow—referring to the direction and distribution of heat conduction during the L-PBF process—can be manipulated to tailor local thermal gradients and cooling rates, which directly affect solidification behavior; this enables the promotion of equiaxed grain structures over columnar growth, thereby reducing microstructural anisotropy and improving mechanical uniformity in the fabricated components [61, 69, 70]. Kirka et al. demonstrated that a point heat source filling strategy in EBM-fabricated Inconel 718 facilitated the formation of equiaxed grain structures [69]. Nadammal et al. observed that increasing the scanning vector length by tenfold reduced texture strength by half, attributed to finer recrystallized grains due to altered thermal gradients [70]. Carter et al. highlighted that a partitioned scanning strategy in CM247LC alloy could locally induce equiaxed grain structures [61]. These findings underscore the potential of scanning strategy optimization to control microstructural characteristics, enhancing uniformity and texture properties in nickel-based superalloys fabricated by L-PBF.

Scanning strategies have been shown to significantly improve the mechanical properties of L-PBF-fabricated nickel-based superalloys [68, 71, 72]. Wan et al. [68] explored the influence of scanning strategies on the mechanical properties of Inconel 718. Their results revealed that non-rotational interlayer scanning produced samples with superior tensile strength and fatigue strength compared to those fabricated using a 90° interlayer rotational bidirectional scanning strategy. This performance

enhancement was primarily attributed to the fine-grain structure induced by processing, rather than porosity size, crystal orientation, or dendritic structure. Wang et al. [71] studied the effects of stripe scanning and checkerboard scanning strategies on the room-temperature tensile properties of GH4169 alloy. They observed that checkerboard scanned samples exhibited higher tensile strength. The enhanced work-hardening capability was linked to differences in residual stress distribution and the uneven grain structure in checkerboard scanned samples. McLouth et al. [72] demonstrated that a continuous scanning strategy significantly improved the creep performance of L-PBF-fabricated Inconel 718. Compared to the island scanning strategy, the continuous scanning approach aligned the crystal texture parallel to the loading direction, resulting in a 51% increase in creep elongation. Therefore, by fine-tuning the scanning approach, it is possible to improve microstructural characteristics, suppress crack formation, and achieve significant enhancements in the mechanical performance of L-PBF-fabricated components.

In conclusion, scanning strategies significantly impact the L-PBF fabrication of nickel-based superalloys by influencing heat dissipation, solidification, and thermal history within the molten pool. Optimizing scanning strategies minimizes defects such as cracks and porosity while enhancing microstructural uniformity, improving tensile strength, fatigue resistance, and creep performance. However, for high-crack-sensitivity alloys like IN738LC, key gaps remain. The interaction between scanning strategies and IN738LC's thermal and mechanical properties is not fully understood. Research is needed to tailor scanning patterns for its unique characteristics, particularly to optimize the distribution of gamma prime phases and mitigate residual stress. Additionally, the combined effect of scanning strategies and laser energy density on defect suppression and microstructure control warrants further exploration. Integrated regulation of scanning strategies, laser energy density, and preheating will be crucial for advancing the performance of IN738LC, enabling its application in high-demand sectors.

2.3 Metal Matrix Composites via Additive Manufacturing

2.3.1 Ceramic Reinforcements in Metal Matrix Composites

Metal Matrix Composites (MMCs) are composed of a metal matrix phase and at least one reinforcing phase, which may take the form of particles, flakes, whiskers, or fibers, often made of ceramics, carbides, or other metallic materials [73]. Compared to traditional single-phase metal alloys, MMCs have garnered significant attention in structural applications due to their enhanced mechanical and physical properties, offering cost-effectiveness and performance customization tailored to specific requirements, particularly in the aerospace and automotive industries [74]. Since the late 1950s, MMCs have become a focus of research, initially motivated by the need to meet the high temperature demands of aerospace engines. By the 1960s, ceramic whiskers were being employed as discontinuous reinforcements in metals. Subsequently, the 1970s and 1980s saw the widespread adoption of MMCs in the automotive industry, driven by goals of lightweighting and performance enhancement [75]. Over the past two decades, advances in manufacturing technologies and materials science have urged unprecedented growth in MMC research and applications. Investigations into their mechanical behavior and strengthening mechanisms have led to substantial improvements in strength, stiffness, and weight reduction [76]. Currently, significant attention is focused on aluminum, copper, iron, nickel, and titanium-based composites, along with a wide range of reinforcing phases (e.g., carbides, nitrides, oxides) and matrix combinations, which have been extensively studied in the literature [73]. MMCs remain a high-potential material class for both scientific exploration and industrial application.

Additive Manufacturing (AM) has emerged as a transformative technology, gaining considerable attention for its applications in the fabrication of ceramics and ceramic-reinforced metal matrix composites (MMCs), and is increasingly becoming a focal point of research [73]. Figure 2.8 illustrates the mechanism by which the addition of TiC optimizes the microstructure of AA2024 composites, enhancing their performance by suppressing columnar dendritic structures and promoting equiaxed grain formation

[77]. Unlike traditional subtractive manufacturing methods, the ASTM defines AM as "a process of joining materials layer by layer from 3D model data to create an object" [12]. AM technology demonstrates substantial advantages in fabricating complex-shaped components, including [2, 3]: (1) High design flexibility; (2) Customization capability; (3) Reduced production cycles; (4) Elimination of molds or assembly and (5) Lower energy consumption. Therefore, these unique attributes make AM an ideal platform for manufacturing ceramics and ceramic-reinforced MMCs, facilitating their broader adoption in high-performance and complex application environments.

The improvement in mechanical properties of particle-reinforced composites is typically governed by three primary mechanisms [78, 79]: grain refinement, load-bearing strengthening, and Orowan strengthening. Grain refinement increases the density of grain boundaries, which act as barriers to dislocation motion, thereby enhancing strength through the Hall–Petch effect. Load-bearing strengthening arises when rigid second-phase particles support a portion of the applied stress, reducing the load transferred to the matrix. Orowan strengthening occurs as dislocations are forced to bypass non-deformable particles by looping around them, which increases resistance to plastic deformation. The synergistic action of these mechanisms leads to significant improvements in strength and deformation resistance.

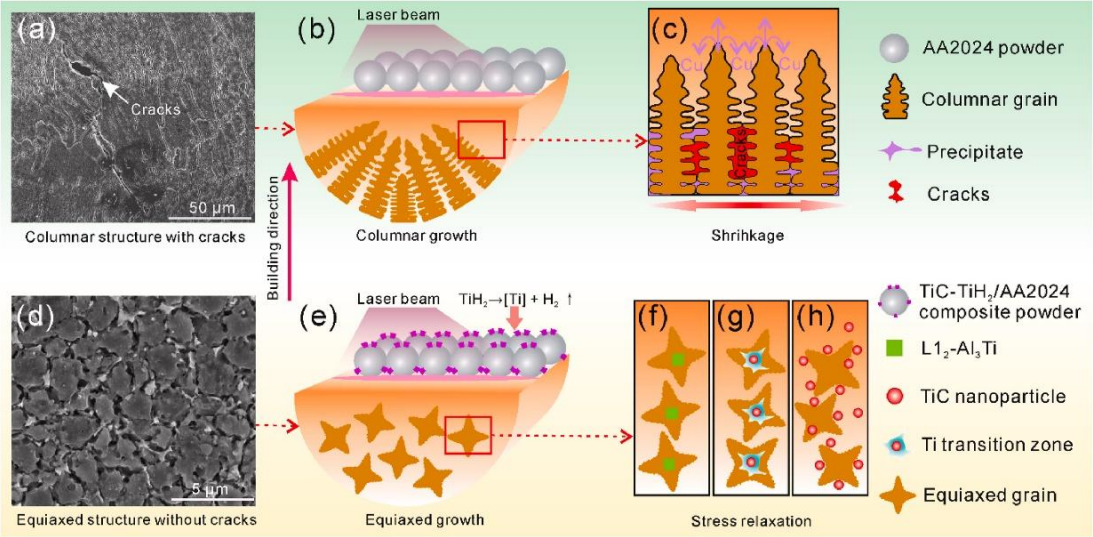

Figure 2.8 Schematic illustrations of microstructures and solidification mechanisms in L-PBF-processed AA2024 alloy (a–c) and TiC–TiH_2/AA2024 composite materials (d–h). (a) Columnar grain structure with cracks in the AA2024 alloy; (b–c) Columnar grain growth during the solidification process of the AA2024 alloy; (d) Equiaxed grain structure in TiC–TiH_2/AA2024 composite; (e–h) Equiaxed grain growth during the solidification of the AA2024 alloy with TiC–TiH_2 [77]..

In conclusion, nano-reinforced MMCs in AM hold significant potential due to their enhanced properties from nanostructures, such as improved strength, wear resistance, and thermal stability. However, key gaps remain, including achieving uniform nanoparticle dispersion to prevent agglomeration, optimizing the bonding interface for efficient load transfer, and understanding the influence of AM parameters on microstructure and defect formation. Additionally, the high-temperature performance, fatigue behavior, and long-term durability of these materials require further exploration. Addressing these challenges is critical to unlocking their full potential for applications in aerospace, automotive, and energy sectors.

2.3.2 Ceramic-Reinforced Nickel-Based MMCs and Strengthening Mechanisms

Incorporating ceramic particles as a reinforcing phase into a Nickel metal matrix leads to the formation of metal matrix composites (Ni-MMCs), which effectively combine the advantages of ceramics and Nickels [80]. This approach imparts high strength, wear resistance, and corrosion resistance to metal materials, significantly enhancing their durability and service life in harsh environments [81]. Moreover, the introduction of

ceramic particles has been shown to enhance the overall performance of Ni-MMCs, establishing it as a key focus of current research [80, 81].

Incorporating reinforcing particles into nickel-based composites using L-PBF has shown significant potential to enhance material performance by optimizing interfacial bonding and tailoring the microstructure. Zhang et al. [82] investigated the microstructure and mechanical properties of GTD222 and TiC/GTD222 nickel-based composites fabricated via L-PBF following solution and aging heat treatments. Their findings revealed that the TiC/GTD222 composite featured finer grains and a higher density of precipitates, leading to superior yield strength and reduced elongation at both room and elevated temperatures. The enhancement in yield strength was attributed to the improved grain load-bearing capacity and the synergistic Orowan strengthening effect. Mandal et al. [83] compared the performance of TiC/B4C-reinforced IN718 metal matrix composites fabricated via L-PBF. They found that TiC-reinforced composites exhibited strong interfacial bonding, whereas B4C-reinforced composites suffered from microcracks at the interface due to substantial differences in their thermal expansion coefficients. Additionally, as the TiC volume fraction increased, the wear volume of the composite progressively decreased, reaching a minimum at 20 vol% TiC, which highlighted the exceptional wear resistance of TiC-reinforced materials.

The study of nickel-based composites has increasingly focused on enhancing their mechanical properties by changing melt pool dynamics through the incorporation of reinforced particles, utilizing their thermal mismatch with the nickel alloy. Shi et al. [84] investigated micron-sized WC particle-reinforced IN718 composites fabricated via L-PBF. They observed that WC particles formed fine dendritic structures at the matrix interface, with dendrites nucleating and growing along the interface, nearly perpendicular to the WC particle edges. The study concluded that the annular heat flow and radial temperature gradient surrounding the WC particles increased the contact area between the matrix and the particles, resulting in enhanced interfacial bonding, improved wear resistance, and superior mechanical properties. Chen et al. [85] explored

nano-graphene (GNP)-reinforced K418 nickel-based composites using L-PBF. Their findings revealed that the rapid cooling rate of up to 10^8 K/s generated Marangoni convection, enabling uniform distribution of GNPs within the γ-matrix grains. This process led to the formation of a near-equiaxed grain structure and a crack-free microstructure. With the incorporation of GNPs, the material exhibited enhanced mechanical properties, with the yield strength increasing from 912 MPa to 1018 MPa and the ultimate tensile strength improving from 1078 MPa to 1200 MPa.

The reinforced particles were found to effectively reduce defects. Han et al. [86] investigated the L-PBF fabrication of 1.0 wt.% submicron WC-reinforced Hastelloy X nickel-based composites and observed that the incorporation of WC particles led to the formation of intergranular microcracks, which propagated along grain boundaries and extended across multiple deposition layers. The grain size ranged from a few micrometers to hundreds of micrometers. Despite negligible changes in elongation, the addition of WC resulted in a 13% increase in yield strength, attributed to the enhancement of dislocation density, thereby improving the mechanical properties. Lerda et al. [87] investigated 1.0 wt.% submicron TiC-reinforced IN625 composites fabricated via L-PBF. They found that submicron TiC powders exhibited better flowability, effectively reducing internal defects. The hardness of the TiC-reinforced IN625 material increased by 60%, while yield strength and tensile strength improved by 23% and 25%, respectively, with similar elongation. Figure 2.9 illustrates the microstructure of a 3D network structure Ni-based composite reinforced with TiN nanoparticles [88]. This structure leads to significant grain size refinement and enhances the material's strength.

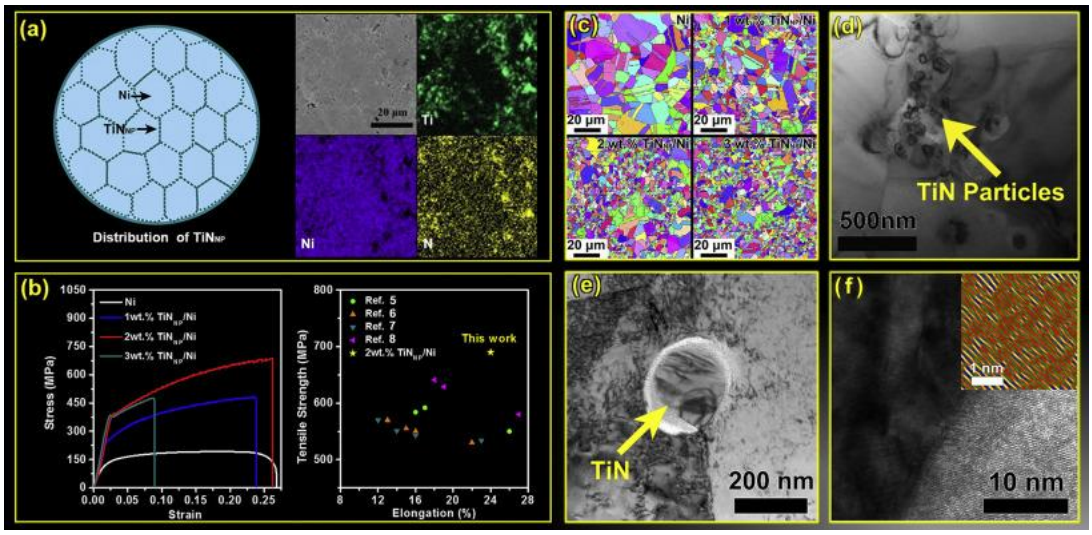

Figure 2.9 Preparation of TiN nanoparticle-reinforced Ni-based composite with a 3D network structure. The composite exhibits improved mechanical properties due to grain refinement and increased dislocation density at the TiN/Ni interface [88].

Reinforcing particles can serve various functional purposes, enabling the creation of specialized surfaces, such as superhydrophobic surfaces, and unique microstructures. Zhang et al. [89] explored the development of a superhydrophobic surface in TiC/IN718 nanocomposites fabricated via L-PBF. At a scanning speed of 600 mm/s, the surface exhibited a micro-metal particle structure coupled with uniformly distributed nanoparticles, achieving a contact angle of 151.5°. This surface demonstrated excellent corrosion resistance, effectively preventing the penetration of corrosive media in a 3.5 wt.% NaCl solution. Zhao et al. [90] investigated the microstructure and mechanical properties of TiB_2-reinforced IN718 composites fabricated via L-PBF. Under optimal process parameters, the relative densities of IN718-1.0 wt.% TiB_2 and IN718-2.0 wt.% TiB_2 composites reached 99.71% and 99.67%, respectively. The IN718-2.0 composite exhibited superior grain refinement, leading to room-temperature enhancements in microhardness (19.93%), yield strength (24.83%), and ultimate tensile strength (11.07%). At 650°C, its yield strength and ultimate tensile strength further increased by 31.76% and 17.62%, respectively, demonstrating remarkable high-temperature performance advantages. Xing et al. [91] successfully fabricated nano-TiC/Ni-Cr-W superalloys. The incorporation of nano-TiC led to significant grain refinement, characterized by the elimination of columnar crystals and a reduction in the secondary

dendrite arm spacing. These microstructural improvements resulted in a substantial enhancement of the alloy's ultimate tensile strength and yield strength, primarily attributed to the strengthening effect of grain refinement. Moreover, the formation of MC-type carbides provided anchoring points for dislocation, promoting load transfer and further reinforcing the mechanical strength.

In conclusion, incorporating ceramic particles into the metal matrix enhances nucleation, promotes grain refinement, improves molten pool dynamics, and reduces residual stress, offsetting performance degradation from γ′ phase coarsening or dissolution [81]. As a result, ceramic-reinforced alloys demonstrate superior strength, wear resistance, and creep resistance across a range of temperatures. Despite these advantages, challenges remain, including ensuring uniform particle dispersion, improving interfacial bonding between the particles and the matrix, and maintaining phase stability under high-temperature conditions. Overcoming these obstacles is crucial for fully unlocking the potential of ceramic-reinforced nickel-based superalloys in high-performance applications.

2.4 Powder Integrity in the L-PBF Process

L-PBF process is characterized by complex interactions among the laser, powder particles, melt pool, and metal vapor [92]. During the melting process, variations in powder characteristics and the influence of melt pool dynamics and other instabilities often lead to the formation of metallurgical defects and these defects compromise the printing quality, reduce densification, and impair the mechanical properties [92]. In particular, in nickel superalloys, these challenges cannot be fully mitigated through process parameter optimization alone [16, 93]. For example, increasing the laser power exacerbates the evaporation of alloying elements, leading to porosity defects and surface balling phenomena [93].

For the hard-to-weld, or non-weldable materials such as GH3230, CM247LC, and IN738LC superalloys, the L-PBF process window is inherently narrow. Consequently,

relying solely on process parameter optimization is often inadequate for achieving significant improvements in fabrication quality [55, 56, 94]. To address these challenges, optimizing powder characteristics is essential for enhancing the quality and performance of fabricated samples [92].

In the L-PBF process, powder characteristics are broadly categorized into three primary types [92]:

1) **Powder particle characteristics:** These include particle size, morphology, surface condition, humidity, and thermal conductivity. These parameters define the fundamental particle properties and aggregation behavior, exerting a direct influence on the powder's flowability and packing performance.
2) **Powder flow characteristics:** Metrics such as Hall flow rate, angle of repose, and rheological behavior describe the flowability and spreading dynamics of the powder during static or dynamic motion. These characteristics are pivotal for achieving uniform powder spreading throughout the L-PBF process.
3) **Powder packing characteristics:** Parameters like packing density, tapped density, and the Hausner ratio characterize the packing behavior of powders under varying motion and loading conditions. These attributes directly impact the density of the powder layer and the melt pool stability during processing.

This section explores the significant influence of powder particle characteristics on flowability, packing behavior, and printing quality. By examining particle size, morphology, and preparation methods, it investigates their impact on L-PBF, aiming to enhance the quality and performance of L-PBF-fabricated components.

2.4.1 Impact of Powder Particle Size Distribution on the L-PBF Process

Powder particle size is a critical factor influencing the quality of L-PBF fabrication, and its optimization is essential for improving the overall quality of fabricated components [95]. To ensure the uniformity and density of the powder layer, the powder layer thickness is generally required to be more than twice the particle size [92]. Smaller

powder particles, due to their larger specific surface area, can absorb more energy, facilitating adequate melting and densification. However, excessively small particles tend to aggregate, leading to reduced flowability, uneven powder spreading, and potential balling phenomena. Conversely, overly large particles can reduce melt pool stability, increase powder spatter, and degrade the surface quality of L-PBFed samples [93]. To achieve high densification and optimal surface quality, the L-PBF process typically utilizes a balanced particle size distribution. This approach leverages finer particles to fill the gaps between coarser particles, establishing a continuous melt pool and enhancing the overall printing quality [93, 95].

Powder particle size distribution is a crucial factor affecting packing density [96]. Figure 2.10 illustrates the relationship between particle size mixing and packing density [97]. According to particle packing theory:

- For mono-size ideal spherical particles, the packing density in a random loose packing state is generally below 60%.
- Introducing particles of varying sizes allows smaller particles to occupy the voids between larger particles, exceeding the packing density limits of mono-size systems.

Under ideal conditions [97]:

- With a diameter ratio of 2.41:1 and a number ratio of 1:1 (large to small particles), the packing density can increase to 92%.
- Incorporating three particle sizes (with diameter ratios of 9.23:3.83:1 and number ratios of 1:1:4) further raises the packing density to 95.7%.

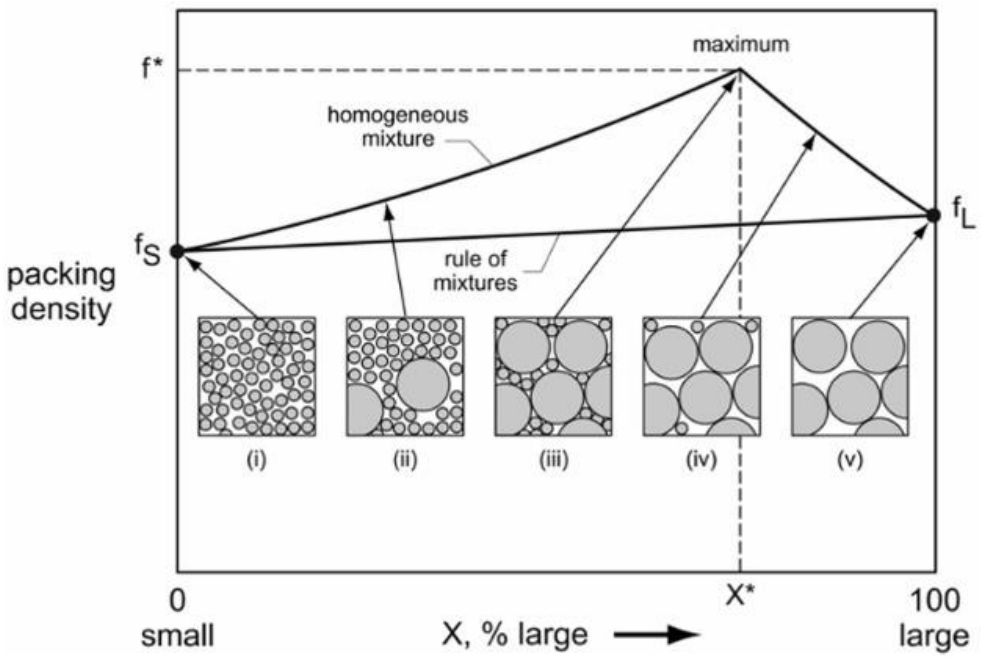

Figure 2.10 Packing density (f) as a function of the mixture of small particles (s) and large particles (L) in the particle size distribution, highlighting the maximum filling density ($f*$) [97].

This rational distribution of multi-sized particles minimizes void fraction, bringing the packing density close to the theoretical maximum density. However, in the practical L-PBF process, the powder packing density typically only reaches 50%-60%, which is far below the predictions of theoretical models [95]. This difference arises primarily due to: (1) The continuous variation in the particle size range of L-PBF powders, which hinders ideal particle arrangement and complete void filling; (2) The L-PBF process is constrained by powder layer thickness (usually 0.02-0.1 mm) as well as the powder flowability, which necessitates that the maximum particle size must be smaller than the layer thickness [95].

In summary, optimizing particle size distribution to improve the packing density of the powder bed is crucial for enhancing L-PBF fabrication quality and has been shown to improve sample performance. However, how to effectively refine particle size distribution remains a key gap, particularly for composite materials, where challenges related to preparation processes make this issue even more critical. Further research is needed to address these challenges.

2.4.2 Enhancing Performance Through Optimization of Particle Size Distribution

The particle size distribution of powder is closely related to the manufacturing process, and the particle size characteristics of powders produced by different processes have a significant impact on the L-PBF process and the quality of fabrication [98]. Figure 2.11 illustrates several common metal powder production techniques [99]. Plasma Rotating Electrode Process (PREP): Powders produced by PREP exhibit a narrow particle size range and are generally coarser. After sieving, the proportion of fine particles (<30 μm) in PREP powder is relatively low, which helps reduce particle adhesion, thereby improving flowability and packing density. Gas Atomization (GA): This process uses high-pressure gas to atomize molten metal, resulting in powders with a wider particle size range. GA powders have a higher proportion of ultrafine particles (<30 μm), but the proportion of coarser particles (70-100 μm) still dominates. Plasma Atomization (PA): The particle size distribution of PA powders is similar to that of GA powders, but PA powders have a higher proportion of 50–70 μm particles compared to coarse particles (70–100 μm) [100]. The characteristics of different powder production processes determine their suitability for L-PBF [101]. PREP powders are suitable for processes requiring high flowability and packing density, whereas GA and PA powders, with higher fine particle content, are better suited for complex fabrication [100]. This highlights the critical role of selecting an appropriate powder production method and optimizing particle size distribution to enhance the quality of L-PBF-fabricated samples.

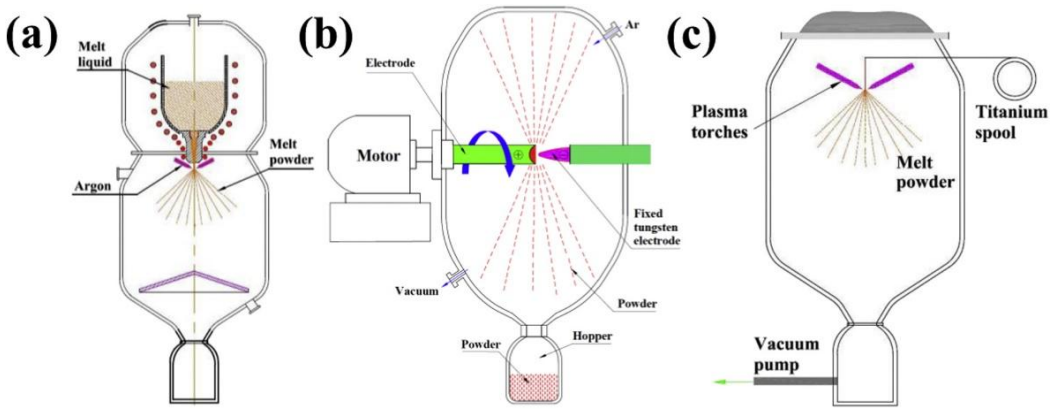

Figure 2.11 Schematic illustration of different powder manufacturing methods: (a) Gas Atomization (GA), (b) Plasma Rotating Electrode Process (PREP), and (c) Plasma Atomization (PA) [99].

According to the bimodal model, the optimal packing density can be achieved by the rational mixing of coarse and fine particles [102]. However, the effectiveness of coarse and fine particle mixing in the L-PBF process varies significantly [95]. When coarse particles dominate: large voids remain unfilled by fine particles, resulting in low packing density. When fine particles dominate, two key challenges arise: (1) While fine particles fill the voids, an excessive proportion creates a wedging effect, pushing coarse particles apart and reducing the packing density; (2) The high specific surface area of fine particles increases interparticle adhesion, resulting in agglomeration, which reduces the powder bed's packing density [95, 103]. Therefore, in the L-PBF process, it is crucial to optimize the ratio and size distribution of coarse and fine particles to avoid the agglomeration caused by an excessive proportion of fine particles, while ensuring that fine particles effectively fill the voids between coarse particles.

Farzadfar et al. [104] optimized IN718 powders using the maximum packing density model. Their experiments involved adding varying proportions of fine powders (D10: 6.2 μm, D50: 10.5 μm, D90: 16.9 μm) to coarse powders (D10: 26.5 μm, D50: 35.5 μm, D90: 50.5 μm), with a particle size ratio of 3:4. The results demonstrated that incorporating an appropriate amount of fine powder effectively filled the voids between coarse particles, significantly enhancing both packing density and tapped density. As illustrated in Figure 2.12 [104], the mechanical performance indicates that the mixed powder exhibits higher tensile strength than the original powder.

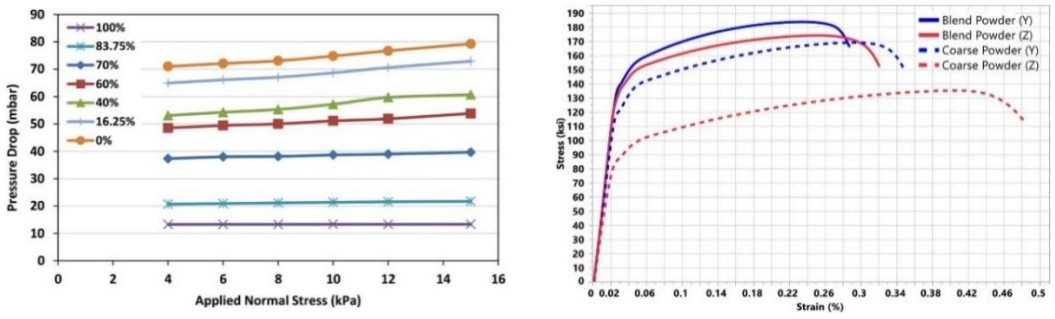

Figure 2.12 (Left) Permeability measurements under different normal stresses (4–15 kPa) with coarse particle volume fractions indicated. (Right) Engineering stress-strain curves comparing 83.75%/16.25& mixed powder (solid line) and coarse particle powder (dashed line), showing enhanced strength but reduced ductility in mixed powder samples [104].

However, it is important to note that in bimodal particle size distribution systems, high laser energy density can lead to the vaporization of fine particles, causing a decrease in densification [105]. Figure 2.13 illustrates the relationship between the relative density of samples fabricated with unimodal (GH) and bimodal (BIMO) feedstock powders and VED, as validated by Coe's study [106]. In the fabrication of 316L stainless steel, a performance comparison of unimodal powder (D50 = 36.31 μm) and bimodal powder (D50, L = 36.31 μm, D50, S = 5.52 μm) revealed the following: (1) At low laser power (107–178 W), bimodal powders achieved lower porosity and higher densification; (2) At higher laser power, the vaporization of fine particles reduced densification [106]. Similarly, Haferkamp et al. [107] studied the performance of 316L powders (D50 = 20.3 μm and 60.3 μm) mixed in 3:1, 1:1, and 1:3 weight ratios. The findings indicated that as the proportion of coarse powder increased, the instability of the laser melt pool intensified, solidification irregularities in single tracks became more pronounced, and porosity increased significantly.

Based on the above discussion, optimizing the mixing ratio of coarse and fine particles and aligning it with laser energy density is critical for enhancing packing density, melt pool dynamics, and overall fabrication quality. Therefore, further research is particularly needed to control particle size distribution in nickel-based composites, where the addition of secondary particles complicates powder interactions. Improving these interactions and energy absorption is critical for enhancing the performance of L-PBF-fabricated components.

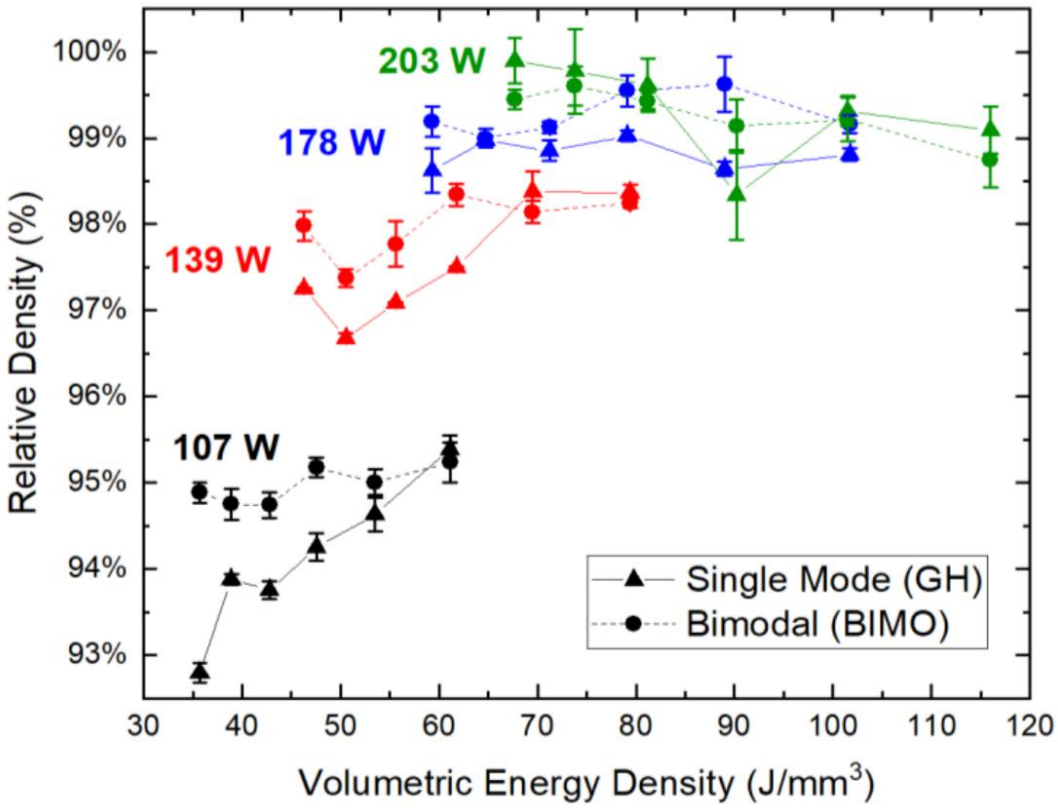

Figure 2.13 Relative density of 316L samples as a function of VED, comparing single-mode (GH) and bimodal (BIMO) feedstock powders [106].

2.4.3 Influence of Powder Morphology on Mechanical Properties and Performance

Different methods of metal powder production result in a variety of particle shapes, including spherical, near-spherical, plate-like, and irregular polygonal shapes and the flowability and packing density of powders are closely related to particle shape [98]. Non-spherical particles exhibit larger contact areas, which increase interparticle friction, resulting in lower flowability and reduced packing density [107]. In contrast, spherical powders, characterized by their smaller contact areas and lower frictional resistance, generally demonstrate superior flowability and higher packing density [98].

In the L-PBF process, powder flowability and packing density are critical parameters that directly influence the fabrication quality [98, 100]. Good flowability ensures uniform powder spreading, while a high packing density contributes to establishing a denser powder layer [108]. Highly spherical powder particles facilitate uniform powder

layer thickness, promoting process stability and enhancing the densification and surface quality of fabricated components [109]. However, during powder production, defective particles such as satellite particles and hollow particles are often unavoidable [107]. These defects can trap residual gases within fabricated samples, resulting in porosity and significantly degrading their mechanical performance [19]. Although such particles are challenging to remove via post-production sieving, they can be effectively mitigated during powder production by employing techniques such as increasing cooling rates or spheroidization treatments [110]. Highly spherical powders exhibit superior dynamic flowability and spreading behavior, which enhance powder bed packing density, improve densification, and elevate the overall quality of fabricated samples. As shown in Figure 2.14, higher powder sphericity significantly improves flowability; the closer the particle shape is to a perfect sphere, the better the flowability [111].

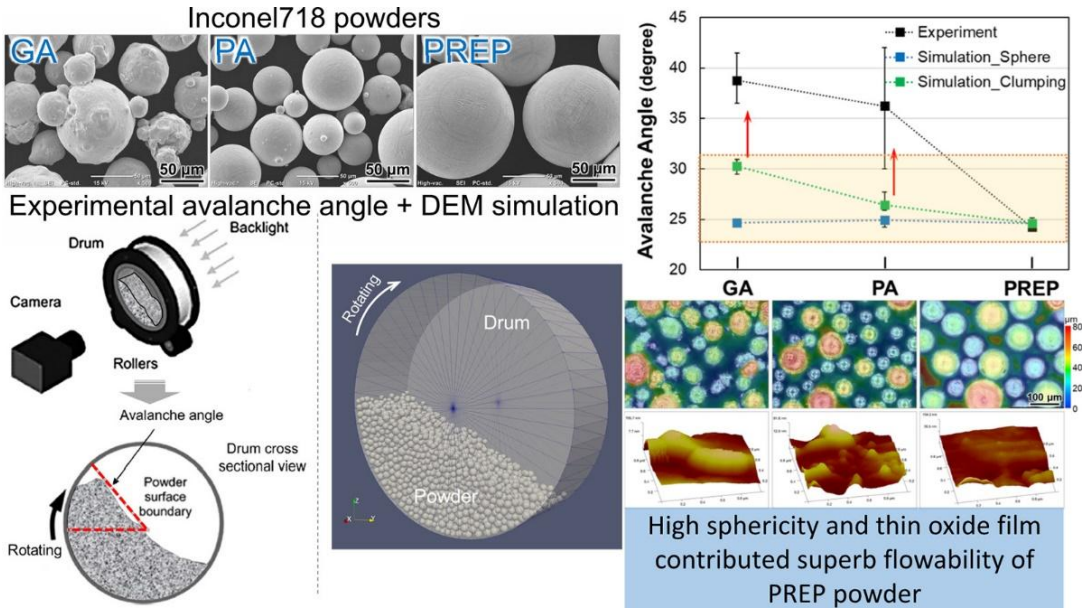

Figure 2.14 Impact of surface roughness and oxidation on powder flowability, highlighting high sphericity and thin oxide layers as critical factors for the superior flowability of PREP powders [111].

The morphology of metal powders is significantly influenced by the powder production process [100]. Among the leading techniques for producing spherical powders, GA, PREP, and plasma atomization (PA) consistently yield powders with higher sphericity, which is critical for improving powder bed packing density and the densification of

fabricated samples [100, 111]. Ruan et al. [101] investigated the characteristics and fabrication performance of IN718 powders produced via GA and PREP processes. Their findings revealed that, although the mechanical properties of fabricated samples were comparable under optimized L-PBF parameters, differences in powder morphology had a significant impact on the processable parameter window. Due to their higher sphericity and smoother surfaces, PREP powders exhibited superior packing density and flowability, enabling a broader processable window. Riener et al. [96] analyzed three gas-atomized powders and one plasma-atomized powder of AlSi10Mg material, concluding that higher powder sphericity led to significant improvements in fabrication densification. Similarly, Brika et al. [112] compared Ti6Al4V powders produced by two PA processes and one GA process. Their research established a positive correlation between powder sphericity and flowability. Figure 2.15 provides SEM images of powders produced by various methods, highlighting the superior sphericity and quality of PREP powders [113]. These results emphasize the significance of optimizing powder production techniques to enhance powder sphericity as an important strategy for improving L-PBF fabrication quality.

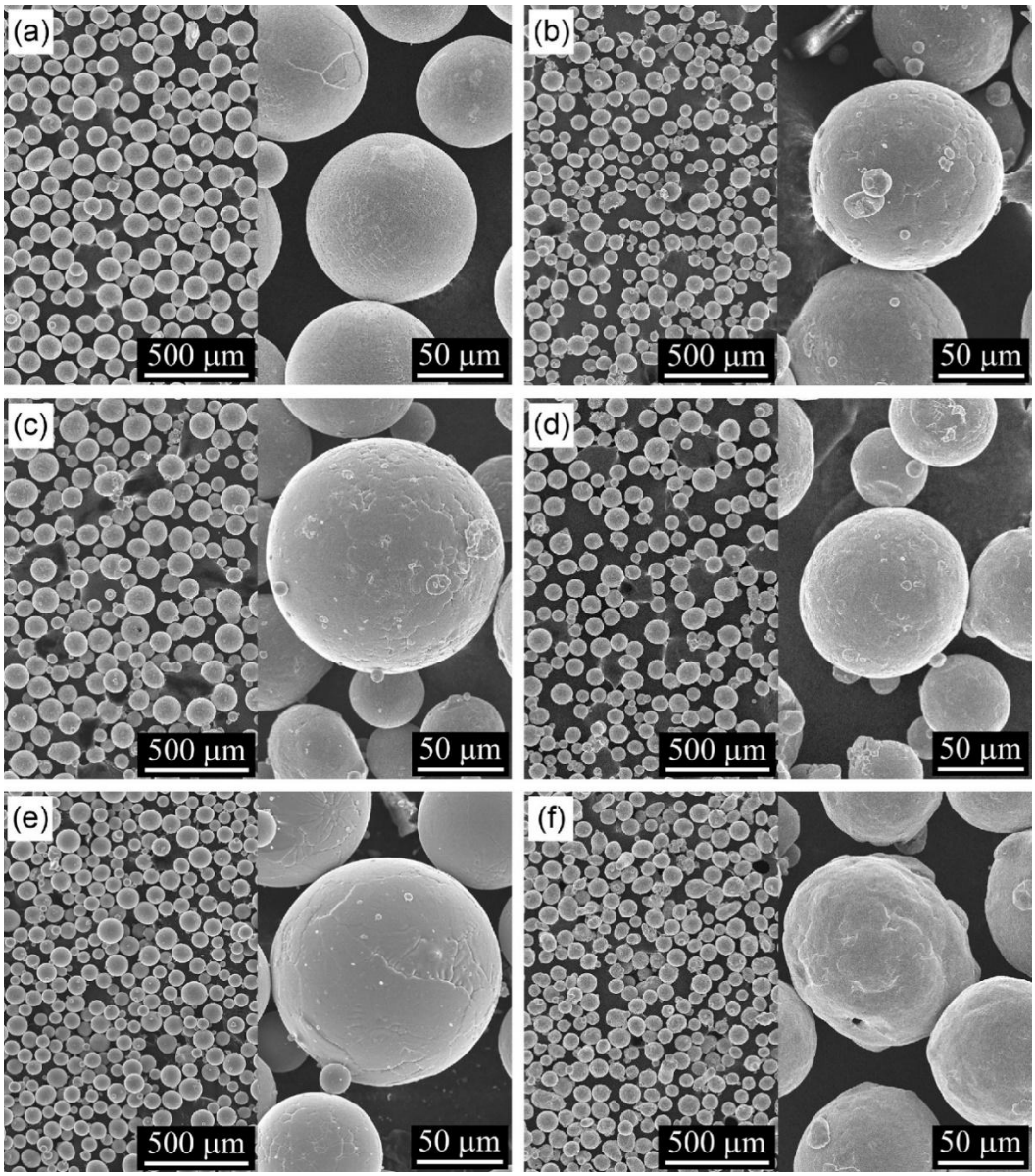

Figure 2.15 SEM images of Ti-6Al-4V powders provided by: (a) TIMET, (b) Puris, (c) ATI, (d) Hoeganaes, (e) AP&C, and (f) Praxair [113].

Although PREP and PA powders, with their high sphericity and excellent flowability, are more effective at enhancing powder bed density and fabrication quality, their high costs limit their use. In contrast, water atomization (WA), due to its low cost, has been considered as an potential alternative to GA in L-PBF [100]. However, the irregular morphology of WA powders results in performance that is significantly inferior to that of gas-atomized (GA) powders [114-117]. Fedina et al. [114] compared the performance of low-alloy steel powders produced by WA and GA processes in laser fabrication. WA powders, with their irregular shapes, were prone to clumping, bridging,

and interlocking, resulting in lower packing density than GA powders. During the L-PBF process, the low powder bed density of WA powders caused a 15% reduction in melt pool height and a 31% smaller cross-sectional area compared to GA powders. Similarly, Engeli et al. [115] evaluated the L-PBF performance of eight batches of IN738LC powders. Under identical process parameters, samples fabricated using GA powders exhibited porosities below 1.2%, while those using WA powders showed porosities as high as 3.5%. The study highlighted those powders with better flowability achieved higher powder bed density, significantly reducing the porosity and crack density of fabricated samples. Irrinki et al. [116] compared WA powders and GA powders of 17-4PH stainless steel, finding that GA powders, with their superior sphericity, yielded components with greater densification. Likewise, Abdelwahed's research [117] on WA-produced Fe-C-Cr-Mo alloy powders demonstrated that powder characteristics not only influence densification but also significantly affect the microstructure and mechanical properties of L-PBF samples. Therefore, while the WA process provides a cost advantage, its powders fall short of those produced by the GA process in terms of sphericity, flowability, and powder bed density. As a result, the densification and mechanical performance of samples fabricated with WA powders are comparatively inferior. Table 2.3 presents a detailed comparison of different powder manufacturing processes, highlighting their key characteristics, advantages, and limitations [118].

Table 2.3 Comparison of different powder manufacturing routes [118].

Powder manufacturing process	**Vacuum induction melting GA (VIGA)**	**Electrode induction melting GA (EIGA)**	**PREP**	**PA**	**PS**
Raw material	Elemental material, ingots, rods	Precision-machined rods	Precision-machined rods	Wire	Irregular powder
Powder size distribution	Broad size distribution, includes a	Broad size distribution, includes a	Narrow size distribution, low	Broad size distribution, higher	Closely related to raw powder,

Powder manufacturing process	**Vacuum induction melting GA (VIGA)**	**Electrode induction melting GA (EIGA)**	**PREP**	**PA**	**PS**
	proportion of fine powder (-325 mesh)	proportion of fine powder	proportion of fine powder	proportion of fine powder compared to VIGA and EIGA	includes a proportion of fine powder
Productivity	~100 kg/8 hours	~100 kg/8 hours	150–200 kg/8 hours	<100 kg/8 hours	<100 kg/8 hours
Powder morphology	Near-spherical, sphericity >80 %	Near-spherical, sphericity >80 %	Spherical, sphericity >90 %	Spherical, sphericity >85 %	Spherical, sphericity >85 %
Powder characteristics	Contains some satellite and porous powder, slightly higher oxygen content	Contains some satellite and porous powder, slightly higher oxygen content	Fewer satellite and porous powders, lowest oxygen content	Few satellite and porous powders, slightly higher oxygen content	Minimal satellite and porous powders, relatively higher oxygen content
Limitations	Potential contamination by impurities	High gas consumption	Low proportion of fine powder	Suitable for wire feedstock	Suitable for raw powder feedstock

In conclusion, powder morphology is a critical factor in L-PBF, particularly for composites, as the powder preparation process often causes deformations, irregular shapes, and surface defects in the powder particles. These morphological issues can reduce packing density, disrupt uniform energy absorption, and lead to defects such as porosity and poor interfacial bonding. For composite materials, where secondary reinforcements are often introduced, these challenges are further amplified, as achieving uniform dispersion and minimizing agglomeration are critical yet difficult. Despite its importance, the relationship between powder morphology, reinforcement dispersion, and the resulting mechanical and microstructure properties of L-PBF-fabricated samples remains insufficiently understood. Further research is needed to systematically study how variations in powder morphology affect critical aspects of the

L-PBF process, such as melt pool stability, microstructural evolution, and defect suppression. This understanding will guide the development of improved powder preparation techniques and enable the production of high-performance composite components with enhanced reliability and consistency.

2.4.4 Effect of Powder Cohesion on the L-PBF Process

In the L-PBF process, samples are fabricated through the layer-by-layer spreading of metal powders followed by laser melting. Among the critical particle characteristics, powder cohesion plays a pivotal role in determining spreading uniformity and fabrication quality [119]. Alongside particle size and morphology, cohesion emerges as a key factor influencing the process [95]. Optimizing the cohesion properties of metal powders is crucial for enhancing fabrication quality in the L-PBF process [120].

According to the Geldart classification [121], powders are divided into four groups based on their gas-solid fluidization behavior: Group A (aeratable), Group B (bubbling), Group C (cohesive), and Group D (spouting). Metal powders used in additive manufacturing primarily fall into Group A and Group C:

- **Group A powders:** Coarse particles with sizes ≥40–100 μm, characterized by good flowability.
- **Group C powders:** Finer particles exhibit increased specific surface area, elevated surface energy, and enhanced cohesion, resulting in cohesive behavior that significantly reduces flowability and spreading performance.

Given that the L-PBF process typically employs metal powders with particle sizes of 15–53 μm or 20–63 μm, the cohesion properties within this range are pivotal in influencing powder flowability and spreading behavior [10, 121]. Therefore, investigating and optimizing cohesion is critical for improving powder flowability and ensuring uniform powder spreading.

In the field of additive manufacturing, Gärtner et al. [120] addressed the issues of poor

flowability and low powder bed density in gas-atomized CoCrFeNi powders by coating the surface of powders smaller than 20 μm with nanoscale silica. When the concentration of the coated particles reached 0.153 wt.%, the dynamic angle of repose (AOR) decreased by 50%, and the packing density increased by 30%. These findings highlight that surface coating is effective in reducing powder cohesion, significantly enhancing powder flowability and spreading density, and consequently improving the fabrication quality.

In summary, optimizing particle size distribution, enhancing powder sphericity, and reducing cohesion are essential strategies for improving packing density and powder spreading quality in L-PBF. These enhancements play a critical role in minimizing porosity and lack-of-fusion defects, thereby achieving higher density. Although optimizing powder characteristics—such as greater sphericity and a well-balanced particle size distribution—shows potential for reducing crack formation, it remains insufficiently studied in hard-to-weld nickel superalloys. Significant challenges persist for these alloys, particularly in understanding the influence of powder surface chemistry and particle interactions on cohesion and spreading behavior. Addressing these gaps is crucial for developing tailored powder preparation methods that enhance fabrication quality, crack resistance, and overall mechanical performance.

2.5 Numerical Simulation of L-PBF

The L-PBF process involves complex physical interactions between the high-energy laser beam and metal powder, encompassing the propagation and penetration of the laser through the discretely stacked powder particles [122]. These phenomena are influenced by factors such as the powder stacking configuration, composition and physical properties of the powder, and powder layer thickness. Within the melt pool, the dynamics of heat conduction and mass transfer play a pivotal role in determining the microstructure, and mechanical properties and fabrication quality of L-PBFed samples [123].

Compared to the DED process, the L-PBF process generates a smaller melt pool with a higher temperature gradient and introduces complex phenomena such as molten powder spattering and vaporization [124]. The spherical metal powders tailored for L-PBF typically have a particle size of less than 60 μm, while the laser beam diameter is generally under 100 μm [122]. The micron-scale precision required for L-PBF, combined with the limitations of current real-time monitoring technologies in accurately observing melting/solidification dynamics and heat/mass transfer phenomena within the melt pool, underscores the need to investigate the physical phenomena of the L-PBF process through high-fidelity simulation [123, 124].

Therefore, a comprehensive understanding of the melting and solidification behavior of powders, along with metallurgical principles in the L-PBF process, is essential for uncovering the complex interactions between the laser and particles. High-fidelity simulation serves as a crucial link between melt pool dynamics and thermal characteristics [122]. Furthermore, L-PBF simulations provide valuable insights into the physical mechanisms that govern the evolution of fabrication quality, microstructural characteristics, and mechanical performance [124]. Thus, it will offer a critical theoretical foundation of high-performance nickel-based superalloys in laser additive manufacturing.

This section primarily discusses the simulation of L-PBF, exploring various phenomena observed during the simulation and their correlation with potential defects. It then focuses on the relationship between microstructural simulations and fabrication quality. Lastly, it delves into spattering phenomena, their formation mechanisms, and the primary defects they cause, thereby enhancing the understanding of the L-PBF process and providing a foundation and reference for process optimization.

2.5.1 Thermo-Mechanical Simulation of L-PBF

In the process of L-PBF, powdered materials undergo cyclic heating and cooling, ultimately transforming into a solid state [1]. This process represents a non-equilibrium thermodynamic phenomenon, characterized by microstructural heterogeneity, thermal plasticity, and phase transformation plasticity [124]. Residual stresses in the as-built samples may induce microdefects and macroscopic failures, such as microcracks and deformations [125]. Studies [126, 127] have shown that process parameters—including laser power, scanning speed and scanning strategy—have a significant impact on the distribution of residual stress during L-PBF. However, due to the complexity and variability of residual stress distributions, along with the inherent challenges of directly measuring internal stresses experimentally, most experimental techniques fail to provide accurate insights. To address this, researchers have turned to finite element simulation as a tool for understanding how process parameters influence residual stress distribution and formation mechanisms as illustrated in Figure 2.16 [126]. These simulations offer theoretical support for analyzing and predicting the evolution of thermal stress and residual stress.

The coupled thermal-mechanical model is crucial for simulating residual stress in L-PBF simulations. Cao et al. [128] developed a three-dimensional transient fully coupled thermal-mechanical model to analyze deformation and residual stress distribution of Ti-6Al-4V alloy. Their study revealed that deformation increased significantly during the deposition of the first 2–3 layers but decreased as the number of layers increased. Moreover, at least two preheating treatments effectively reduced deformation and residual stress. Yang et al. [129] introduced a coupled modeling approach to predict the microstructure, hardness, residual stress, and deformation of large L-PBFed parts. By employing a moving heat source model, they accurately predicted temperature variations and leveraged sequentially coupled thermal-mechanical analyses to explore the relationships among residual stress, deformation, and structural stiffness. Zhao et al. [130] studied the temperature and stress distribution of GH4169 alloy during the L-PBF process. Their findings indicated that L-PBF is a dynamic process characterized by

rapid melting and solidification. Significant temperature gradients at the overlapping regions between scan tracks induced thermal strain and stress concentrations, leading to warping deformation. In areas distant from the melt pool, stress gradually increased, with tensile stress dominating the forming zone, while compressive stress occurred near the melt pool. When the part cooled to room temperature, tensile stress concentrated at the edges of the component, and residual stress along the z-axis caused additional warping deformation.

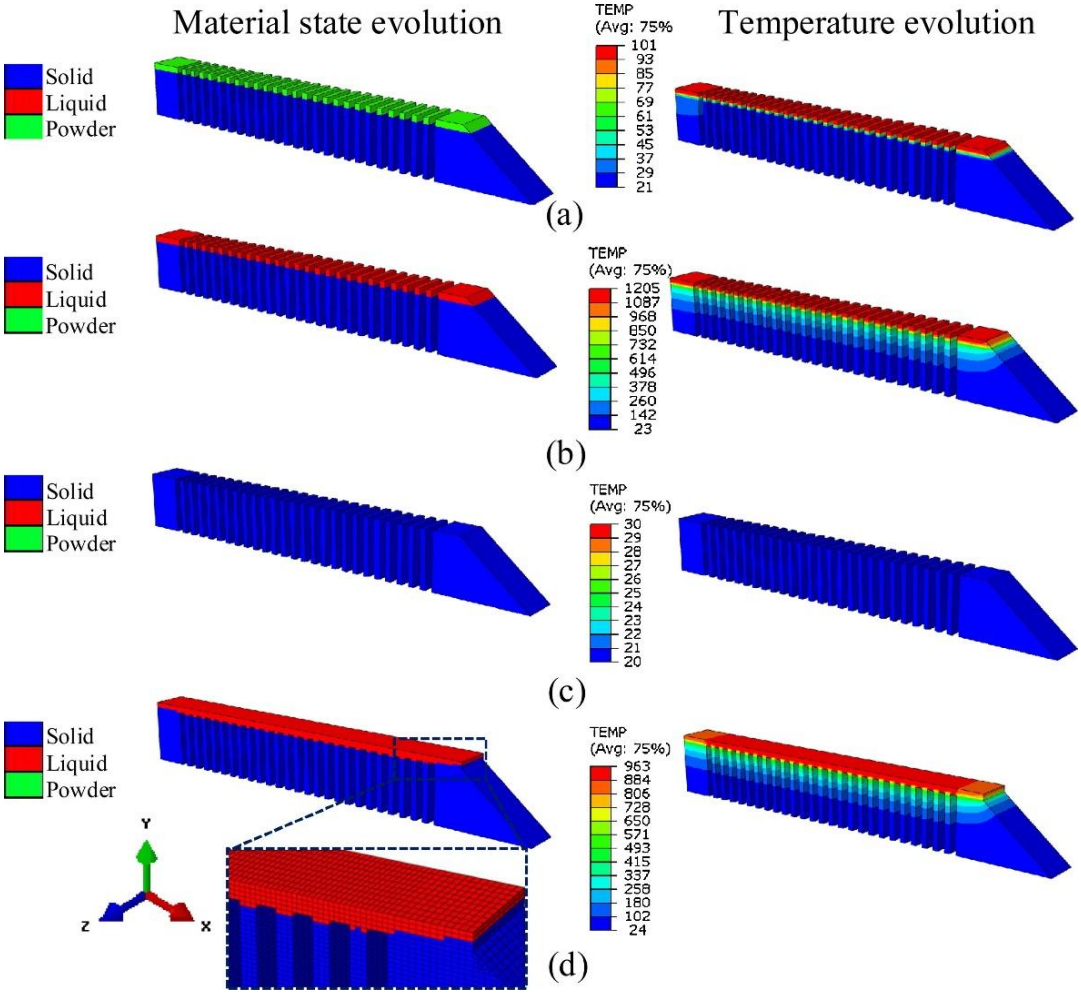

Figure 2.16 Evolution of material state and temperature field during L-PBF: (a) newly deposited powder layer, (b) fully melted layer, (c) solidified layer, and (d) re-melted layer [126].

Scanning strategies play a crucial role in simulations aimed at understanding the effects of residual stress. Parry et al. [131] employed a thermally coupled model to study the influence of laser scanning strategies on residual stress distribution during L-PBF. Their

findings revealed that the largest stress components aligned parallel to the laser scanning direction, resulting in anisotropic stress distributions within the workpiece. Moreover, variations in laser scanning strategies altered the characteristics of stress distribution. Bian et al. [132] investigated the influence of varying laser power and scanning strategies on residual stress during L-PBF. They found that residual stress gradually decreased along the height of the as-built sample. Marques et al. [133] proposed a thermally coupled finite element model to systematically analyze the transition of powder from liquid to solid, encompassing melting, solidification, and cooling phenomena. Their work examined the effects of scanning strategies on stress field distribution and compared the thermal histories and stress distributions of unidirectional and alternating scanning strategies. The results revealed that residual stress in the sample was primarily caused by non-uniform thermal expansion and contraction, with higher temperature gradients corresponding to greater residual stresses. However, the differences in von Mises equivalent stress under different scanning strategies were found to be insignificant.

Although substantial progress has been made in numerical simulations of stress fields during L-PBF, most studies have focused on the effects of process parameters on residual stress and temperature distributions. Relatively few studies have investigated melt pool dynamics at the powder scale. Furthermore, current simulation methodologies are constrained by the limitations of the element-birth technique, hindering in-depth exploration of melt pool dynamics and their fundamental role in residual stress formation. To address these limitations, further advancements and refinements in numerical simulation techniques are essential for uncovering the intricate correlations between melt pool dynamics and residual stress mechanisms.

2.5.2 Powder-Based Simulation of L-PBF: Melt Pool Dynamics and Thermal Characteristics

The physical interaction mechanism between the high-energy laser beam and metal powder is fundamental to studying the melt pool dynamics in L-PBF [134]. Yang et al. [135], based on the ray-tracing principle, utilized theoretical modeling and calculations to reveal the influence of metal powder properties on laser absorptivity, establishing a quantitative relationship between laser absorptivity and material properties, particle size distribution and laser spot size. Additionally, to address the issue of low laser absorptivity in aluminum alloys, a multi-physics model of laser-powder interaction, based on the principle of ray irradiation, was developed [135]. The model revealed that, during laser transmission through the powder bed, multiple reflections and refractions occur, resulting in energy attenuation. These investigations offer critical theoretical insights into the efficiency of laser energy utilization in the L-PBF process.

Based on the aforementioned physical interaction mechanisms, Yuan et al. [136] conceptualized the L-PBF powder bed as a continuum and applied thermofluid dynamics principles to develop a multiphase flow physical model. This model systematically analyzed the influence of the L-PBF process on the temperature field, velocity field, and melt pool dynamics. Additionally, it elucidated the mechanism by which laser energy density governs the densification of L-PBF components. Similarly, Yan et al. [137] employed the finite element method combined with the physical interactions between the laser and powder to construct a continuous finite element model. This model investigated the processes of solid-liquid phase transition, material vaporization, and volumetric shrinkage under high-energy laser irradiation. Furthermore, it established a quantitative relationship between the process parameter and the dimensional accuracy of fabricated components.

By simulating the interaction between the high-energy laser beam and powder particles, phenomena such as vaporization and powder spattering are revealed. These phenomena significantly influence the melt pool dynamics, uncovering the underlying causes of L-

PBF defects [124]. For example, in light alloy laser additive manufacturing, elemental burnout and vaporization, caused by high-energy laser irradiation, exert a significant impact on the thermophysical properties and heat/mass transfer behavior of the melt pool [138]. Figure 2.17 highlights the physical phenomena occurring during the L-PBF process, alongside multi-physics simulations that capture these interactions [122].

Furthermore, powder spattering is an inevitable phenomenon during the L-PBF process, particularly under high laser energy density conditions, where melt pool instability results in significant spatter formation. In the high-fidelity models, this spattering behavior was found to not only disrupt heat and mass transfer at the melt pool's liquid/gas interface but also cause localized melt accumulation and defect formation, thereby adversely impacting fabrication quality [137, 138]. These complex phenomena underscore the importance of understanding the interaction mechanisms between the laser and powder through L-PBF simulations, as well as their impact on melt pool dynamics. Such understanding is essential for optimizing process parameters, improving melt pool stability, and enhancing the quality of fabricated components.

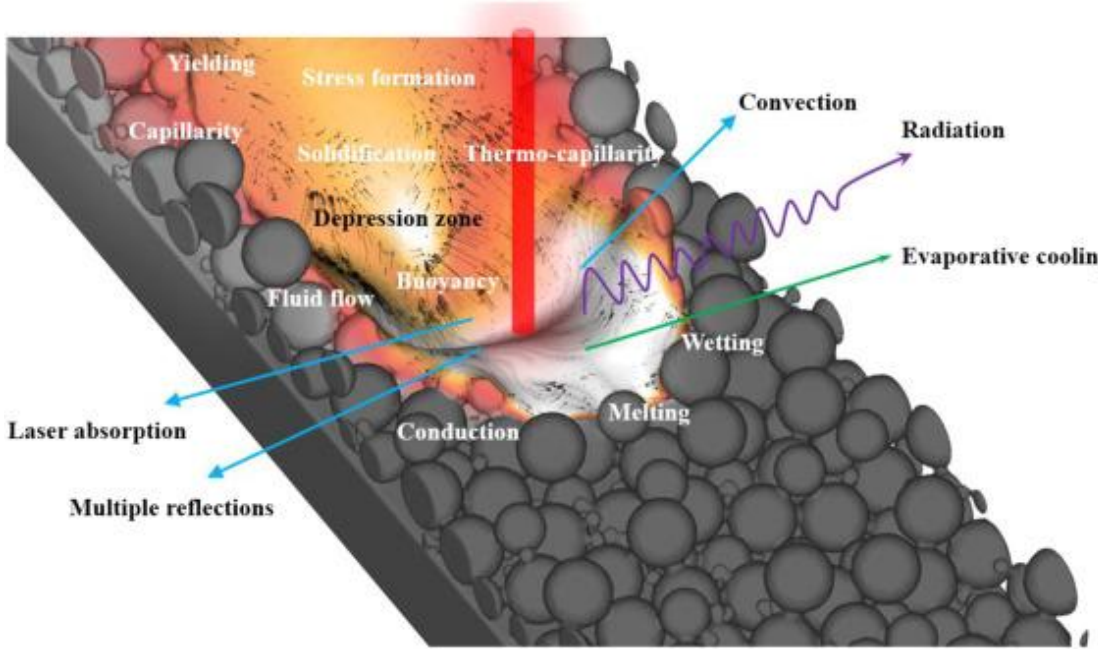

Figure 2.17 Illustration of multiple types of physical phenomena during the L-PBF process [122].

In summary, high-fidelity simulations play a crucial role in elucidating the phenomena and defect mechanisms associated with L-PBF process, offering insights often beyond the reach of experimental methods. Although significant progress has been made, key gaps remain in fully integrating powder morphology and real powder surface properties into simulation models. For MMCs, accurately capturing the interaction between the matrix and reinforcement particles at the microscale, as well as the effects of particle agglomeration and dispersion, is critical for improving simulation accuracy. Further advancements in simulation techniques are essential to bridge these gaps and enable predictive modeling of microstructure evolution, mechanical performance, and defect mitigation in MMCs during L-PBF.

2.5.3 Impact of Melt Pool Dynamics on Microstructure

The thermodynamic behavior of the melt pool is essential not only for the fabrication quality of L-PBF components but also for determining their microstructural characteristics [139]. Current research has predominantly focused on the temperature field and velocity field within the melt pool during L-PBF and their influence on solidification microstructures. These effects are primarily demonstrated in the following two aspects:

(1) Non-equilibrium solidification behavior of the liquid phase in the melt pool:

In the L-PBF process, the high-energy laser beam creates a significant temperature gradient in the melt pool, which affects the diffusion behavior of elements in composites [121]. The temperature characteristics within the melt pool determine solidification, including elemental diffusion capacity, distribution, and solidification rate. These factors contribute to a complex non-equilibrium solidification mechanism and variations in the resulting microstructures [122].

Zhang et al. [140] reported that lower laser scanning speeds during the L-PBF fabrication of high-strength aluminum alloys result in reduced cooling rates within the melt pool. This limited diffusion capacity of transition elements enables the

precipitation of the strengthening phase $Al_3(Sc,Zr)$ at the melt pool boundaries, facilitating the formation of high-strength aluminum alloys. In the case of ceramic particle-reinforced MMCs, controlling the melt pool's liquid-phase temperature field enables the calculation of the dissolution capacity of ceramic reinforcements and the elemental diffusion mode [122]. This approach allows for precise control over the formation and growth of in situ reinforcing phases, offering a novel strategy for the design and fabrication of MMCs with innovative in situ reinforcements.

(2) Characteristics of microstructures during solidification growth:

The temperature gradient within the melt pool during the L-PBF process influences solidification growth behavior and the resulting microstructures [124]. The layer-by-layer accumulation characteristic of the process introduces additional complexity, as the solidified microstructure may undergo remelting or recrystallization during subsequent laser scans, resulting in a highly complex growth process [139].

By simulating the temperature field of the melt pool in L-PBF and applying the cellular automaton algorithm, the growth patterns of microstructures during liquid-phase solidification under various process conditions can be revealed [139]. For instance, simulation results demonstrate that changes in the temperature gradient and solidification rate can produce diverse microstructural morphologies, including columnar grains, cellular structures, and equiaxed grains [141, 142]. Figure 2.18 illustrates a comparison between EBSD data obtained from coupled single-track simulation and experimentally measured EBSD data [143]. These findings elucidate the mechanisms governing the formation of complex solidification microstructures in L-PBF, providing a theoretical foundation for optimizing process parameters and enhancing mechanical performance.

In summary, understanding the interactions between heat and mass transfer and solidification behavior within the melt pool, optimizing thermodynamic parameters, controlling cooling rates and solidification growth are pivotal for tailoring and

controlling microstructures. These efforts are essential for enhancing the strength, toughness, and fatigue resistance of components fabricated via L-PBF and provide valuable strategies for designing high-performance composites. However, key gaps remain in fully elucidating the complex interplay between melt pool dynamics, cooling rates, and microstructural evolution, particularly for composite materials. The influence of secondary phases and reinforcement particles on solidification behavior and heat dissipation is not yet fully understood. Additionally, the effects of varying thermal gradients and localized temperature fluctuations on phase distribution and grain morphology require further investigation. Addressing these gaps is crucial for advancing the design of tailored microstructures and optimizing the performance of L-PBF-fabricated composites.

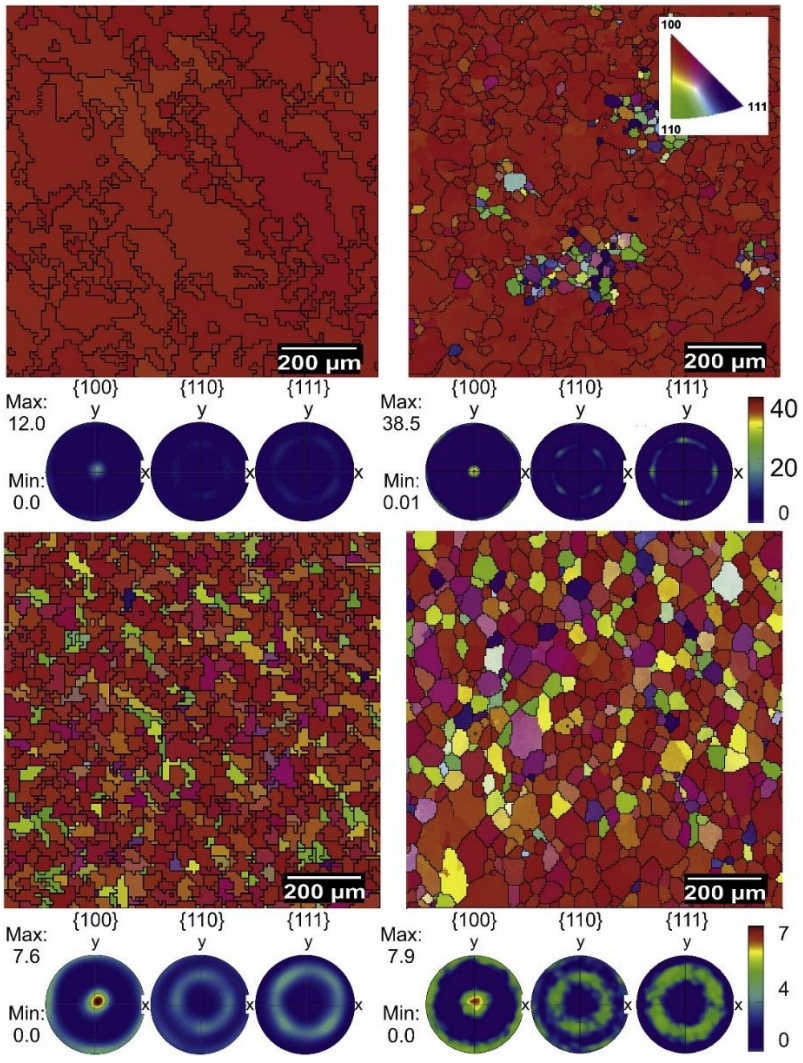

Figure 2.18 Comparison between simulated EBSD (left) and experimental EBSD results (right) [143].

2.5.4 Spattering Behavior and Formation Mechanisms in L-PBF

In laser welding processes, the study of spattering behavior is relatively well-established, providing important references for understanding the spattering mechanisms in the L-PBF process [144]. Research [145, 146] indicates that spattering in laser welding primarily originates from the ejection of molten powder around the keyhole opening. Li et al. [145] found that this phenomenon is associated with the shear forces exerted by high-temperature metal vapor ejected from the keyhole, which act on the molten material in the melt pool. Furthermore, Cai et al. [146] identified that spattering is influenced not only by the shear friction forces of metal vapor but also by the flow dynamics within the melt pool. Their findings underscore the complex mechanical interactions of metal vapor and their significant impact on spattering mechanisms.

As laser power density increases, spattering behavior intensifies [144]. Zhang M. J. et al. [147] observed that under high energy density, the frequency of ripple oscillations on the melt pool surface increases significantly. This phenomenon is attributed to the enhanced evaporation and vaporization efficiency of the molten metal. The intensified ripple oscillations cause localized molten material to detach from the rear of the melt pool, resulting in the formation of spattered droplets. The recoil pressure of metal vapor serves as the primary driving force behind liquid metal flow and spatter formation. Simultaneously, ripple oscillations on the melt pool surface affect the efficiency of laser energy absorption, further exacerbating the dynamic instability of the melt pool [144, 147]. These studies provide a critical theoretical foundation for understanding the spattering mechanisms in the L-PBF process.

Compared to laser welding, the L-PBF process utilizes spherical powder particles, introducing greater complexity to the laser reflection, absorption, and transfer processes within the powder bed [122]. This increased complexity results in significant differences in the dynamics and heat transfer processes of the melt pool compared to laser welding. Consequently, the factors influencing spattering in L-PBF are more

diverse, and the mechanisms of spatter formation are challenging to precisely define [144]. Figure 2.19 illustrates the formation mechanisms of several common spatter types [144].

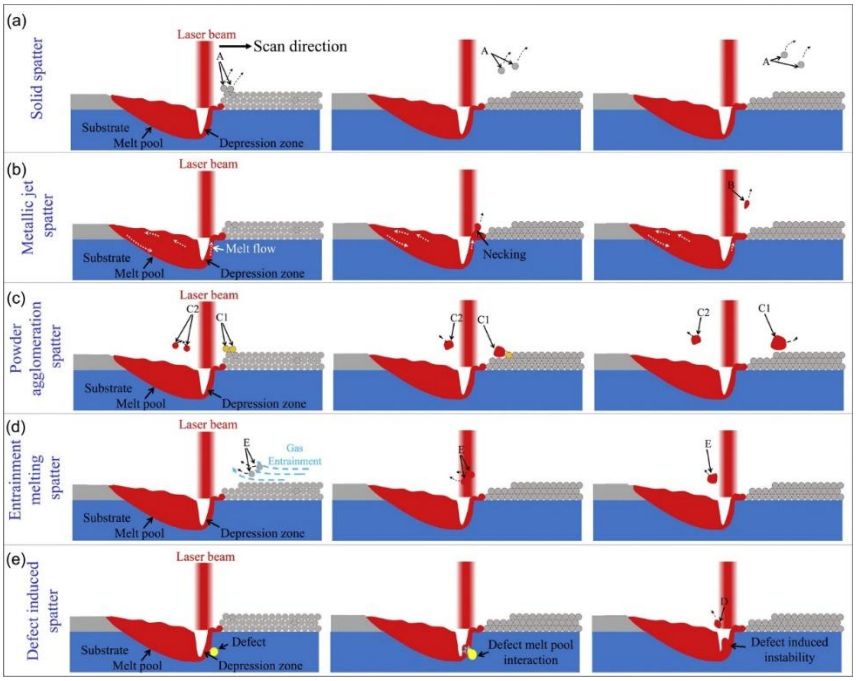

Figure 2.19 Schematic of formation mechanisms for different spatter types: (a) Solid spatter, (b) Metal vapor spatter, (c) Powder agglomeration spatter, (d) Vortex-induced melted powder spatter, and (e) Defect-induced spatter [144].

Sonny Ly et al. [148] examined the spattering phenomena in L-PBF through high-speed imaging and simulation, categorizing two primary spatter types:

1) The first spatter type, caused by the recoil force of metal vapor, involves molten metal undergoing bulging, elongation, and necking before escaping as droplets at velocities of 3–8 m/s. This accounts for approximately 15% of total spatter.
2) The second spatter type originates from metal particles on the powder bed escaping due to violent gas flow entrainment. These particles either form droplets after laser heating (60% of total spatter, velocities of 6–20 m/s) or remain as powder spatter without heating (25% of total spatter, velocities of 2–4 m/s).

Simulation analysis further explored the influence of metal vapor pressure on keyhole shape and its correlation with spatter behavior [144]. When laser power and scanning

speed generate sufficient vaporization to produce a deep, vertical melt pool, spatter primarily ejects in the vertical direction. Otherwise, spatter occurs at an obtuse angle relative to the scanning path. P. Bidare et al. [149] additionally observed a third type of spatter, characterized by ejection at an acute angle during single-track L-PBF experiments. These three ejection angles are closely correlated with the laser energy density [144, 149]. In summary, spattering in L-PBF results from a combination of factors, including powder characteristics, gas flow dynamics, laser input parameters, and melt pool dynamics. A thorough understanding of these mechanisms is essential for optimizing process parameters, minimizing spatter, and enhancing fabrication quality.

Due to the limitations of high-speed imaging technology in capturing the contour and depth information of the melt pool, Cang Zhao et al. [150] employed X-ray imaging technology to visualize the melt pool dynamics in L-PBF. During L-PBF experiments, heat and mass transfer within the melt pool rapidly spread to the surrounding powder, driven by the combined effects of the Marangoni effect and recoil pressure. Recoil pressure from metal evaporation generated significant spattered particles. Using X-ray imaging, the trajectories and characteristics of these spattered particles were effectively captured, allowing spattering phenomena to be categorized into three distinct types [150]:

1) Droplet spattering: Caused by the recoil force of metal vapor, where liquid metal escapes from the melt pool surface during the initial stage of laser melting.
2) Powder-induced spattering: Metal powder migrates to the melt pool due to surface tension, melts under the laser, and forms spattered droplets.
3) Composite particle spattering: Large spattered particles formed by the fusion of multiple small powders or existing spattered particles.

These classifications provide a precise depiction of the diverse causes of spattering phenomena in the L-PBF process. Comparative experiments under varying VED conditions have highlighted how non-uniform melt pool surface tension and recoil pressure result in differences in dynamic melt pool flow, further elucidating the

asymmetric angular distribution of spattered particles [148-151]. The findings underscore the correlation between melt pool dynamics and spattering behavior in L-PBF processing, both of which are influenced by processing parameters [149, 151]. The integration of X-ray imaging technology has provided critical insights into spatter formation mechanisms, offering robust experimental evidence for the optimization of L-PBF process parameters [150]. Figure 2.20 demonstrates an example of analyzing spatter formation mechanisms using dynamic X-ray imaging [144]. The results indicate that adjusting process parameters can effectively minimize spattering, thereby improving the surface quality and density of samples.

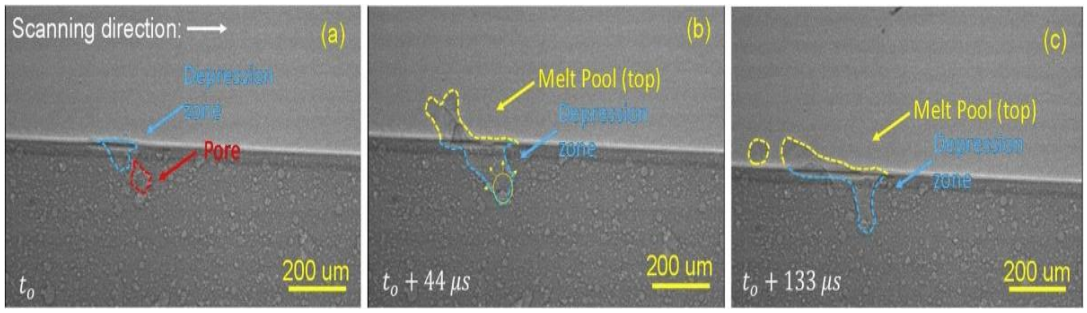

Figure 2.20 Dynamic X-ray imaging of defect-induced spattering: (a) A depression zone (blue dashed line) approaches a pre-existing pore (red dashed line); (b) Interaction between the melt pool and the defect causes sudden ejection; (c) A large liquid droplet separates, leading to spattering (yellow highlights) [137].

In summary, employing spattering phenomena as a signal for real-time monitoring and quality control in the L-PBF process has introduced novel research and application pathways in the field of additive manufacturing [152-154]. Statistical analysis of the quantity, distribution, and size of spattered particles enables the real-time detection of processing condition changes and rapid feedback to support the optimization of process parameters [153]. Furthermore, the integration of advanced image acquisition technologies with deep learning algorithms allows spatter monitoring systems to achieve high-precision classification and prediction while minimizing data processing demands [144]. However, the key gaps remain in understanding the relationships between spattering behaviour, microstructural evolution, and defect formation mechanisms. Current spatter monitoring techniques often lack the resolution needed to

correlate spattering phenomena with localized thermal and stress conditions in the melt pool. Additionally, the effects of spattering on powder bed characteristics, such as surface roughness and packing density, are not fully understood. L-PBF simulations can help bridge these gaps by providing detailed insights into melt pool dynamics, thermal gradients, and spattering interactions with the powder bed. Yet, current models are constrained by computational complexity and their inability to fully capture the transient nature of spatter phenomena, highlighting the need for further refinement. Another critical gap lies in developing standardized protocols for interpreting spatter data, considering variations in machine configurations, material properties, and environmental factors. Integrating real-time monitoring with advanced L-PBF simulations and adaptive algorithms will enable seamless process optimization and defect control, advancing the precision and reliability of the L-PBF process.

2.6 Summary

This chapter provides a comprehensive review of the current state-of-the-art research and future development directions in additive manufacturing, with a focus on the main challenges of nickel-based superalloys and their applications in the L-PBF process. It includes an in-depth discussion on numerical simulation techniques in L-PBF and highlights the potential advantages of introducing nano-reinforcement phases into nickel-based superalloys. The literature review identifies several unresolved critical issues that require further investigation, as outlined below:

- The mechanism underlying high-Ti and high-Al content nano-reinforced nickel-based superalloys remains incompletely understood. Systematic studies on newly developed Ni-MMCs are necessary, particularly to explore the relationship between L-PBF process parameters and fabrication quality. Moreover, the dispersion effect of nanoparticles in nickel-based composites requires further investigation.

- While the addition of nanoparticles enhances strength, it significantly reduces toughness. Improving the preparation process to optimize nanoparticle

distribution is essential to achieve strength enhancement while minimizing the adverse effects on ductility. With improved properties, strengthening mechanisms such as grain refinement and Orowan strengthening should be established.

- Additionally, the morphology and sphericity of the powder should be thoroughly studied and correlated with material properties, supported by evidence from characterization techniques.

- Simulations addressing the influence of powder morphology on defect formation require significant development. For composite material powders, a loss of sphericity can greatly affect melt pool dynamics during the L-PBF process. Employing DEM-CFD simulations to model various powder morphologies offers the potential to reveal the mechanisms governing powder behavior and defect formation. These simulations can provide valuable insights into the principles underlying different preparation routes in the L-PBF process.

References

1. Zhou L, Miller J, Vezza J, Mayster M, Raffay M, Justice Q, et al. Additive Manufacturing: A Comprehensive Review. Sensors. 2024;24(9):2668.
2. Ngo TD, Kashani A, Imbalzano G, Nguyen KT, Hui D. Additive manufacturing (3D printing): A review of materials, methods, applications and challenges. Composites Part B: Engineering. 2018;143:172-96.
3. Rouf S, Malik A, Singh N, Raina A, Naveed N, Siddiqui MIH, et al. Additive manufacturing technologies: Industrial and medical applications. Sustainable Operations and Computers. 2022;3:258-74.
4. Klenam DEP, Bamisaye OS, Williams IE, van der Merwe JW, Bodunrin MO. Global perspective and African outlook on additive manufacturing research– an overview. Manufacturing Review. 2022;9:35.
5. Lee J-Y, Nagalingam AP, Yeo S. A review on the state-of-the-art of surface finishing processes and related ISO/ASTM standards for metal additive manufactured components. Virtual and Physical Prototyping. 2021;16(1):68-96.
6. Svetlizky D, Das M, Zheng B, Vyatskikh AL, Bose S, Bandyopadhyay A, et al. Directed energy deposition (DED) additive manufacturing: Physical characteristics, defects, challenges and applications. Materials Today. 2021;49:271-95.
7. Svetlizky D, Zheng B, Vyatskikh A, Das M, Bose S, Bandyopadhyay A, et al. Laser-based directed energy deposition (DED-LB) of advanced materials. Materials Science and Engineering: A. 2022;840:142967.
8. Yi H, Wang Q, Cao H. Wire-arc directed energy deposition of magnesium alloys: microstructure, properties and quality optimization strategies. Journal of Materials Research and Technology. 2022;20:627-49.
9. Bhavar V, Kattire P, Patil V, Khot S, Gujar K, Singh R. A review on powder bed fusion technology of metal additive manufacturing. Additive manufacturing handbook. 2017:251-3.
10. Singh DD, Mahender T, Reddy AR. Powder bed fusion process: A brief review. Materials Today: Proceedings. 2021;46:350-5.
11. Leung CLA, Marussi S, Towrie M, del Val Garcia J, Atwood RC, Bodey AJ, et al. Laser-matter interactions in additive manufacturing of stainless steel SS316L and 13-93 bioactive glass revealed by in situ X-ray imaging. Additive Manufacturing. 2018;24:647-57.
12. Amaya-Rivas JL, Perero BS, Helguero CG, Hurel JL, Peralta JM, Flores FA, et al. Future trends of additive manufacturing in medical applications: An overview. Heliyon. 2024.
13. Kharat VJ, Singh P, Raju GS, Yadav DK, Gupta MS, Arun V, et al. Additive manufacturing (3D printing): A review of materials, methods, applications and

challenges. Materials Today: Proceedings. 2023.
14. Cerro A, Romero PE, Yiğit O, Bustillo A. Use of machine learning algorithms for surface roughness prediction of printed parts in polyvinyl butyral via fused deposition modeling. The International Journal of Advanced Manufacturing Technology. 2021;115(7):2465-75.
15. Hyer H, Zhou L, Park S, Gottsfritz G, Benson G, Tolentino B, et al. Understanding the laser powder bed fusion of AlSi10Mg alloy. Metallography, Microstructure, and Analysis. 2020;9:484-502.
16. Narasimharaju SR, Zeng W, See TL, Zhu Z, Scott P, Jiang X, et al. A comprehensive review on laser powder bed fusion of steels: Processing, microstructure, defects and control methods, mechanical properties, current challenges and future trends. Journal of Manufacturing Processes. 2022;75:375-414.
17. Blakey-Milner B, Gradl P, Snedden G, Brooks M, Pitot J, Lopez E, et al. Metal additive manufacturing in aerospace: A review. Materials & Design. 2021;209:110008.
18. Liu G, Zhang X, Chen X, He Y, Cheng L, Huo M, et al. Additive manufacturing of structural materials. Materials Science and Engineering: R: Reports. 2021;145:100596.
19. Sanchez S, Smith P, Xu Z, Gaspard G, Hyde CJ, Wits WW, et al. Powder Bed Fusion of nickel-based superalloys: A review. International Journal of Machine Tools and Manufacture. 2021;165:103729.
20. Ma T, Zhang G-P, Tan P, Zhang B. Effects of homogenization temperature on creep performance of laser powder bed fusion-fabricated Inconel 718 at 650° C. Materials Science and Engineering: A. 2022;853:143794.
21. Sun K, Mohamed AE-MA, Jeong M, Head J, Lewis ER, Ibrahim P, et al. On the origin of cracking in laser powder bed fusion processed LaCe (Fe, Mn, Si) 13, and the impact of post-processing. Journal of Alloys and Compounds. 2023;968:172017.
22. Choi J-P, Shin G-H, Yang S, Yang D-Y, Lee J-S, Brochu M, et al. Densification and microstructural investigation of Inconel 718 parts fabricated by selective laser melting. Powder Technology. 2017;310:60-6.
23. Chlebus E, Gruber K, Kuźnicka B, Kurzac J, Kurzynowski T. Effect of heat treatment on the microstructure and mechanical properties of Inconel 718 processed by selective laser melting. Materials Science and Engineering: A. 2015;639:647-55.
24. Lu Y, Zhou Y, Wen P, Luo F, Cao J, Xu Y, et al. Effect of laser power on microstructure and mechanical properties of K418 nickel-based alloy prepared by selective laser melting. Journal of Materials Research and Technology. 2023;27:2964-75.
25. Tang YT, Ghoussoub JN, Panwisawas C, Collins DM, Amirkhanlou S, Clark JW, et al., editors. The effect of heat treatment on tensile yielding response of the new superalloy ABD-900AM for additive manufacturing. Superalloys 2020: Proceedings of the 14th International Symposium on Superalloys; 2020: Springer.

26. Griffiths S, Ghasemi-Tabasi H, De Luca A, Pado J, Joglekar SS, Jhabvala J, et al. Influence of Hf on the heat treatment response of additively manufactured Ni-base superalloy CM247LC. Materials Characterization. 2021;171:110815.
27. Han Q, Mertens R, Montero-Sistiaga ML, Yang S, Setchi R, Vanmeensel K, et al. Laser powder bed fusion of Hastelloy X: Effects of hot isostatic pressing and the hot cracking mechanism. Materials Science and Engineering: A. 2018;732:228-39.
28. Boswell JH, Clark D, Li W, Attallah MM. Cracking during thermal post-processing of laser powder bed fabricated CM247LC Ni-superalloy. Materials & Design. 2019;174:107793.
29. Wang H, Zhang X, Wang G, Shen J, Zhang G, Li Y, et al. Selective laser melting of the hard-to-weld IN738LC superalloy: Efforts to mitigate defects and the resultant microstructural and mechanical properties. Journal of Alloys and Compounds. 2019;807:151662.
30. Li S, Wei Q, Shi Y, Zhu Z, Zhang D. Microstructure characteristics of Inconel 625 superalloy manufactured by selective laser melting. Journal of Materials Science & Technology. 2015;31(9):946-52.
31. Calvin Samuel S, Arivarasu M, Ram Prabhu T. High-Temperature solid particle erosion behavior of laser powder bed fused Inconel 718. Journal of Tribology. 2022;144(9):091705.
32. Zhang S, Wang L, Lin X, Yang H, Huang W. The formation and dissolution mechanisms of Laves phase in Inconel 718 fabricated by selective laser melting compared to directed energy deposition and cast. Composites Part B: Engineering. 2022;239:109994.
33. Leary M, Mazur M, Williams H, Yang E, Alghamdi A, Lozanovski B, et al. Inconel 625 lattice structures manufactured by selective laser melting (SLM): Mechanical properties, deformation and failure modes. Materials & Design. 2018;157:179-99.
34. Babu SS, Raghavan N, Raplee J, Foster SJ, Frederick C, Haines M, et al. Additive manufacturing of nickel superalloys: opportunities for innovation and challenges related to qualification. Metallurgical and Materials Transactions A. 2018;49:3764-80.
35. Adegoke O, Andersson J, Brodin H, Pederson R. Review of laser powder bed fusion of gamma-prime-strengthened nickel-based superalloys. Metals. 2020;10(8):996.
36. Rickenbacher L, Etter T, Hövel S, Wegener K. High temperature material properties of IN738LC processed by selective laser melting (SLM) technology. Rapid Prototyping Journal. 2013;19(4):282-90.
37. Xu J, Lin X, Guo P, Yang H, Xue L, Huang W. The microstructure evolution and strengthening mechanism of a γ′-strengthening superalloy prepared by induction-assisted laser solid forming. Journal of Alloys and Compounds. 2019;780:461-75.
38. Cloots M, Kunze K, Uggowitzer PJ, Wegener K. Microstructural characteristics of

the nickel-based alloy IN738LC and the cobalt-based alloy Mar-M509 produced by selective laser melting. Materials Science and Engineering: A. 2016;658:68-76.
39. Perevoshchikova N, Rigaud J, Sha Y, Heilmaier M, Finnin B, Labelle E, et al. Optimisation of selective laser melting parameters for the Ni-based superalloy IN-738 LC using Doehlert's design. Rapid Prototyping Journal. 2017;23(5):881-92.
40. Engeli R, Etter T, Geiger F, Stankowski A, Wegener K. Effect of Si on the SLM processability of IN738LC. 2015.
41. Lee B, Mahtab M, Neo T, Farooqi I, Khursheed A. A comprehensive review of Design of experiment (DOE) for water and wastewater treatment application-Key concepts, methodology and contextualized application. Journal of Water Process Engineering. 2022;47:102673.
42. Pereira JLJ, Oliver GA, Francisco MB, Cunha Jr SS, Gomes GF. A review of multi-objective optimization: methods and algorithms in mechanical engineering problems. Archives of Computational Methods in Engineering. 2022;29(4):2285-308.
43. Berger PD, Maurer RE, Celli GB. Experimental design. CA (USA): Wadsworth Group Belmont. 2002.
44. Oimoen S. Classical Designs: Full Factorial Designs. STAT Center of Excellence: Dayton, OH, USA. 2019.
45. Buhairi MA, Foudzi FM, Jamhari FI, Sulong AB, Radzuan NAM, Muhamad N, et al. Review on volumetric energy density: influence on morphology and mechanical properties of Ti6Al4V manufactured via laser powder bed fusion. Progress in Additive Manufacturing. 2023;8(2):265-83.
46. Kumar P, Chakravadhhanula V, Manwatkar SK, Chakravarthy P, Murty SN. Establishing the qualitative relationship between process parameters: microstructure, phases and defects in SLM-PBF manufactured and heat treated Inconel 718 alloy. Transactions of the Indian National Academy of Engineering. 2021;6(4):1083-97.
47. Wang L, Xing H, Li Y, Wang J. Toward multiscale simulations for solidification microstructure and microsegregation for selective laser melting of nickel-based superalloys. Journal of Materials Research and Technology. 2023;25:3574-87.
48. Xiao W, Xu Y, Xiao H, Li S, Song L. Investigation of the Nb element segregation for laser additive manufacturing of nickel-based superalloys. International Journal of Heat and Mass Transfer. 2021;180:121800.
49. Lee Y, Nordin M, Babu SS, Farson DF. Effect of fluid convection on dendrite arm spacing in laser deposition. Metallurgical and Materials Transactions B. 2014;45:1520-9.
50. LIU J, PENG Q, XIE J. Grain structure and metallurgical defects regulation of selective laser melted René 88DT superalloy. Acta Metall Sin. 2020;57(2):191-204.
51. Watring DS, Benzing JT, Hrabe N, Spear AD. Effects of laser-energy density and build orientation on the structure–property relationships in as-built Inconel 718

manufactured by laser powder bed fusion. Additive manufacturing. 2020;36:101425.
52. Huang Y, Fleming TG, Clark SJ, Marussi S, Fezzaa K, Thiyagalingam J, et al. Keyhole fluctuation and pore formation mechanisms during laser powder bed fusion additive manufacturing. Nature communications. 2022;13(1):1170.
53. Du J, Cheng W, Sun Y, Ma R, Liu H, Song X, et al. The Effect of Precipitates on the Stress Rupture Properties of Laser Powder Bed Fusion Inconel 718 Alloy. Coatings. 2023;13(12):2087.
54. Zhang X, Mu Y, Lu N, Li Q, Chen S, Zhou Y, et al. Effect of solid solution elements on cracking susceptibility of Ni-based superalloys during additive manufacturing. Journal of Materials Science & Technology. 2024;190:218-28.
55. Hu P, Liu Z, Chen M, Li Y, Qi X, Xie J. Reducing cracking sensitivity of CM247LC processed via laser powder bed fusion through composition modification. Journal of Materials Research and Technology. 2024;29:3074-88.
56. Tian Z, Zheng Y, Wang H, Wang S, Chen J, Chen H, et al. Crack inhibition of non-weldable Inconel 738 alloy in ultrasound-assisted laser directed energy deposition. Materials Science and Engineering: A. 2024:147607.
57. Carter LN. Selective laser melting of nickel superalloys for high temperature applications: University of Birmingham; 2013.
58. Mumtaz KA, Erasenthiran P, Hopkinson N. High density selective laser melting of Waspaloy®. Journal of materials processing technology. 2008;195(1-3):77-87.
59. Hanzl P, Zetek M, Bakša T, Kroupa T. The influence of processing parameters on the mechanical properties of SLM parts. Procedia Engineering. 2015;100:1405-13.
60. Shipley H, McDonnell D, Culleton M, Coull R, Lupoi R, O'Donnell G, et al. Optimisation of process parameters to address fundamental challenges during selective laser melting of Ti-6Al-4V: A review. International Journal of Machine Tools and Manufacture. 2018;128:1-20.
61. Carter LN, Martin C, Withers PJ, Attallah MM. The influence of the laser scan strategy on grain structure and cracking behaviour in SLM powder-bed fabricated nickel superalloy. Journal of Alloys and Compounds. 2014;615:338-47.
62. Du Plessis A. Effects of process parameters on porosity in laser powder bed fusion revealed by X-ray tomography. Additive Manufacturing. 2019;30:100871.
63. Vukkum V, Gupta R. Review on corrosion performance of laser powder-bed fusion printed 316L stainless steel: Effect of processing parameters, manufacturing defects, post-processing, feedstock, and microstructure. Materials & Design. 2022;221:110874.
64. Jia H, Sun H, Wang H, Wu Y, Wang H. Scanning strategy in selective laser melting (SLM): a review. The International Journal of Advanced Manufacturing Technology. 2021;113:2413-35.
65. Catchpole-Smith S, Aboulkhair N, Parry L, Tuck C, Ashcroft IA, Clare A. Fractal scan strategies for selective laser melting of ‘unweldable’nickel superalloys. Additive

Manufacturing. 2017;15:113-22.
66. Lu Y, Wu S, Gan Y, Huang T, Yang C, Junjie L, et al. Study on the microstructure, mechanical property and residual stress of SLM Inconel-718 alloy manufactured by differing island scanning strategy. Optics & Laser Technology. 2015;75:197-206.
67. Sun S-H, Hagihara K, Nakano T. Effect of scanning strategy on texture formation in Ni-25 at.% Mo alloys fabricated by selective laser melting. Materials & Design. 2018;140:307-16.
68. Wan H, Zhou Z, Li C, Chen G, Zhang G. Effect of scanning strategy on mechanical properties of selective laser melted Inconel 718. Materials Science and Engineering: A. 2019;753:42-8.
69. Kirka M, Unocic K, Raghavan N, Medina F, Dehoff R, Babu S. Microstructure development in electron beam-melted Inconel 718 and associated tensile properties. Jom. 2016;68(3):1012-20.
70. Nadammal N, Mishurova T, Fritsch T, Serrano-Munoz I, Kromm A, Haberland C, et al. Critical role of scan strategies on the development of microstructure, texture, and residual stresses during laser powder bed fusion additive manufacturing. Additive Manufacturing. 2021;38:101792.
71. Wang Y, Lei L, Shi L, Wan H, Liang F, Zhang G. Scanning strategy dependent tensile properties of selective laser melted GH4169. Materials Science and Engineering: A. 2020;788:139616.
72. McLouth TD, Bean GE, Witkin DB, Sitzman SD, Adams PM, Patel DN, et al. The effect of laser focus shift on microstructural variation of Inconel 718 produced by selective laser melting. Materials & Design. 2018;149:205-13.
73. Hu Y, Cong W. A review on laser deposition-additive manufacturing of ceramics and ceramic reinforced metal matrix composites. Ceramics International. 2018;44(17):20599-612.
74. Huda M, Hashmi M, El-Baradie M. MMCs: materials, manufacturing and mechanical properties. Key engineering materials. 1995;104:37-64.
75. Cyriac AJ. Metal matrix composites: history, status, factors and future: Oklahoma State University; 2011.
76. Zhu Z, Hu Z, Seet HL, Liu T, Liao W, Ramamurty U, et al. Recent progress on the additive manufacturing of aluminum alloys and aluminum matrix composites: Microstructure, properties, and applications. International Journal of Machine Tools and Manufacture. 2023;190:104047.
77. Liu X, Liu Y, Zhou Z, Wang K, Zhan Q, Xiao X. Grain refinement and crack inhibition of selective laser melted AA2024 aluminum alloy via inoculation with TiC–TiH2. Materials Science and Engineering: A. 2021;813:141171.
78. Shu C, Chen S, Shu X, Abdel-Wahab A, Essa K. Enhanced high-temperature mechanical properties and strengthening mechanisms of chemically prepared nano-TiC

reinforced IN738LC via laser powder bed fusion. Materials Characterization. 2024;217:114434.
79. Shu C, Chen S, Zheng Z, Lu X, Li W, De Lisi M, et al. Fabrication and strengthening mechanism of crack-free nano-TiC reinforced IN738LC with enhanced mechanical properties by laser powder bed fusion. Journal of Materials Research and Technology. 2023;27:3835-48.
80. Priyadarshi P, Katiyar PK, Maurya R. A review on mechanical, tribological and electrochemical performance of ceramic particle-reinforced Ni-based electrodeposited composite coatings. Journal of Materials Science. 2022;57(41):19179-211.
81. Shi J, Wang Y. Development of metal matrix composites by laser-assisted additive manufacturing technologies: a review. Journal of Materials Science. 2020;55(23):9883-917.
82. Zhang Z, Wang R, Lv Y, Liu W, Liu Y. Microstructures and mechanical properties of heat treated TiC/GTD222 nickel-based composite prepared by selective laser melting. Materials Science and Engineering: A. 2022;851:143588.
83. Mandal V, Tripathi P, Kumar A, Singh SS, Ramkumar J. A study on selective laser melting (SLM) of TiC and B4C reinforced IN718 metal matrix composites (MMCs). Journal of Alloys and Compounds. 2022;901:163527.
84. Shi Q, Gu D, Lin K, Chen W, Xia M, Dai D. The role of reinforcing particle size in tailoring interfacial microstructure and wear performance of selective laser melting WC/Inconel 718 composites. Journal of Manufacturing Science and Engineering. 2018;140(11):111019.
85. Chen Z, Wei P, Zhang S, Lu B, Zhang L, Yang X, et al. Graphene reinforced nickel-based superalloy composites fabricated by additive manufacturing. Materials Science and Engineering: A. 2020;769:138484.
86. Han Q, Gu Y, Gu H, Yin Y, Song J, Zhang Z, et al. Laser powder bed fusion of WC-reinforced Hastelloy-X composite: microstructure and mechanical properties. Journal of Materials Science. 2021;56:1768-82.
87. Lerda S, Marchese G, Bassini E, Lombardi M, Ugues D, Fino P, et al. Understanding the microstructure and mechanical performance of heat-treated Inconel 625/TiC composite produced by laser powder bed fusion. Materials Science and Engineering: A. 2023;883:145508.
88. Wang R, Zhu G, Zhou W, Wang W, Wang D, Dong A, et al. An enhanced strength Ni matrix composite reinforced by a 3D network structure of TiN nano-particles. Materials & Design. 2020;191:108638.
89. Zhang J, Meng G, Zhu L, Yang Z, Xue P, Xu P. Formation mechanism and mechanical properties of TiC reinforced Inconel 718 composite coatings by laser cladding on H13 steel. The International Journal of Advanced Manufacturing Technology. 2022;121(5):3597-611.

90. Zhao M, Song J, Tang Q, Zhang Z, Feng Q, Han Q, et al. Laser powder bed fusion of Inconel 718-based composites: Effect of TiB2 content on microstructure and mechanical performance. Optics & Laser Technology. 2023;167:109596.
91. Xing L, Hao S, Huang H, Yao L, Ding A, Zhang M, et al. Ni-base superalloys enhanced by in-situ MC carbides precipitant on TiC nanoparticles. Materials Today Communications. 2024;38:108262.
92. Abd-Elaziem W, Elkatatny S, Abd-Elaziem A-E, Khedr M, Abd El-baky MA, Hassan MA, et al. On the current research progress of metallic materials fabricated by laser powder bed fusion process: a review. Journal of Materials Research and Technology. 2022;20:681-707.
93. Chowdhury S, Yadaiah N, Prakash C, Ramakrishna S, Dixit S, Gupta LR, et al. Laser powder bed fusion: a state-of-the-art review of the technology, materials, properties & defects, and numerical modelling. Journal of Materials Research and Technology. 2022;20:2109-72.
94. Xi X, Lin D, Song X, Luo X, Ma R, Shi Z, et al. Strength-plasticity transition mechanism after the solution treatment of GH3230 superalloy fabricated via laser powder bed fusion. Materials Science and Engineering: A. 2023;876:145124.
95. Sehhat MH, Mahdianikhotbesara A. Powder spreading in laser-powder bed fusion process. Granular matter. 2021;23(4):89.
96. Riener K, Albrecht N, Ziegelmeier S, Ramakrishnan R, Haferkamp L, Spierings AB, et al. Influence of particle size distribution and morphology on the properties of the powder feedstock as well as of AlSi10Mg parts produced by laser powder bed fusion (LPBF). Additive Manufacturing. 2020;34:101286.
97. Abdullah EC, Geldart D. The use of bulk density measurements as flowability indicators. Powder technology. 1999;102(2):151-65.
98. Brika SE, Letenneur M, Dion CA, Brailovski V. Influence of particle morphology and size distribution on the powder flowability and laser powder bed fusion manufacturability of Ti-6Al-4V alloy. Additive Manufacturing. 2020;31:100929.
99. Chen G, Zhao S, Tan P, Wang J, Xiang C, Tang H. A comparative study of Ti-6Al-4V powders for additive manufacturing by gas atomization, plasma rotating electrode process and plasma atomization. Powder technology. 2018;333:38-46.
100. Higashitani K, Makino H, Matsusaka S. Powder technology handbook: CRC Press; 2019.
101. Ruan G, Liu C, Qu H, Guo C, Li G, Li X, et al. A comparative study on laser powder bed fusion of IN718 powders produced by gas atomization and plasma rotating electrode process. Materials Science and Engineering: A. 2022;850:143589.
102. Bourot P, Weiss L, Boisselier D, Laheurte P. Effect of bimodal size distribution on the behavioural properties of powders used in the LPBF process. Powder Technology. 2024;439:119670.

103. Xiang Z, Zhang M, Yan R, Yin Q, Zhang K. Powder-spreading dynamics and packing quality improvement for laser powder bed fusion additive manufacturing. Powder Technology. 2021;389:278-91.
104. Farzadfar SA, Murtagh MJ, Venugopal N. Impact of IN718 bimodal powder size distribution on the performance and productivity of laser powder bed fusion additive manufacturing process. Powder technology. 2020;375:60-80.
105. Coe HG. On the Role of Particle Size Distribution in Selective Laser Melting of 316L Stainless Steel. 2019.
106. Coe HG, Pasebani S. Use of bimodal particle size distribution in selective laser melting of 316L stainless steel. Journal of Manufacturing and Materials Processing. 2020;4(1):8.
107. Haferkamp L, Haudenschild L, Spierings A, Wegener K, Riener K, Ziegelmeier S, et al. The influence of particle shape, powder flowability, and powder layer density on part density in laser powder bed fusion. Metals. 2021;11(3):418.
108. Rosenholm JB. Sizing and packing of particles–Characterization of mono-, di- and trimodal particle assemblies. Advances in Colloid and Interface Science. 2023;315:102887.
109. Carter LN, Villapún VM, Grover L, Cox SC. Exploring the duality of powder adhesion and underlying surface roughness in laser powder bed fusion processed Ti-6Al-4V. Journal of Manufacturing Processes. 2022;81:14-26.
110. Liao D, Li M, Wang J, Zhang M, Qiu M, An C. A review on the preparation and characterization methods of spherical explosive crystals. Journal of Materials Research and Technology. 2023.
111. Zhao Y, Cui Y, Hasebe Y, Bian H, Yamanaka K, Aoyagi K, et al. Controlling factors determining flowability of powders for additive manufacturing: A combined experimental and simulation study. Powder Technology. 2021;393:482-93.
112. Brika SE, Brailovski V. Influence of powder particle morphology on the static and fatigue properties of laser powder bed-fused Ti-6Al-4V components. Journal of Manufacturing and Materials Processing. 2020;4(4):107.
113. Sun Y, Aindow M, Hebert RJ. Comparison of virgin Ti-6Al-4V powders for additive manufacturing. Additive Manufacturing. 2018;21:544-55.
114. Fedina T, Sundqvist J, Powell J, Kaplan AF. A comparative study of water and gas atomized low alloy steel powders for additive manufacturing. Additive Manufacturing. 2020;36:101675.
115. Engeli R, Etter T, Hövel S, Wegener K. Processability of different IN738LC powder batches by selective laser melting. Journal of Materials Processing Technology. 2016;229:484-91.
116. Irrinki H, Nath SD, Alhofors M, Stitzel J, Gulsoy O, Atre SV. Microstructures,

properties, and applications of laser sintered 17‐4PH stainless steel. Journal of the American Ceramic Society. 2019;102(9):5679-90.
117. Abdelwahed M, Bengsston S, Casati R, Larsson A, Vedani M. L-PBF Verarbeitung von Stahlpulvern hergestellt durch Gas-und Wasseratomisierung. BHM Berg-und Hüttenmännische Monatshefte. 2021;166:40-5.
118. Fang ZZ, Paramore JD, Sun P, Chandran KR, Zhang Y, Xia Y, et al. Powder metallurgy of titanium–past, present, and future. International Materials Reviews. 2018;63(7):407-59.
119. Gruber K, Smolina I, Kasprowicz M, Kurzynowski T. Evaluation of inconel 718 metallic powder to optimize the reuse of powder and to improve the performance and sustainability of the laser powder bed fusion (LPBF) process. Materials. 2021;14(6):1538.
120. Gärtner E, Jung HY, Peter NJ, Dehm G, Jägle EA, Uhlenwinkel V, et al. Reducing cohesion of metal powders for additive manufacturing by nanoparticle dry-coating. Powder Technology. 2021;379:585-95.
121. Yang W-C. Modification and re-interpretation of Geldart's classification of powders. Powder technology. 2007;171(2):69-74.
122. Bayat M, Dong W, Thorborg J, To AC, Hattel JH. A review of multi-scale and multi-physics simulations of metal additive manufacturing processes with focus on modeling strategies. Additive Manufacturing. 2021;47:102278.
123. Bandyopadhyay A, Traxel KD. Invited review article: Metal-additive manufacturing—Modeling strategies for application-optimized designs. Additive manufacturing. 2018;22:758-74.
124. Sarkar D, Kapil A, Sharma A. Advances in computational modeling for laser powder bed fusion additive manufacturing: A comprehensive review of finite element techniques and strategies. Additive Manufacturing. 2024:104157.
125. Ali H, Ghadbeigi H, Mumtaz K. Residual stress development in selective laser-melted Ti6Al4V: a parametric thermal modelling approach. The International Journal of Advanced Manufacturing Technology. 2018;97:2621-33.
126. Li C, Liu J, Fang X, Guo Y. Efficient predictive model of part distortion and residual stress in selective laser melting. Additive Manufacturing. 2017;17:157-68.
127. Fang Z-C, Wu Z-L, Huang C-G, Wu C-W. Review on residual stress in selective laser melting additive manufacturing of alloy parts. Optics & Laser Technology. 2020;129:106283.
128. Cao J, Gharghouri MA, Nash P. Finite-element analysis and experimental validation of thermal residual stress and distortion in electron beam additive manufactured Ti-6Al-4V build plates. Journal of Materials Processing Technology. 2016;237:409-19.

129. Yang Y, Jamshidinia M, Boulware P, Kelly S. Prediction of microstructure, residual stress, and deformation in laser powder bed fusion process. Computational Mechanics. 2018;61:599-615.
130. Zhao Z, Li L, Tan L, Bai P, Li J, Wu L, et al. Simulation of stress field during the selective laser melting process of the nickel-based superalloy, GH4169. Materials. 2018;11(9):1525.
131. Parry L, Ashcroft I, Wildman RD. Understanding the effect of laser scan strategy on residual stress in selective laser melting through thermo-mechanical simulation. Additive Manufacturing. 2016;12:1-15.
132. Bian P, Shi J, Liu Y, Xie Y. Influence of laser power and scanning strategy on residual stress distribution in additively manufactured 316L steel. Optics & Laser Technology. 2020;132:106477.
133. Marques BM, Andrade CM, Neto DM, Oliveira MC, Alves JL, Menezes LF. Numerical analysis of residual stresses in parts produced by selective laser melting process. Procedia Manufacturing. 2020;47:1170-7.
134. Chen H, Wei Q, Zhang Y, Chen F, Shi Y, Yan W. Powder-spreading mechanisms in powder-bed-based additive manufacturing: Experiments and computational modeling. Acta Materialia. 2019;179:158-71.
135. Yang Y, Gu D, Dai D, Ma C. Laser energy absorption behavior of powder particles using ray tracing method during selective laser melting additive manufacturing of aluminum alloy. Materials & Design. 2018;143:12-9.
136. Yuan W, Chen H, Li S, Heng Y, Yin S, Wei Q. Understanding of adopting flat-top laser in laser powder bed fusion processed Inconel 718 alloy: simulation of single-track scanning and experiment. Journal of Materials Research and Technology. 2022;16:1388-401.
137. Yan W, Ge W, Qian Y, Lin S, Zhou B, Liu WK, et al. Multi-physics modeling of single/multiple-track defect mechanisms in electron beam selective melting. Acta Materialia. 2017;134:324-33.
138. Yin J, Zhang W, Ke L, Wei H, Wang D, Yang L, et al. Vaporization of alloying elements and explosion behavior during laser powder bed fusion of Cu–10Zn alloy. International Journal of Machine Tools and Manufacture. 2021;161:103686.
139. Tan JHK, Sing SL, Yeong WY. Microstructure modelling for metallic additive manufacturing: a review. Virtual and Physical Prototyping. 2020;15(1):87-105.
140. Zhang W, Yuan X, Jia Z-h, Yang X-f, Qing L, Zhu C-l. Effect of minor Sc and Zr addition on microstructure and properties of ultra-high strength aluminum alloy. Transactions of Nonferrous Metals Society of China. 2014;24(12):3866-71.
141. Zhan X, Lin X, Gao Z, Qi C, Zhou J, Gu D. Modeling and simulation of the columnar-to-equiaxed transition during laser melting deposition of Invar alloy. Journal of Alloys and Compounds. 2018;755:123-34.

142. Wang W, Liu W, Yang X, Xu R, Dai Q. Multi-scale simulation of columnar-to-equiaxed transition during laser selective melting of rare earth magnesium alloy. Journal of Materials Science & Technology. 2022;119:11-24.
143. Koepf JA, Gotterbarm MR, Markl M, Körner C. 3D multi-layer grain structure simulation of powder bed fusion additive manufacturing. Acta Materialia. 2018;152:119-26.
144. Young ZA, Guo Q, Parab ND, Zhao C, Qu M, Escano LI, et al. Types of spatter and their features and formation mechanisms in laser powder bed fusion additive manufacturing process. Additive Manufacturing. 2020;36:101438.
145. Li S, Chen G, Katayama S, Zhang Y. Relationship between spatter formation and dynamic molten pool during high-power deep-penetration laser welding. Applied Surface Science. 2014;303:481-8.
146. Cai W, Shu L, Geng S, Zhou Q, Cao L. Real-time tracking method for motion spatter in high-power laser welding of stainless steel plate based on a lightweight deep learning model. Expert Systems with Applications. 2024:124386.
147. Zhang M, Chen G, Zhou Y, Li S, Deng H. Observation of spatter formation mechanisms in high-power fiber laser welding of thick plate. Applied Surface Science. 2013;280:868-75.
148. Ly S, Rubenchik AM, Khairallah SA, Guss G, Matthews MJ. Metal vapor micro-jet controls material redistribution in laser powder bed fusion additive manufacturing. Scientific reports. 2017;7(1):4085.
149. Bidare P, Bitharas I, Ward R, Attallah M, Moore AJ. Fluid and particle dynamics in laser powder bed fusion. Acta Materialia. 2018;142:107-20.
150. Zhao C, Fezzaa K, Cunningham RW, Wen H, De Carlo F, Chen L, et al. Real-time monitoring of laser powder bed fusion process using high-speed X-ray imaging and diffraction. Scientific reports. 2017;7(1):3602.
151. Liu Z, Yang Y, Han C, Zhou H, Wang M, Liu L, et al. Effects of gas flow parameters on droplet spatter features and dynamics during large-scale laser powder bed fusion. Materials & Design. 2023;225:111534.
152. Repossini G, Laguzza V, Grasso M, Colosimo BM. On the use of spatter signature for in-situ monitoring of Laser Powder Bed Fusion. Additive Manufacturing. 2017;16:35-48.
153. Ye D, Fuh JYH, Zhang Y, Hong GS, Zhu K. In situ monitoring of selective laser melting using plume and spatter signatures by deep belief networks. ISA transactions. 2018;81:96-104.
154. Ye D, Zhu K, Fuh JYH, Zhang Y, Soon HG. The investigation of plume and spatter signatures on melted states in selective laser melting. Optics & Laser Technology. 2019;111:395-406.

CHAPTER 3 FABRICATION AND STRENGTHENING MECHANISM OF CRACK-FREE NANO-TIC REINFORCED IN738LC WITH ENHANCED MECHANICAL PROPERTIES BY LASER POWDER BED FUSION

Authors Contributions:

This chapter of the alternative thesis format is published in the *Journal of Materials Research and Technology (2023).* As the first author of this publication, I have outlined the paper's details and the contributions of my co-authors below.

Shu, C., *Chen, S., Zheng, Z., Lu, X., Li, W., De Lisi, M., ... & Essa, K. (2023). Fabrication and strengthening mechanism of crack-free nano-TiC reinforced IN738LC with enhanced mechanical properties by laser powder bed fusion. Journal of Materials Research and Technology, 27, 3835-3848.*

CRediT authorship contribution statement

Chang Shu: Writing – original draft, Visualization, Methodology, Formal analysis, Data curation, Conceptualization.

Siyuan Chen: Resources, Methodology, Data curation.

Zhiyu Zheng: Data curation.

Xuben Lu: Resources.

Weining Li: Methodology.

Michele De Lisi: Methodology.

Prveen Bidare: Writing – review & editing, Supervision.

Xuedao Shu: Writing – review & editing, Supervision, Resources.

Khamis Essa: Writing – review & editing, Supervision, Resources, Project administration, Funding acquisition.

CHAPTER 3:

FABRICATION AND STRENGTHENING MECHANISM OF CRACK-FREE NANO-TIC REINFORCED IN738LC WITH ENHANCED MECHANICAL PROPERTIES BY LASER POWDER BED FUSION

Abstract

IN738LC alloy has broad application potential in modern aerospace and energy industries due to its excellent high-temperature durability, excellent corrosion and fatigue resistance, however, its application has been greatly limited due to its high crack sensitivity. To address this challenge, this research proposes a method of incorporating TiC nanoparticles to mitigate cracks and enhance the strength of the nickel-based materials. The crack-free TiC-IN738LC materials were successfully fabricated using laser-powder bed fusion. The relationship between the processing parameters and processed quality was studied. The fracture morphology and mechanical properties of samples were analyzed and the strengthening mechanisms of nano-TiC particles were clarified. The results showed that volume energy density (VED) =111.1J/mm^3 is the optimal processing parameter with the laser energy 225W, scanning speed 750mm/s, and 0.09mm hatch distance. The effects of processing parameters were discussed in depth. Compared with the virgin IN738LC, the microhardness of TiC-IN738LC is improved by 20% to 40%, and the tensile strength of TiC-IN738LC is enhanced by 5%-30%, respectively, which indicates the significant strengthening effect of nano-TiC on IN738LC. The synergistic effect of fine grain strengthening, load-bearing strengthening and Orowan strengthening mechanisms was accounted for the performance enhancement. The research results provide an experimental reference for selecting the processing parameters of TiC-IN738LC.

Keywords: Nanoparticles, IN738LC, Laser-powder bed fusion, Mechanical properties, Strengthening mechanism

3.1 Introduction

Additive manufacturing (AM) is a transformative manufacturing technology that rapidly developed in the past 30 years. Laser-powder bed fusion (L-PBF) has a high cooling rate (about 10^4-10^6 ℃/s), and via layer-by-layer deposition and laser-induced non-equilibrium cooling and solidification process, a finer microstructure will be generated [1-4]. Studies have shown that L-PBF is an effective method for fabricating geometrically complex metal components that offer high mechanical performance [1-3, 5-7]. Given its promising capabilities, L-PBF has been widely used in numerous applications, including aviation, aerospace, biomedical sensors, and deep-sea explorations [8]. Metal matrix composites are also popular in sectors such as aviation, aerospace, biomedical sensors, deep-sea explorations, and energy industries, owing to their multi-functional properties. Currently, the production of high-quality composite materials using L-PBF is an area of active research.

Due to the high volume fraction of Ni3(Al,Ti)- γ', the hard-to-weld nickel superalloy IN738LC boasts a range of exceptional properties, such as high-temperature performance, creep resistance, hot corrosion, and oxidation resistance. IN738LC is a staple in modern aerospace and energy industries [1, 9, 10]. Using the L-PBF method to produce IN738LC paves the way for its expanded application in diverse sectors. Wang et al. [8] examined the processing parameters of IN738LC in L-PBF and successfully achieved IN738LC with high density, minimal porosity, and a reduced crack rate, thereby establishing the optimal processing parameter window for IN738LC. Nonetheless, hot cracking remains a significant challenge when working with hard-to-machine nickel superalloys. Identifying strategies to mitigate hot cracking is a primary research objective in the field.

To enhance the γ' precipitation strength of nickel superalloys, incorporating nanoparticles with high modulus and outstanding heat resistance is considered an effective approach to improve their properties and reduce cracking [11-13]. Wang et al. [12] integrated TiC into nickel superalloy GTD222, not only effectively suppressing

cracks but also enhancing mechanical properties. Lv et al. [9] improved the mechanical attributes of CM247LC by introducing 1wt% TiC. The strengthening mechanism imparted by nanoparticles was elucidated through microscopic data analysis. Many studies have illustrated the strengthening mechanism of ceramic particles as reinforcements. The primary strengthening mechanisms encompass Orowan strengthening, fine grain strengthening, load-bearing strengthening, and dislocation strengthening [9, 14-16]. However, the elucidation of these mechanisms is mostly based on nickel superalloys such as In718, In625, etc. [16-19]. For the nanoparticles reinforced hard-to-weld nickels, the mechanisms are barely discussed and there are still gaps needed to fill in.

The processing parameters play a critical role in the materials quality [7, 20]. For L-PBFed metal materials, prevalent defects, such as pores, cracks, and lack of fusion, detrimentally impact the mechanical properties of the printed sample. Hence, it's crucial to optimize processing parameters to diminish defects and uplift processed quality [7]. The statistical Design of Experiments (DoE) method is currently the main research approach to obtain the relationship between processing parameters and processed quality. Koutiri et al. [21] studied the processing parameters of L-PBFed-IN625 by DoE, and obtained the relationship with the processed quality (surface roughness, porosity rate and tensile strength). The as-printed sample with low porosity and high strength was obtained and provided a valuable processing parameter window as the reference for the future work of L-PBFed-In625. Wang et al. [8] designed L-PBFed IN738LC through full factorials DoE, obtained the relationship diagram of processing parameters, found the correlation between defects and processing parameters, and successfully fabricated the high-density (~99.76%), crack-free samples. The microstructural results and mechanical tests validated the significant improvement of the properties. Khorasani et al. [5] studied the rheological phenomena of molten pools under different parameters, these results were consistent with the results of density and hardness. By correlating the results of processing parameters and hardness tests as well as the numerical model’s validation, the mechanism of molten pool formation and processing parameters were

clarified. Zhou et al. [13] successfully printed and strengthened TiC-IN738LC by using L-PBF, but this study only applied one set of processing parameters (laser power 300W, scan speed 1000mm/s, powder layer thickness 30um, hatch space 90um), the effect on other sets of parameters is not covered. Therefore, although the above research is devoted to the parameter study of Ni-superalloys, there are many blank gaps that have not been studied, especially for the processing parameter analysis of the reinforced difficult-to-machine nickel composite materials.

In this work, the difficult-to-machine nickel superalloy IN738LC was selected as the matrix and the TiC nanoparticles were used as the reinforcements to form TiC-IN738LC metal matrix composite. The processing parameters of TiC-IN738LC by L-PBF were systematically studied. The relationship between processing parameters and the properties including density, porosity, hardness, and tensile strength was revealed. By obtaining the processing parameter network diagram, the optimal parameters of L-PBFed TiC-IN738LC were achieved. Meanwhile, by the analysis of microstructural morphology and mechanical behavior, the strengthening mechanisms and the effect of nano-TiC particles in the L-PBF process were analysed.

3.2 Experiments

3.2.1 Materials

To ensure the high printing quality, spherical shape IN738LC powder (China North Industries Group Corporation Limited, China) was selected in this study, with d10=15.9 um, d50=34.3 um and d90=60.2 um. The chemical composition of IN738LC is shown in Table 3.1. Figure 3.1(a) shows the morphology of IN738LC and it shows the powder with the good quality of sphericity. The 50 nm TiC with 99.5% purity (China North Industries Group Corporation Limited, China) was chosen as the ceramic reinforcement in this work. The morphology of nano-TiC is shown in Figure 3.1(b). A 4-planetary ball mill machine (QM-QX, Nanjing Nanda Instrument Plant, China) was used to mix the 2wt% TiC and Nickel superalloy IN738LC. During the ball mill, the Argon gas was filled as the inert gas to prevent the impurity phase that was caused from the oxidation

reaction with the powders. To fully disperse and attach the nano-TiC to IN738LC, a set of parameters from ball milling are used: 4:1 ball-to-powder ratio, 200 rpm ball mill speed and 6 hours ball mill time. Figure 3.1(c) and (d) show the morphology of TiC-IN738LC after ball milling, and it can be seen that the nano-TiC nanoparticles were evenly distributed to the surface of IN738LC. Figures 3.1(e) and 1(f) displayed the EDS graphs and the presence of both Ti and Ni elements confirms that the TiC nanoparticles were uniformly dispersed around the IN738LC powders before printing.

Table 3.1 Chemical composition of IN738LC (wt%).

Ni	Cr	Nb	W	Mo	Ta	Ti	Al	Co	C	Sn	Mn	B	Zr
Bal	16	0.8	2.6	1.75	1.7	3.5	3.5	8.5	0.1	0.03	0.03	0.02	0.02

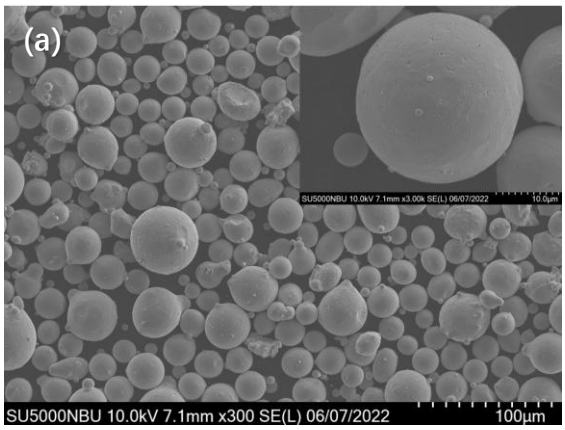

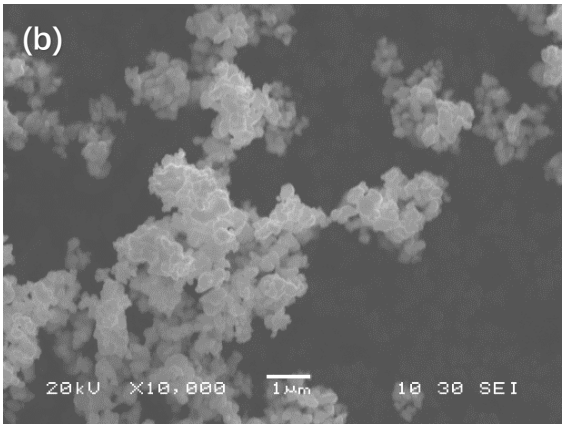

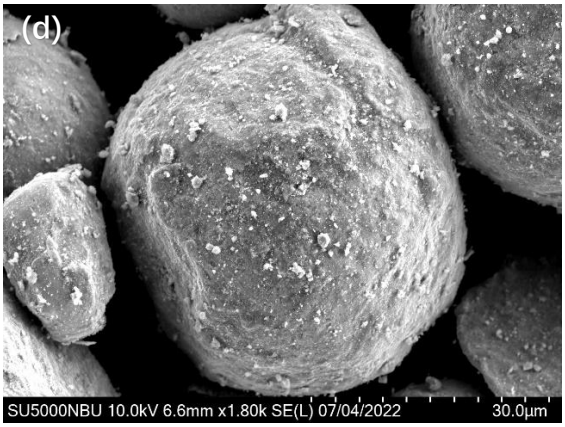

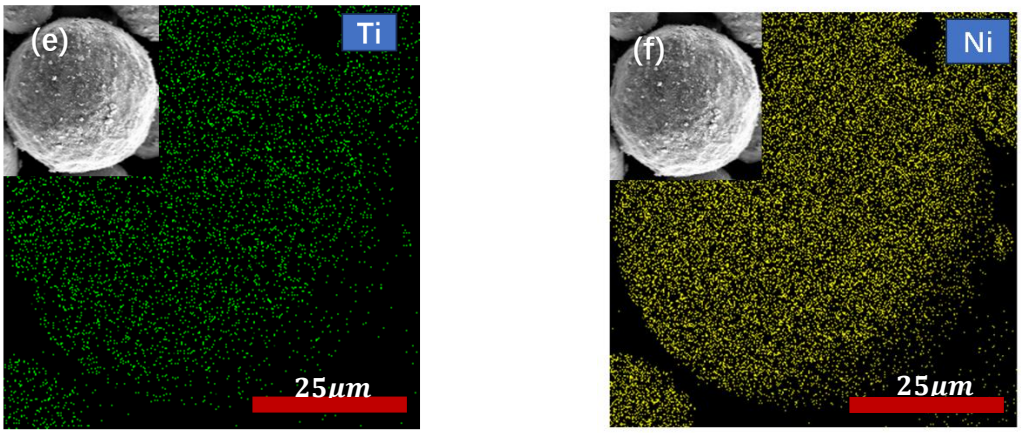

Figure 3.1. SEM morphology (a) IN738LC virgin powder, (b) nano-TiC powder, (c) nano-TiC attached to the IN738LC after ball milling, (d) higher magnification of the particle attachment, (e) EDS graph of Ti element and (f) EDS graph of Ni element on the prepared powder.

3.2.2 L-PBF process and Design of Experiment

A commercial L-PBF machine (HBD-150D, Shanghai Hanbang United 3D Tech Co., Ltd., China) was used in this work to fabricate the TiC/IN738LC. It is equipped with a 400W IPG fiber laser and a laser spot with a diameter of 70 um. Figure 3.2 shows the L-PBF schematic diagram, where the cubic samples (8 mm×8 mm×8 mm) are used for the microstructural observation, and the tensile test specimen adopts the ASTM dimensions and standard [22]. Prior to the printing, the prepared powder was put into a furnace filled with inert gas and dried for 5 hours at 40 °C. The L-PBF scanning strategy adopted the 67° rotation in the layer-by-layer scanning direction [9].

A full factorial design with three variables and three levels was used in this work. The three design variables were the laser power (150 W-300 W), scanning speed (500 mm/s-1000 mm/s) and hatch space (0.09 mm-0.12 mm). The layer thickness was set as 0.03 mm for all the trials. Table 3.2 shows the details of the DoE. For each set of the process parameter, it corresponds to a volumetric energy density (VED) value, which is generally used as an important reference to correlate the interactions between the laser source and powder [23], namely the equation (3.1):

$$VED = \frac{P}{vhd}\left(\frac{J}{mm^3}\right) \tag{3.1}$$

where P, v, h and d stand for laser power, scanning speed, hatch space and layer thickness, respectively.

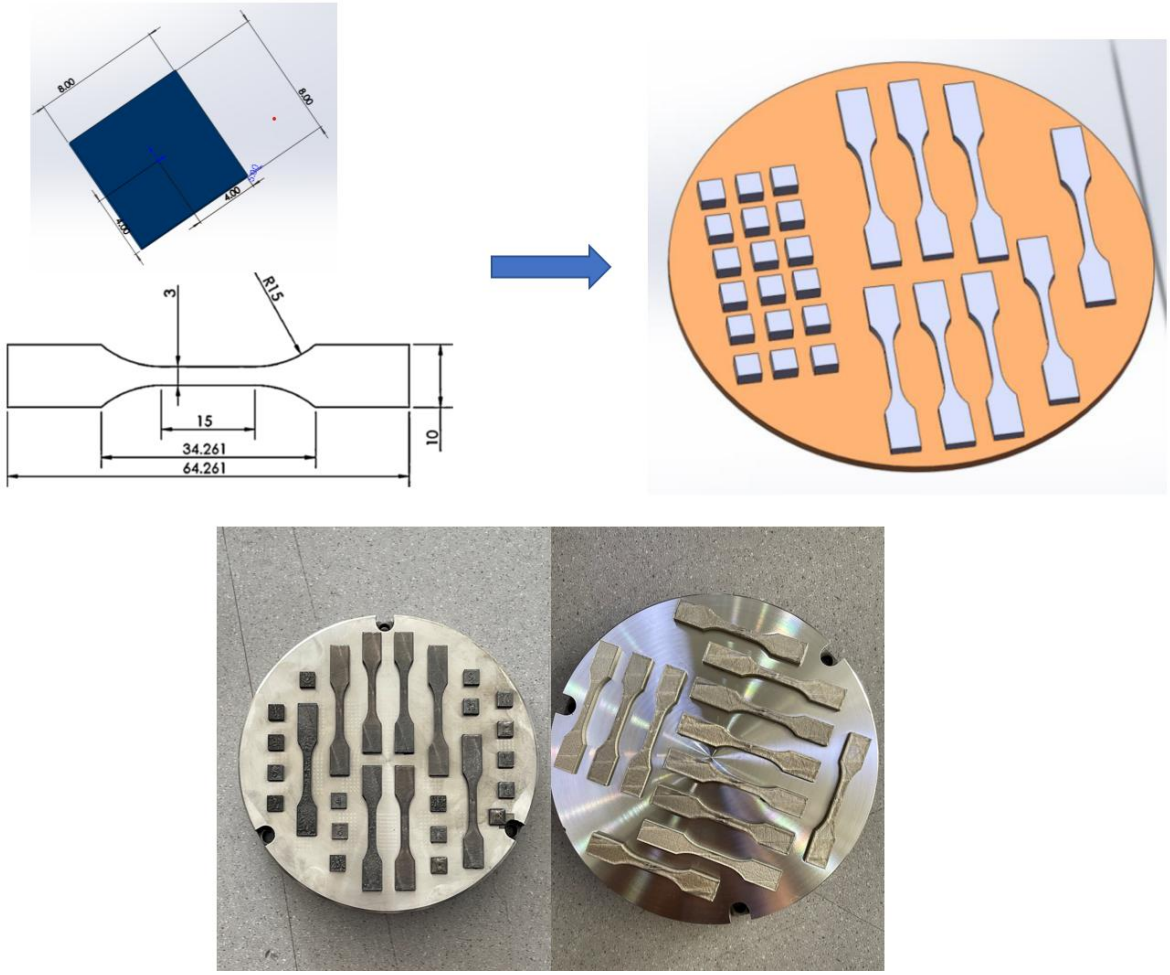

Figure 3.2 Schematic diagram of L-PBF process. Dimensional illustration of microstructural samples, tensile samples, and L-PBF as-printed samples.

Table 3.2 Design of Experiments of L-PBFed TiC-IN738LC.

# Samples	Layer thickness = 30um		
	Laser Power (W)	Scanning speed (mm/s)	Hatch space (mm)
1	150	500	0.090
2	150	500	0.105
3	150	500	0.120
4	150	750	0.090
5	150	750	0.105
6	150	750	0.120

7	150	1000	0.090
8	150	1000	0.105
9	150	1000	0.120
10	225	500	0.090
11	225	500	0.105
12	225	500	0.120
13	225	750	0.090
14	225	750	0.105
15	225	750	0.120
16	225	1000	0.090
17	225	1000	0.105
18	225	1000	0.120
19	300	500	0.090
20	300	500	0.105
21	300	500	0.120
22	300	750	0.090
23	300	750	0.105
24	300	750	0.120
25	300	1000	0.090
26	300	1000	0.105
27	300	1000	0.120

3.2.3 Characterization

Optical microscope (OM) was used to observe porosity as well as the melt pool morphology, and the samples should be well polished before the observations. Scanning electron microscope (SEM) (Hitachi SU5000, Japan) was used to observe the morphology of the fracture and microstructure. Before observation, the samples were ground, mounted, well-polished and etched. The samples were etched for 30 s with the selected etching solution 12mlH_3PO_4+48mlH_2SO_4+40mlHNO_3 [13]. Electron Back Scatter Diffraction (EBSD) was acquired with 20 kV accelerating voltage and 250 nm step size.

The Archimedes principle was used to measure the density of the as-printed sample ρ_f in this work, with a high-precision (0.001g) weighing scale. The relative density was obtained by the ratio of measured sample density ρ_f to the bulk density ρ_b, where ρ_b is given from the supplier. The images collected by optical microscopy (OM) were used

for the porosity and crack analysis. The build direction (BD) of cubic samples was taken as the investigated plane, and each sample collected five different regions on this plane, four of which are at the corners, and one is at the center. ImageJ, an open-source image analysis software, was used to measure porosity rate in this study. The threshold for image processing and adjustment was selected according to Reference [24], where to fix the lower limit on the pores from the segmentation, all the pores with the cubic-voxels smaller than 27 (3×3×3) are automatically neglected.

A Vickers microhardness tester (Wilson VH1102 Micro Hardness Testers, USA) was used for hardness testing in this study. The sample was well-polished to meet the criteria of the microhardness test. Two planes of the sample were used for microhardness testing, which are the building direction (BD) and scanning direction (SD). The sampling points were the straight line on the measured plane and the points were evenly taken with a distance of 0.2 mm. For each point, a 300 N load was applied with a dwell time of 10 s. The microhardness tester was calibrated before the test to ensure the accuracy of the result, and the measured systematic error was less than 0.05%. The final microhardness value was calculated by averaging at least 10 points of data on each measured plane.

A tensile machine (Zwick Amsler 100 HFT, Germany) was used for tensile testing. The tensile tests were performed at a rate of 1 mm/min, and the load direction was perpendicular to the building direction of the sample. For each parameter, three identical samples were used to perform the repeated experiments to ensure the accuracy of the results. The solution heat treatment was performed at 1120℃ with accelerated air cooling and 850℃ aging for 24 hours.

3.3 Results and Discussion

3.3.1 Density and porosity

Density is a frequently used metric to evaluate L-PBF as-printed samples due to its straightforward examination procedure. Multiple studies have established correlations among density, porosity, and mechanical properties [25]. Because of the inherent variations in material properties, the relationships between density and both microstructure and mechanical performance differ. Therefore, the density insights provided in this study will be valuable for future research on new composite materials.

Figure 3.3 illustrates the relationship between VED and density. As depicted, when the VED is low (40-80 J/mm^3), the relative densities range between 80% to 90%. For VED values between 80-100 J/mm^3, the relative densities notably increase to 96% to 98%. At a VED of 100-140 J/mm^3, the sample density peaks, achieving high-density (>99%) as-printed samples. However, when the VED exceeds 140 J/mm^3, the sample's density starts to decline, settling between 96% and 99%. It's important to highlight that the relative density at higher VED values remains substantially greater than at lower VED values. A lower VED, indicating reduced energy input, can lead to incomplete fusion and unmelted regions. This can result in the development of porous structures and cracks, thereby reducing the sample's density. Conversely, at higher VED values, excessive energy input can impact the molten pool's Marangoni effect. This can trap inert gas in the molten pool, leading to a gas trap effect, which produces fewer pores [26] and reduces relative density. To further optimize the processing parameter window, methodologies like data visualization and correlation quantification can be employed for machine learning [27] , offering reliable predictions of the relationship between density and VED. Table 3.3 shows the results from the DoE table. In this study, the tensile samples were printed with 5 sets of parameters, which the parameters were selected according to the results of density. Overall, the density analysis shows that the VED value of 100-140 J/mm^3 is the ideal processing parameter window, and the microstructural analysis in the following will further optimize the processing parameter window.

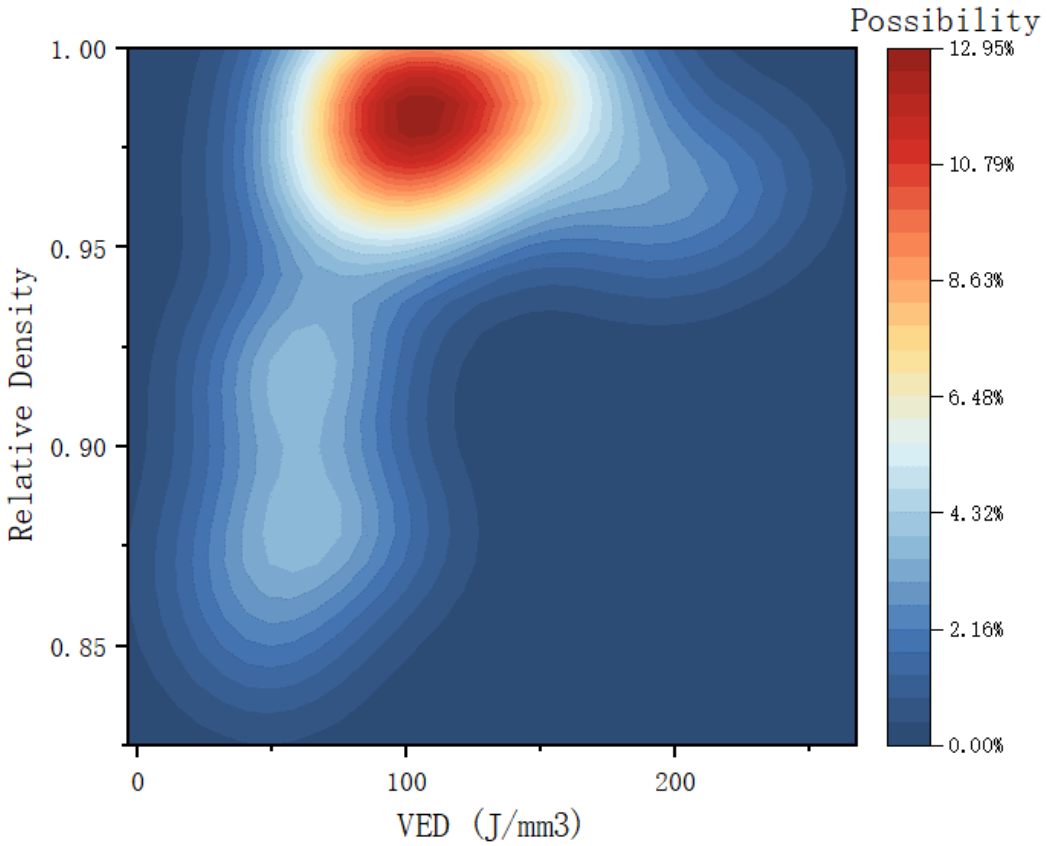

Figure 3.3 Relationship between VED and the relative density of as-printed samples.

Table 3.3 DoE table with the results of relative density and porosity.

Sample #	Laser power (W)	Scan velocity (mm/s)	Hatch space (mm)	VED (J/mm^3)	Relative density (%)	Porosity (%)
1	150	500	0.090	111.11	96.79	0.15
2	150	500	0.105	95.24	96.05	0.23
3	150	500	0.120	83.33	97.33	0.15
4	150	750	0.090	74.07	99.93	0.32
5	150	750	0.105	63.49	96.33	5.79
6	150	750	0.120	55.56	90.85	6.32
7	150	1000	0.090	55.56	92.18	0.52
8	150	1000	0.105	47.62	85.08	7.09
9	150	1000	0.120	41.67	87.29	7.52
10	225	500	0.090	166.67	97.29	0.42
11	225	500	0.105	142.86	99.86	0.26
12	225	500	0.120	125.00	96.86	1.42
13	225	750	0.090	111.11	99.02	0.17
14	225	750	0.105	95.24	99.05	0.12
15	225	750	0.120	83.33	97.08	3.17

16	225	1000	0.090	83.33	99.01	0.13
17	225	1000	0.105	71.43	92.83	0.19
18	225	1000	0.120	62.50	88.55	0.13
19	300	500	0.090	222.22	96.63	1.90
20	300	500	0.105	190.48	95.77	2.38
21	300	500	0.120	166.67	99.34	0.28
22	300	750	0.090	148.15	99.26	0.15
23	300	750	0.105	126.98	98.87	1.41
24	300	750	0.120	111.11	97.93	0.25
25	300	1000	0.090	111.11	98.79	0.15
26	300	1000	0.105	95.24	99.40	0.36
27	300	1000	0.120	83.33	87.70	0.14

Lack of fusion (LoF) and keyhole are the two main types of porosity in L-PBFed metal parts. It has been reported that the shape of pores by lack of fusion are usually in the irregular shape, with the size ranging from 10 μm to several millimeters. The lack of fusion can be attributed to insufficient penetration of the upper melt pool into the substrate or previously deposited layers [28]. Figure 3.4 shows the porosity graphs under each processing parameter. LoF and keyhole usually exist in samples with lower VED, for example, comparing the porosity with the laser energy of 225 W and 300 W, the laser energy of 150 W with higher scanning velocity formed more keyholes and unmelted regions, as shown in Figure 3.4 With the greater VED, the melting mode of the molten pool changes from the conduction mode to the keyhole mode, resulting in the molten pool forming the deep V shape [29], If the keyhole mode is not carefully controlled, the keyhole will become unstable and repeatedly form and collapse, eventually becoming the deep spherical pores within the sample [30]. As can be seen in Figure 3.4, the deep spherical pores were found in samples at high VED.

Figure 3.5 shows the relationship between VED and porosity, and the red curve is a third-order polynomial fitting curve, which is used to represent the trend of the data and to predict the data. As evidenced by Figures 3.4 and 3.5, a noteworthy observation can be made in the context of VED ranging between 100-120 J/mm^3. Within this spectrum, the L-PBFed TiC-IN738LC composite resulted in a considerably low porosity, below

0.3%, and a lack of cracks. This substantiates the claim that a comprehensive understanding and manipulation of processing parameters can facilitate control over crack inhibition in this innovative composite material. Meanwhile, based on the conclusion drawn from Figure 3.3, it agrees with the results in Figure 3.5, namely when the VED is within 100-140 J/mm^3, the density is higher and the porosity is lower; when VED is less than 100 J/mm^3 or greater than 140 J/mm^3, due to the defects such as lack of fusion and keyhole (as shown in Figure 3.4), the density is lower and porosity rate is higher. In summary, to achieve the prominent printability (porosity below 0.4% and crack-free) of L-PBFed samples, the optimal processing window of VED is between 100 J/mm^3 and 120 J/mm^3.

Figure 3.6 shows the relationship between each processing parameter and porosity rate. Figure 3.6 is an important reference for determining the effect of specific parameters on porosity rate. The laser power, for instance, has a significant impact on porosity rate, with lower power levels resulting in the formation of keyholes and cracks due to the generation of LoF. Higher laser power inputs, on the other hand, provide more energy to the melt pool dynamics, particularly at lower scanning speeds and smaller hatch distances. This greater energy enables the melt pool to fully melt the powder and produce fewer LoF, resulting in a lower porosity rate. Scanning speed also affects porosity rate, with slower speeds resulting in a higher VED and a longer interaction time between the laser and powder, leading to a lower porosity rate. Conversely, faster scanning speeds reduce the interaction time, resulting in the formation of LoF. Hatch distance, which indicates the density of the neighbouring powder, also affects porosity rate, with shorter distances enabling more complete interaction between the powder and laser, resulting in a lower porosity rate. In summary, the combination of the lowest porosity rate is built under the conditions: the laser power of 225 W, scan velocity of 500 mm/s and hatch space of 0.09 mm.

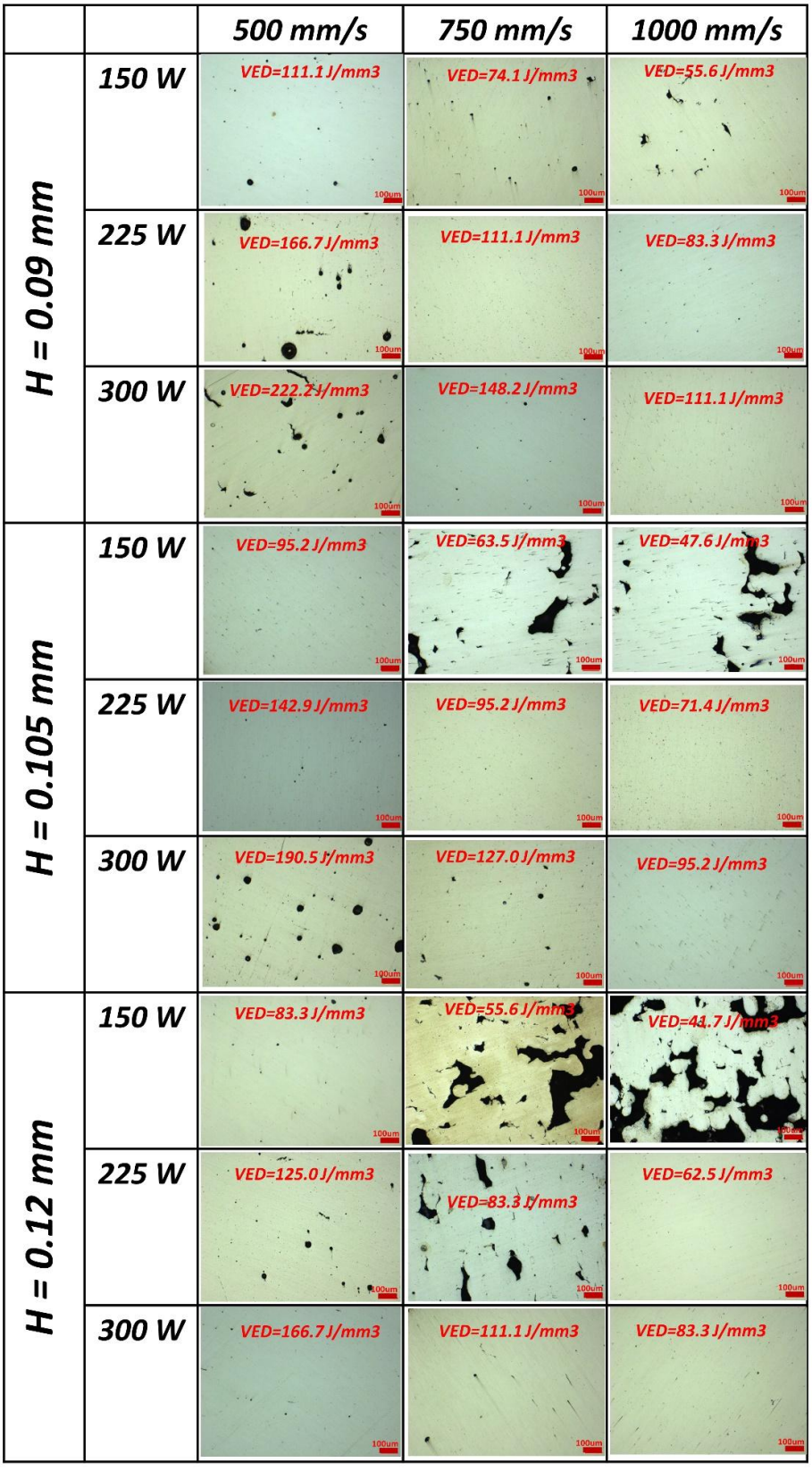

Figure 3.4 Results of porosity rate under each processing parameter for all 27 L-PBFed as-printed samples. All the pictures have the same scale bar (100 μm).

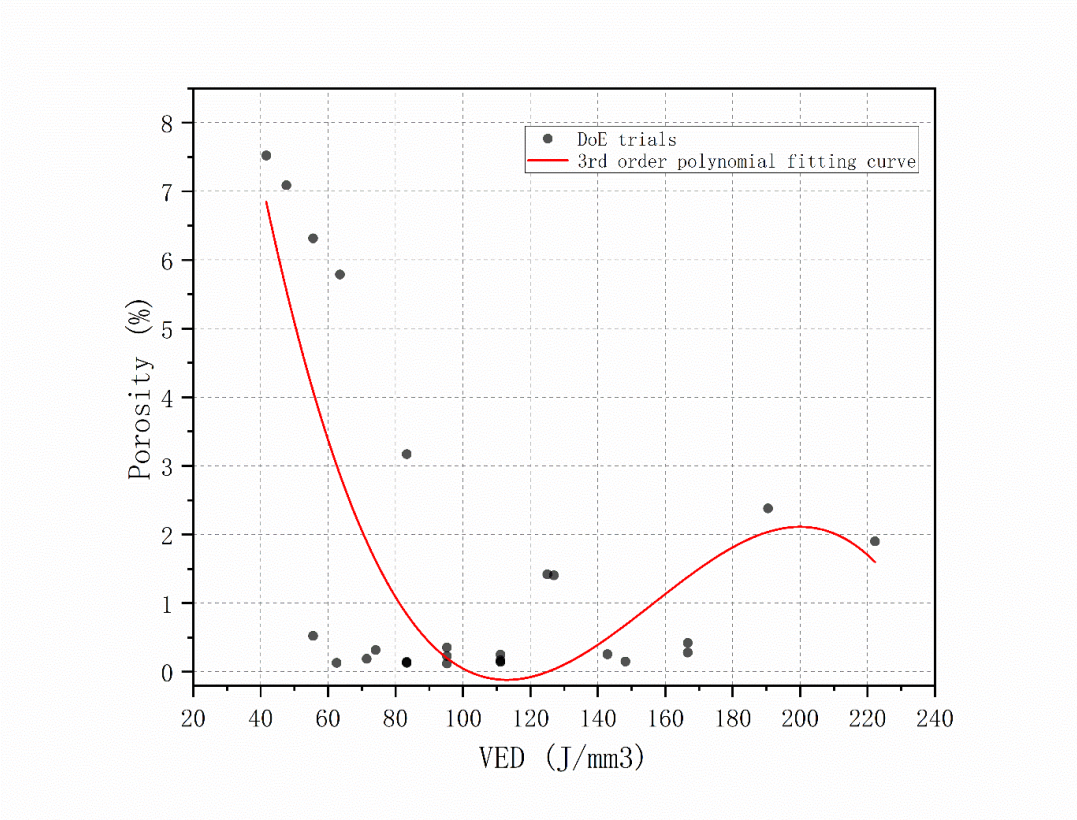

Figure 3.5 Relationship between VED and porosity rate of as-printed samples.

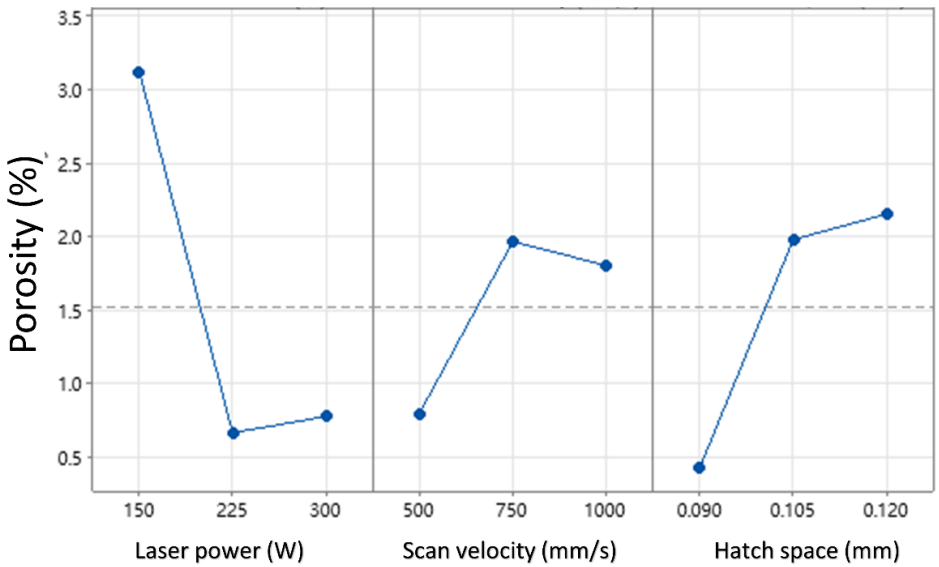

Figure 3.6 The relationship between porosity rate and each processing parameter.

3.3.2 Microhardness

A set of 7 groups of parameters were selected for the microhardness experiment based on the density and porosity results, as shown in Table 3.4. The results of the Vickers hardness test are shown in Figure 3.7. For the microhardness in the scan direction, it is obvious to find the maximum value of 625 ± 53 HV is measured at the VED=111.1 J/mm^3, while the minimum value of 468 ± 50 HV is measured at VED=74.1 J/mm^3. When VED continues to increase (>111.1 J/mm^3), the porosity rate gradually increases due to the gas trapping effect, causing the density to decrease, and eventually lowering in the microhardness value. It is worth noting that the microhardness at low VED is much smaller than that at high VED due to the fact that cracks and keyholes are more likely to occur at low VED. For the microhardness in the build direction, the overall hardness value is smaller than that in the scanning direction, and the results follow the similar trend as the scanning direction, namely, VED=111.1 J/mm^3 has the largest microhardness and the values are smaller at other VEDs. As shown in Figure 3.7, the overall disparity of microhardness in build direction is not as noticeable as the scanning direction. One of the reasons is that the build direction transfers more heat to the substrate or the previous layer, thus it has a more complex thermal cycle history than that in the scanning direction, thus, in building direction, the thermal gradient is larger, causing the greater residual stress and smaller microhardness [31]. According to the previous study, the high density and low porosity will contribute to the enhancement of microhardness [6], the similar conclusion has also been found in this study. In summary, the optimal microhardness was obtained at VED=111.1 J/mm^3 with 527 HV in the build direction and 678 HV in the scan direction.

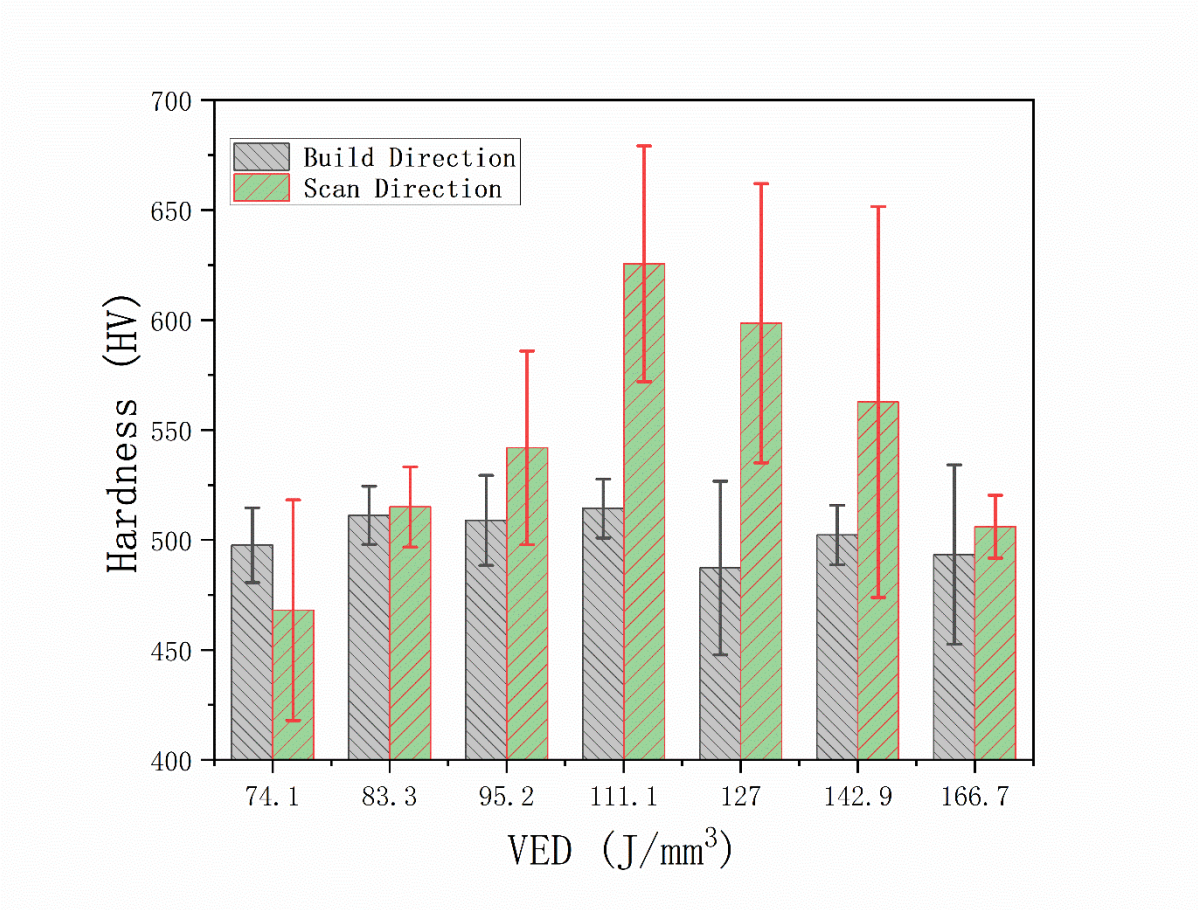

Figure 3.7 Microhardness results in the build directions and scan direction.

Table 3.4 The details of L-PBFed microhardness samples.

Sample #	Laser power (W)	Scan velocity (mm/s)	Hatch space (mm)	VED (J/mm^3)	Density (%)	Porosity (%)	BD Microhardness (HV)	SD Microhardness (HV)
1	150	750	0.090	74.1	98.93	0.32	497.6	468.0
2	225	500	0.105	142.9	99.86	0.26	502.2	562.7
3	225	750	0.090	111.1	99.02	0.17	514.2	625.8
4	225	750	0.120	83.3	97.08	3.17	511.2	515.0
5	300	500	0.120	166.7	99.34	0.28	493.3	506.0
6	300	1000	0.105	95.2	99.40	0.36	508.9	541.9
7	300	750	0.105	127.0	98.87	1.41	487.2	598.5

Figure 3.8 shows the comparison of microhardness between the TiC-IN738LC and IN738LC. It is obvious that TiC modified IN738LC has greater microhardness than IN738LC in both scanning direction and the building direction. In the scanning

direction, the microhardness of TiC-IN738LC is about 35% higher than that of IN738LC, and about 20% higher in the building direction. For the L-PBFed IN738LC, the trend follows the similar pattern as the TiC-IN738LC, which it has the highest hardness when VED=111.1 J/mm^3 or VED=95.2 J/mm^3, its hardness will gradually decrease at other VEDs. For the TiC-IN738LC, due to the higher hardness of nano-ceramic particles TiC, by attaching the nanoparticles TiC to the IN738LC, several strengthening mechanisms will arise during the laser interaction. Since the nanoparticles have greater heat transfer coefficient, it will cause the thermal mismatch effect, along with the Marangoni effect of the molten pool, nanoparticles are easy to nucleate and crystallize on the grain boundary, and the slip movement along the grain boundary becomes difficult, resulting in the inhibition of dislocation, thus, enhancing its strength to resist the deformation, these strengthening mechanisms have been demonstrated and elucidated in previous studies [9, 15, 26]. It also should be noted that the previous section has shown the good attachment of TiC to IN738LC, the wetting characteristics are ensured, which is essential for printing the high-quality samples. In summary, via the addition of nanoparticles, it will cause thermal mismatch and dislocation effects, thereby the microhardness performance of TiC-IN738LC is reinforced and better than the virgin IN738LC.

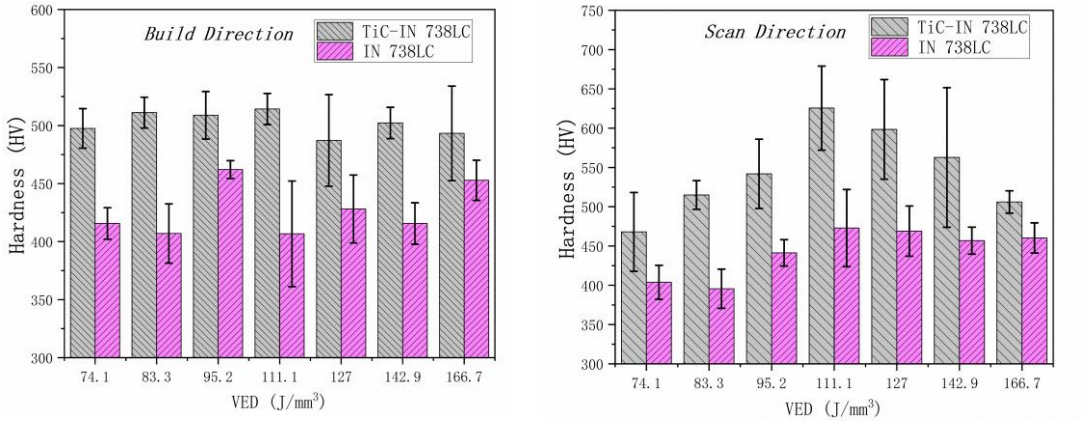

Figure 3.8 Microhardness comparisons between the TiC-IN738LC and IN738LC in different directions.

3.3.3 Tensile strength

Figure 3.9 shows the results of the tensile test of L-PBFed TiC-IN738LC and IN738LC and the detailed data are given in Table 3.5. In the tensile test of three groups of TiC-IN738LC, it can be seen that the sample at VED=95.2 J/mm^2 has the largest yield stress and ultimate tensile strength, which is 9.7% and 1.4% higher than that at VED=111.1 J/mm^2, and 29.7% and 19.7% higher than that at VED =142.8J/mm^2, respectively. When VED=111.1 J/mm^2, the elongation rate is higher than the other two groups, which is 45.2% higher than VED=95.2J/mm^2 and 60% higher than VED=142.8J/mm^2. Overall, although the sample at VED=111.1 J/mm^2 sacrifices slightly in tensile strength, the lower porosity rate, crack-free and better ductility make the VED=111.1 J/mm^2 the optimal processing parameter. This work also compared the TiC-IN738LC and IN738LC in tensile tests. The IN738LC in Figure 3.9 adopts the optimal parameters determined in the previous research [8], and is fabricated by the same L-PBF machine in this study to ensure the consistency of the data and eliminate the potential errors between the different L-PBF machines. The ductility of IN738LC is much greater than that of TiC-IN738LC, which is 50%, 72% and 80% higher than VED=111.1 J/mm^2, VED95.2 J/mm^2, and VED=142.8 J/mm^2, respectively. However, the yield strength and ultimate tensile strength are much smaller than those of the nano-TiC modified IN738LC. This phenomenon widely exists in the ceramic-reinforced metal matrix composites, and the heat treatment is usually to be considered as an approach to improve the elongation [8]. Figure 3.10 shows the results obtained in this study compared with the previous studies on hard-to-machine Ni-superalloys [8, 32-36]. It should be noted that none of the Nickels were heat treated in Figure 3.10. It can be concluded from Figure 3.10 that the TiC-IN738LC developed in this study has significantly enhanced mechanical strength and thereby having the considerable potential value to furtherly research.

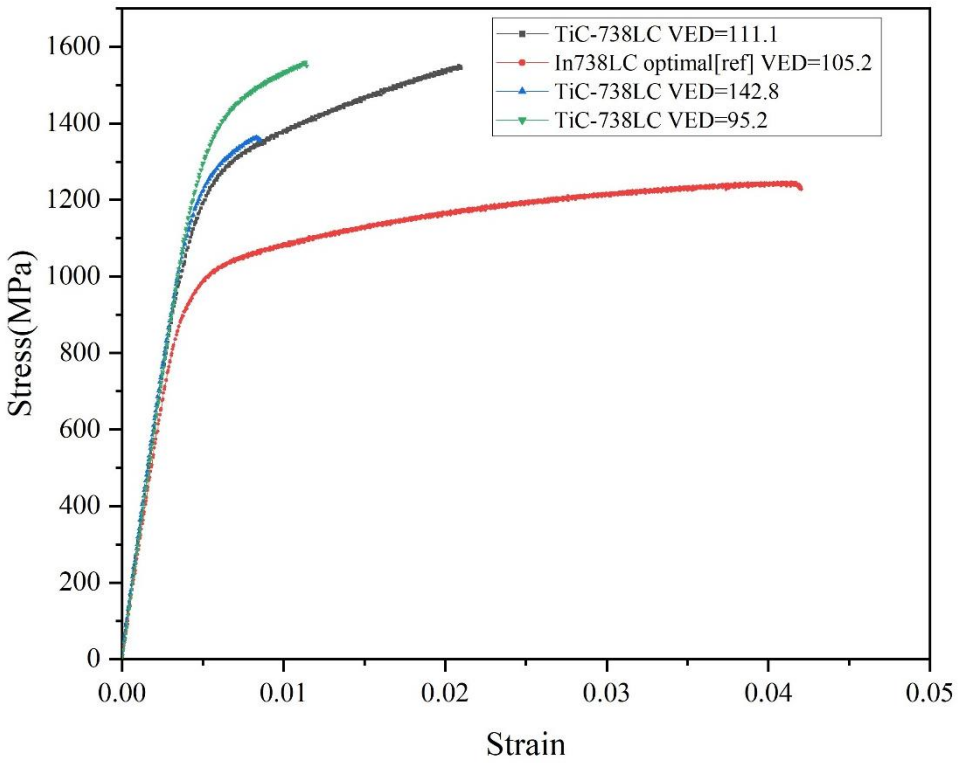

Figure 3.9 Tensile test results of TiC-IN738LC under different VED.

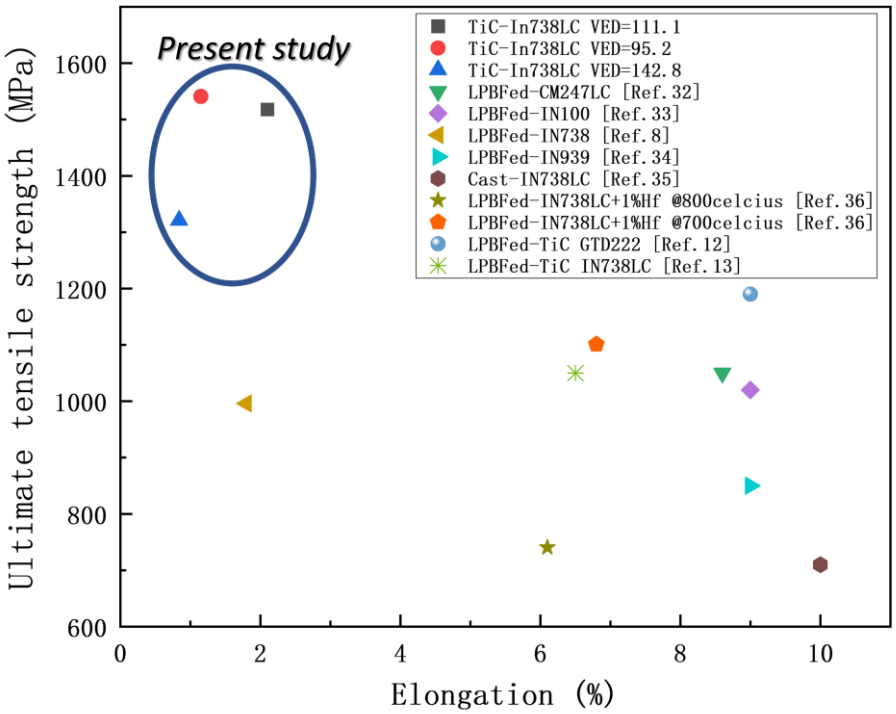

Figure 3.10 Comparison of elongation rate and ultimate tensile strength between this study (circled in the graph) and other difficult-to-machine nickel superalloys studies.

The microstructural fracture morphology reveals the fracture mechanisms in depth. Figures 3.11 compares the difference between brittle fracture and ductile fracture and shows clear dissimilarity of brittle and ductile fractures in the microstructures. On the surface of the brittle fracture, there are lumpy blocks, which are in the shape of regular strips. Meanwhile, the long grooves and large protrusions on the surface will significantly reduce the tensile strength. These coarse blocks and strips are less congregated than dimples (Figure 3.11a, b, c) and it is easier to cause the defects and undermine ductile properties. On the other hand, there are many dimples on the ductile fracture (Figure 3.11d). The deformation of the dimples can improve the plasticity of the material [37, 38]. When VED=95.2 J/mm^3, the ductility of the material decreases significantly, as there are many unmelted particles and irregular blocks, which will eventually become the source of cracks and lead to the brittle fractures (Figure 3.11a). In comparison, when VED=142.8 J/mm^3, the fracture still has the apparent characteristics of brittle fracture, however, due to the high energy input, there is no unmelted particle found (Figure 3.11c). When VED=111.1 J/mm^3, there are some dimples arisen (Figure 3.11b) and the ductile property is improved as shown in Figure 3.9. However, when comparing the fracture morphology with the IN738LC, the IN738LC has much denser dimples than TiC-IN738LC (Figure 3.11d) and thereby a better ductility as presented in Figure 3.9. Previous studies have clarified that the ductile fracture initiates from the fracture source and rapidly propagates to the final fracture zone, however, when the protruding cracks encounter the internal micro-pores or unmelted powder, they will stop extending and lead to a clear boundary on the fracture morphology. The fibre stripes are unevenly distributed at the edge of the fracture and prone to generate the large stress concentration region, eventually leading to the ductile fracture [39]. The dimples are beneficial to the ductility but when the excessive dimples happen, it is prone to generate a larger stress concentration area and causing the strength in the tensile direction is impaired. As discussed above, the evidence of the fracture morphology agrees with the tensile test results.

Table 3.5 The results of the tensile test.

Description	Yield Strength (MPa)	Ultimate Tensile Strength (MPa)	Elongation (%)
TiC-In738LC VED=111.1	1110±21	1518±12	2.1±0.05
TiC-In738LC VED=95.2	1230±33	1541±23	1.15±0.04
TiC-In738LC VED=142.8	1141±15	1321±16	0.84±0.02
In738LC VED=105.2	864±24	1238±45	4.2±0.10

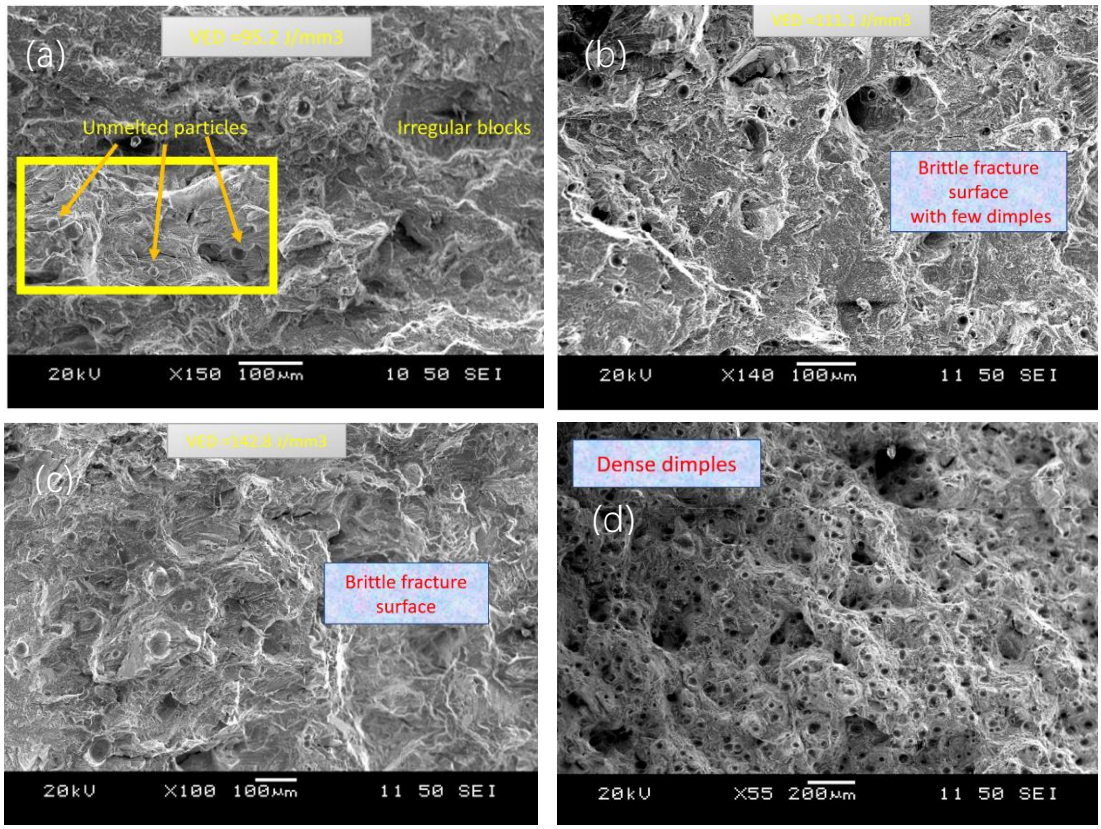

Figure 3.11 Fracture morphologies under different processing parameters. (a) TiC-IN738LC with VED=95.2 J/mm^3 with magnified region inside; (b) TiC-IN738LC with VED=111.1 J/mm^3; (c) TiC-IN738LC with VED=142.8 J/mm^3; and d) IN738LC.

3.3.4. The strengthening mechanisms of nano-TiC particles

The anisotropic nature of materials by the L-PBF process is often reflected by the grain shape and size. Figures 3.12 shows the EBSD data of the IN738LC and TiC-IN738LC. As visible in Figure 3.12a, L-PBFed IN738LC alloy is characterized by elongated

grains. An example of a completely different grain structure is shown in Figure 3.12b: the alloy containing some TiC nanoparticles is indeed characterized by a fine distribution of the columnar grains, by impeding the grain boundary growth and forming the new nucleate sites. Figure 3.12c and Figure 3.12d show the grain size of pure IN738LC and TiC-IN738LC, and with the addition of the nano-TiC, the grain size is fully refined and much smaller than the pure IN738LC [40]. These nanoparticles prevent grain overgrowth and interfere with recrystallization. The occurrence of recrystallization is related to the accumulated internal strain energy. This energy exists in the form of dislocation density. Without recrystallization, large dendrites would remain and reduce mechanical properties [41].

According to the Hall-Petch formula, smaller grain sizes result in higher yield strengths [42]. The formula states that the yield strength of a polycrystalline material is inversely proportional to the square root of its grain size. Mathematically, the Hall-Petch formula can be expressed as equation (3.2):

$$\sigma_y = \sigma_0 + k_y d^{-\frac{1}{2}} \tag{3.2}$$

where σ_y is the yield strength of the material, σ_0 is the intrinsic strength of material, k_y is a constant term called the Hall-Petch slope and d is the average grain size of the material. According to the literature [43], the grain size strengthening $\Delta\sigma_y$ can be solved, with the lower limit 88 MPa to the upper limit 187 MPa, where in present work, the $\Delta\sigma_y$ is around 200 MPa and it slightly higher than the Hall-Petch method. Overall, the smaller grain size explains why the tensile strength is improved by the addition of the nano-TiC particles.

Figure 3.13 shows the schematics of nano-TiC reinforced IN738LC mechanism. When IN738LC powders are heated to high temperatures, the nanoparticles within them can impede the columnar growth and rearrange IN738LC matrix to form the smaller grains. One of the reasons is that nanoparticles can act as pinning sites for grain boundaries. Grain boundaries are the regions between individual grains, and they can be areas of

high energy. When the IN738LC powders is heated, atoms can diffuse across grain boundaries and cause the grains to grow. However, if there are nano particles in the material, they can act as obstacles to this diffusion and grain boundary migration process, impeding grain growth [44]. Also, due to size of nano particles, they are typically much smaller than the grains themselves. When a material is heated, the larger grains will tend to grow at the expense of the smaller ones driven by interface energy. However, if there are nano particles present, they can act as nucleation sites for new grains, which can compete with the existing larger grains for material. This competition can impede the growth of the larger grains, leading to a finer microstructure [45].

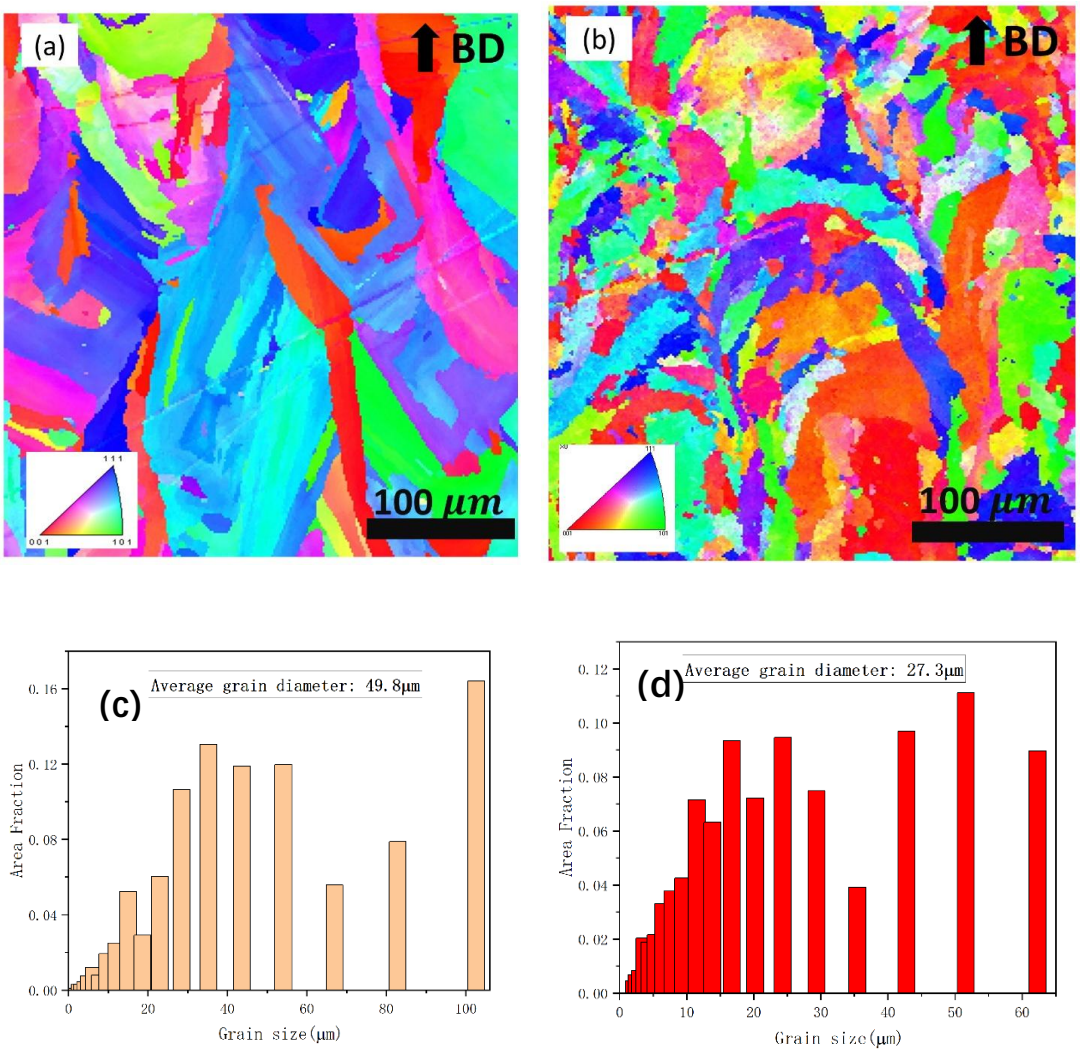

Figure 3.12 EBSD results of IN738LC and TiC-IN738LC composite: (a) IPF of IN738LC; (b) IPF of TiC modified IN738LC; (c) Grain size distribution graphs of pure IN738LC; (d) Grain size distribution graphs of TiC-IN738LC.

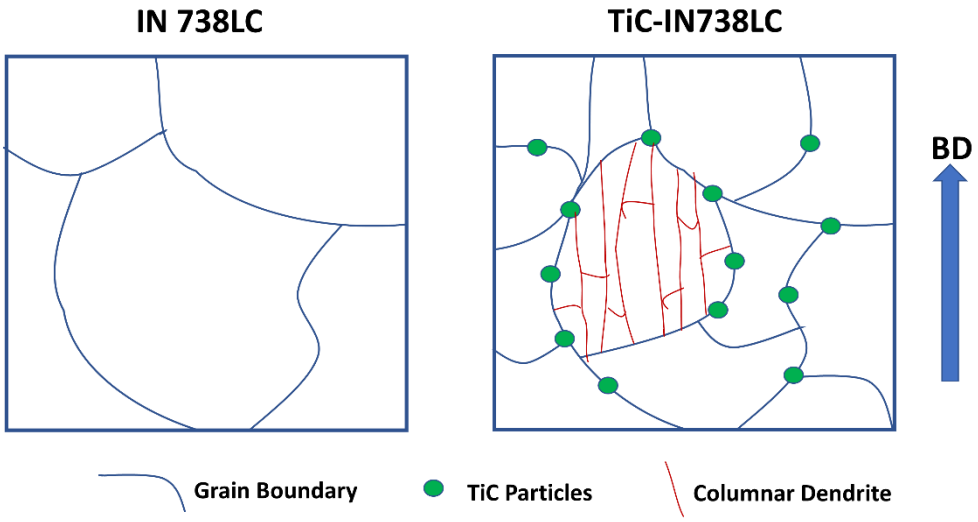

Figure 3.13 Schematic of nano-TiC reinforced IN738LC strengthening mechanism. The columnar dendrites are not shown on all the grains for the simplification.

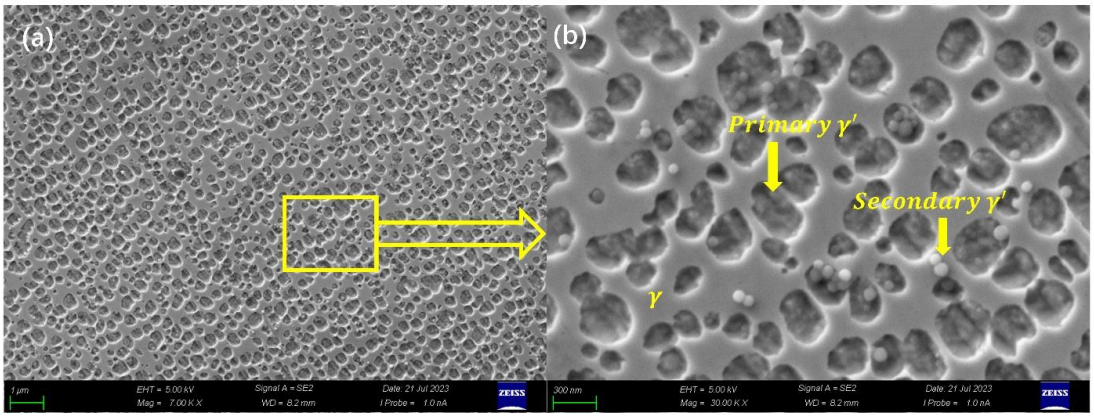

Figure 3.14 The microstructure of TiC-IN738LC. The primary γ' phase and secondary γ' phase.

Figure 3.14 illustrates the microstructure of TiC-IN738LC, clearly depicting the presence of the γ' phase and the smaller secondary γ' precipitates. This observation substantiates the hypothesis that the introduction of nano-TiC nanoparticles does not obstruct the γ' phase generation, but rather augments its proliferation. The load-bearing strengthening mechanism is typically relevant to coherent precipitates, such as primary and secondary gamma prime (γ') phases, often observed in nickel-based superalloys [46]. The significant contribution of these γ' phases to the tensile strength of the material

should be recognized. When subjected to external stress, the load distribution is facilitated between the material matrix and the precipitates. Owing to their intrinsic strength and stability, the precipitates effectively enhance the overall material strength by bearing a portion of the applied load. Essentially, these precipitates function as reinforcing elements within the matrix. The smaller secondary γ' precipitates play a pivotal role not only in load distribution but also in obstructing dislocation movement. The introduction of these precipitates increases the obstacle density that dislocations have to circumnavigate, resulting in additional strengthening. This process elevates the yield strength, which is instrumental in improving the overall tensile strength of the material.

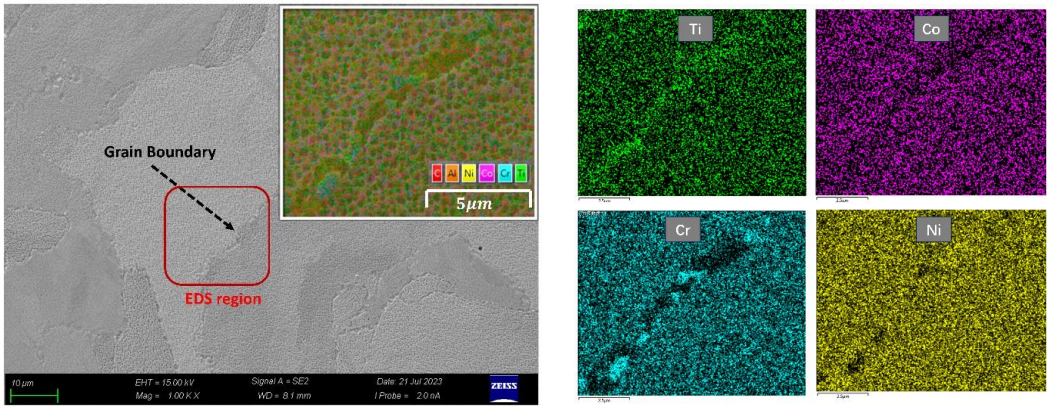

Figure 3.15 SEM/EDS of the TiC-IN738LC at the grain boundary region.

In Figure 3.15, EDS analysis was examined specifically in the grain boundary region. The analysis indicates a high concentration of Ti elements within this area, suggesting that the incorporation of TiC nanoparticles tends to accumulate at the grain boundary and the TiC nanoparticles function as impediments to dislocation movement. The EBSD result validates this observation, highlighting that the addition of these nanoparticles results in a significantly reduced average grain size compared to pure IN738LC. This phenomenon aligns with the Orowan strengthening mechanism, which posits that the creation of a dislocation loop around a nanoparticle demands more energy than navigating through an unobstructed lattice [47]. Consequently, the introduction of TiC nanoparticles increases the energy threshold required for the plastic

deformation of the material. This increased energy requirement, in turn, amplifies the material's yield strength and hardness.

According to the experimental data, the processing parameters, which define the VED, correlate with the microhardness and tensile strength. From Figure 3.3 and Figure 3.7, at high scanning speeds, the obtained density and hardness are lower, which may be related to wettability and Rayleigh instability. The temperature of molten pool is calculated using Equation (3.3) below [48]:

$$Tmp = \frac{C_2}{\lambda \ln\left(\frac{C_1 S_S H_S}{L_P \lambda^5} + 1\right)} \tag{3.3}$$

where $C1$ and $C2$ are the Planck's distribution constants, λ is the wavelength of the laser. Scanning speed is inversely proportional to melt pool temperature, and a higher scanning speed leads to a lower temperature and higher surface tension (according to the thermocapillary effect) [30,31]:

$$\gamma = \gamma^* \left(\frac{T_C - T_0}{T_C}\right)\left[1 - \left[\frac{C_2}{(T_C - T_0)\lambda \ln\left(\frac{C_1 S_S H_S}{L_P \lambda^5} + 1\right)} - \frac{T_C - T_0}{T_C}\right]\right]^n \tag{3.4}$$

For Equation (3.4), γ^* is constant for each liquid, Tc is the critical temperature and T_0 is the reference temperature. Therefore, based on Equations (3.5), the surface tension values of the solid-liquid and liquid-gas phases are larger, increasing the chance of droplet generation [48-50]. This phenomenon will lead to low wettability and an increasing chance of spheroidization, which is a common defect in metal AM and causes the porosity rate to increase and decrease the density and hardness [5, 48].

$$S = \gamma_{SG} - (\gamma_{SL} + \gamma_{LG});$$

$$If\ S > 0 \Rightarrow Filmappears \tag{3.5}$$

$$If\ S < 0 \Rightarrow Dropletappears;$$

Figure 3.3 and Figure 3.7 show that lower hardness and density were obtained with the

lower input of laser power. According to Equation (3.3), less energy is transmitted to the molten pool at the lower laser power and the temperature of the molten pool is therefore decreased. In this case, due to the lack of the Marangoni convection, causing the higher heat penetration and generating more steam and bubbles within the molten pool. The bubbles tend to escape from the molten pool, and the interaction of steam forces with the hydrostatic pressure and surface tension will result in the formation of small pores and eventually weaken hardness properties. The steam force is directly related to the diameter of the pores. In a smaller diameter pore, the larger pressure on the pores results in larger forces, the steam tends to move to the top surface of the molten pool to escape and overcome the hydrostatic pressure as well as the surface tension, thus the keyhole is formed. Furtherly, this leads to the lack of fusion and the creation of large pores, even the cracks, thereby lowering the mechanical properties [5]. The morphology of the melt pool and grain structure are significantly affected Under different VED. A higher VED results in a deeper and wider melt pool, while a lower VED leads to a shallower and narrower one. The flow and spread of the powder also depend on VED. Differences in crystallization rates influence the distribution of TiC at grain boundaries, which directly relates to the material's mechanical and thermal properties. In summary, as stated above, the quality of an as-printed sample has a close relationship with the processing parameters, and research on optimizing the processing parameters and obtaining the correlations with microstructural data will gain a comprehensive understanding of material properties during the L-PBF process.

In this work, it can be concluded that cracks can be effectively suppressed by adding nano-ceramic particles. There are two main mechanisms for crack formation: liquefaction of low-melting phases and structural liquefaction [50, 51]. Carbides in the heat-affected zone have been considered as the primary phase which causes the structural liquefaction [52]. During the L-PBF, the thermal cycling of carbides can be very intense. However, due to the large temperature gradient and fast cooling rate, carbides do not have enough time to dissolve into the surrounding matrix. It has been clarified in previous studies that even introducing the higher carbon content, no liquid

film was found at the interface between the carbide and the matrix by the characterization, namely no cracks caused by the structural liquefaction were observed. Similar findings were found in these studies [50, 51], which the tendency of structural liquefaction is a strong function of the carbide size. In this study, the TiC particles are the size of 50 nm, therefore, by the addition of the nano-TiC particles will benefit to mitigate the liquefaction effect and reduce the cracks.

3.4 Conclusions

This paper proposes a method of adding 2wt% nano- TiC particles to fabricate the IN738LC via L-PBF and the crack-free samples were achieved. The relationship between the processing parameters and the quality of as-printed samples was studied. Based on the nano-TiC strengthening principle, combined with the results from fracture morphology and mechanical tests, the mechanisms of obtaining high-quality TiC-IN738LC were theoretically described. The main conclusions of this study can be summarized as follows:

(1). The effects of process parameters on the density, porosity, hardness and tensile strength of nano-TiC reinforced IN738LC were comprehensively examined, and by optimizing the parameters, high-strength TiC-IN738LC could be prepared.

(2). The optimal parameters of high-density and low-porosity L-PBFed TiC-IN738LC are VED= 111.1J/mm3 (laser energy 225W, scanning speed 750mm/s, hatch spacing 0.09mm), and powder layer thickness 0.03mm.

(3). By adding TiC nanoparticle to IN738LC, a low-porosity and high-strength TiC-IN738LC was fabricated; Compared with the L-PBFed IN738LC, the microhardness of TiC-IN738LC increased by 20%-40%, and the tensile strength of TiC-IN738LC improved by 10%-30%. The synergistic effect of fine grain strengthening mechanism, load-bearing strengthening mechanism and Orowan strengthening mechanism was accounted for the performance enhancement.

(4). The results in this work provide an experimental reference for the L-PBF parameters of TiC-IN738LC and furtherly expand the applications in terms of metal matrix composite in the fields of aerospace and deep-ocean exploration.

Acknowledgements

This work was supported by the National Natural Science Foundation of China [Grant number 51975301], Natural Science Foundation of Zhejiang, China [Grant number LZ22E050002] and the University of Birmingham that provided the funding.

References

1. Sanchez, S., et al., *Powder Bed Fusion of nickel-based superalloys: A review.* International Journal of Machine Tools and Manufacture, 2021. **165**https://doi.org/10.1016/j.ijmachtools.2021.103729.

2. Shi, J. and Y. Wang, *Development of metal matrix composites by laser-assisted additive manufacturing technologies: a review.* Journal of Materials Science, 2020. **55**(23): p. 9883-9917https://doi.org/10.1007/s10853-020-04730-3.

3. Han, Q., et al., *Laser powder bed fusion of WC-reinforced Hastelloy-X composite: microstructure and mechanical properties.* Journal of Materials Science, 2020. **56**(2): p. 1768-1782https://doi.org/10.1007/s10853-020-05327-6.

4. Chen, L., et al., *Microstructure evolution, mechanical properties, and strengthening mechanism of TiC reinforced Inconel 625 nanocomposites fabricated by selective laser melting.* Materials Science and Engineering: A, 2020. **792**https://doi.org/10.1016/j.msea.2020.139655.

5. Khorasani, A., et al., *The effect of SLM process parameters on density, hardness, tensile strength and surface quality of Ti-6Al-4V.* Additive Manufacturing, 2019. **25**: p. 176-186https://doi.org/10.1016/j.addma.2018.09.002.

6. Tucho, W.M., et al., *Investigation of effects of process parameters on microstructure and hardness of SLM manufactured SS316L.* Journal of Alloys and Compounds, 2018. **740**: p. 910-925https://doi.org/10.1016/j.jallcom.2018.01.098.

7. Kasperovich, G., et al., *Correlation between porosity and processing parameters in TiAl6V4 produced by selective laser melting.* Materials & Design, 2016. **105**: p. 160-170https://doi.org/10.1016/j.matdes.2016.05.070.

8. Wang, H., et al., *Selective laser melting of the hard-to-weld IN738LC superalloy: Efforts to mitigate defects and the resultant microstructural and mechanical properties.* Journal of Alloys and Compounds, 2019. **807**https://doi.org/10.1016/j.jallcom.2019.151662.

9. Lv, Y., et al., *Cracking inhibition behavior and the strengthening effect of TiC particles on the CM247LC superalloy prepared by selective laser melting.* Materials Science and Engineering: A, 2022. **858**https://doi.org/10.1016/j.msea.2022.144119.

10. Ogunbiyi, O.F., et al., *Microstructural characteristics and thermophysical properties of spark plasma sintered Inconel 738LC.* The International Journal of Advanced Manufacturing Technology, 2019. **104**(1-4): p. 1425-1436https://doi.org/10.1007/s00170-019-03983-w.

11. Lemos, G., et al., *Creep resistance improvement of a polycrystalline Ni-based superalloy via TiC particles reinforcement.* Materials Science and Engineering: A, 2022. **854**https://doi.org/10.1016/j.msea.2022.143821.

12. Wang, R., et al., *Novel selective laser melting processed in-situ TiC particle-*

reinforced Ni matrix composite with excellent processability and mechanical properties. Materials Science and Engineering: A, 2020. **797**https://doi.org/10.1016/j.msea.2020.140145.

13. Zhou, W., et al., *Inhibition of cracking by grain boundary modification in a non-weldable nickel-based superalloy processed by laser powder bed fusion.* Materials Science and Engineering: A, 2020. **791**https://doi.org/10.1016/j.msea.2020.139745.

14. Gu, D., et al., *Laser additive manufacturing of nano-TiC reinforced Ni-based nanocomposites with tailored microstructure and performance.* Composites Part B: Engineering, 2019. **163**: p. 585-597https://doi.org/10.1016/j.compositesb.2018.12.146.

15. Jia, Q. and D. Gu, *Selective laser melting additive manufacturing of TiC/Inconel 718 bulk-form nanocomposites: Densification, microstructure, and performance.* Journal of Materials Research, 2014. **29**(17): p. 1960-1969https://doi.org/10.1557/jmr.2014.130.

16. Rong, T., et al., *Effects of tailored gradient interface on wear properties of WC/Inconel 718 composites using selective laser melting.* Surface and Coatings Technology, 2016. **307**: p. 418-427https://doi.org/10.1016/j.surfcoat.2016.09.011.

17. Zhang, B., et al., *Comparison of carbon-based reinforcement on laser aided additive manufacturing Inconel 625 composites.* Applied Surface Science, 2019. **490**: p. 522-534https://doi.org/10.1016/j.apsusc.2019.06.008.

18. Zhang, B., et al., *Microstructure and mechanical properties of Inconel 625/nano-TiB2 composite fabricated by LAAM.* Materials & Design, 2016. **111**: p. 70-79https://doi.org/10.1016/j.matdes.2016.08.078.

19. Zhang, H., et al., *Understanding tensile and creep properties of WC reinforced nickel-based composites fabricated by selective laser melting.* Materials Science and Engineering: A, 2021. **802**https://doi.org/10.1016/j.msea.2020.140431.

20. Mishurova, T., et al., *New aspects about the search for the most relevant parameters optimizing SLM materials.* Additive Manufacturing, 2019. **25**: p. 325-334https://doi.org/10.1016/j.addma.2018.11.023.

21. Koutiri, I., et al., *Influence of SLM process parameters on the surface finish, porosity rate and fatigue behavior of as-built Inconel 625 parts.* Journal of Materials Processing Technology, 2018. **255**: p. 536-546https://doi.org/10.1016/j.jmatprotec.2017.12.043.

22. Zhang, S., et al., *An experimental study of tensile property variability in selective laser melting.* Journal of Manufacturing Processes, 2019. **43**: p. 26-35https://doi.org/10.1016/j.jmapro.2019.03.045.

23. Majeed, A., et al., *Investigation of T4 and T6 heat treatment influences on relative density and porosity of AlSi10Mg alloy components manufactured by SLM.* Computers & Industrial Engineering, 2020. **139**https://doi.org/10.1016/j.cie.2019.106194.

24. Damon, J., et al., *Process dependent porosity and the influence of shot peening on*

porosity morphology regarding selective laser melted AlSi10Mg parts. Additive Manufacturing, 2018. **20**: p. 77-89https://doi.org/10.1016/j.addma.2018.01.001.

25. Al-Maharma, A.Y., S.P. Patil, and B. Markert, *Effects of porosity on the mechanical properties of additively manufactured components: A critical review.* Materials Research Express, 2020. **7**(12): p. 122001https://doi.org/10.1088/2053-1591/abcc5d.

26. Hu, Y. and W. Cong, *A review on laser deposition-additive manufacturing of ceramics and ceramic reinforced metal matrix composites.* Ceramics International, 2018. **44**(17): p. 20599-20612https://doi.org/10.1016/j.ceramint.2018.08.083.

27. Webster, S., et al., *Physical mechanisms in hybrid additive manufacturing: A process design framework.* Journal of Materials Processing Technology, 2021. **291**: p. 117048https://doi.org/10.1016/j.jmatprotec.2021.117048.

28. Brennan, M., J. Keist, and T. Palmer, *Defects in metal additive manufacturing processes.* Journal of Materials Engineering and Performance, 2021. **30**(7): p. 4808-4818https://doi.org/10.1007/s11665-021-05919-6.

29. Fu, J., et al., *Multi-scale defects in powder-based additively manufactured metals and alloys.* Journal of Materials Science & Technology, 2022https://doi.org/10.1016/j.jmst.2022.02.015.

30. Khairallah, S.A., et al., *Laser powder-bed fusion additive manufacturing: Physics of complex melt flow and formation mechanisms of pores, spatter, and denudation zones.* Acta Materialia, 2016. **108**: p. 36-45https://doi.org/10.1016/j.actamat.2016.02.014.

31. Mohd Yusuf, S., et al., *Investigation on porosity and microhardness of 316L stainless steel fabricated by selective laser melting.* Metals, 2017. **7**(2): p. 64https://doi.org/10.3390/met7020064.

32. Wang, X., et al., *Microstructure and yield strength of SLM-fabricated CM247LC Ni-Superalloy.* Acta Materialia, 2017. **128**: p. 87-95https://doi.org/10.1016/j.actamat.2017.02.007.

33. Bi, G., et al., *Microstructure and tensile properties of superalloy IN100 fabricated by micro-laser aided additive manufacturing.* Materials & Design, 2014. **60**: p. 401-408https://doi.org/10.1016/j.matdes.2014.04.020.

34. Li, Y., et al., *Microstructures and mechanical properties evolution of IN939 alloy during electron beam selective melting process.* Journal of Alloys and Compounds, 2021. **883**: p. 160934https://doi.org/10.1016/j.jallcom.2021.160934.

35. Perevoshchikova, N., et al., *Optimisation of selective laser melting parameters for the Ni-based superalloy IN-738 LC using Doehlert's design.* Rapid Prototyping Journal, 2017. **23**(5): p. 881-892https://doi.org/10.1108/RPJ-04-2016-0063.

36. Yu, Z., et al., *The effect of Hf on solidification cracking inhibition of IN738LC processed by Selective Laser Melting.* Materials Science and Engineering: A, 2021. **804**: p. 140733https://doi.org/10.1016/j.msea.2021.140733.

37. Wei, S., et al., *Competitive failure analysis on tensile fracture of laser-deposited*

material for martensitic stainless steel. Materials & Design, 2017. **118**: p. 1-10https://doi.org/10.1016/j.matdes.2017.01.014.

38. Yadollahi, A., et al., *Effects of process time interval and heat treatment on the mechanical and microstructural properties of direct laser deposited 316L stainless steel.* Materials Science and Engineering: A, 2015. **644**: p. 171-183https://doi.org/10.1016/j.msea.2015.07.056.

39. Li, P., et al., *Tensile fracture behavior of 316L stainless steel components fabricated with hybrid directed energy deposition and thermal milling manufacturing.* Applied Physics A, 2021. **127**(3): p. 1-10https://doi.org/10.1007/s00339-021-04381-4.

40. Fiocchi, J., A. Tuissi, and C. Biffi, *Heat treatment of aluminium alloys produced by laser powder bed fusion: A review.* Materials & Design, 2021. **204**: p. 109651https://doi.org/10.1016/j.matdes.2021.109651.

41. Godec, M., et al., *Hybrid additive manufacturing of Inconel 718 for future space applications.* Materials Characterization, 2021. **172**: p. 110842https://doi.org/10.1016/j.matchar.2020.110842.

42. Zhang, S., et al., *Graphene/ZrO2/aluminum alloy composite with enhanced strength and ductility fabricated by laser powder bed fusion.* Journal of Alloys and Compounds, 2022. **910**: p. 164941https://doi.org/doi.org/10.1016/j.jallcom.2022.164941.

43. Chen, Z., et al., *Graphene reinforced nickel-based superalloy composites fabricated by additive manufacturing.* Materials Science and Engineering: A, 2020. **769**: p. 138484https://doi.org/10.1016/j.msea.2019.138484.

44. Hansen, N., *Hall–Petch relation and boundary strengthening.* Scripta materialia, 2004. **51**(8): p. 801-806https://doi.org/10.1016/j.scriptamat.2004.06.002.

45. El-Awady, J.A., *Unravelling the physics of size-dependent dislocation-mediated plasticity.* Nature communications, 2015. **6**(1): p. 5926https://doi.org/10.1038/ncomms6926.

46. Zhang, Z., et al., *Microstructure and mechanical properties of ultrafine grained CoCrFeNi and CoCrFeNiAl0.3 high entropy alloys reinforced with Cr2O3/ Al2O3 nanoparticles.* Materials Science and Engineering a-Structural Materials Properties Microstructure and Processing, 2021. **816**https://doi.org/10.1016/j.msea.2021.141313.

47. Coakley, J., et al., *Lattice parameter misfit evolution during creep of a cobalt-based superalloy single crystal with cuboidal and rafted gamma-prime microstructures.* Acta Materialia, 2017. **136**: p. 118-125https://doi.org/10.1016/j.actamat.2017.06.025.

48. Khorasani, A.M., I. Gibson, and A.R. Ghaderi, *Rheological characterization of process parameters influence on surface quality of Ti-6Al-4V parts manufactured by selective laser melting.* The International Journal of Advanced Manufacturing Technology, 2018. **97**(9): p. 3761-3775https://doi.org/doi.org/10.1007/s00170-018-2168-6.

49. Tian, Y., et al., *Influences of processing parameters on surface roughness of Hastelloy X produced by selective laser melting.* Additive Manufacturing, 2017. **13**: p. 103-112https://doi.org/10.1016/j.addma.2016.10.010.

50. Zhong, M., et al., *Boundary liquation and interface cracking characterization in laser deposition of Inconel 738 on directionally solidified Ni-based superalloy.* Scripta materialia, 2005. **53**(2): p. 159-164https://doi.org/10.1016/j.scriptamat.2005.03.047.

51. Zhou, W., et al., *Effect of carbon content on the microstructure, tensile properties and cracking susceptibility of IN738 superalloy processed by laser powder bed fusion.* Additive Manufacturing, 2022. **58**: p. 103016https://doi.org/10.1016/j.addma.2022.103016.

52. Dye, D., O. Hunziker, and R. Reed, *Numerical analysis of the weldability of superalloys.* Acta materialia, 2001. **49**(4): p. 683-697https://doi.org/10.1016/S1359-6454(00)00361-X.

CHAPTER 4 ENHANCED HIGH-TEMPERATURE MECHANICAL PROPERTIES AND STRENGTHENING MECHANISMS OF CHEMICALLY PREPARED NANO-TIC REINFORCED IN738LC VIA LASER POWDER BED FUSION

Authors Contributions:

This chapter of the alternative thesis format is published in *Materials Characterization (2024).* As the first author of this publication, I have outlined the paper's details and the contributions of my co-authors below.

Shu, C., *Chen, S., Shu, X., Abdel-Wahab, A., & Essa, K. (2024). Enhanced high-temperature mechanical properties and strengthening mechanisms of chemically prepared nano-TiC reinforced IN738LC via laser powder bed fusion. Materials Characterization, 217, 114434.*

CRediT authorship contribution statement

Chang Shu: Writing – original draft, Visualization, Methodology, Formal analysis, Data curation, Conceptualization.

Siyuan Chen: Resources, Methodology, Data curation.

Xuedao Shu: Writing – review & editing, Supervision, Resources.

Adel Abdel-Wahab: Writing – review & editing, Supervision.

Khamis Essa: Writing – review & editing, Supervision, Resources, Project administration, Funding acquisition.

CHAPTER 4:

ENHANCED HIGH-TEMPERATURE MECHANICAL PROPERTIES AND STRENGTHENING MECHANISMS OF CHEMICALLY PREPARED NANO-TIC REINFORCED IN738LC VIA LASER POWDER BED FUSION

Abstract

Fabrication of high-strength nickel-based composites to meet the demanding service requirements in aerospace environments is a significant challenge. This paper introduces the wet chemical method to prepare the nano-TiC reinforced IN738LC. In contrast to the conventional ball milling approach, this method attains superior attachment of nanoparticles. By employing a full-factorial experimental design, the correlation between Laser-powder bed fusion (L-PBF) processing parameters and the porosity, micro-hardness, and high-temperature tensile strength of as-built samples was examined. The results indicate that the optimal processing parameters are a laser power of 225W, scanning speed of 750 mm/s, and hatch space of 0.09 mm, with a Volumetric energy density (VED) of 111.1 J/mm^3. Compared to IN738LC, the chemically prepared TiC-IN738LC exhibits a 45% increase in room temperature tensile strength (400 MPa) and a 65% increase in high-temperature tensile strength (120 MPa). Compared with ball-milled TiC-IN738LC, the chemically prepared samples present superior microstructure with more equiaxed grains. The morphological analysis of the tensile samples reveals that the presence of dimples are crucial in enhancing the ductility properties. Furthermore, this study identifies the Orowan strengthening mechanism and the grain refinement strengthening mechanism as the principal mechanisms of reinforcement by nano-ceramics.

Keywords: Laser powder bed fusion; Powder preparation; Metal matrix composites; Strengthening mechanism; High-temperature tensile strength.

4.1 Introduction

Nickel superalloys are critically employed in extreme environments, particularly in aerospace applications [1-3]. Alloys such as IN738LC, CM247LC, and Hastelloy X are highly valued for their exceptional creep resistance and corrosion resistance at high temperatures [4-6]. Their machinability is compromised by the significant volume of (Al, Ti) precipitates that strengthen the gamma prime matrix, thereby posing constraints on their application [7, 8]. Laser Powder Bed Fusion (L-PBF) utilizes a high-temperature, rapid fusion of powder and laser to fabricate the required sample parts [1, 9]. Compared to the traditional machining processes for these challenging nickel alloys, L-PBF, with its high cooling rates and rapid solidification, coupled with optimal processing parameters, allows the fabrication of complex geometrical parts with ideal microstructures and outstanding mechanical properties [10-12]. Therefore, fabricating hard-to-print nickel-based composites using L-PBF has substantial engineering significance.

The gamma prime phase can be enhanced by introducing nanoparticles, thereby improving the mechanical properties of nickel-based composites [4, 13, 14]. The distribution of nanoparticles onto the matrix material is crucial to achieving high-performance nickel-based composites. Ball milling is widely acknowledged as an efficient and simple approach for mechanically mixing nanoparticles with the nickel powders. This process enables the adhesion of harder nanoparticles to the surfaces of nickel matrix powder through mechanical collisions [15-17]. Several researchers have succeeded in enhancing various nickel-based alloys. Zhang et al. [18] successfully enhanced IN625 with nano-TiB2, improving its tensile strength, microhardness, and wear resistance compared to the IN625. Rong et al. [19] introduced WC particles into IN718, significantly improving its wear resistance, and elucidated the reinforcement mechanism by examining the WC-IN718 interface. Gu et al. [20] incorporated nano-TiC into the IN718 matrix, successfully obtaining reinforced TiC-IN718 with high hardness and low friction coefficient, and further explained the reinforcement mechanism by analyzing the microstructure and the refinement effect of nanoparticles

on the spacing between columnar dendrites. Numerous studies have successfully prepared nickel-based composites using ball milling [4, 19-23]. However, during the powder preparation process using ball milling, the inevitable collision between the spherical powder particles and milling balls in this high-energy process leads to changes in morphology and the agglomeration of the secondary phase nanoparticles, introducing impurities and thereby diminishing composite purity and mechanical properties [24, 25]. Hence, there is an ongoing effort to develop alternative powder preparation techniques that enhance the powder sphericity and the bonding of nanomaterials.

Wet chemical methods for preparing composites not only effectively enhance the adhesion of nanoparticles and reduce their agglomeration but also protect the powder from collision-induced defects, improving the sphericity of the powder [26, 27]. Abreu-Castillo et al. [28] introduced WC nanoparticles using an in-situ wet chemical method, successfully preparing aluminide coatings. Scanning Electron Microscopy (SEM) and Energy Dispersive X-Ray Spectroscopy (EDS) analyses confirmed the excellent adhesion of the nanoparticles and the sphericity of the base material, leading to enhanced hardness test results. Molina-Claros et al. [29] used a chemical method to introduce WC nanoparticles into nickel-based materials, the resulting reinforced composite material exhibited a more uniform nanoparticle distribution with better wear resistance than unreinforced nickel materials. Vishwanatha et al. [30] generated aluminum-alumina bulk nanocomposites through a dual-phase ultrasonic process, resulting in an exceptionally uniform distribution of alumina particles within the aluminum matrix, which led to enhanced nanoparticle uniformity and mechanical properties. Overall, chemical preparation methods effectively mitigate the morphological irregularities of spherical powders found in ball milling, concurrently improving the nanoparticle cohesion. Consequently, enhancing the quality of powder preparation in composite materials.

Processing parameters play a crucial role in L-PBF and significantly affect the quality of the as-built samples [31, 32]. Optimizing the processing parameters can substantially

diminish micro-defects such as lack of fusion pores (LoF), cracks, and voids, resulting in specimens with enhanced mechanical properties [33, 34]. The Design of Experiment (DoE) method, a fundamental approach in experimental design, explores the correlation between different L-PBF parameters and the quality of as-built samples through multifactorial experiments. This method facilitates the production of high-quality, high-performance L-PBF samples. Majeed et al. [35] explored the processing parameters of $AlSi_{10}Mg$ in L-PBF, using the full factorial DoE method to analyze the effect of laser power on surface quality and applied statistical methods to obtain optimized parameters for the best surface quality. Tucho et al. [36] manufactured SS316L using L-PBF and successfully fabricated high-density (>99.8%) samples using DoE, demonstrating that increasing energy density can optimize and attain maximum sample density. Wang et al. [37] investigated the influence of L-PBF processing parameters on IN738LC, focusing on density, cracking, and mechanical properties, and successfully produced crack-free, high-density (~99.76%) samples. Ghodsi et al. [38] assessed the influence of L-PBF process parameters on surface integrity, microstructure, porosity, and microhardness of the samples, elucidating the effects of these parameters on submicron yttria-stabilized zirconia (YSZ) reinforced Inconel 625, and successfully achieved the fabrication of nickel-based composite materials with high mechanical performance. Historically, research on MMCs has primarily centered around the ball milling technique for developing such composites. However, there has been limited exploration into chemical methodologies for synthesizing nickel-based materials thus far. Furthermore, the reinforcement mechanism of powder materials prepared through chemical routes is not thoroughly understood. Moreover, studies investigating the high-temperature performance of chemically prepared methods are scarce.

This study highlights that the wet chemical method for composite material preparation represents an advanced technique, with successful applications in specific materials, contributing substantially to the evolution of L-PBF technology. However, there is a significant lack of literature on the chemical preparation of TiC-IN738LC nickel-based composite. As a result, this research is dedicated to fabricating TiC-IN738LC

composites using the chemical methods and L-PBF additive manufacturing process. The study encompasses a comprehensive experimental design of process parameters to investigate the correlation between L-PBF parameters and crucial properties such as porosity, microhardness, and high-temperature tensile strength. The paper provides an in-depth analysis of the fracture morphologies of tensile samples. Additionally, through SEM and TEM analysis of the microstructure, the study provides additional insight into the strengthening mechanisms by nano-ceramic reinforcement.

4.2 Methodology

4.2.1 Materials

The spherical IN738LC powder used in our previous research (d_{10} = 15.9 μm, d_{50} = 34.3 μm, d_{90} = 60.2 μm) and 50 nm TiC with a purity of 99.5% were selected as the ceramic reinforcement. The chemical method was employed to mix 2 wt% TiC nano-enhancer particles with the nickel matrix. The chemical preparation method involved a multi-step process: the nanoparticles were weighed and dispersed in anhydrous ethanol, sonicated for 90 minutes, followed by adding nickel base IN738LC powder and stirring magnetically at 1600rpm for 90 minutes to improve the impregnation of nanoparticles on the nickel particle surface. The mixture was subsequently dried at 313 K (40 °C) for 90 minutes in a muffle furnace to finalize the powder mixture preparation. Figure 4.1 shows the SEM images of the powder morphology, including (a) the pure IN738LC; (b) the TiC-IN738LC nickel-based composite material. Figure 4.1c and 4.1d are high-magnification images of TiC-IN738LC; and Figure 4.1 (e-h) are EDS analysis of Ni, Ti, Cr and Al element, respectively. As shown in Figure 4.1c and 4.1d , nano TiC was uniformly attached to IN738LC, and the IN738LC maintained a high sphericity, thereby enhancing the quality of the powder [39]. EDS analysis in Figure 4.1 (e-h) indicates that nano TiC is uniformly distributed in the nickel base material.

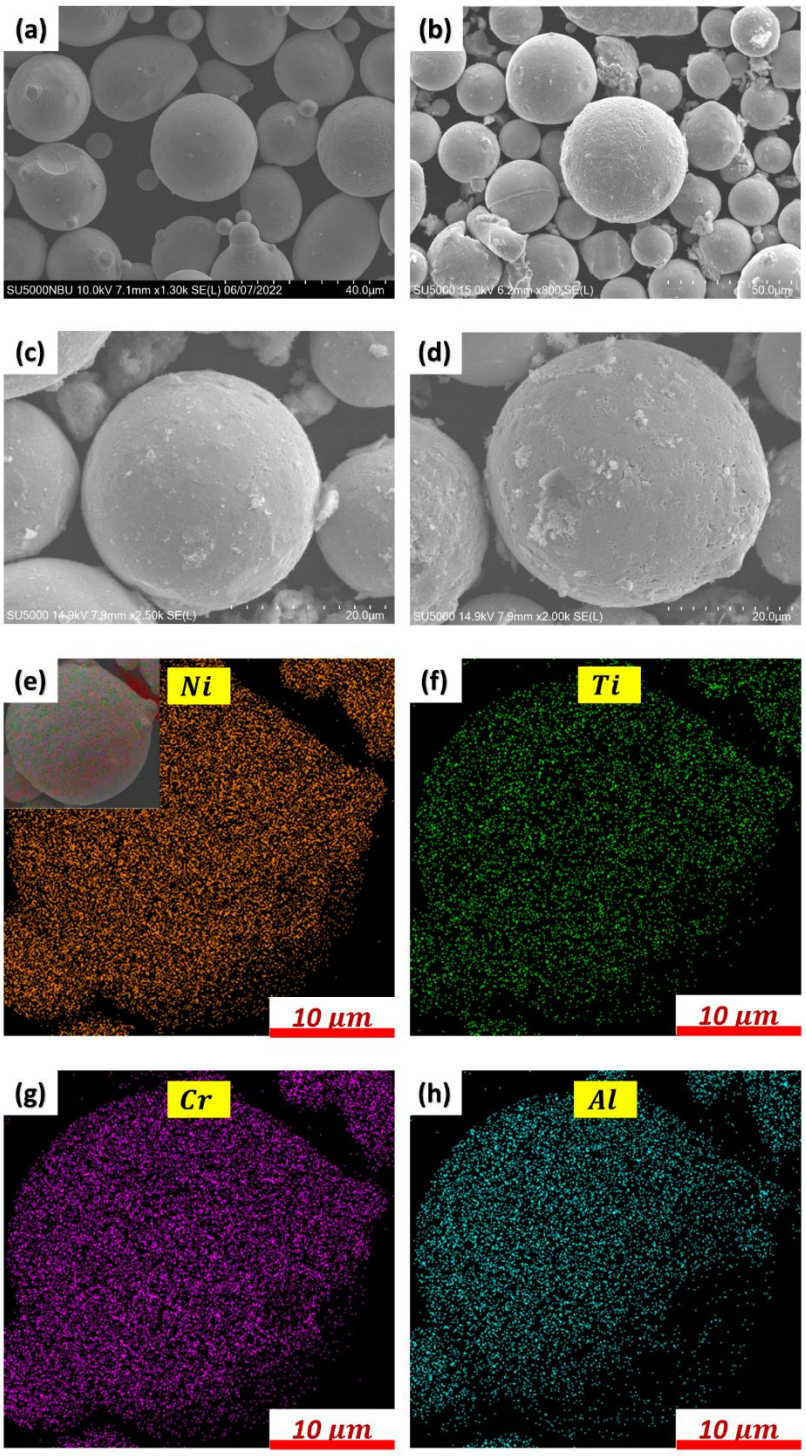

Figure 4.1. SEM images of powder morphology and EDS mapping of TiC-IN738LC powder: (a) IN738LC; (b) chemically prepared TiC-IN738LC; (c-d) high magnification images of TiC-IN738LC; (e-h) EDS graph of Ni element, Ti element, Cr element, and Al element in TiC-IN738LC, subsequently.

4.2.2 L-PBF process and design of experiment

In this study, a commercial L-PBF machine (HBD-150D, Shanghai Hanbang United 3D Tech Co., Ltd., China) was used to fabricate the chemically prepared nickel-based composite material TiC-IN738LC. The machine is equipped with a 400W IPG fiber laser, with a laser spot diameter of 70 μm. Figure 4.2 provides a schematic of the L-PBF process, where a chessboard unidirectional scanning strategy was adopted [40]. Cubical samples measuring 10mm × 10mm × 10mm were specifically prepared for the analysis of microstructures, and the tensile test samples were produced in accordance with ASTM dimensions and standards [41]. Prior to the printing process, the prepared powder was placed in an oven filled with inert gas and dried at 40 °C for 5 hours to ensure the removal of moisture.

A full factorial design was employed by Minitab with three variables and three levels. Table 4.1 shows the information of the Design of Experiment (DoE). The three design variables were laser power (150 W–300 W), scanning speed (500 mm/s-1000 mm/s), and hatch space (0.09 mm–0.12 mm). The layer thickness for all experiments was set at 0.03 mm. Each combination of process parameters was associated with a specific Volume Energy Density (VED) value. This VED value serves as a critical metric for evaluating the interaction between the laser source and the powder [42], as indicated by equation (4.1):

$$VED = \frac{P}{vhd}\left(\frac{\mathrm{J}}{\mathrm{mm}^3}\right) \tag{4.1}$$

Where P, v, h and d represent the laser powder, scanning speed, hatch space and layer thickness, respectively.

Table 4.1. Full factorials design of experiments.

Parameter	Lower level	Mid-level	Higher-level
Laser power (W)	150	225	300
Scan velocity (mm/s)	500	750	1000
Hatch space (mm)	0.09	0.105	0.12

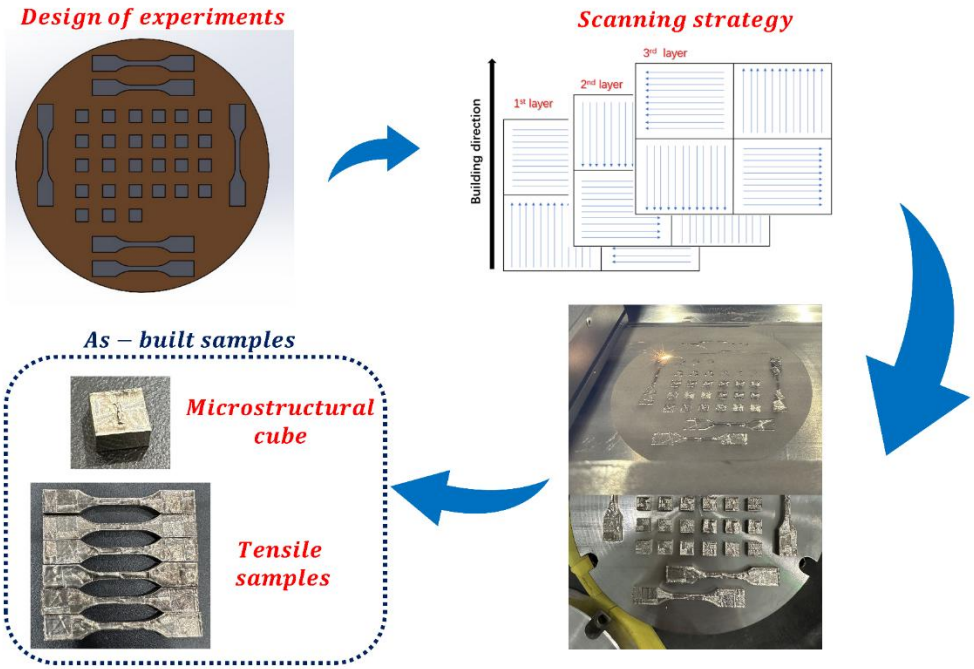

Figure 4.2. Schematic diagram of the experimental process.

4.2.3 Characterization

An optical microscope (OM) was used to observe porosity and the morphology of the melt pool, with the samples being thoroughly polished before observation. Images captured by the OM were employed for the examination of porosity and cracks. In this study, the open-source image analysis software ImageJ was employed to measure porosity. A Scanning Electron Microscope (SEM) (Hitachi SU5000, Japan) was used to observe the fracture morphology and microstructure. Before observation, the samples were ground, mounted, polished, and etched. The selected etching solution of $12\ ml\ H_3PO_4\ +\ 48\ ml\ H_2SO_4\ +\ 40\ ml\ HNO_3$ was used to electrolytically etch the samples at 6V for 4-6 seconds [43]. Electron Backscatter Diffraction (EBSD) results were obtained using a 20 kV acceleration voltage and a 250 nm step size. The EBSD data analysis was performed using Oxford HKL Channel5 software. Grain boundaries with misorientation greater than 15° are considered high-angle grain boundaries (HAGBs). Transmission Electron Microscopy (TEM) utilizes the JEM-F200 instrument (JEOL Ltd, Japan). It employs a focused ion beam for sample preparation to observe the microstructure and precipitate phases of the sample.

The Vickers microhardness tester (Wilson VH1102 Microhardness Tester, USA) was used for microhardness testing. The samples were well polished and met the standards for microhardness testing. Five distinct regions were sampled on each plane of the specimen, comprising four at the corners and one at the center, for the purpose of measurement and to derive an average value. For each point, a load of 300 N was applied with a dwell time of 10 seconds. Before testing, the microhardness tester was calibrated using a calibration block to ensure the accuracy of the results, with the measured system error being less than 0.05%.

Tensile tests were conducted using a tensile testing machine (Zwick Amsler 100 HFT, Germany). The room temperature tensile tests were performed at a rate of 1mm/min, with the load direction perpendicular to the printing direction of the sample. High-temperature tensile tests were conducted at the same rate at 850°C. Before conducting high-temperature tensile tests, both the tensile specimens and their fixtures were heated for half an hour to ensure that the samples reached the temperature required for the experiment. For each set of tensile test parameters, three identical samples were used for repeated experiments to ensure the accuracy of the results. After the testing, the solution heat treatment involved heating at a temperature of 1120 °C for two hours, followed by accelerated air cooling, and then aging at 850°C for 24 hours to ensure the deposition of the γ/γ' phase for microstructural observations.

4.3 Result and discussion

4.3.1 Effect of processing parameters on porosity

Porosity serves as a crucial metric for assessing the printing quality in L-PBF processes [44]. The primary defects in L-PBF include LoF, cracks, and pores. LoF defects are due to insufficient energy density leading to incomplete fusion, while pores are formed due to high energy density causing gas to be trapped inside the melt pool [45]. Figure 4.3 displays the porosity images under various parameters. In this study, all three types of defects were observed. From Figure 4.3, it can be inferred that when the energy density is low, specifically when VED is less than 83.3J/mm^3, LoF defects and cracks occur. In

contrast, when VED exceeds 166.7 J/mm^3, distinct circular gas pores are noticeable, and their quantity increases with higher energy density. Within a VED range of 83.3 J/mm^3 to 127.0 J/mm^3, the quality of L-PBFed samples improves, showing fewer observable pores and no apparent cracks.

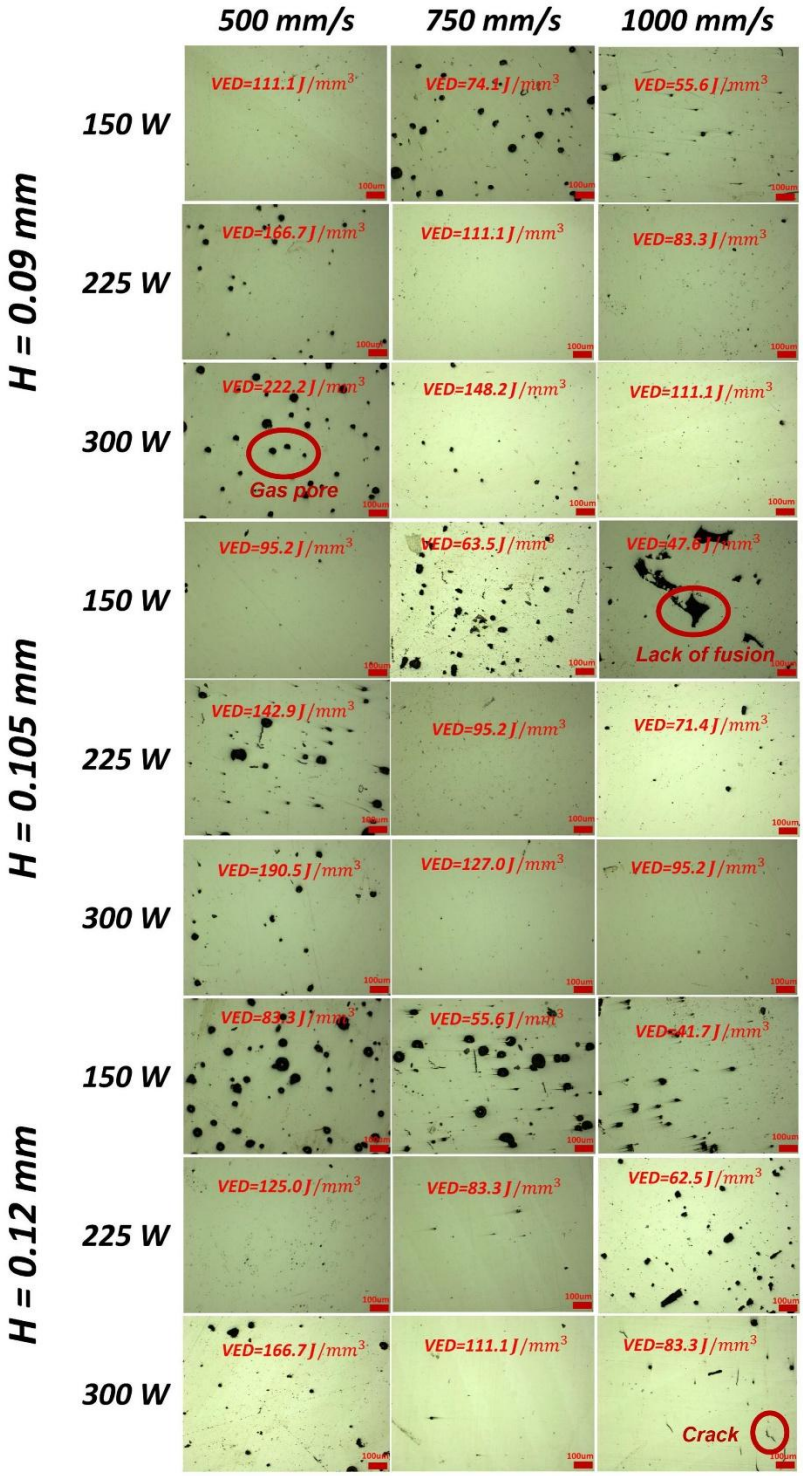

Figure 4.3. Porosity results for each processing parameter are depicted in the graphs, with consistent scale bars (100 μm) across all figures.

Figures 4.4(a-c) illustrates the relationship between three L-PBF design variables (laser power, scanning speed, and hatch space) and porosity. As seen in Figure 4.4a, the highest porosity occurs at a laser power of 150W, decreasing to its lowest at 225W. Although the porosity increases again at 300W, it remains significantly lower than at 150W. Combined with Figure 4.3, it can be inferred that high porosity is mainly due to LoF and crack, making 225W as the optimal laser power. Figure 4.4b shows that while scanning speed doesn't impact porosity as significantly as laser power, a lower speed of 500mm/s results in excessive energy density and pore formation, thereby increasing porosity. On the other hand, higher speeds lead to inadequate energy input, heightening LoF occurrences. Samples printed at scanning speeds of 750mm/s-1000mm/s are within the ideal energy density range compared to those at 500mm/s, thus reducing porosity under these parameters. Hence, the selection of scanning speed must be carefully coordinated with other two parameters, with 750mm/s identified as the optimal speed in Figure 4.4b. Figure 4.4c clearly demonstrates a proportional relationship between hatch space and porosity. As the hatch space decreases, the size and number of pores notably diminish. This finding aligns with previous research [46], suggesting that a critical impact of hatch space on pore distribution and morphology, and its influence on the transition between keyhole pores and conduction melting modes. A smaller hatch space ensures higher quality energy input from the laser to the powder, thereby reducing porosity. Thus, the study identifies 0.09mm as the optimal hatch space. Statistical analysis using the Analysis of Variance (ANOVA) approach was conducted on the obtained results, with a 95% confidence level. The P-value for the three factors (i.e., Laser Power, Scan Speed, and Hatch Spacing) was less than 0.05, indicating that these factors have a significant effect on porosity. The interaction effects were not tested as they are outside the scope of this investigation. Figure 4.4d presents a VED versus porosity distribution and the different zones are divided according to the porosity of the as-built samples, suggesting that the ideal parameter window for TiC-IN738LC should be maintained within an energy density range of 97 J/mm^3 to 130 J/mm^3.

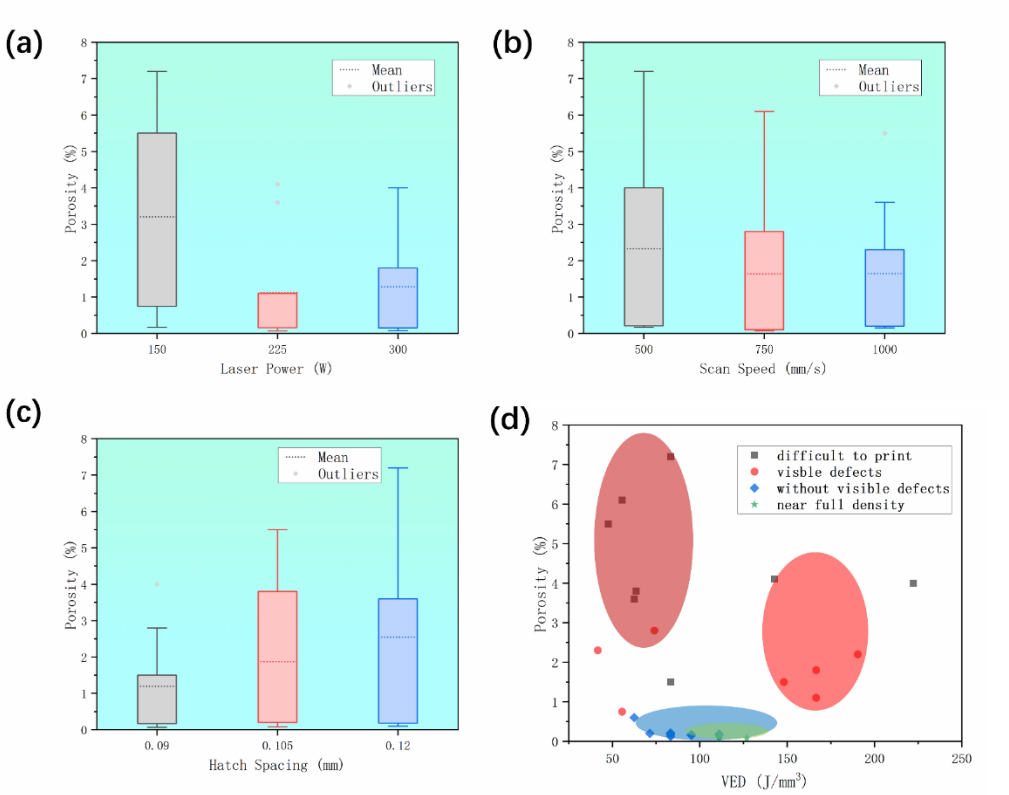

Figure 4.4. (a) – (c) Correlation chart: porosity vs. laser power, scan speed, and hatch spacing; (d) Porosity and VED correlation diagram.

4.3.2 Effect of processing parameters on microhardness

Microhardness serves as a simple yet effective indicator of mechanical properties, and it is a crucial metric in the evaluation of samples fabricated via L-PBF [47]. As illustrated in Figure 4.5a, microhardness results can be categorized into three distinct VED ranges: 40 J/ mm^3-100 J/ mm^3, 110 J/ mm^3-140 J/ mm^3, and 150 J/ mm^3-220 J/ mm^3. Table 4.2 provides a comprehensive set of data on porosity and microhardness for all the samples based on the DoE. Within the VED spectrum spanning from 40 J/mm³ to 100 J/mm³, the presence of lower energy density, as evidenced by porosity results, gives rise to defects like LoF and cracks. Consequently, this contributes to a decreased density in the samples, ultimately leading to a reduction in microhardness. Within the VED range spanning from 110 J/mm³ to 140 J/mm³, the energy density falls within an optimal window. This range is marked by fewer pores and an absence of cracks, leading to a notable improvement in microhardness. Moving into the range of 150 J/mm³ to 220 J/mm³, a slight reduction in microhardness is observed. The main factor contributing to

this phenomenon is that, although gas trapped pore defects are present, their influence on microhardness is much less significant than defects like LoF and cracks, thus not significantly reducing microhardness performance [48]. Therefore, the increase in microhardness can be attributed to the higher densification achieved under different energy densities.

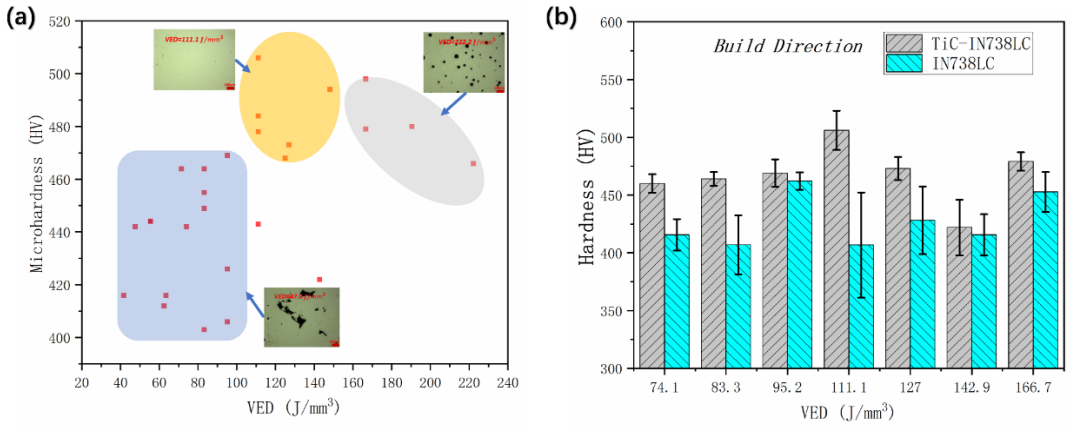

Figure 4.5. (a) Microhardness and VED correlation diagram; (b) Microhardness of TiC-IN738LC and IN738LC.

Table 4.2. Detailed porosity and microhardness data for all DoE samples.

#	Laser power (W)	scan velocity (mm/s)	hatch space (mm)	layer thickness (mm)	VED (J/mm³)	Porosity %	Microhardness (HV)
1	150	500	0.09	0.03	111.1	0.17	478± 29
2	150	500	0.105	0.03	95.2	0.21	426± 23
3	150	500	0.12	0.03	83.3	7.20	449± 6
4	150	750	0.09	0.03	74.1	2.80	460± 8
5	150	750	0.105	0.03	63.5	3.80	438± 24
6	150	750	0.12	0.03	55.6	6.10	444± 29
7	150	1000	0.09	0.03	55.6	0.75	444± 6
8	150	1000	0.105	0.03	47.6	5.50	442± 6
9	150	1000	0.12	0.03	41.7	2.30	416± 8
10	225	500	0.09	0.03	166.7	1.10	498± 16
11	225	500	0.105	0.03	142.9	4.10	422± 24
12	225	500	0.12	0.03	125.0	0.18	468± 14
13	225	750	0.09	0.03	111.1	0.07	506± 17
14	225	750	0.105	0.03	95.2	0.16	406± 41
15	225	750	0.12	0.03	83.3	0.12	464± 6
16	225	1000	0.09	0.03	83.3	0.20	455± 15

17	225	1000	0.105	0.03	71.4	0.60	464± 51
18	225	1000	0.12	0.03	62.5	3.60	412± 18
19	300	500	0.09	0.03	222.2	4.00	466± 2
20	300	500	0.105	0.03	190.5	2.20	480± 16
21	300	500	0.12	0.03	166.7	1.80	479± 8
22	300	750	0.09	0.03	148.1	1.50	494± 12
23	300	750	0.105	0.03	127.0	0.08	473± 10
24	300	750	0.12	0.03	111.1	0.10	484± 6
25	300	1000	0.09	0.03	111.1	0.15	443± 9
26	300	1000	0.105	0.03	95.2	0.20	469± 12
27	300	1000	0.12	0.03	83.3	1.50	403± 44

Figure 4.5b compares the microhardness of TiC-IN738LC and IN738LC, with the data for IN738LC obtained from our previous study [47]. Table 4.3 provides detailed data on the microhardness of both IN738LC and TiC-IN738LC. It is evident that the microhardness of chemically prepared TiC-IN738LC shows a significant improvement compared to the unreinforced IN738LC. Specifically, at a VED of 111.1 J/mm³, TiC-IN738LC exhibits peak hardness, surpassing that of IN738LC under identical conditions by about 110HV, which translates to an approximate 23% improvement in microhardness. The IN738LC achieves its maximum microhardness value of around 460HV at VED of 95.2 J/mm³, which is less than the 520HV of TiC-IN738LC. The introduction of nanoparticles plays a crucial role in enhancing microhardness. Owing to the high hardness of the nano-ceramic particles TiC, their uniform adhesion to IN738LC, coupled with the rapid heating and cooling process in L-PBF, leads to multiple strengthening mechanisms such as thermal mismatch, dislocation effects, and grain refinement [13, 14]. Previous research [47] indicates that introduced nanoparticles hinder grain growth, thereby reducing the average grain size. Grain refinement significantly impacts microhardness, as smaller grains typically exhibit higher microhardness [49]. Additionally, the error bars in the graph suggests that the addition of nano TiC particles reduces data variability. This reduction in variability indicates that nano TiC particles contribute not only to the refinement of grains but also the enhancement of structural uniformity. Overall, the introduction of nanoparticles in the L-PBF process enables a range of strengthening mechanisms, thereby significantly

enhancing the microhardness of TiC-IN738LC and markedly outperforming the pure IN738LC.

Table 4.3. Detailed data on the microhardness of IN738LC and TiC-IN738LC.

#	Laser power (W)	Scan velocity (mm/s)	Hatch space (mm)	VED (J/mm3)	Microhardness （HV）	
					TiC-IN738LC	IN738LC
1	150	750	0.09	74.1	460±8	418±15
2	225	750	0.12	83.3	464±6	406±26
3	300	1000	0.105	95.2	469±12	459±8
4	225	750	0.09	111.1	506±17	405±40
5	300	750	0.105	127.0	473±10	420±28
6	225	500	0.105	142.9	422±24	418±17
7	300	500	0.12	166.7	479±8	458±16

4.3.3 Mechanical tensile tests

Tensile tests were conducted at room temperature and at a typical temperature of 850°C for IN738LC [50]. As depicted in Figure 4.6, it is evident that at both room temperature and 850°C, TiC-IN738LC demonstrates a significant increase in strength. However, there is a noticeable reduction in ductility compared to IN738LC.The tensile samples of TiC-IN738LC were printed using two different VED parameters that resulted in low porosity and high microhardness. It can be seen from Figure 4.6 that TiC-IN738LC samples with different VED parameters had different tensile results. Specifically, under room temperature testing, the sample with VED=111 J/mm³ had a 39% higher elongation (0.009) and about 10% lower tensile strength (120MPa) compared to the sample with VED=127 J/mm³. At 850°C, its elongation was 27% higher (0.017) and tensile strength 25% lower (100MPa) than VED=127 J/mm³. Compared to the IN738LC, the TiC-IN738LC at room temperature showed at least a 45% (400MPa) increase in tensile strength, but a significant decrease in ductility by at least 30% (0.013). At high temperatures, the strength of both TiC-IN738LC and IN738LC decreased due to softening at high temperatures and grain growth, leading to increased ductility and weakened tensile strength [50, 51]. In this study, the TiC-IN738LC compared to IN738LC, showed at least a 65% (120MPa) increase in strength and at least a 30%

(0.036) decrease in ductility at high temperatures. Table 4.4 provides specific data from the tensile tests including yield strength, ultimate tensile strength, and elongation. The introduction of nano-ceramic particles leads to a sacrifice in ductility due to the effect of dispersion strengthening, a phenomenon widely observed in ceramic-reinforced metal matrix composites [4, 47, 52]. This research, in comparison to previous studies using ball-milled powder [47], successfully enhanced the ductility of the composite while maintaining its strength.

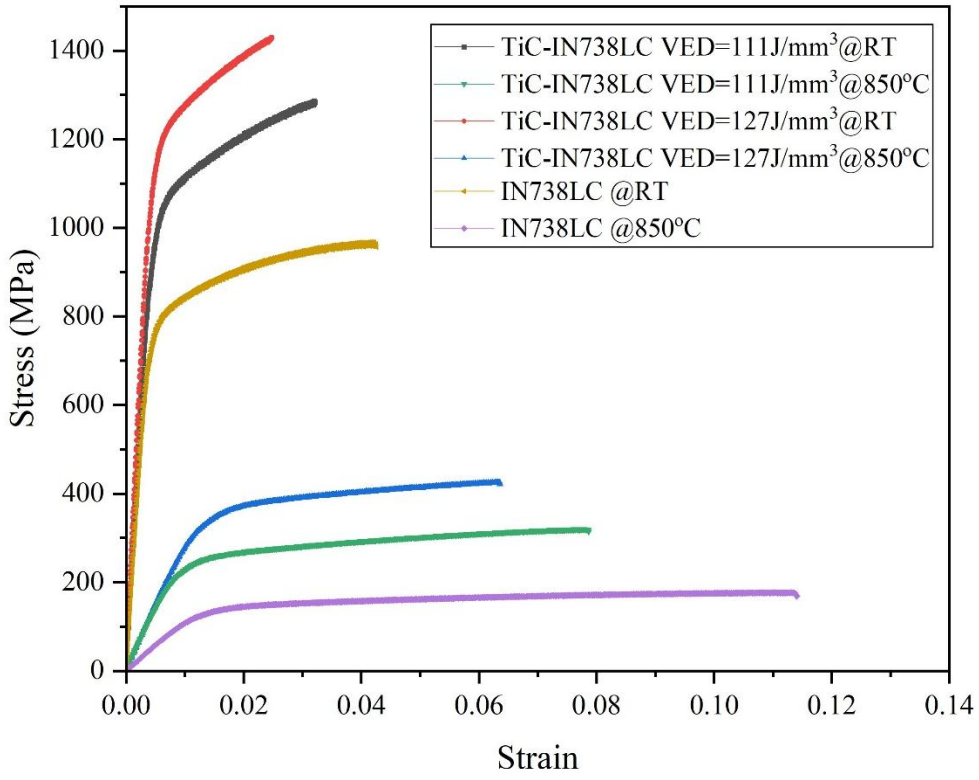

Figure 4.6. Tensile testing results of TiC-IN738LC and IN738LC at room temperature and 850°C.

Figure 4.7 presents the morphology of fracture surfaces in tensile specimens, providing insightful correlation with the tensile curves depicted in Figure 4.6. Figures 4.7a and 4.7b depict the fracture surfaces of TiC-IN738LC with a VED of 111 J/ mm^3 at room temperature and high temperature (850°C), respectively. The room temperature fracture surface exhibits obvious cracks, leading to stress concentration and consequently brittle fracture [53]. However, a few dimples are also present, indicating some ductility,

thereby characterizing the fracture as a mix of brittle and ductile [54]. The high-temperature fracture surface shows more dimples, explaining the increased ductility, while the voids in Figure 4.7b lead to a reduction in tensile strength [55]. Figures 4.7c and 4.7d show the fracture surfaces of TiC-IN738LC with a VED of 127 J/ mm^3 at room temperature and high temperature. Figure 4.7c reveals a typical brittle fracture with a lack of dimples, resulting in low ductility. At high temperatures, Figure 4.7d shows crack healing along with grain growth and the formation of a few dimples, thus improving ductility. Figures 4.7e and 4.7f display the fracture surfaces of IN738LC at room temperature and high temperature (850°C), respectively. It is evident that the unreinforced IN738LC with many dimples ensures good ductility, characteristic of ductile fracture. Figure 4.7f shows denser dimples formed during high-temperature tensile testing, with some refined dimples, explaining the higher ductility [56]. The inclusion of nano-ceramic particles in TiC-IN738LC imparts ceramic-like brittleness, leading to either brittle or mixed brittle-ductile fracture modes while concurrently enhancing the material's strength [47]. This work, through chemical preparation, successfully achieves a more evenly dispersed ceramic reinforcement, thus enhancing the ductility of the ceramic-reinforced material [26, 27, 30].

Table 4.4. Detailed results of tensile tests.

Description	**Yield Strength (MPa)**	**Ultimate Tensile Strength (MPa)**	**Elongation (%)**
TiC–IN738LC (VED=111 J/mm^3) @RT	1020 ± 25	1280 ± 30	3.2 ± 0.1
TiC–IN738LC (VED=111 J/mm^3) @850°	210 ± 30	320 ± 40	7.8 ± 0.1
TiC–IN738LC (VED=127 J/mm^3) @RT	1180 ± 32	1420 ± 20	2.3 ± 0.05
TiC–IN738LC (VED=127 J/mm^3) @850°	320 ± 25	410 ± 35	6.3 ± 0.2
IN738LC @RT	710 ± 35	920 ± 25	4.2 ± 0.2
IN738LC @850°	108 ± 10	160 ± 15	11.5 ± 0.2

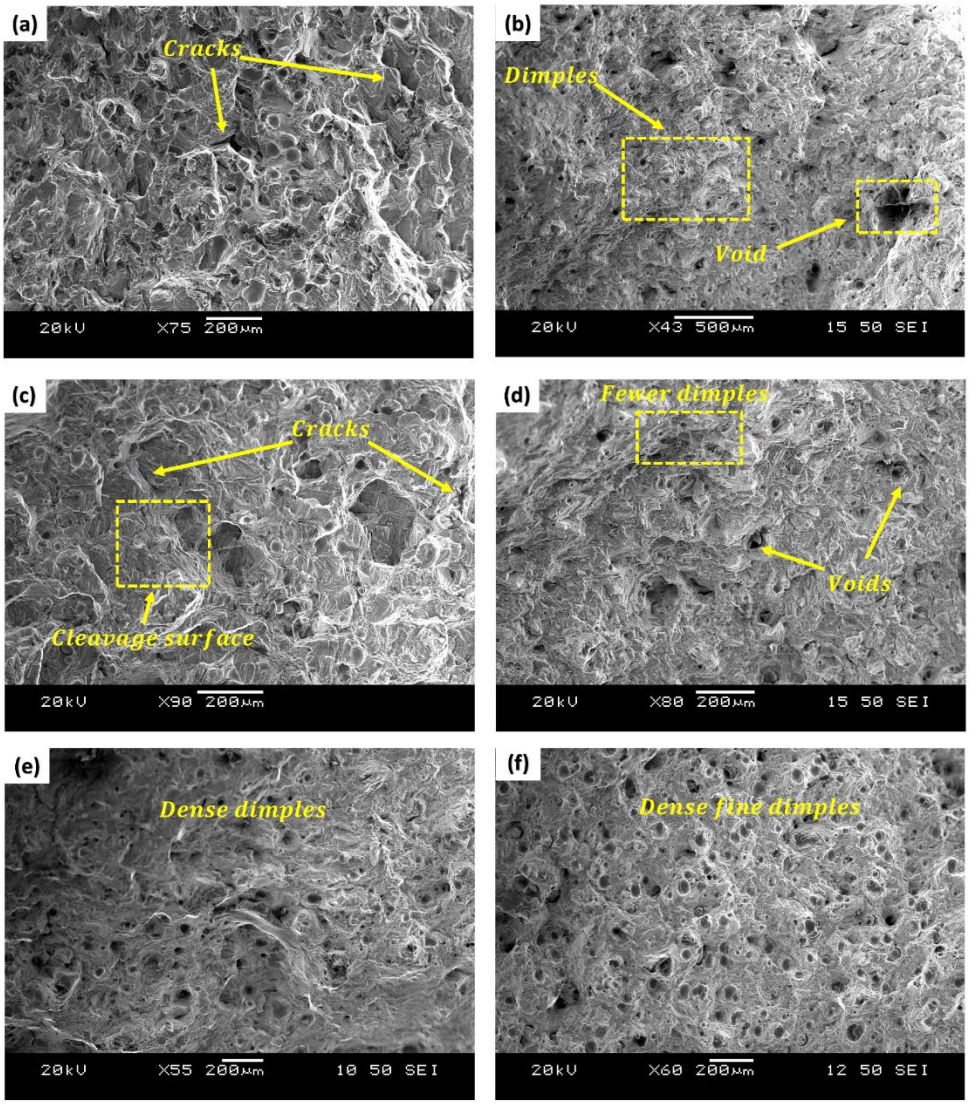

Figure 4.7. Fractographic of tensile samples: (a) room temperature tensile sample of TiC-IN738LC with VED=111 J/ mm^3; (b) high temperature (850°C) tensile sample of TiC-IN738LC with VED=111 J/ mm^3; (c) room temperature tensile sample of TiC-IN738LC with VED=127 J/ mm^3; (d) high temperature (850°C) tensile sample of TiC-IN738LC with VED=127 J/ mm^3; (e) room temperature tensile sample of IN738LC; (f) high temperature (850°C) tensile sample of IN738LC.

4.3.4 Strengthening mechanism of nanoparticles

Utilizing nano-ceramic particles as crystallization nuclei during the L-PBF process inhibits grain boundary migration and grain growth, resulting in refined grain sizes, a critical reinforcement mechanism in composite materials [4, 18, 47, 52]. Comparing Figures 4.8a1 and 4.8c1, it is evident that the grain size of TiC-IN738LC with added nano-ceramic particles is significantly smaller than that of nickel-based IN738LC, indicating a grain refinement effect [4]. Nano-particles like TiC obstruct grain growth,

producing more equiaxed grains [57]. In contrast, the IN738LC in Figure 4.8c1, lacking nano-ceramic particles that absorb the internal strain energy of grain growth and dislocation density energy, allows excessive grain growth, leading to more columnar dendritic grains in the building direction and thus reducing tensile strength [58]. After high-temperature tensile testing (Figure 4.8b1), grains in IN738LC regrow into columnar dendrites. However, nano-ceramic particles hinder excessive dendritic growth due to their thermal mismatch strengthening properties[59]. This suggests that nano-ceramic reinforcements improve high-temperature performance. Notably, this study also compares the EBSD of optimal processing parameters [47] of ball-milled TiC-IN738LC with chemically prepared TiC-IN738LC. Figure 4.8d1 shows that ball-milled samples exhibit grain refinement, but chemically prepared samples display more uniform, equiaxed grains, significantly reducing columnar structures, improving anisotropy, and enhancing overall performance [60]. The results of the Kernel Average Misorientation (KAM) analysis indicate that the local strain in samples prepared by ball milling and chemical routes is significantly lower than that of IN738LC superalloy. This finding demonstrates that the introduction of TiC particles can reduce stress concentration, thereby improving the crack sensitivity of the composite material [4]. The Geometrically Necessary Dislocations (GND) map further supports KAM conclusion, showing that the GND intensity is highest in the IN738LC superalloy, making it more prone to crack formation compared to TiC-IN738LC composites. The average misorientation angle (MA) of chemically prepared TiC-IN738LC is slightly higher than that of IN738LC, while ball-milled TiC-IN738LC exhibits an even higher MA, indicating the presence of more HAGBs. Low-angle grain boundaries (LAGBs) act as "soft barriers," allowing certain dislocations to pass through, and compared to HAGBs, LAGBs demonstrate a superior ability to regulate the balance between strength and ductility [61]. The MA results suggest that the chemical preparation method promotes the formation of more LAGBs than the ball-milled method, which could benefit the ductile properties. However, when compared to IN738LC, the chemically prepared TiC-IN738LC contains more HAGBs, which, while contributing to increased strength, simultaneously reduce ductility. Grain size distribution (GZ)

confirm that both chemically prepared and ball-milled TiC-IN738LC samples exhibit finer grain sizes. The presence of nano-particles promote recrystallization during melting, thereby inhibiting crack formation [4, 62]. Additionally, the chemically prepared TiC-IN738LC achieved even finer grains ($\sim 33.5 \mu m$) than those obtained via ball milling ($\sim 38.1 \mu m$), representing a 12% improvement over the ball-milled method. Therefore, the chemical preparation process promotes a more uniform distribution of nano-ceramic particles within the matrix, alleviating nanoparticle agglomeration and spherical powder deformation found in ball milling, thereby improving the overall build quality [27].

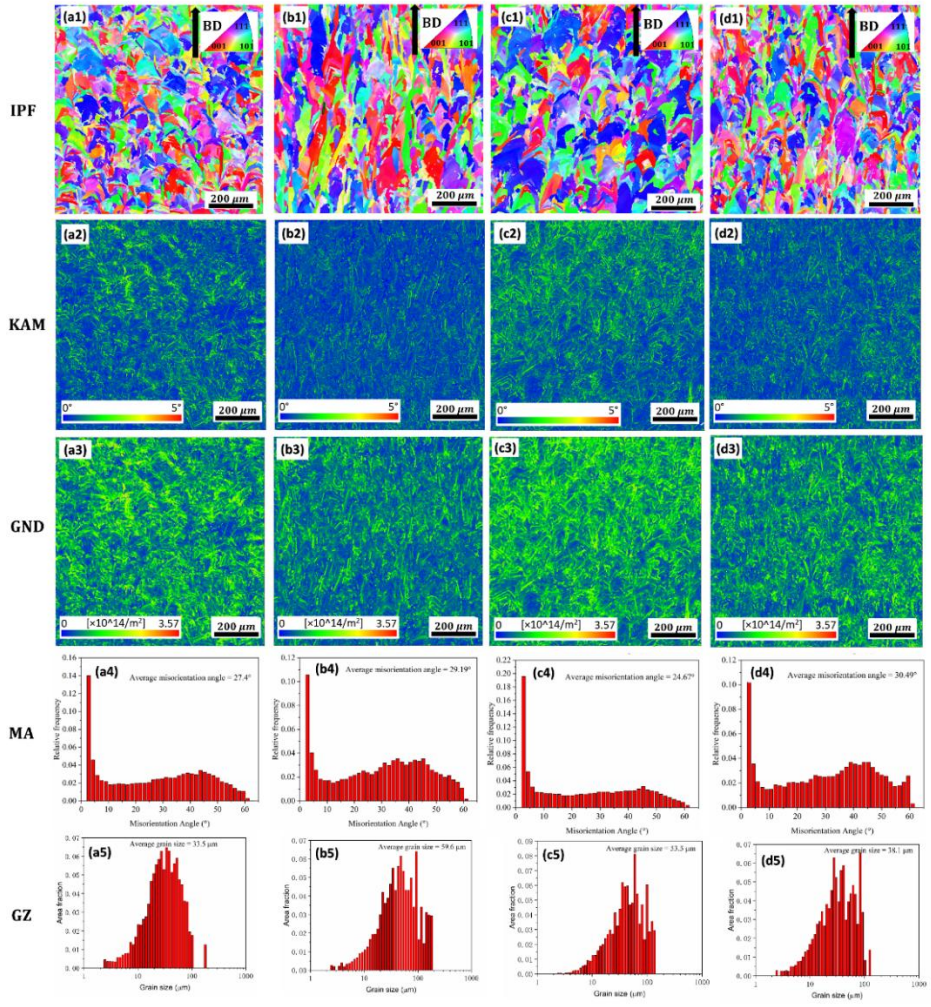

Figure 4.8. EBSD results of IPF, KAM, GND, MA and GZ. (a1-a5): room temperature tensile sample of chemically prepared TiC-IN738LC; (b1-b5) high temperature (850°C) tensile sample of chemically prepared TiC-IN738LC; (c1-c5) room temperature tensile sample of IN738LC; (d1-d5) room temperature tensile sample of ball-milled prepared TiC-IN738LC.

EBSD analysis reveals that nano-TiC contributes to the refinement of grain sizes. Columnar dendrites, a primary cause of anisotropy in L-PBF, tend to overgrow in the printing direction, resulting in excessively large grain sizes [47]. Harrison et al. [11] proposed a relationship between the primary dendrite arm λ_1 and various parameters, such as thermal gradient, which can be represented by the equations (4.2):

$$\lambda_1 = 97 \pm 5 \left(\frac{\partial T}{\partial t}\right)^{0.36 \pm 0.01}$$
$$\frac{\partial T}{\partial t} = GR \tag{4.2}$$

where G is the temperature gradient at the solid/liquid interface, and R is the growth rate. The equations suggest that the columnar dendrites vary under different energy density inputs. Optimizing these parameters to achieve the optimal energy density is crucial in minimizing the development of undesirable structures. TiC particles enhance the cooling of the melt pool during L-PBF. This acceleration in cooling increases both the diffusion driving force and the solidification rate, effectively restricting dendritic growth and, therefore, refining the grain size [20]. In summary, nano-TiC particles play a significant role in the refinement of dendrites.

According to the Hall-Petch formula, smaller grain sizes result in increased tensile strength [63]. This formula implies that the strength of a polycrystalline material increases as its grain size decreases, a phenomenon known as grain boundary strengthening. Therefore, this theory substantiates the findings of this research, indicating that the finer grain size observed in Figure 4.8a compared to Figure 4.8c is associated with improved tensile strength. The Hall-Petch equation is expressed as equation (4.3):

$$\sigma_y = \sigma_0 + k_y d^{-\frac{1}{2}} \tag{4.3}$$

where σ_y is the yield strength of the material, σ_0 is the intrinsic strength of the material, k_y is a constant known as the Hall-Petch slope, and d is the average grain size of the material.

Figures 4.9(a-d) respectively represent the EBSD pole figures of chemically prepared

TiC-IN738LC at room temperature, chemically prepared TiC-IN738LC at high temperature (850°C), IN738LC, and ball-milled TiC-IN738LC. A comparison of Figures 4.9a and 4.9c reveals that the composite TiC-IN738LC exhibits a lower texture degree (3.90 mud) compared to IN738LC (6.91 mud), indicating a reduction in maximum texture index. This reduction is likely due to the role of TiC particles as heterogeneous nucleation sites, which impede grain growth along the (100) direction [4]. Similarly, Figures 4.9a and 4.9c show that TiC-IN738LC have more dispersed distribution pole figures compared to the IN738LC. This dispersion is due to the newly formed equiaxed grains from partial nanoparticle nucleation sites, which have random grain orientations instead of following epitaxial growth directions [58]. Comparing Figures 4.9c and 4.9d, ball-milled TiC-IN738LC, with a maximum texture degree of 2.57 mud, is lower than that of IN738LC. This implies that nano-enhanced nickel bases reduce the maximum texture degree compared to the unreinforced nickel alloy, consistent with the findings in TiC-reinforced CM247LC work [4]. Comparing Figures 4.9a and 4.9b, high-temperature tensile testing at 850°C led to grain regrowth, particularly promoting the regrowth of columnar grains with the (100) orientation, aligning with the IPF map. It is noteworthy that the literatures suggest that for face-centered cubic (FCC) or body-centered cubic (BCC) alloys, the preferred solidification crystallization direction is the (100) direction [4, 60]. Figures 4.9a and 4.9d show that chemically prepared samples, compared to ball-milled samples, exhibit a weaker (100) texture distribution, which can be attributed to nanoparticle interference with grain growth along the building direction, reducing columnar dendrites formation and promoting more equiaxed crystal structures. This observation implies that chemical preparation enhances nanoparticles bonding and distribution, changing melt pool dynamics and thereby affecting the microstructural features.

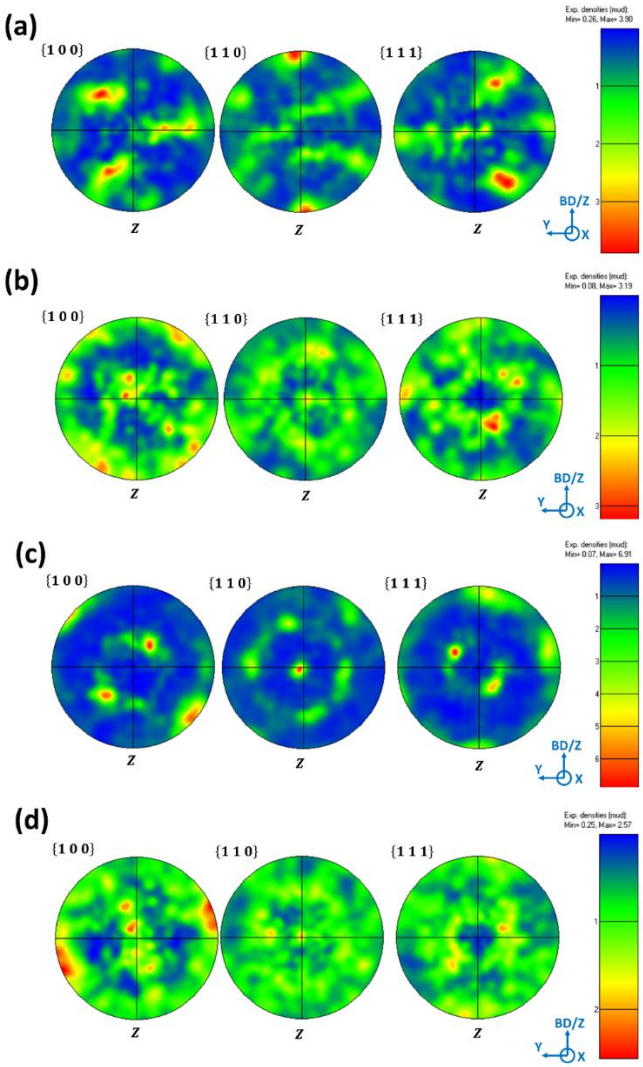

Figure 4.9. EBSD PF results: (a-b) room and high temperature (850°C) tensile sample of chemically prepared TiC-IN738LC; (c) room temperature tensile sample of IN738LC; (d) room temperature tensile sample of ball-milled TiC-IN738LC.

SEM images of TiC-IN738LC, as displayed in Figures 4.10(a and b), reveal that IN738LC reinforced with nano-TiC precipitates both the primary γ' phase and a secondary γ' phase. The primary γ' phase, an important strengthening phase in nickel-based superalloys, significantly enhances the properties of these alloys. It is noteworthy that these SEM images were observed after the tensile tests from as-built samples, showing that some of the γ' had experienced deformation. The size of the γ' identified in this study closely aligns with that reported by Xu et al. in the IN738LC alloy, where approximately 200 nm diameter of fine γ' phases can improve the performance at room temperature, with carbides functioning as a supplementary

strengthening mechanism, further improve the material's properties [64]. Elemental analysis via EDS in Figures 4.10(c-f) indicates that γ/γ' eutectic observed in Figure 4.10a are enriched with Cr, typically indicative of $M_{23}C_6$ carbides [43]. The increase in tensile strength may be attributed to the $M_{23}C_6$ carbides, which enhance grain boundary energy and increase the material's resistance to plastic deformation [65]. $M_{23}C_6$ carbides also play a critical role in inhibiting the expansion of microcracks during tensile tests [65]. Additionally, by heat treatment routes, these MC carbides can be optimized to increase the proportion of γ', resulting in further enhancements in performance [66]. Finally, the precipitation of the secondary γ' phase is also significant. The secondary γ' precipitates typically ranging from 10 to 50 nanometers in size [67]. The presence of these secondary γ' precipitate particles critically influences the mechanical properties of the nickel alloy, especially in terms of low temperature tensile and creep properties [68].

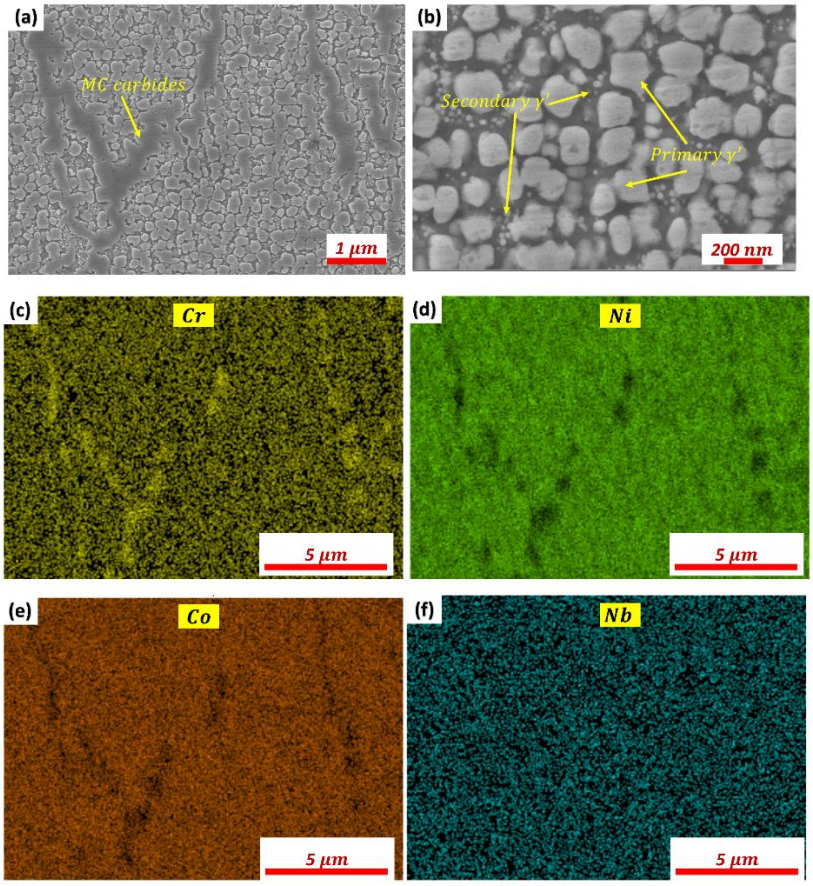

Figure 4.10. SEM and EDS graphs of the chemically prepared as-built TiC-IN738LC post tensile test. The primary γ' phase (cubelike) and secondary γ' phase (spherical shape) are marked in the graph.

Figure 4.11 presents the TEM and EDS results for chemically prepared TiC-IN738LC. From Figure 4.11a, a dense dislocation network embedded at sub-grain boundaries can be observed, a similar dislocation network has also been identified in IN738LC nickel-based superalloys [69]. Furtherly, Figure 4.11a reveals numerous dislocation loops in TiC-IN738LC. Considering the introduction of nano-TiC particles, it can be inferred that Orowan strengthening mechanism has occurred. This is primarily attributed to the obstruction by ceramic particles to the passage of dislocations [70]. Figure 4.11b provides further evidence by showing nano-TiC particles are located on dislocations, hindering their movement. Figures 4.11(c-f) present the results of TEM and EDS. The EDS analysis clearly shows the location of nano-TiC particles, confirming their role in impeding dislocation movement, thereby enhancing mechanical properties. This finding further elucidates the strengthening mechanisms of TiC-IN738LC.

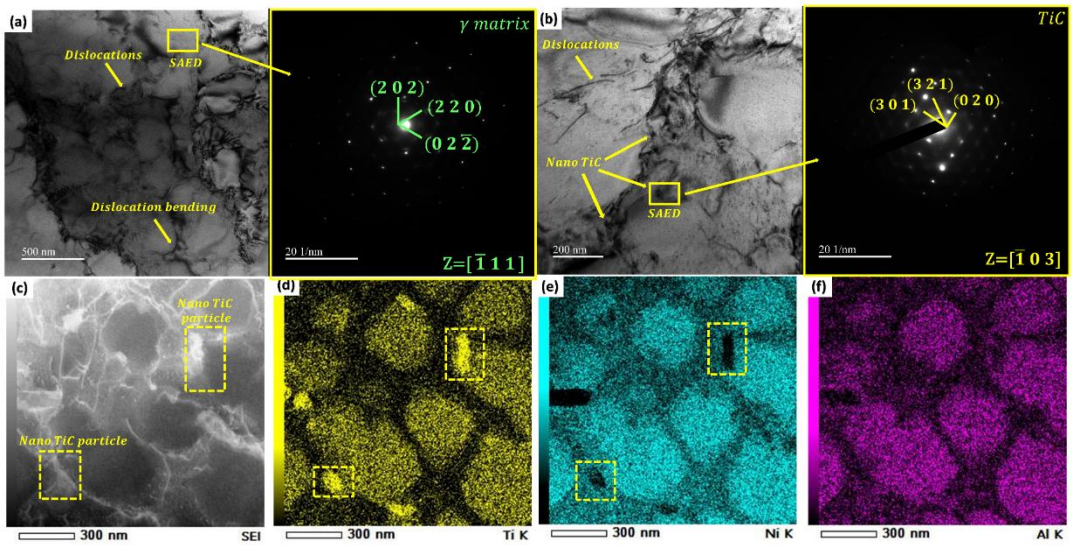

Figure 4.11. TEM results of chemically prepared TiC-IN738LC. (a) cellular sub-grains and SAED gamma phase; (b) high magnification of the grains and SAED of TiC; (c) TEM-EDS mapping region; (d) Ti element distribution within mapping region; (e) Ni element distribution within mapping region; (f) Al element distribution within mapping region.

TEM results indicate that nano-TiC particles hinder the dislocations. This effect is mainly attributed to the pre-solidification propulsion of nano particles by the melt pool, causing most particles to distribute along grain boundaries and within columnar dendrites [20]. The particle flotation velocity can be described by the following Stokes'

equation [71]:

$$v_{\mathrm{p}} = \frac{2}{9}\frac{a r_p^2 (\rho_\iota - \rho_{\mathrm{p}})}{\eta} \tag{4.4}$$

where v_P denotes the solidification velocity of the particle, r_p is the particle radius, ρ_ι and ρ_{p} are the densities of the liquid metal and the reinforcing particles, respectively, a refers to gravitational acceleration and η is the viscosity of the liquid metal.

From the equation, the nano-sized TiC particles, under different processing parameters, will exhibit various energy densities and result in different melt pool dynamics. This affects the distribution of nano-TiC, leading to the particles being trapped and distributed within the grains before solidification as their movement speed is lower than the rate of solidification [20]. However, the nano-TiC particles found in this study are predominantly located at grain boundaries. This can be attributed to optimizing the L-PBF processing parameters that have optimal melt pool dynamics, thereby improving the distribution of nano particles within the grains.

Figure 4.12 is used to illustrate the schematic of the enhancement mechanism of nanoparticles at different stages of L-PBF. As shown in Figure 4.12a, during the crystallization process, nanoparticles, which possess a high melting point (> 3000 ℃), can act as nuclei to promote grain crystallization and impede continuous grain growth, thus preventing excessive grain growth [58, 59]. This phenomenon is consistent with the EBSD data previously mentioned. Figure 4.12b demonstrates the dynamics of nanoparticles within the melt pool. Smaller particles enhance the Marangoni effect in the melt pool, leading to a more uniform flow rather than unidirectional excessive movement, which facilitates heat distribution and dissipation. Particularly, nanoparticles play a pivotal role in the dynamics of the melt pool, preventing localized excessive heat accumulation and guiding the heat to distribute more uniformly across the multi-layer structure of L-PBF, thus improving both the melt pool dynamics and the quality of as-built sample [72]. Figure 4.12c illustrates the role of nanoparticles and the

γ' phase in tensile tests. According to SEM results in Figure 4.10, nano-TiC does not inhibit the production of γ', but rather promotes the formation of finer γ', playing a crucial role in resisting deformation during tensile tests [64, 69]. Moreover, more strain energy is required for materials to deform due to the high internal strain energy of nanoparticles impeded the dislocation, which enhances the tensile strength of the composite material with the addition of nano-TiC [73]. Figure 4.12d presents the crystal structure of γ and γ'. Essentially, the γ' phase is an intermetallic compound of $Ni_3(Al, Ti)$, determining the material's high-temperature strength and resistance to creep deformation [65]. After the high-temperature melting process in L-PBF, thermodynamics favor the precipitation of ordered γ' phases. The addition of nano-TiC, with some TiC atoms decomposing into Ti during the melting process and replacing Al atoms in the γ lattice, leads to an increase in γ', thus confirming that the addition of nano-TiC indeed facilitates the formation of γ' [47]. Prior research suggests that adjusting the aluminum to titanium ratio can control the misfit, thereby regulating the amount of γ' and manipulating the properties of the Nickel alloys [74, 75].

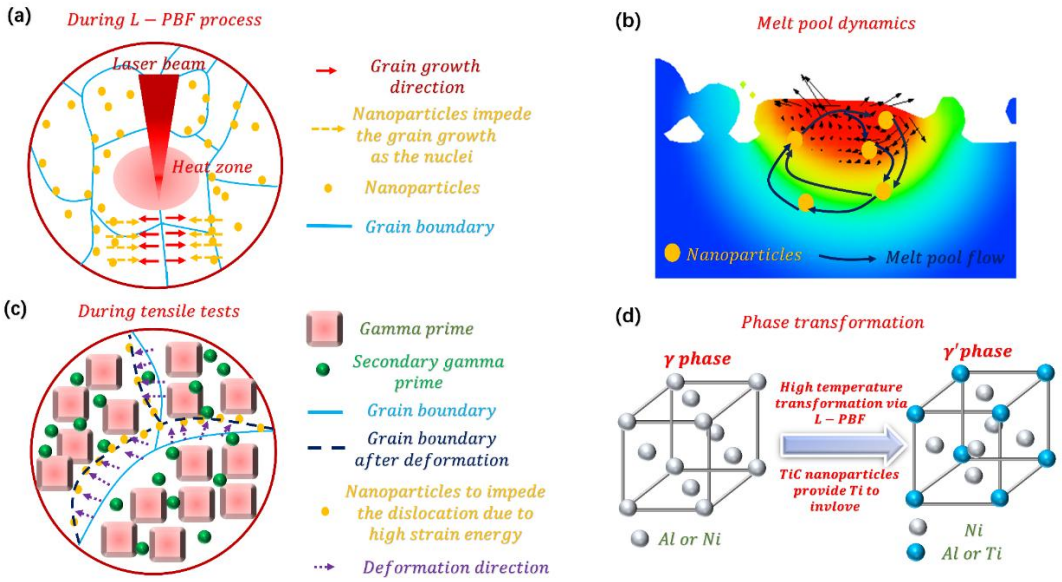

Figure 4.12. (a) The mechanism of nano-TiC inhibiting grain growth; (b) Illustration of the effect of nanoparticles on melt pool dynamics in L-PBF; (c) The role of nanoparticles and γ' in hindering dislocations during the tensile process; (d) The mechanism of TiC promoting the transition from γ to γ'.

4.4 Conclusions

In this study, the preparation of nano-TiC reinforced IN738LC was conducted using a wet chemical method. The process involved a systematic analysis of the L-PBF processing parameters, testing of mechanical properties under optimized parameter windows, and in-depth investigation using SEM, EBSD and TEM techniques. The research clarified the mechanisms behind the reinforcement of nano-ceramic materials and compared the chemically prepared TiC-IN738LC with ball-milled approach. The study emphasized the advantages of the chemical preparation method, with the following principal conclusions:

1) The nano-TiC reinforced IN738LC, prepared through the wet chemical method, demonstrated a significant improvement in particle sphericity and uniformity in nano-particle adherence. This advancement led to a notable 65% improvement in tensile strength at high temperatures, ensuring its application in high-strength, extreme conditions of aerospace.

2) The influence of processing parameters on the porosity, micro-hardness, and tensile strength of TiC-IN738LC were determined, and obtained the optimal L-PBF processing parameters. The processing window was identified to be within the range of VED=100 J/ mm^3 to VED=130 J/ mm^3, with the optimal parameters being laser power = 225W, scan velocity = 750 mm/s, hatch space = 0.09 mm, layer thickness = 0.03 mm, and VED = 111.1 J/ mm^3.

3) The reinforcement mechanisms of chemically prepared TiC-IN738LC were clarified. These mechanisms involve the synergistic effect of grain size refinement, load-bearing strengthening, and Orowan strengthening, contributing to the enhanced performance of the material.

Acknowledgements

This work was supported by the National Natural Science Foundation of China (U23A20629, No.52375346), Natural Science Foundation of Zhejiang, China (No. LZ22E050002), Science and Technology Innovation 2025 Major Project of Ningbo (No.2022Z064), Royal Society project (IEC\NSFC\211480) and the University of Birmingham that provided the funding.

References

1. Sanchez S, Smith P, Xu Z, Gaspard G, Hyde CJ, Wits WW, et al. Powder Bed Fusion of nickel-based superalloys: A review. International Journal of Machine Tools and Manufacture. 2021;165:103729.
2. Ogunbiyi O, Jamiru T, Sadiku E, Beneke L, Adesina O, Adegbola TA. Microstructural characteristics and thermophysical properties of spark plasma sintered Inconel 738LC. The International Journal of Advanced Manufacturing Technology. 2019;104:1425-36.
3. Sreenu B, Sarkar R, Kumar SS, Chatterjee S, Rao GA. Microstructure and mechanical behaviour of an advanced powder metallurgy nickel base superalloy processed through hot isostatic pressing route for aerospace applications. Materials Science and Engineering: A. 2020;797:140254.
4. Lv Y, Zhang Z, Zhang Q, Wang R, Sun G, Chen X, et al. Cracking inhibition behavior and the strengthening effect of TiC particles on the CM247LC superalloy prepared by selective laser melting. Materials Science and Engineering: A. 2022;858:144119.
5. Han Q, Gu Y, Setchi R, Lacan F, Johnston R, Evans SL, et al. Additive manufacturing of high-strength crack-free Ni-based Hastelloy X superalloy. Additive Manufacturing. 2019;30:100919.
6. Balikci E, Raman A. Characteristics of the γ′ precipitates at high temperatures in Ni-base polycrystalline superalloy IN738LC. Journal of materials science. 2000;35:3593-7.
7. Reed RC, Tao T, Warnken N. Alloys-by-design: application to nickel-based single crystal superalloys. Acta Materialia. 2009;57(19):5898-913.
8. Thellaputta GR, Chandra PS, Rao C. Machinability of nickel based superalloys: a review. Materials Today: Proceedings. 2017;4(2):3712-21.
9. Wang Y, Roy S, Choi H, Rimon T. Cracking suppression in additive manufacturing of hard-to-weld nickel-based superalloy through layer-wise ultrasonic impact peening. Journal of Manufacturing Processes. 2022;80:320-7.
10. Herlach DM. Non-equilibrium solidification of undercooled metallic metls. Materials Science and Engineering: R: Reports. 1994;12(4-5):177-272.
11. Harrison NJ, Todd I, Mumtaz K. Reduction of micro-cracking in nickel superalloys processed by Selective Laser Melting: A fundamental alloy design approach. Acta Materialia. 2015;94:59-68.
12. Zagade P, Gautham B, De A, DebRoy T. Analytical estimation of fusion zone dimensions and cooling rates in part scale laser powder bed fusion. Additive Manufacturing. 2021;46:102222.
13. Guo C, Yu Z, Hu X, Li G, Zhou F, Xu Z, et al. Y2O3 nanoparticles decorated

IN738LC superalloy manufactured by laser powder bed fusion: Cracking inhibition, microstructures and mechanical properties. Composites Part B: Engineering. 2022;230:109555.

14. Guo C, Yu Z, Liu C, Li X, Zhu Q, Ward RM. Effects of Y2O3 nanoparticles on the high-temperature oxidation behavior of IN738LC manufactured by laser powder bed fusion. Corrosion Science. 2020;171:108715.

15. Yue H, Yao L, Gao X, Zhang S, Guo E, Zhang H, et al. Effect of ball-milling and graphene contents on the mechanical properties and fracture mechanisms of graphene nanosheets reinforced copper matrix composites. Journal of Alloys and Compounds. 2017;691:755-62.

16. Gao X, Yue H, Guo E, Zhang H, Lin X, Yao L, et al. Preparation and tensile properties of homogeneously dispersed graphene reinforced aluminum matrix composites. Materials & design. 2016;94:54-60.

17. Suryanarayana C, Al-Aqeeli N. Mechanically alloyed nanocomposites. Progress in Materials Science. 2013;58(4):383-502.

18. Zhang B, Bi G, Wang P, Bai J, Chew Y, Nai MS. Microstructure and mechanical properties of Inconel 625/nano-TiB2 composite fabricated by LAAM. Materials & Design. 2016;111:70-9.

19. Rong T, Gu D. Formation of novel graded interface and its function on mechanical properties of WC1− x reinforced Inconel 718 composites processed by selective laser melting. Journal of Alloys and Compounds. 2016;680:333-42.

20. Gu D, Zhang H, Dai D, Xia M, Hong C, Poprawe R. Laser additive manufacturing of nano-TiC reinforced Ni-based nanocomposites with tailored microstructure and performance. Composites Part B: Engineering. 2019;163:585-97.

21. Babalola BJ, Shongwe MB, Rominiyi AL, Jeje SO, Olubambi PA. A study of nanocrystalline nickel powders developed via high-energy ball milling. The International Journal of Advanced Manufacturing Technology. 2019;102:3657-65.

22. Chen Z, Wei P, Zhang S, Lu B, Zhang L, Yang X, et al. Graphene reinforced nickel-based superalloy composites fabricated by additive manufacturing. Materials Science and Engineering: A. 2020;769:138484.

23. Zhou W, Zhu G, Wang R, Yang C, Tian Y, Zhang L, et al. Inhibition of cracking by grain boundary modification in a non-weldable nickel-based superalloy processed by laser powder bed fusion. Materials Science and Engineering: A. 2020;791:139745.

24. Zhao S, Zheng Z, Huang Z, Dong S, Luo P, Zhang Z, et al. Cu matrix composites reinforced with aligned carbon nanotubes: Mechanical, electrical and thermal properties. Materials Science and Engineering: A. 2016;675:82-91.

25. Kónya Z, Zhu J, Niesz K, Mehn D, Kiricsi I. End morphology of ball milled carbon nanotubes. Carbon. 2004;42(10):2001-8.

26. Qin YQ, Tian Y, Peng YQ, Luo LM, Zan X, Xu Q, et al. Research status and

development trend of preparation technology of ceramic particle dispersion strengthened copper-matrix composites. Journal of Alloys and Compounds. 2020;848:156475.
27. Han L, Wang J, Chen Y, Huang Y, Liu Y, Wang Z. Fabrication and mechanical properties of WC nanoparticle dispersion-strengthened copper. Materials Science and Engineering: A. 2021;817:141274.
28. Abreu-Castillo HO, Bueno BP, d'Oliveira ASC. In situ processing aluminide coatings with and without tungsten carbide. The International Journal of Advanced Manufacturing Technology. 2022;119(1-2):477-88.
29. Molina-Claros J, Hdz-García H, Alvarez-Vera M, Pech-Canul M, Muñoz-Arroyo R, García-Vázquez F, et al. Characterisation of PTA processed overlays without and with WC nanoparticles. Surface Engineering. 2017;33(11):857-65.
30. Vishwanatha H, Eravelly J, Kumar CS, Ghosh S. Dispersion of ceramic nano-particles in the Al-Cu alloy matrix using two-step ultrasonic casting and resultant strengthening. Materials Science and Engineering: A. 2017;708:222-9.
31. Kasperovich G, Haubrich J, Gussone J, Requena G. Correlation between porosity and processing parameters in TiAl6V4 produced by selective laser melting. Materials & Design. 2016;105:160-70.
32. Mishurova T, Artzt K, Haubrich J, Requena G, Bruno G. New aspects about the search for the most relevant parameters optimizing SLM materials. Additive Manufacturing. 2019;25:325-34.
33. Narasimharaju SR, Zeng W, See TL, Zhu Z, Scott P, Jiang X, et al. A comprehensive review on laser powder bed fusion of steels: Processing, microstructure, defects and control methods, mechanical properties, current challenges and future trends. Journal of Manufacturing Processes. 2022;75:375-414.
34. Chowdhury S, Yadaiah N, Prakash C, Ramakrishna S, Dixit S, Gupta LR, et al. Laser powder bed fusion: A state-of-the-art review of the technology, materials, properties & defects, and numerical modelling. Journal of Materials Research and Technology. 2022;20:2109-72.
35. Majeed A, Ahmed A, Salam A, Sheikh MZ. Surface quality improvement by parameters analysis, optimization and heat treatment of AlSi10Mg parts manufactured by SLM additive manufacturing. International Journal of Lightweight Materials and Manufacture. 2019;2(4):288-95.
36. Tucho WM, Lysne VH, Austbø H, Sjolyst-Kverneland A, Hansen V. Investigation of effects of process parameters on microstructure and hardness of SLM manufactured SS316L. Journal of Alloys and Compounds. 2018;740:910-25.
37. Wang H, Zhang X, Wang G, Shen J, Zhang G, Li Y, et al. Selective laser melting of the hard-to-weld IN738LC superalloy: Efforts to mitigate defects and the resultant microstructural and mechanical properties. Journal of Alloys and Compounds.

2019;807:151662.
38. Ghodsi M, Khademzadeh S, Marzbanrad E, Razmpoosh M, De Marchi N, Toyserkani E. Development of Yttria-stabilized zirconia reinforced Inconel 625 metal matrix composite by laser powder bed fusion. Materials Science and Engineering: A. 2021;827:142037.
39. Wei W-H, Wang L-Z, Chen T, Duan X-M, Li W. Study on the flow properties of Ti-6Al-4V powders prepared by radio-frequency plasma spheroidization. Advanced Powder Technology. 2017;28(9):2431-7.
40. Jia H, Sun H, Wang H, Wu Y, Wang H. Scanning strategy in selective laser melting (SLM): a review. The International Journal of Advanced Manufacturing Technology. 2021;113:2413-35.
41. Zhang S, Rauniyar S, Shrestha S, Ward A, Chou K. An experimental study of tensile property variability in selective laser melting. Journal of Manufacturing Processes. 2019;43:26-35.
42. Majeed A, Zhang Y, Lv J, Peng T, Atta Z, Ahmed A. Investigation of T4 and T6 heat treatment influences on relative density and porosity of AlSi10Mg alloy components manufactured by SLM. Computers & Industrial Engineering. 2020;139:106194.
43. Egbewande A, Zhang H, Sidhu R, Ojo O. Improvement in laser weldability of INCONEL 738 superalloy through microstructural modification. Metallurgical and Materials Transactions A. 2009;40:2694-704.
44. Chen L, Richter B, Zhang X, Ren X, Pfefferkorn FE. Modification of surface characteristics and electrochemical corrosion behavior of laser powder bed fused stainless-steel 316L after laser polishing. Additive Manufacturing. 2020;32:101013.
45. Svetlizky D, Das M, Zheng B, Vyatskikh AL, Bose S, Bandyopadhyay A, et al. Directed energy deposition (DED) additive manufacturing: Physical characteristics, defects, challenges and applications. Materials Today. 2021;49:271-95.
46. Li X, Liu Y, Zhou Z. Influence of hatch distance on processing, microstructure and mechanical properties of AlMgScZr alloy fabricated by laser powder bed fusion. Journal of Manufacturing Processes. 2022;81:78-91.
47. Shu C, Chen S, Zheng Z, Lu X, Li W, De Lisi M, et al. Fabrication and strengthening mechanism of crack-free nano-TiC reinforced IN738LC with enhanced mechanical properties by laser powder bed fusion. Journal of Materials Research and Technology. 2023;27:3835-48.
48. Liu K, Gu D, Guo M, Sun J. Effects of processing parameters on densification behavior, microstructure evolution and mechanical properties of W–Ti alloy fabricated by laser powder bed fusion. Materials Science and Engineering: A. 2022;829:142177.
49. Lee H-J, Han J-K, Janakiraman S, Ahn B, Kawasaki M, Langdon TG. Significance of grain refinement on microstructure and mechanical properties of an Al-3% Mg alloy

processed by high-pressure torsion. Journal of Alloys and Compounds. 2016;686:998-1007.

50. Jena A, Atabay SE, Brochu M. Microstructure and mechanical properties of crack-free Inconel 738 fabricated by laser powder bed fusion. Materials Science and Engineering: A. 2022;850:143524.

51. Zhang Z, Han Q, Liu Z, Wang X, Wang L, Yang X, et al. Influence of the TiB2 content on the processability, microstructure and high-temperature tensile performance of a Ni-based superalloy by laser powder bed fusion. Journal of Alloys and Compounds. 2022;908:164656.

52. Chen L, Sun Y, Li L, Ren X. Microstructure evolution, mechanical properties, and strengthening mechanism of TiC reinforced Inconel 625 nanocomposites fabricated by selective laser melting. Materials Science and Engineering: A. 2020;792:139655.

53. Yin Y, Zhang J, Gao J, Zhang Z, Han Q, Zan Z. Laser powder bed fusion of Ni-based Hastelloy X superalloy: Microstructure, anisotropic mechanical properties and strengthening mechanisms. Materials Science and Engineering: A. 2021;827:142076.

54. Gao X, Shih CF. A parametric study of mixed-mode I/III ductile fracture in tough materials under small scale yielding. Engineering Fracture Mechanics. 1998;60(4):407-20.

55. Zhu H, Wu B, Li D, Zhang D, Chen Y. Influence of voids on the tensile performance of carbon/epoxy fabric laminates. Journal of Materials Science & Technology. 2011;27(1):69-73.

56. Ishikawa K. Fractals in dimple patterns of ductile fracture. Journal of materials science letters. 1990;9(4):400-2.

57. Tian Y, Muñiz-Lerma J, Brochu M. Nickel-based superalloy microstructure obtained by pulsed laser powder bed fusion. Materials characterization. 2017;131:306-15.

58. Zhang Z, Han Q, Yang S, Yin Y, Gao J, Setchi R. Laser powder bed fusion of advanced submicrometer TiB2 reinforced high-performance Ni-based composite. Materials Science and Engineering: A. 2021;817:141416.

59. Zhang X, Li S, Pan B, Pan D, Zhou S, Yang S, et al. A novel strengthening effect of in-situ nano Al2O3w on CNTs reinforced aluminum matrix nanocomposites and the matched strengthening mechanisms. Journal of Alloys and Compounds. 2018;764:279-88.

60. Qin H, Fallah V, Dong Q, Brochu M, Daymond MR, Gallerneault M. Solidification pattern, microstructure and texture development in Laser Powder Bed Fusion (LPBF) of Al10SiMg alloy. Materials Characterization. 2018;145:29-38.

61. Chen S, Yu Q. The role of low angle grain boundary in deformation of titanium and its size effect. Scripta Materialia. 2019;163:148-51.

62. Liu L, Wang D, Deng G, Han C, Zhou H, Tan C, et al. Crack inhibition and

mechanical property enhancement of a CM247LC alloy fabricated by laser powder bed fusion through remelting strategy. Materials Characterization. 2024:114073.
63. Hansen N. Hall–Petch relation and boundary strengthening. Scripta materialia. 2004;51(8):801-6.
64. Xu J, Lin X, Guo P, Yang H, Xue L, Huang W. The microstructure evolution and strengthening mechanism of a γ′-strengthening superalloy prepared by induction-assisted laser solid forming. Journal of Alloys and Compounds. 2019;780:461-75.
65. Zhang L, Li Y, Zhang Q, Zhang S. Microstructure evolution, phase transformation and mechanical properties of IN738 superalloy fabricated by selective laser melting under different heat treatments. Materials Science and Engineering: A. 2022;844:142947.
66. Jena A, Atabay SE, Gontcharov A, Lowden P, Brochu M. Laser powder bed fusion of a new high gamma prime Ni-based superalloy with improved weldability. Materials & Design. 2021;208:109895.
67. Wilson B, Fuchs G. The effect of secondary gamma-prime on the primary creep behavior of single-crystal nickel-base superalloys. Metallurgical and materials transactions A. 2010;41:1235-45.
68. Devaux A, Nazé L, Molins R, Pineau A, Organista A, Guédou J, et al. Gamma double prime precipitation kinetic in Alloy 718. Materials Science and Engineering: A. 2008;486(1-2):117-22.
69. Messé O, Muñoz-Moreno R, Illston T, Baker S, Stone H. Metastable carbides and their impact on recrystallisation in IN738LC processed by selective laser melting. Additive Manufacturing. 2018;22:394-404.
70. Zhang Z, Chen D. Consideration of Orowan strengthening effect in particulate-reinforced metal matrix nanocomposites: A model for predicting their yield strength. Scripta materialia. 2006;54(7):1321-6.
71. Hadji L. Morphological instability prior to particle engulfment by a solidifying interface. Scripta materialia. 2003;48(6):665-9.
72. Qu M, Guo Q, Escano LI, Yuan J, Hojjatzadeh SMH, Clark SJ, et al. Controlling melt flow by nanoparticles to eliminate surface wave induced surface fluctuation. Additive Manufacturing. 2022;59:103081.
73. Liu Y, Song Z, Guo Y, Zhu G, Fan Y, Wang H, et al. Simultaneously enhancing strength and ductility of LPBF Ti alloy via trace Y2O3 nanoparticle addition. Journal of Materials Science & Technology. 2024;191:146-56.
74. Murakami H, Harada H, Bhadeshia H. The location of atoms in Re-and V-containing multicomponent nickel-base single-crystal superalloys. Applied Surface Science. 1994;76:177-83.
75. Capdevila C, Bhadeshia HK. Manufacturing and microstructural evolution of mechanuically alloyed oxide dispersion strengthened superalloys. Advanced

Engineering Materials. 2001;3(9):647-56.

CHAPTER 5 EFFECT AND MECHANISM OF POWDER MORPHOLOGY ON THE MECHANICAL PROPERTIES OF NICKEL-BASED METAL MATRIX COMPOSITES TIC-IN738LC IN LASER POWDER BED FUSION

Authors Contributions:

This chapter of the alternative thesis format is published in *Progress in Additive Manufacturing (2025).* As the first author of this manuscript, I have outlined the paper's details and the contributions of my co-authors below.

Shu, C., *Chen, S., Lei, P., Shu, X., Abdel-Wahab, A., & Essa, K. (2025). Effect and mechanism of powder morphology on mechanical properties of nickel-based metal matrix composites TiC-IN738LC in laser powder bed fusion. Progress in Additive Manufacturing, 1-19.*

CRediT authorship contribution statement

Chang Shu: Writing – original draft, Visualization, Methodology, Formal analysis, Data curation, Conceptualization.

Siyuan Chen: Resources, Methodology, Data curation.

Peiran Lei: Methodology.

Xuedao Shu: Writing – review & editing, Supervision, Resources.

Adel Abdel-Wahab: Writing – review & editing, Supervision.

Khamis Essa: Writing – review & editing, Supervision, Resources, Project administration, Funding acquisition.

CHAPTER 5:
EFFECT AND MECHANISM OF POWDER MORPHOLOGY ON THE MECHANICAL PROPERTIES OF NICKEL-BASED METAL MATRIX COMPOSITES TIC-IN738LC IN LASER POWDER BED FUSION

Abstract

The fabrication of high-performance nickel-based metal matrix composites through laser powder bed fusion (L-PBF) represents a dominant area of research. This study introduces Titanium Carbide (TiC) nanoparticles and prepares the TiC-IN738LC composites using mechanical and wet chemical mixing methods. The morphology and sphericity of the powders produced by these methods were analyzed and observed that powders processed chemically retained superior morphology and characteristics over ball-milled, such as enhanced sphericity and uniform nanoparticle distribution. The mechanical properties of both methods were examined, revealing that powder morphology significantly influences the mechanical performance. Tensile tests indicated that TiC-IN738LC composites prepared chemically exhibited a ductility of 3.26%, a 55% improvement over the ball-milled method, although their strength of 1416 MPa was marginally lower than the 1518 MPa achieved through ball-milled. Additionally, microstructural defects are mitigated by wet chemically mixing route. A high-fidelity Computational Fluid Dynamics (CFD) modelling was employed to investigate the effects of powder sphericity on melt pool dynamics, elucidating the mechanisms behind lack of fusion and verifying the influence of powder physical characteristics on the microstructure and mechanical properties. This study clarifies the role of powder morphology in determining the mechanical properties of nickel-based metal composites in L-PBF processes.

Keywords: Metal matrix composites; Laser powder bed fusion; Powder preparation; Defect formation mechanism

5.1 Introduction

Nickel-based metal composites, recognized for their high-temperature resistance, corrosion resistance, and high strength, find extensive application in the aerospace industry [1-3]. IN738LC, a commonly used nickel-based superalloy for high-temperature applications, maintains high mechanical strength, excellent creep, and fatigue properties at elevated temperatures [4-6]. However, its high aluminum and titanium content promotes the formation of additional gamma prime (γ') phases, leading to material hardening and making it more prone to strain-age cracking [7]. As a result, it presents significant challenges for machining, forging, welding, and hybrid additive manufacturing [8, 9]. Laser powder bed fusion (L-PBF), an advanced additive manufacturing technique, effectively merges the capabilities of laser and powder to bypass the constraints of conventional processing methods, facilitating the production of IN738LC [10]. A very recent study reported that IN738LC with nano-TiC reinforcement fabricated via L-PBF has significantly enhanced mechanical performance [11].

Ball milling, a prevalent technique in metal matrix composites (MMCs) preparation, entails mixing powders in a high-energy ball mill to achieve atomic alloying via continuous deformation, cold welding, and fracturing [12]. This approach is extensively utilized in MMCs production [13-15]. Zhang et al. [16] successfully modified ball milling parameters to uniformly attach nano-sized TiC particles to the nickel-based material IN625, obtaining the high-performance TiC-IN625 nickel-based composites. Similarly, Rong et al. [17] used ball milling to develop WC-reinforced nickel-based IN718 composites, enhancing the mechanical properties. Several studies [18-20] have successfully employed conventional ball milling for composite preparation with TiC particles as the reinforcement, confirming its versatility and reliability. Despite the advantages of ball milling, such as simple operation, short processing time, high production efficiency, and effectiveness in composite material preparation, this high-energy process can alter the sphericity of powder particles due to energy accumulation and collisions. This leads to defects such as surface microcracks and satellite particles,

which impair the powder's characteristics. Furthermore, the agglomeration of secondary-phase nanoparticles and the potential introduction of impurities during the milling process can negatively impact the performance of the composite materials [21].

Recent years have seen a surge in interest and research into in-situ wet chemical methods as novel approaches for preparing composite materials. Han et al. [22] found that ultrasonic dispersion and stirring effectively prevent the agglomeration of secondary phase nanoparticles. Vishwanatha et al. [23] utilized dual-step ultrasonic processing to produce aluminum-alumina bulk nanocomposites, resulting in an exceptionally uniform distribution of alumina particles within the aluminum matrix and subsequently enhancing mechanical properties. Abreu-Castillo et al. [24] applied in-situ chemical synthesis to uniformly adhere the reinforcing phase onto the matrix material's surface, confirmed by Scanning Electron Microscopy/Energy Dispersive Spectroscopy (SEM/EDS) analysis, leading to the creation of tungsten aluminum carbides with enhanced mechanical characteristics. Similarly, Molina-Claros et al. [25] adopted this chemical synthesis method, integrating WC nanoparticles into nickel-based materials, thereby improving WC particle distribution and preventing microcrack extension in coatings by altering the liquid phase's viscosity, ultimately improving performance. Therefore, the wet chemical method offers an effective approach for bonding nanoparticles and ensuring a more uniform distribution on the matrix powders, facilitated by its higher mixing speed. Enhanced attachment and reduced sphericity loss are essential for improving material properties.

The morphology of powder plays a crucial role in determining its flow characteristics, which in turn significantly impacts the quality of the L-PBF process. Wei et al. [26] observed that the flowability significantly affect the quality of L-PBF printed samples. Brika et al. [27] reported that powders with increased sphericity exhibit higher adjustable packing density and superior flowability. Gao et al. [28] reported that non-spherical particles reduce packing density and increase surface roughness. Zhao et al.

[29] demonstrated that processing with spherical powders provides a broader process window, effectively suppressing microstructural defects. Haferkamp et al. [30] investigated the impact of particle shape on powder flowability and powder layer density in LPBF. Their findings indicate that more spherical particles exhibit improved flowability, resulting in higher powder layer density. Mussatto et al. [31] observed that highly spherical powders containing satellite particles exhibit slightly lower flowability compared to less spherical, smoother powders. This is attributed to the higher degree of mechanical interlocking between satellite particles, which naturally hinders flow. Additionally, powders with a high fraction of fine particles (< 25 μm) demonstrate increased cohesive forces, leading to higher specific energy and greater sensitivity to flow rate variations. Consequently, utilizing the in-situ chemical methods to fabricate nickel-based metal composites with high sphericity and uniform nanoparticles distribution can effectively improve the mechanical performance. Previous investigations into MMCs have mainly looked at ball milling technique to develop such composites. To date, the synthesis of nickel materials through wet chemical methods remains understudied. Additionally, studies on modelling L-PBF with consideration of powder morphology in MMCs within numerical simulations are scarce. Furthermore, microscopic characterization techniques offer deeper insights into the different preparation methods and their impact on microstructure and mechanical properties.

This research article studies the incorporation of TiC nanoparticles into IN738LC nickel superalloy using ball milling and wet chemical mixing methods. Initially, it examines the effects of these preparation methods on the powder's morphology and sphericity. Subsequently, the study explores the impact of these differing powder morphologies on the mechanical properties of L-PBF printed samples. This investigation includes tensile tests and fracture analyses to understand the correlation between powder morphology and the mechanical properties. Additionally, Computational Fluid Dynamics (CFD) simulations are utilized to model the L-PBF process, evaluating the effects of the two powder preparation methods on print quality. The CFD models are used to reveal the underlying mechanisms behind the improved mechanical properties achieved through

wet chemical mixing. Overall, this study provides critical theoretical insights for producing high-quality TiC-IN738LC composites via L-PBF.

5.2 Materials and methods

5.2.1 Experiments

This study utilized spherical IN738LC powder (China North Industries Group Corporation Limited, China) with a particle size distribution of d_{10} = 16.7 μm, d_{50} = 32.3 μm, and d_{90} = 45.2 μm. Additionally, 50 nm TiC ceramic reinforcements with a purity of 99.5%, sourced from the same supplier, were employed in this work. In the mechanical mixing method, a four-planetary ball mill machine (QM-QX, Nanjing Nanda Instrument Plant, China) was used to mix 2 wt% TiC with the nickel-based superalloy IN738LC. The milling balls, with diameters ranging from 5 mm to 10 mm, and the 500 mL milling pots were both made of zirconia. During the ball mill, the Argon gas was filled as the inert gas to prevent the impurity phase that was caused from the oxidation reaction with the powders. To fully disperse and attach the nano-TiC to IN738LC, a set of parameters from ball milling are used: 4:1 ball-to-powder ratio, 200 rpm ball mill speed and 6 h ball mill time [11]. The reduction in nanoparticle size leads to high surface energy, causing a strong tendency for agglomeration, which hinders the homogenization of the powder. To mitigate agglomeration, the wet chemical mixing method was used to adhere nanoparticles to the surface of nickel particles [24, 25]. This wet chemical preparation method involved a multi-step process to prepare the powder mixture of nickel-based matrix composite containing 2 wt% TiC nanoparticles. The nanoparticles were weighed and dispersed in ethanol, ultrasonicated for 90 minutes, followed by the addition of IN738LC nickel-based powder and magnetically stirred at 1600 rpm for 90 minutes to improve the impregnation of nanoparticles on the nickel particle surfaces. Finally, the mixture was dried in a muffle furnace at 313 K for 90 minutes. For wet chemical mixing, each batch is prepared by mixing 25 grams of material, consisting of 24.5 grams of IN738LC and 0.5 grams of nano-TiC. Wet chemical mixing uses ethanol as the medium and operates at a much higher mixing speed, enhancing TiC embedding into nickel powders due to its significantly greater

hardness. This mechanism has been previously discussed in the literature [9].

This study utilized a commercial laser powder bed fusion machine (HBD-150D, Shanghai Hanbang United 3D Tech Co., Ltd., China) for the fabrication of TiC-IN738LC composites using two powder preparation methods. The machine, equipped with a 400W IPG fiber laser, features a laser spot diameter of 70 μm. Prior to printing, the prepared powders were placed in a furnace filled with inert gas and dried at 40°C for three hours to remove moisture. The L-PBF process adopted a checkerboard unidirectional scanning strategy [32, 33]. Tensile specimens were prepared following ASTM dimensions and standards [34]. The selection of tensile testing results was based on the optimal performance exhibited by each powder preparation method. The optimal processing parameters for chemically prepared TiC-IN738LC were obtained from previous work [9], while the optimal parameters for ball-milled TiC-IN738LC and pure IN738LC were derived from prior research [11].

Particle size and shape analyses were conducted using the MICROTRAC MRB FLOWSYNC (Microtrac Inc., USA) with a wet dispersion method, employing laser diffraction and dynamic image analysis to characterize the particles. Porosity and melt pool morphology of printed samples were observed using an optical microscope (OM), with samples thoroughly polished prior to observations. Fracture morphology and microstructure of printed samples were examined using a Scanning Electron Microscope (SEM) (Hitachi SU5000, Japan). Tensile tests of printed samples were performed using a tensile testing machine (Zwick Amsler 100 HFT, Germany) at a rate of 2 mm/min, with the load applied perpendicular to the sample's build direction. Three identical samples were tested to ensure the accuracy of the results. The tap density of both batches was measured as 4.88 g/cm³ for the wet chemical route and 4.69 g/cm³ for the ball-milled route. The apparent density was 4.19 g/cm³ for the wet chemical batches and 4.06 g/cm³ for the ball-milled batches. Figure 5.1 presents the schematic of this study.

Thermal camera ZLV-FLIRE49001 was used to monitor the temperature distributions. As indicated in the study by H. Krauss et al. [35], employing normalized heat intensity circumvents the approximation of absolute temperatures and demonstrates minimal thermal uncertainty during the L-PBF process. Therefore, this work considers absolute radiative intensity as the measurement variable. For a pre-set emissivity value of 1.0, this value is in direct proportion to the camera's output signal.

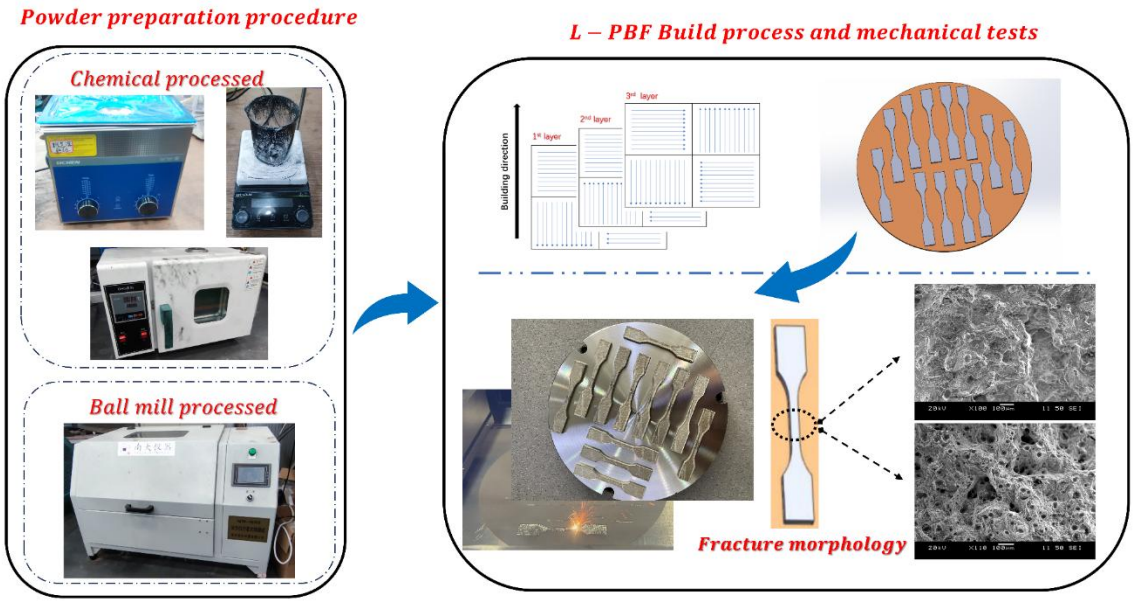

Figure 5.1 Schematic of this study from the powder preparation methods to the L-PBF process and as-built samples analysis.

5.2.2 Numerical modelling method

This study utilized the Discrete Element Method (DEM) software EDEM Altair to model four distinct powder morphologies [36]. As shown in Figure 5.2, SEM experimental data were obtained from ball-milled experiments. In the DEM powder model, three primary defects and one normal form are represented: satellite morphology, crater morphology, numerous small asteroid forms, and powder with normal sphericity. In the ball milling method, these four powder forms were distributed in equal proportions, with particle size distribution assumed to follow experimental measurements. The diameters were proportionally distributed between 15-53 μm, following a Gaussian distribution. For the wet chemical mixing powder, the distribution

was set at 1:1, with 50% being defective forms and 50% normal sphericity, also with diameters ranging from 15-53 μm and following a Gaussian distribution. Figure 5.2 illustrates projections of typical particles analyzed by the particle size analyzer. Different powder bed morphologies were used in CFD simulations to study the effect of sphericity on the L-PBF process, thereby elucidating the differences in L-PBF quality between ball milling and wet chemical methods. Schematic illustrations of the powder beds prepared by ball milling and chemical mixing, with the melt track areas highlighted in red, are shown in Figure 5.3(a-d).

In this study, the CFD model was constructed and performed in the CFD software FLOW-3D with customized subroutines. Several assumptions were introduced during the model development process to simplify the computations. These assumptions include: (1) the molten material in the melt pool was conceptualized as an incompressible Newtonian fluid; (2) a mushy zone was delineated to represent the region where solid and liquid phases coexist, thereby aiding in the simulation of the melt pool's thermodynamic characteristics; and (3) ignoring the mass loss due to metal evaporation, assuming mass conservation throughout the process [37].

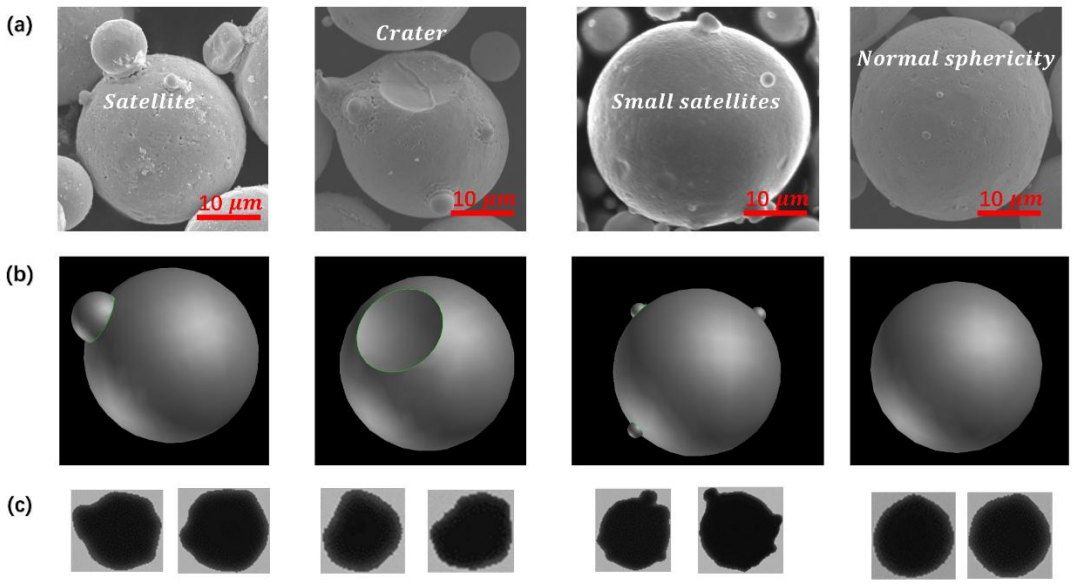

Figure 5.2 SEM images of four distinct powder morphologies from (a) experiments, (b) the corresponding powder shapes utilized in the simulation, and (c) powder projections derived from particle size analysis results.

5.2.2.1 Governing equations

To study the dynamic flow within the melt pool, the model integrates the fundamental principles of conservation, encompassing the equations for mass, momentum, and energy. These equations are articulated as equations (5.1-5.3) [38, 39]:

Mass Conservation Equation:

$$\nabla \cdot (\rho \vec{v}) = 0 \tag{5.1}$$

Momentum Conservation Equation:

$$\frac{\partial \rho \vec{v}}{\partial t} + \nabla(\rho \vec{v} \otimes \vec{v}) = -\nabla p + \rho \vec{g} + \overrightarrow{f_B} + \mu_T \nabla^2 \vec{v} - K\vec{v} \tag{5.2}$$

Energy Conservation Law:

$$\frac{\partial \rho h}{\partial t} + \nabla(\rho \vec{v} h) = \nabla \cdot (k \nabla T) + R_{ESOR} \tag{5.3}$$

Where $\vec{v}$ denotes the velocity of the melt pool, μ_T is the viscosity of the liquid material, t represents time, p indicates pressure, $\vec{g}$ is the gravitational acceleration, T refers to the fluid temperature, h is the enthalpy, while ρ and k are the density and thermal conductivity, respectively. R_{ESOR} is the energy term.

The buoyancy force $\overrightarrow{f_B}$ is calculated using the Boussinesq approximation as shown in equation (5.4):

$$\overrightarrow{f_B} = \rho g \beta \left(T - T_{ref}\right) \tag{5.4}$$

Where β is the coefficient of thermal expansion, T_{ref} represents the reference temperature.

In this study, the interface where liquid and solid phases coexist was modelled as a mushy zone. Within this context, the flow of liquid metal through this zone is treated analogously to flow within a porous medium, which is expressed in equation (5.5):

$$K = C \frac{F_s^2}{(1 - F_s)^3 + B} \tag{5.5}$$

Here, C represents a constant characterizing the morphology of the mushy zone, F_s

denotes the solid fraction, and B is a small constant introduced to prevent division by zero.

The Volume of Fluid (VOF) method [40] was utilized to capture the free surface dynamics, with the VOF equation (5.6) formulated as follows:

$$\frac{\partial V_F}{\partial t} + \nabla(\vec{v} \cdot V_F) = 0 \tag{5.6}$$

where V_F denotes the volume fraction of metal within a cell. When $V_F = 1$ indicates that the cell is completely filled with liquid, while $V_F = 0$ implies the absence of liquid in the cell. Intermediate values V_F of signify the presence of a free surface within the cell.

5.2.2.2 Driving Forces and Boundary Conditions

One of the primary driving forces is the Marangoni force, which originates from variations in surface tension. This force is particularly pertinent as the surface tension of liquid metal is often represented as a linear function of its temperature in equation (5.7) [40]:

$$\gamma = \gamma_0 + \frac{d\gamma}{dT}(T - T_m) \tag{5.7}$$

where γ represents surface tension, γ_0 is the surface tension at the melting temperature, and $\frac{d\gamma}{dT}$ is the temperature coefficient of surface tension.

During the L-PBF process, as the temperature of the melt pool approaches or surpasses the evaporation point of the material, recoil pressure is generated. This pressure exerts a significant influence on both the morphology and the properties of the as-printed sample. The recoil pressure can be quantified using the following equation (5.8) [41]:

$$P_R = 0.54 P_0 \exp\left(L_v \frac{T - T_b}{RTT_b}\right) \tag{5.8}$$

where P_0 atmospheric pressure, L_v is the latent heat of evaporation, T_b is the boiling temperature, and R denotes the gas constant.

It is assumed that the power density of the laser beam closely approximates a Gaussian distribution. Throughout the laser scanning process, the laser beam moves at a steady scanning speed in the positive x-direction. Consequently, the laser beam power density can be expressed as equation (5.9):

$$q = \frac{2AP}{\pi R_b^2} \exp\left[-2\frac{(x - vt - x_0)^2 + (y - y_0)^2}{R_b^2}\right] \tag{5.9}$$

where A represents the laser absorptivity of the powder bed, P is the laser power, R_b is the radius of the laser beam, and v is the scanning speed. (x_0, y_0) denotes the initial position of the laser beam center. The radius of the laser beam, R_b is taken as 70μm.

Each surface is considered for convection and radiation, and the evaporation on the melt pool surface cannot be ignored. Hence, the energy equilibrium at the surface of the melt pool is represented as equation (5.10):

$$k\frac{\partial T}{\partial \vec{n}} = q - h_c(T - T_0) - \sigma_0 \varepsilon (T^4 - T_0^4) - q_{evap} \tag{5.10}$$

Where h_c represents the convective heat transfer coefficient, T_0 the ambient temperature, σ_0 denotes the Stefan-Boltzmann constant, and ε is the emissivity. q_{evap} is the heat loss due to evaporation, can be expressed by the following equation (5.11) [42]:

$$q_{\text{evap}} = w_0 L_v = \exp\left(2.52 + 6.121 - \frac{18836}{T} - 0.5\log T\right) L_v \tag{5.11}$$

where ω_0 is the evaporation rate.

L-PBF involves a range of complex physical processes. The primary driving forces under consideration include gravity, surface tension, the Marangoni effect, and vapor recoil force [37]. The energy from the absorbed laser beam serves to melt the powder particles, thereby creating a melt pool where fluid flow is predominantly governed by the gradient in surface tension [40]. The dimensions of the simulation domain were set at 1000μm×270μm×190μm. The initial configuration of the powder layer was established based on results from DEM simulations. The computational domain was

discretized using a uniform 5 μm grid, and the step size was fixed at 1×10^{-8} s [37]. Optimal processing parameters (laser power 225W and scanning speed 750 mm/s) were selected based on the previous study [11]. Detailed physical parameters of the IN738LC material utilized in the simulations are presented in Table 5.1 and Figures 5.3(e-f). The values were obtained from literature and the calculation of phase diagram (JMATPRO) simulations.

Table 5.1 Physical parameters of IN738LC material used in the simulation.

Physical Properties of IN738LC	**Values**	**Unit**	**Reference**
Liquidus	1346	°C	[43]
Solidus	1160	°C	[43]
Boiling point	2786	°C	[43]
Latent heat of melting	163	kJ/kg	[43]
Surface tension	1.6	Kg m^{-1} s^{-1}	[37]
Ambient temperature	300	K	[37]
Universal gas constant	8.314	J/K/mol	[37]

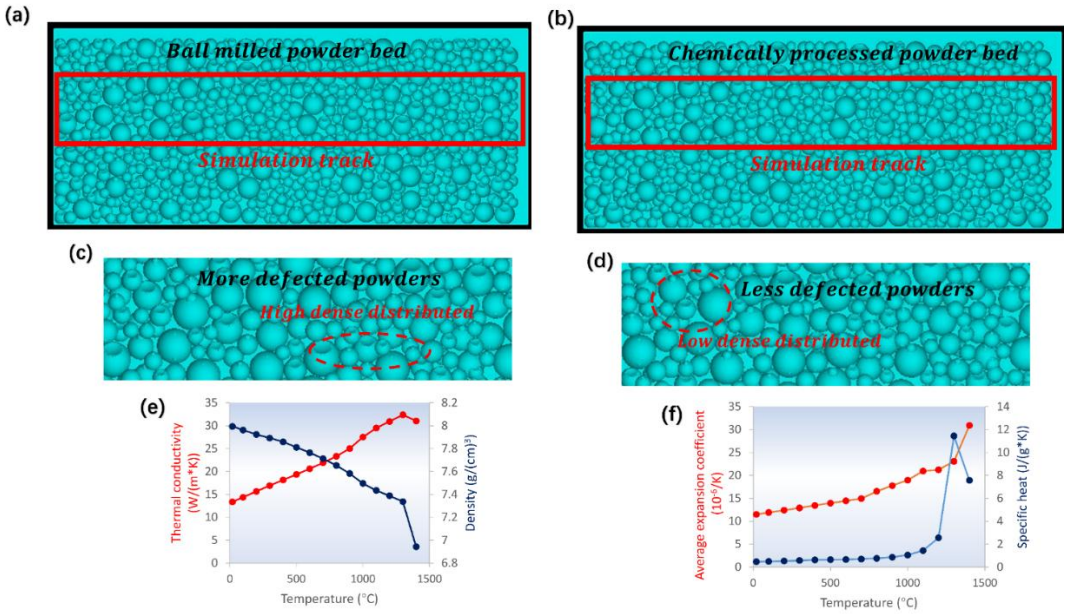

Figure 5.3 (a) Schematic of the powder bed prepared by ball milling; (b) Schematic of the powder bed prepared chemically; (c) Magnified view of ball-milled powder bed showing increased defects powders; (d) Magnified view of chemically prepared powder bed with fewer defects powders; (e) and (f) temperature-dependent parameters used in the process model.

5.3 Results and Discussion

5.3.1 Morphological analysis of powders

In Figures 5.4(a and b), ball-milled powders exhibit deformation due to the inherent mechanics of ball milling. This process involves the kinetic energy accumulation from collisions between the nanoparticles and milling balls, resulting in the deformation of powders and decreased sphericity. Despite the ball milling speed being controlled at 200rpm, the extended duration of milling leads to sphericity degradation, causing surface deformations, pits, and satellite on the spherical powders. Additionally, the nano-properties of TiC particles induce partial agglomeration in the ball milling process [44], further contributing to the irregularities and incomplete adherence to the nickel matrix. Contrastingly, Figures 5.4(c and d) illustrate that chemically prepared powders maintain superior sphericity. The severity of agglomeration in these nanoparticles is less than that observed in ball milling. The improvement is attributed to the ultrasonic cleaning prior to magnetic stirring, allowing the nano TiC particles to be suspended in ethanol, forming a flocculent liquid. Subsequent addition of IN738LC powders facilitated effective collisions between the surface area of the nickel and the nano TiC particles during magnetic stirring, promoting adherence to the nickel powder's surface. Unlike ball milling, despite the higher rotation speed in wet mixing (i.e., 1600rpm), this did not result in significant powder deformation. The wet chemical mixing preparation is conducted in liquid ethanol, where buoyancy and higher rotation speed ensured thorough contact between the nano TiC particles and the IN738LC powder, thereby achieving high-quality composite powders.

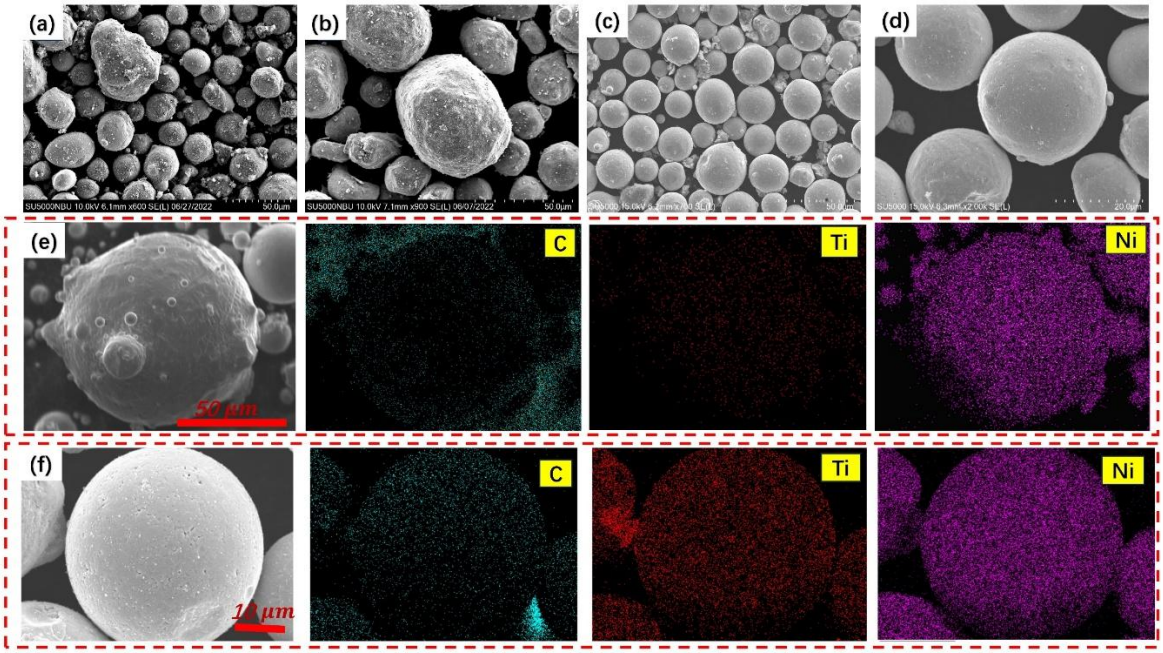

Figure 5.4 (a) SEM of ball-milled powder; (b) High-magnification SEM of ball-milled powder; (c) SEM of wet chemically prepared powder; (d) High-magnification SEM of chemically prepared powder; (e) SEM and EDS elemental analysis of ball-milled powder, showing C, Ti, and Ni elements; (f) SEM and EDS elemental analysis of chemically prepared powder, showing C, Ti, and Ni elements.

Figure 5.4(e and f) shows the results of EDS (Energy Dispersive Spectroscopy) analysis. The surface of the original IN738LC powder contains only small amounts of titanium (Ti) and carbon (C) elements. Further, powders prepared by wet chemical mixing were subjected to a similar EDS analysis. The distribution of Ti and C elements in these analyses indicates that in the chemically prepared composites, TiC nanoparticles are uniformly adhered to the nickel-based material. In comparison with previous studies on powders prepared by ball milling [11], it was observed that powders produced by ball milling show significantly poorer uniformity and adhesion of Ti elements than those prepared chemically. This difference underscores the profound impact of the preparation method on the microstructure and properties of composite materials, especially regarding the uniformity of nanoparticle distribution and surface characteristics of the powders. These findings offer crucial insights for optimizing the preparation of nickel-based metal composite materials.

Particle size analysis enables the acquisition of measurements for each individual

particle. The data for each particle, including its actual image contour, are presented in a table format. Furthermore, the relationship between particle diameter and sphericity is visualized using scatter plots. Sphericity, defined as the degree of similarity to a circle, is quantified on a scale from 0 to 1, with 1 denoting a perfect circle. The algorithm employed to calculate sphericity is outlined below:

$$Sphericity = \left[\frac{4\pi * Area}{Perimeter^2}\right]^{\frac{1}{2}} = \frac{Da}{Dp} \tag{5.12}$$

$$Area\ Equivalent\ diameter: \quad Da = \left(\frac{4Area}{\pi}\right)^{\frac{1}{2}} \tag{5.13}$$

$$Equivalent\ perimeter\ Diameter: \quad Dp = \frac{Perimeter}{\pi} \tag{5.14}$$

$$Area = average\ Area\ of\ a\ sequence\ of\ 3D\ images$$

$$Perimeter = average\ Perimeter\ of\ a\ sequence\ of\ 3D\ images$$

The results of particle size and sphericity for powders prepared by ball milling and wet chemical methods are shown in Figure 5.5. Figures 5.5(a and b) indicate that the sphericity of the ball-milled powders predominantly ranges from 0.86 to 0.97. Statistical analysis of 47,262 particles reveals an average sphericity of 0.91. In contrast, the sphericity of chemically prepared powders mainly lies between 0.93 and 0.98, with an average sphericity of 0.95 derived from 67,225 particles, as depicted in Figures 5.5(c and d). The chemically prepared powders exhibit a higher proportion of well-formed circular shapes compared to those prepared by ball milling. These results are consistent with previous SEM data, further supporting these findings that chemically prepared powders have superior sphericity. In [27], it suggests that powders with better sphericity improve flowability during L-PBF processes, leading to the fabrication of high-quality as-printed samples. Also, in Figures 5.5(a and c), it can be observed that both types of powder exhibit aggregation at a sphericity of 0.9. This is likely due to the algorithm defined by equations (5.12-5.14), and may also be influenced by processing inconsistencies, particle deformation limits, initial particle size distribution, and processing parameters. From Figure 5.5b and 5.5d, the ball-milled powder contains

more large particles (D_{90} and above) compared to the wet chemical method. This is attributed to the planetary milling process, where larger and smaller particles interact, leading to the formation of larger agglomerates. In contrast, the D_{90} of the wet chemical method is smaller than that of the ball-milled powder, and its D_{50} is also lower. Consequently, the wet chemical method has a higher likelihood of achieving a more densely packed powder bed by facilitating better mixing of particles of different sizes. Overall, data indicates that the sphericity achieved by the wet chemical preparation method is generally superior to that achieved by the ball milling method.

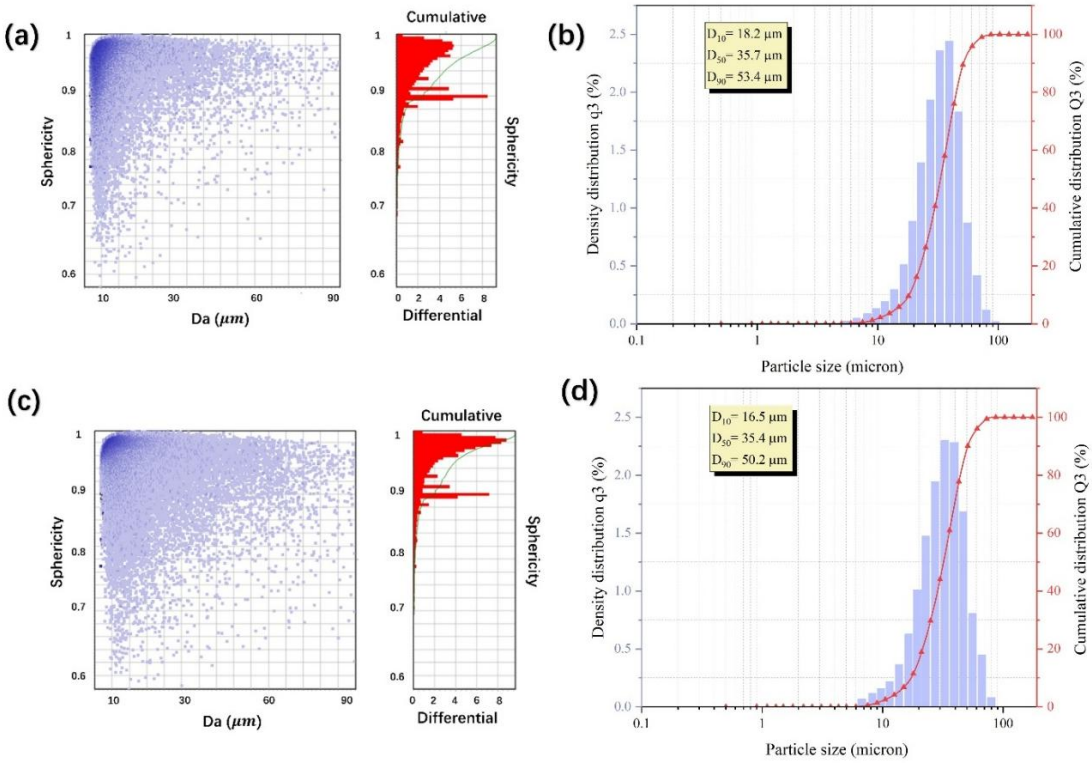

Figure 5.5 (a) Sphericity and distribution statistics of powders prepared by ball milling; (b) Particle size distribution of ball milled batch; (c) Sphericity and distribution statistics of powders prepared chemically; (d) Particle size distribution of wet chemical mixed batch.

5.3.2 Analysis of mechanical properties

Figure 5.6(a) demonstrates that TiC-IN738LC samples prepared by both ball milling and wet chemical methods show increased strength over the IN738LC, with a notable enhancement of approximately 600MPa, equating to an 80% increase. However, incorporating nano-ceramic reinforcing phases in both preparation methods

significantly diminishes ductility. Chemically prepared powders, in contrast to those produced by ball milling, exhibit a 55% improvement in ductility while maintaining comparable strength. This enhancement can be attributed to better adhesion of nano TiC particles and a higher sphericity of the powders, which improves flowability and subsequently the melt pool morphology during the L-PBF process [45, 46]. Despite the improvement in ductility in chemically prepared samples, there remains a significant gap compared to the ductility of unreinforced IN738LC, which can be explained by the ceramic dispersion strengthening effect [12, 47]. Therefore, this study aims to minimize the impact of ceramic phase dispersion strengthening on ductility by designing composite materials with optimized nanoparticle size, shape, and distribution. The use of finer nano TiC particles and preparation processes involving ultrasonication and magnetic stirring ensures a uniform distribution, enhancing the ductility of the dispersion-strengthened materials [22, 23]. Tensile test data are detailed in Table 5.2.

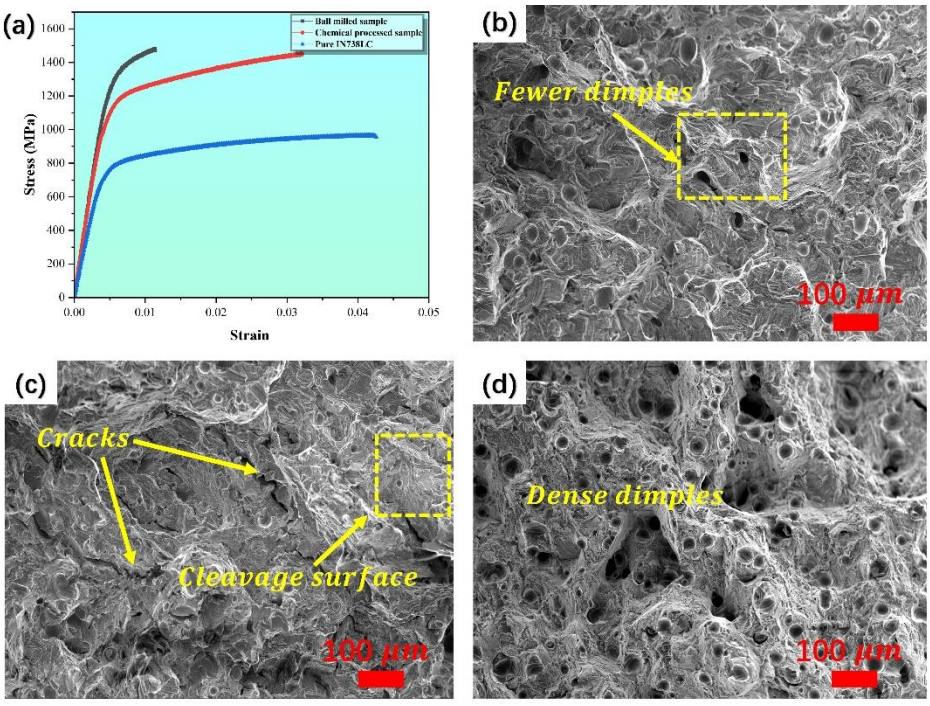

Figure 5.6 (a) Results of tensile tests for TiC-IN738LC and IN738LC superalloy; (b) - (d): SEM images of fracture surfaces of L-PBF specimens: (b) Chemically prepared; (c) Ball-milled; (d) IN738LC superalloy.

Table 5.2 Detailed results of tensile tests.

Description	Yield Strength (MPa)	Ultimate Tensile Strength (MPa)	Elongation (%)
TiC–IN738LC (Ball mill)	1110 ± 21	1518 ± 12	2.1 ± 0.05
TiC–IN738LC (Wet chemically mixing)	1020 ± 36	1416 ± 42	3.26 ± 0.08
IN738LC	708 ± 38	860 ± 45	4.3 ± 0.18

One critical factor influencing the mechanical properties is the difference in packing density between the two powder beds. Lower packing density leads to uneven heat input, causing asymmetric shrinkage of the part and increasing irregularities in the subsequent powder spreading process [48]. The higher tap density improves powder flowability by reducing inter-particle voids and enhancing the densification of the final printed component [49]. The differences in powder sphericity resulting from different MMCs preparation methods directly impact packing density. Higher tap density enables tighter particle packing, reducing gas porosity formation and minimizing the risk of incomplete fusion. Therefore, the wet chemical method, by enhancing powder sphericity, increases packing density and ultimately improves mechanical performance.

Figures 5.6(b, c and d) show the SEM images of fractured surfaces of chemically prepared, ball-milled, and unenhanced IN738LC tensile test samples, respectively. Figure 5.6(b) illustrates a fracture surface characterized by a mix of dimples and pits, indicative of a combined ductile and brittle fracture mode. This is evident by the presence of distinct fracture faces alongside areas of ductile fracture morphology. In contrast, Figure 5.6(c) reveals a fracture surface with numerous crack planes and evident cracks, as highlighted by yellow arrows, denoting the lowest ductility among the samples. Compared to the ball-milled sample in Figure 5.6(c), the chemically prepared sample in Figure 5.6(b) exhibits better plasticity. Figure 5.6(d) displays a fracture surface densely populated with dimples and lacking significant fracture planes, typical of ductile fracture morphology [50]. The data from SEM align with the results of the tensile tests, suggesting that the incorporation of nano-ceramic reinforcing phases

tends to reduce the plasticity of the metal matrix.

5.3.3 Numerical analysis of melt pool formation and microstructural characteristics

This study adopts the normalized heat intensity as the metric for validation [35]. Figures 5.7(a) and 5.7(b) compare the results of L-PBF experiments and simulations using ball milling and chemical methods. From the experimental part of Figure 5.7(a), it can be observed that during the L-PBF process, a large amount of molten powder splattered, and this splatter effect was also captured in the simulation of Figure 5.7(a). At the same time, both in the experiment and simulation, local necking effects caused by uneven heat distribution were captured. Figure 5.7(b), on the other hand, shows the powder bed prepared chemically, where the heat distribution during the L-PBF process was very smooth, with more even heat distribution. The experimentally measured packing densities of the two preparation methods differ. Therefore, this study incorporates experimental packing density values when modeling the powder bed. As shown in the DEM model (Figure 5.3a and 5.3b), the packing density of the ball-milled powder (0.43) is lower than that of the chemically prepared powder (0.54). This causes a change in thermal characteristics during the L-PBF process, leading to uneven heat distribution. This phenomenon is reflected in the experimental comparison in Figures 5.7 as well as the simulation comparison in Figures 5.8. Overall, the simulating model can successfully reflect the splattering of molten powder in the L-PBF process and, based on the results of heat distribution, agrees with the experimental results, thus validating the fidelity of the simulation model.

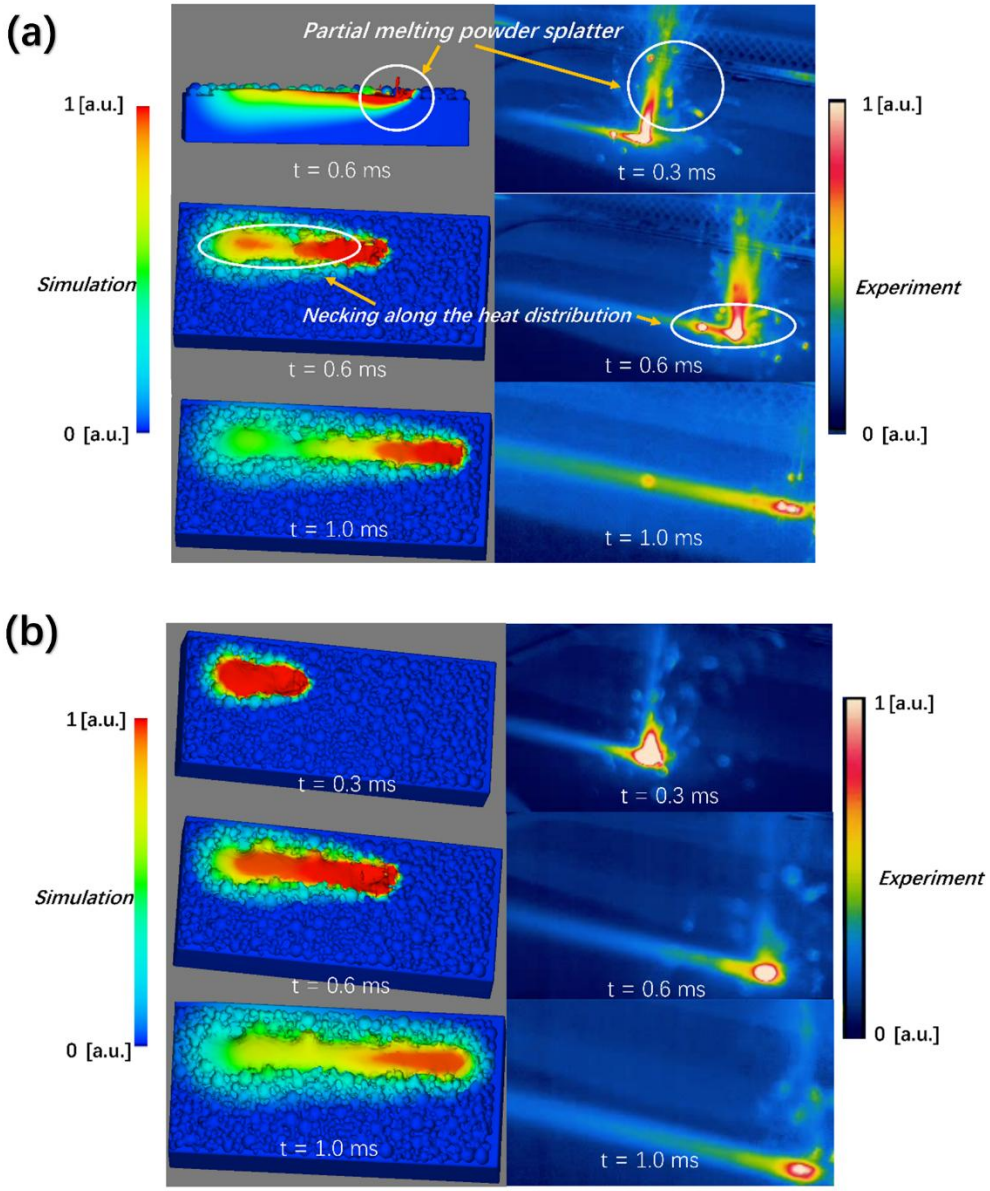

Figure 5.7 Simulation and experimental validation of (a) ball milled powders; (b) Chemically prepared powders.

Figures 5.8 (a) and (b) illustrate the temperature distribution during L-PBF of nano-TiC reinforced IN738LC powder prepared by ball milling and chemical methods respectively. The ball milling method was found to use a higher proportion of defective powders, i.e., powders with lower sphericity, to match the results obtained from experimental tests. Detailed analysis of the melt track revealed that, during the melting process, the heat distribution in the ball-milled powder bed formed a noticeable necking as shown in the white circle, see Figure 5.8. This necking significantly affected the

thermal transfer within the melt track, leading to uneven heat distribution, which in turn influenced the microstructure and properties of the material [51, 52]. In contrast, the chemically prepared powder bed demonstrated superior characteristics, with a more uniform heat distribution. As observed in Figure 5.8, the ball-milled powder bed had a higher cooling rate leading to the formation of columnar dendrites, while the chemically prepared bed exhibited a more uniform heat distribution, reducing the cooling rate and promoting the formation of equiaxed crystals. This improvement mitigates the anisotropy in additive manufacturing and enhances the quality of the as-printed sample [53]. The uniformity of heat distribution also leads to a reduction in grain size, thereby enhancing the material's strength [52, 54]. Overall, the method of powder preparation significantly influences the microstructure and mechanical properties of metal materials. The defects and lower sphericity of powder prepared via ball milling have led to uneven heat distribution and heat transfer, which will adversely affect the microstructure. Conversely, chemical preparation achieves a more uniform heat distribution, favoring the formation of finer grains and improved mechanical strength.

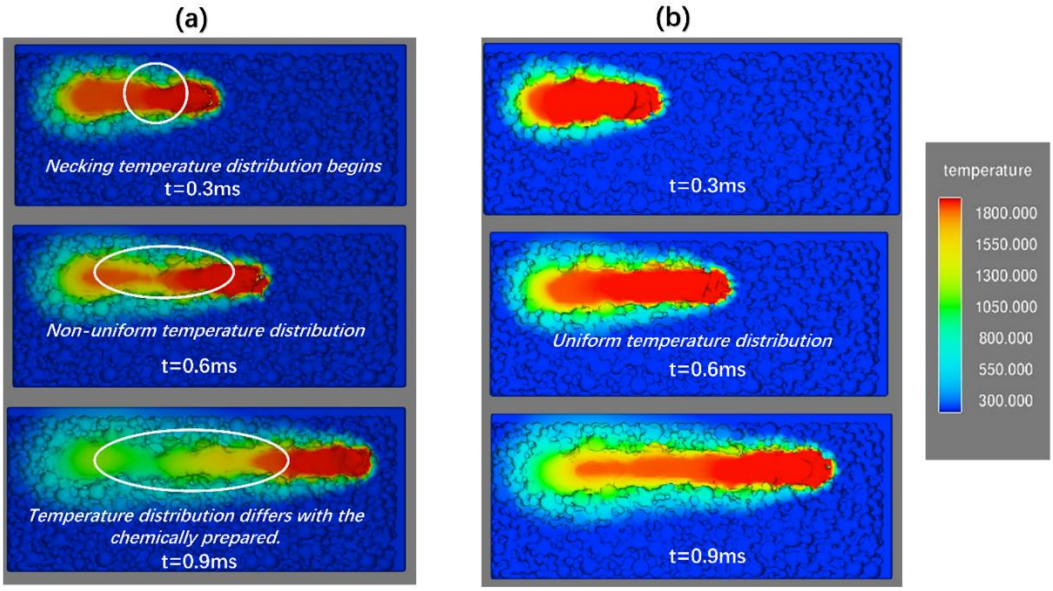

Figure 5.8 Temperature distribution of a single melt track in L-PBF for (a) ball milling method at different times; (b) chemical preparation method at different times.

Figure 5.9 is the side view of the single melt track. It illustrates that during the melting pool process, the melt track of ball-milled powders with lower sphericity exhibited a splattering effect in simulations, as indicated in Figure 5.9(a). It was shown in other studies [55, 56] that the particle size distribution, shape, and flowability of powders significantly influence this splattering phenomenon. Particularly, powders with irregular shapes or uneven particle size distribution are more prone to splattering. In contrast, powders prepared using the chemical mixing method with higher sphericity showed fewer splattering effects in simulations. This difference suggests that besides the physical properties of the powders, the Marangoni effect is another critical factor in explaining the splattering effect. According to Sun et al. [55], powders with lower sphericity in the melt pool lead to abnormal Marangoni flow. This abnormal flow not only increases the likelihood of splattering but also facilitates the formation of detrimental phases, leading to increased surface roughness and reduced material hardness, thereby degrading the quality of the L-PBF samples [53].

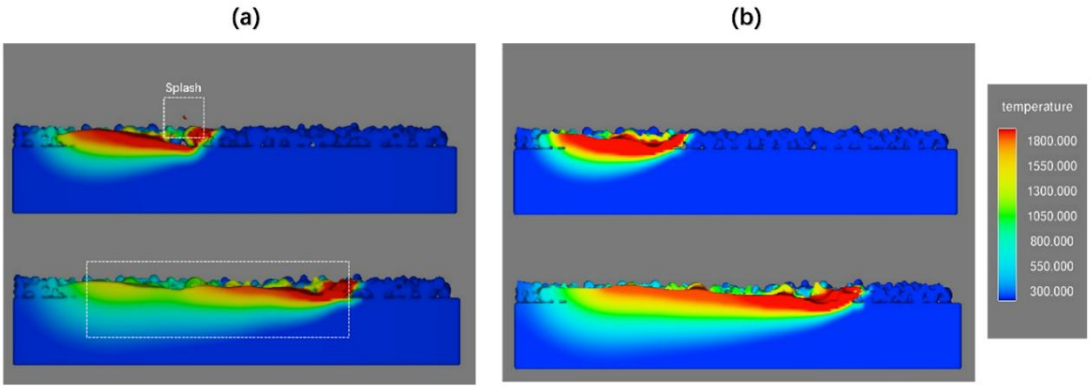

Figure 5.9 Sectional view of melt pool in single L-PBF melt track for (a) ball milling method at different times and (b) chemical preparation method at different times.

An in-depth analysis of temperature vector maps in melt pools during L-PBF process with ball-milled powders has been conducted to explore the relationship between melt pool dynamics and the formation of lack of fusion defects. Sequential images display the temperature vector changes within the same powder region across four distinct time intervals during laser interaction. Figure 5.10(a) shows that small, unmelted voids are present in the melt pool with initial laser contact with the powder. As the laser further

interacts and melts the powder, the melt pool area expands, gradually filling these voids, as shown in Figure 5.10(b). However, as the melting process continues, the melt pool begins to move in the opposite direction before completely filling the voids, leading to the formation of lack of fusion defects, as illustrated in Figures 5.10(c and d). In contrast, the melt pool motion vector maps in Figures 5.10(e – h) of powders prepared by the chemical mixing method exhibit significant differences from those prepared by ball milling. In chemically prepared powders, although small voids also appear with the initial laser contact, the melt pool successfully fills these voids due to better flowability as the laser continues to interact with the powder, effectively preventing the formation of lack of fusion defects. These results further validate the varying flow properties of melt pools with different sphericities, demonstrating distinct phenomena in Marangoni flow patterns. The variation in the internal Marangoni flow of the melt pools can be inferred from previous melt track data in Figure 5.8. Due to the lower sphericity of ball-milled powders, their flowability during laser melting is reduced [46, 55], and their uneven heat distribution and thermal transfer within the melt track lead to an increased likelihood of lack of fusion defects [57]. Moreover, ball-milled powders exhibit more pronounced upward motion vectors in melt pool flow compared to chemically prepared powders in Figures 5.10(d and h), culminating in the splattering effect observed in Figure 5.9(a). These insights are essential for comprehending and optimizing melt pool dynamics in L-PBF processes.

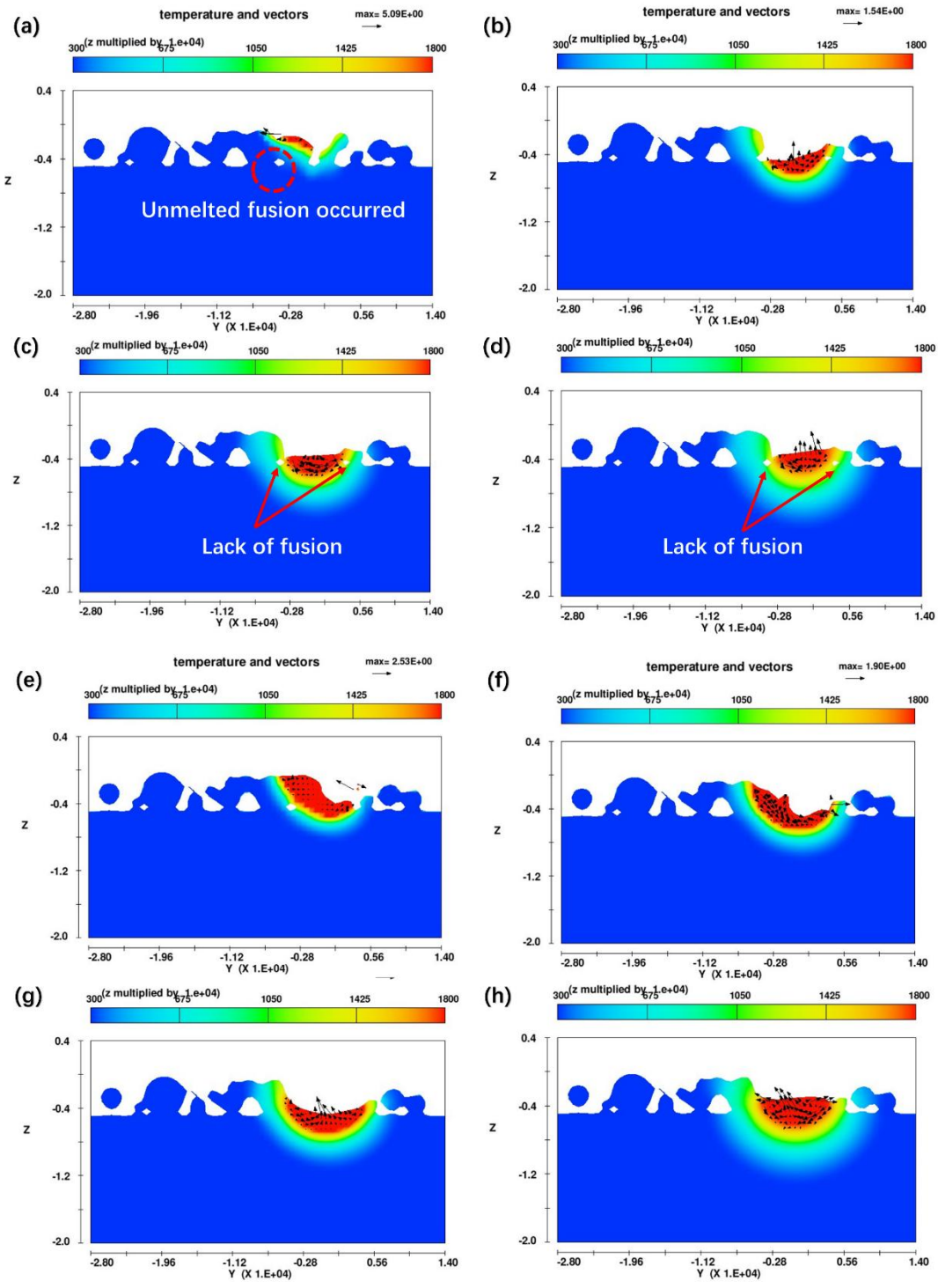

Figure 5.10 (a-d) Vector diagrams of melt pool dynamics in ball milling method at different times; (e-f) Vector diagrams of melt pool dynamics in chemical preparation method at different times.

As shown in Figures 5.11(a and b), the melt pools prepared by ball milling, reveals significant lack of fusion defects and a higher occurrence of porosity within these melt pools. In contrast, Figures 5.11(c and d), representing melt pools for chemically

prepared powders, show a marked reduction in this lack of fusion defects and porosities. This observation aligns with simulation data, supporting that powders with lower sphericity are more prone to lack of fusion defects.

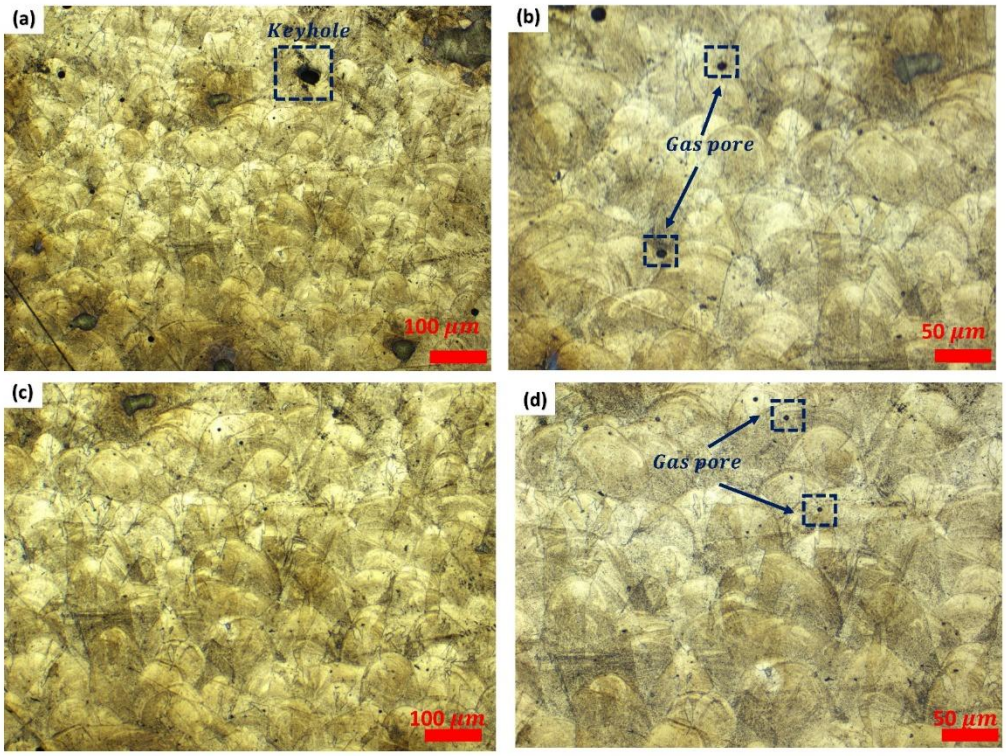

Figure 5.11 (a) Melt pool morphology in L-PBF using ball milling method; (b) High-magnification view of ball milled melt pool; (c) Melt pool morphology in L-PBF using chemical preparation method; (d) High-magnification view of chemical prepared melt pool.

Figures 5.12 depict the SEM images of the ball-milled and chemically prepared methods, respectively. Notably, these SEM images were captured after the as-built samples had been subjected to tensile testing, thereby revealing that some of the gamma prime phases had experienced deformation. As demonstrated in the figures, the ball-milled method, characterized by lower sphericity, more readily produces MC carbides during the L-PBF formation process. Employing heat treatment to dissolve these MC carbides creates additional space for the precipitation of gamma prime, potentially enhancing the material's adherence to strength [58]. Furthermore, since coarse gamma prime can diminish the material's ductility [59], a comparative analysis of Figures 5.12(c and d) indicates that the gamma prime in the chemically prepared samples is

finer than that in the ball-milled samples. Therefore, the different preparation methods result in distinct ductility outcomes in tensile tests. Overall, correlating SEM analyses with tensile test results indicates that powder sphericity differences impact fracture modes, ultimately affecting both microstructure and mechanical properties [27].

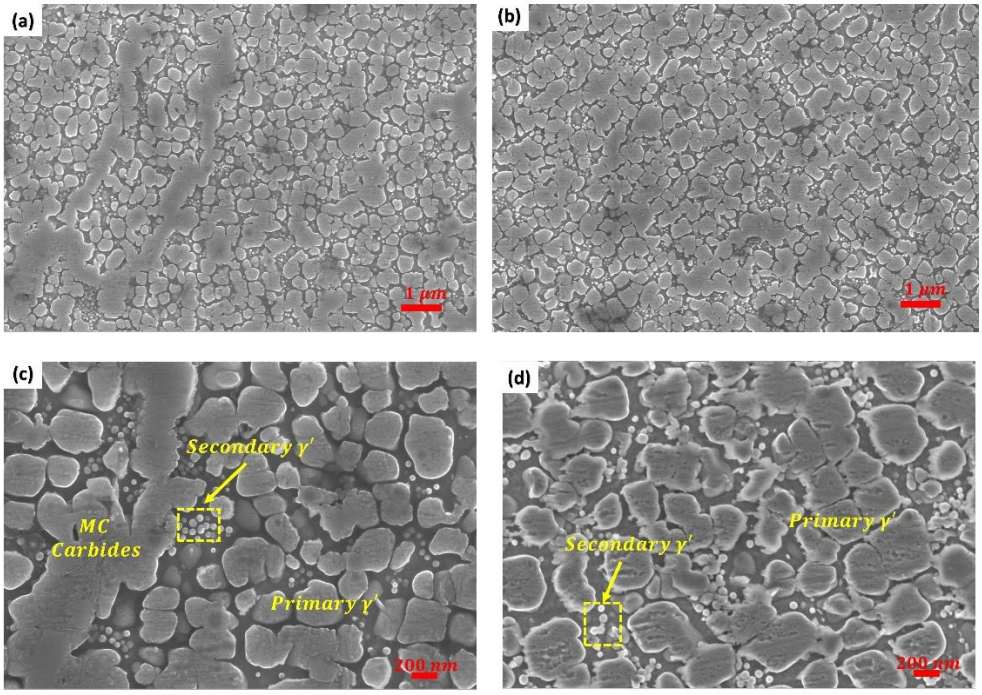

Figure 5.12 SEM images of ball-milled as-built samples after tensile testing: (a) and (c) show higher magnification; chemically prepared samples after tensile testing: (b) and (d) show higher magnification.

Figures 5.13(a) and (b) respectively show the EBSD inverse pole figures (IPF) of TiC-IN738LC prepared by the wet chemical method and the ball milling method. The IPF reveals that the sample prepared by the wet chemical method contains more fine grains, with grain sizes significantly smaller than those prepared by the ball milling method. From Figures 5.13(c) and (d), it can be observed that the average grain size of chemically prepared TiC-IN738LC is reduced by nearly 50%, from 46 μm to 23 μm, compared to ball-milled TiC-IN738LC. This grain refinement mechanism has been also noted in other studies where TiC is used as a reinforcement material [60, 61]. The Kernel average misorientation (KAM) results in Figures 5.13(e) and (f) show that the chemically prepared TiC-IN738LC exhibited greater stress concentration compared to

the ball-milled sample. A similar phenomenon was found in the previous study [60], where the smaller local strain in the ball-milled sample explains its superior tensile strength. Analysis of the misorientation angle in Figures 5.13(g) and (h) indicates that the chemically prepared sample contains more low-angle grain boundaries (LAGBs), while the ball-milled TiC-IN738LC exhibits more high-angle grain boundaries (HAGBs). This further confirms that the strength enhancement in the ball-milled TiC-IN738LC can be attributed to the presence of more HAGBs, which, however, compromises ductility. Achieving an optimal balance between LAGBs and HAGBs is crucial for realizing the best mechanical properties [62]. Figures 5.13(i) and (j) are the pole figures (PF) of both methods. The PF indicates that the sample from the wet chemical method exhibits a weaker (100) texture distribution compared to the ball-milled sample, with a reduced maximum texture index. This may be attributed to the TiC particles acting as heterogeneous nucleation sites, inhibiting grain growth along the (100) direction [60]. Consequently, the presence of nanoparticles is thought to impede grain growth along the build direction, reducing the formation of columnar grains and promoting the development of more equiaxed grains. It can be inferred that the chemically prepared powder improves the attachment of nano-TiC, altering the melt pool dynamics and thereby influencing the microstructural characteristics of the sample.

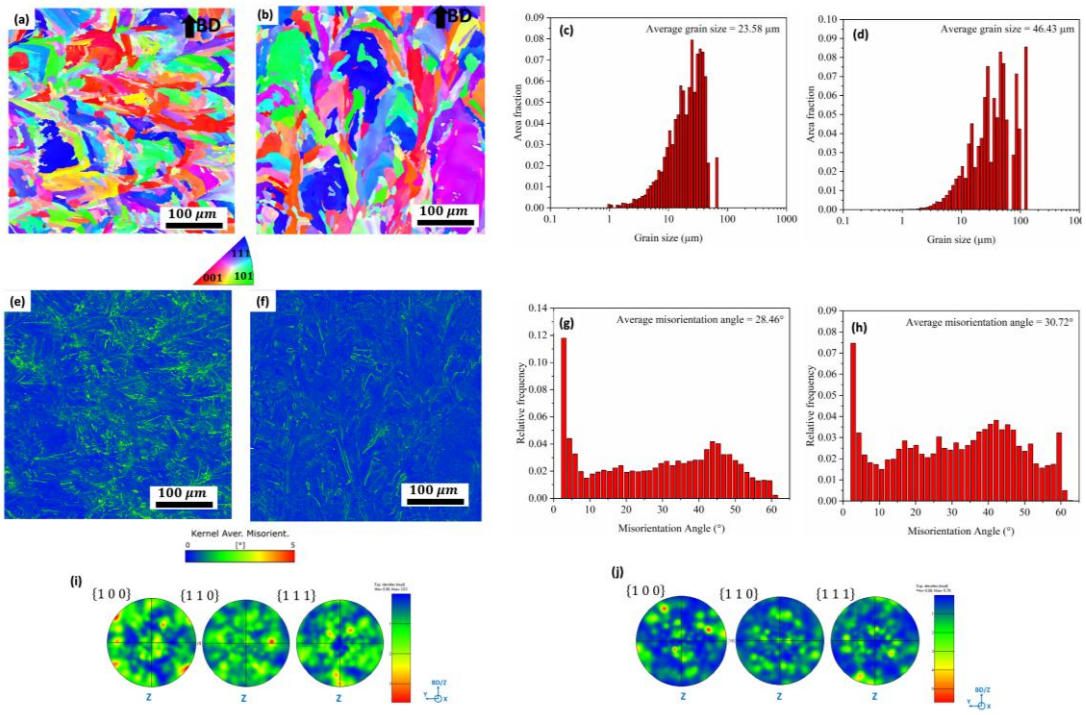

Figure 5.13 EBSD results of TiC-IN738LC prepared by the wet chemical method: (a) IPF; (c) Grain size distribution; (e) KAM; (g) Misorientation angle distribution; (i) PF. EBSD results of ball-milled TiC-IN738LC: (b) IPF; (d) Grain size distribution; (f) KAM; (h) Misorientation angle distribution; (j) PF.

Figure 5.14 elucidates the melt pool dynamics of powders with varying sphericity. From the composition of the powder bed in Figures 5.14(a and b), it can be observed that beds with low sphericity, due to inconsistent shape uniformity, exhibit non-uniform powder spreading. This leads to varying depths of laser energy penetration during the laser melting process. Particles with irregular, low sphericity, having a larger surface area, exhibit higher surface energy absorption, thereby affecting heat transfer. This results in partially melted powder, impacting melt pool flow, and more likely leading to defects such as keyholes and gas pores. Variations in the powder bed heights with different sphericities are observed; Figure 5.14(b) reveals inconsistencies in spreading heights, which also tend to produce spatter effects, aligning with the simulation results presented in this study. Finally, higher sphericity improves packing density, which benefits the melting interaction between the laser and the powder, thereby promoting efficient thermal distribution in the melt pool and enhancing the Marangoni effect, consequently improving the quality of L-PBF process.

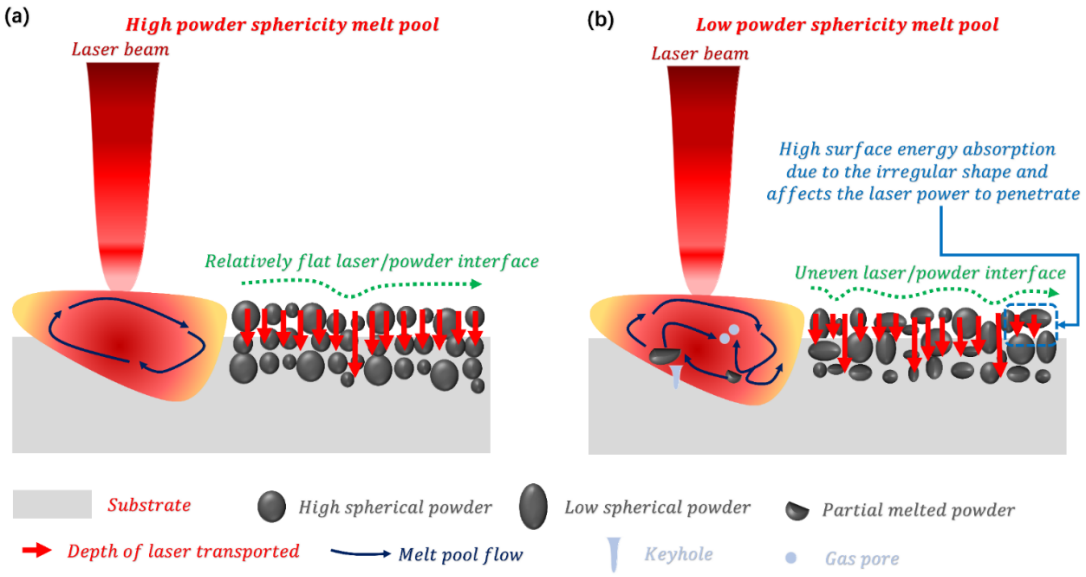

Figure 5.14 Diagram illustrating the mechanism of powder sphericity on the melt pool dynamics.

5.4 Conclusions

This research article investigates the fabrication of TiC-IN738LC composites prepared by wet chemical mixing and ball milling methods via L-PBF. Utilizing both experimental and simulation approaches, it analyzes the impact of powder morphology, particle statistical analysis, and fracture morphologies on the mechanical properties of L-PBF in nickel-based metal matrix composites. The main conclusions of this research are as follows:

1) Wet chemically prepared powders exhibit superior sphericity and fewer morphological defects compared to ball-milled powders. This method effectively preserves the original shape of IN738LC particles, leading to enhanced flowability in the melt pool during L-PBF, which reduces the occurrence of lack of fusion defects and improves mechanical properties.

2) Tensile testing results indicate that the physical morphology of powders significantly influences the fracture modes of tensile specimens. Optimizing powder morphology can effectively control the material's mechanical properties.

3) L-PBF CFD simulations reveal that the sphericity of particles significantly

influences melt pool dynamics. This can lead to irregular Marangoni flow and spattering during the melting process, resulting in the lack of fusion defects. These findings further explain the significant impact of the physical morphology of the powder on the fracture modes of tensile specimens as obtained in tensile tests.

Acknowledgements

This work was supported by the National Natural Science Foundation of China (U23A20629, No.52375346), Natural Science Foundation of Zhejiang, China (No. LZ22E050002), Science and Technology Innovation 2025 Major Project of Ningbo (No.2022Z064), Royal Society project (IEC\NSFC\211480) and the University of Birmingham that provided the funding. Special thanks to Dr. Zheng Ma at Ningbo University for assistance with the EBSD data acquisition.

References

1. Ezugwu E, Wang Z, Machado A. The machinability of nickel-based alloys: a review. Journal of Materials Processing Technology. 1999;86(1-3):1-16.
2. Shi J, Wang Y. Development of metal matrix composites by laser-assisted additive manufacturing technologies: a review. Journal of Materials Science. 2020;55(23):9883-917.
3. Sanchez S, Smith P, Xu Z, Gaspard G, Hyde CJ, Wits WW, et al. Powder Bed Fusion of nickel-based superalloys: A review. International Journal of Machine Tools and Manufacture. 2021;165:103729.
4. Wang H, Zhang X, Wang G, Shen J, Zhang G, Li Y, et al. Selective laser melting of the hard-to-weld IN738LC superalloy: Efforts to mitigate defects and the resultant microstructural and mechanical properties. Journal of Alloys and Compounds. 2019;807:151662.
5. Strunz P, Petrenec M, Gasser U, Tobiáš J, Polák J, Šaroun J. Precipitate microstructure evolution in exposed IN738LC superalloy. Journal of alloys and compounds. 2014;589:462-71.
6. Messé O, Muñoz-Moreno R, Illston T, Baker S, Stone H. Metastable carbides and their impact on recrystallisation in IN738LC processed by selective laser melting. Additive Manufacturing. 2018;22:394-404.
7. Pike L. Development of a fabricable gamma-prime (γ′) strengthened superalloy. Superalloys 2008. 2008:191-200.
8. Wang K, Du D, Liu G, Pu Z, Chang B, Ju J. A study on the additive manufacturing of a high chromium Nickel-based superalloy by extreme high-speed laser metal deposition. Optics & Laser Technology. 2021;133:106504.
9. Shu C, Chen S, Shu X, Abdel-Wahab A, Essa K. Enhanced high-temperature mechanical properties and strengthening mechanisms of chemically prepared nano-TiC reinforced IN738LC via laser powder bed fusion. Materials Characterization. 2024;217:114434.
10. Schulz F, Lindgren K, Xu J, Hryha E. Gamma prime formation in nickel-based superalloy IN738LC manufactured by laser powder bed fusion. Materials Today Communications. 2024;38:107905.
11. Shu C, Chen S, Zheng Z, Lu X, Li W, De Lisi M, et al. Fabrication and strengthening mechanism of crack-free nano-TiC reinforced IN738LC with enhanced mechanical properties by laser powder bed fusion. Journal of Materials Research and Technology. 2023;27:3835-48.
12. Qin YQ, Tian Y, Peng YQ, Luo LM, Zan X, Xu Q, et al. Research status and development trend of preparation technology of ceramic particle dispersion strengthened copper-matrix composites. Journal of Alloys and Compounds. 2020;848:156475.
13. Mendoza-Duarte J, Estrada-Guel I, Carreño-Gallardo C, Martínez-Sánchez R. Study of Al composites prepared by high-energy ball milling; Effect of processing conditions. Journal of Alloys and Compounds. 2015;643:S172-S7.
14. Woo D, Sneed B, Peerally F, Heer F, Brewer L, Hooper J, et al. Synthesis of nanodiamond-reinforced aluminum metal composite powders and coatings using high-

energy ball milling and cold spray. Carbon. 2013;63:404-15.
15. Chen D, Pan Q, Liu Z, Zeng S, Shi Q, Peng J, et al. The strengthening mechanism of mechanical and tribological properties of TiC-reinforced 316L matrix composites fabricated by selective laser melting. Materials Today Communications. 2024;39:108916.
16. Zhang B, Bi G, Wang P, Bai J, Chew Y, Nai MS. Microstructure and mechanical properties of Inconel 625/nano-TiB2 composite fabricated by LAAM. Materials & Design. 2016;111:70-9.
17. Rong T, Gu D, Shi Q, Cao S, Xia M. Effects of tailored gradient interface on wear properties of WC/Inconel 718 composites using selective laser melting. Surface and Coatings Technology. 2016;307:418-27.
18. Chen L, Sun Y, Li L, Ren X. Microstructure evolution, mechanical properties, and strengthening mechanism of TiC reinforced Inconel 625 nanocomposites fabricated by selective laser melting. Materials Science and Engineering: A. 2020;792:139655.
19. Gu D, Zhang H, Dai D, Xia M, Hong C, Poprawe R. Laser additive manufacturing of nano-TiC reinforced Ni-based nanocomposites with tailored microstructure and performance. Composites Part B: Engineering. 2019;163:585-97.
20. Zhao T, Dahmen M, Cai W, Alkhayat M, Schaible J, Albus P, et al. Laser metal deposition for additive manufacturing of AA5024 and nanoparticulate TiC modified AA5024 alloy composites prepared with balling milling process. Optics & Laser Technology. 2020;131:106438.
21. Zhao S, Zheng Z, Huang Z, Dong S, Luo P, Zhang Z, et al. Cu matrix composites reinforced with aligned carbon nanotubes: Mechanical, electrical and thermal properties. Materials Science and Engineering: A. 2016;675:82-91.
22. Han L, Wang J, Chen Y, Huang Y, Liu Y, Wang Z. Fabrication and mechanical properties of WC nanoparticle dispersion-strengthened copper. Materials Science and Engineering: A. 2021;817:141274.
23. Vishwanatha H, Eravelly J, Kumar CS, Ghosh S. Dispersion of ceramic nano-particles in the Al-Cu alloy matrix using two-step ultrasonic casting and resultant strengthening. Materials Science and Engineering: A. 2017;708:222-9.
24. Abreu-Castillo HO, Bueno BP, d'Oliveira ASC. In situ processing aluminide coatings with and without tungsten carbide. The International Journal of Advanced Manufacturing Technology. 2022;119(1-2):477-88.
25. Molina-Claros J, Hdz-García H, Alvarez-Vera M, Pech-Canul M, Muñoz-Arroyo R, García-Vázquez F, et al. Characterisation of PTA processed overlays without and with WC nanoparticles. Surface Engineering. 2017;33(11):857-65.
26. Wei W-H, Wang L-Z, Chen T, Duan X-M, Li W. Study on the flow properties of Ti-6Al-4V powders prepared by radio-frequency plasma spheroidization. Advanced Powder Technology. 2017;28(9):2431-7.
27. Brika SE, Letenneur M, Dion CA, Brailovski V. Influence of particle morphology and size distribution on the powder flowability and laser powder bed fusion manufacturability of Ti-6Al-4V alloy. Additive Manufacturing. 2020;31:100929.
28. Gao X, Faria GA, Zhang W, Wheeler KR. Numerical analysis of non-spherical particle effect on molten pool dynamics in laser-powder bed fusion additive

manufacturing. Computational materials science. 2020;179:109648.
29. Zhao Y, Aoyagi K, Daino Y, Yamanaka K, Chiba A. Significance of powder feedstock characteristics in defect suppression of additively manufactured Inconel 718, Addit. Manuf. 34 (2020) 101277. 2020.
30. Haferkamp L, Haudenschild L, Spierings A, Wegener K, Riener K, Ziegelmeier S, et al. The influence of particle shape, powder flowability, and powder layer density on part density in laser powder bed fusion. Metals. 2021;11(3):418.
31. Mussatto A, Groarke R, O'Neill A, Obeidi MA, Delaure Y, Brabazon D. Influences of powder morphology and spreading parameters on the powder bed topography uniformity in powder bed fusion metal additive manufacturing. Additive Manufacturing. 2021;38:101807.
32. Lu X, Shu C, Zheng Z, Shu X, Chen S, Essa K, et al. Effects of L-PBF Scanning Strategy and Sloping Angle on the Process Properties of TC11 Titanium Alloy. Metals. 2023;13(5):983.
33. Shu C, Zheng Z, Lei P, Xu H, Shu X, Essa K. Optimization of process parameters for TC11 alloy via tailoring scanning strategy in laser powder bed fusion. Frontiers of Materials Science. 2024;18(4):1-15.
34. Zhang S, Rauniyar S, Shrestha S, Ward A, Chou K. An experimental study of tensile property variability in selective laser melting. Journal of Manufacturing Processes. 2019;43:26-35.
35. Krauss H, Eschey C, Zaeh M, editors. Thermography for monitoring the selective laser melting process. 2012 International Solid Freeform Fabrication Symposium; 2012: University of Texas at Austin.
36. Girnth S, Heitkamp T, Wacker C, Waldt N, Klawitter G, Dröder K. Dimensionless quantities in discrete element method: powder model parameterization for additive manufacturing. Progress in Additive Manufacturing. 2024:1-17.
37. Tian Y, Yang L, Zhao D, Huang Y, Pan J. Numerical analysis of powder bed generation and single track forming for selective laser melting of SS316L stainless steel. Journal of manufacturing processes. 2020;58:964-74.
38. Wang S, Zhu L, Fuh JYH, Zhang H, Yan W. Multi-physics modeling and Gaussian process regression analysis of cladding track geometry for direct energy deposition. Optics and Lasers in Engineering. 2020;127:105950.
39. Tang C, Tan JL, Wong CH. A numerical investigation on the physical mechanisms of single track defects in selective laser melting. International Journal of Heat and Mass Transfer. 2018;126:957-68.
40. Lee Y, Zhang W. Modeling of heat transfer, fluid flow and solidification microstructure of nickel-base superalloy fabricated by laser powder bed fusion. Additive Manufacturing. 2016;12:178-88.
41. Wu Y-C, San C-H, Chang C-H, Lin H-J, Marwan R, Baba S, et al. Numerical modeling of melt-pool behavior in selective laser melting with random powder distribution and experimental validation. Journal of Materials Processing Technology. 2018;254:72-8.
42. Bidare P, Bitharas I, Ward R, Attallah M, Moore AJ. Fluid and particle dynamics in laser powder bed fusion. Acta Materialia. 2018;142:107-20.

43. Lam MC, Lim SC, Song H, Zhu Y, Wu X, Huang A. Scanning strategy induced cracking and anisotropic weakening in grain texture of additively manufactured superalloys. Additive Manufacturing. 2022;52:102660.
44. Jensen T, Kelly L, Lazarides A, Schatz GC. Electrodynamics of noble metal nanoparticles and nanoparticle clusters. Journal of Cluster Science. 1999;10:295-317.
45. Wang J, Zhu R, Liu Y, Zhang L. Understanding melt pool characteristics in laser powder bed fusion: An overview of single-and multi-track melt pools for process optimization. Advanced Powder Materials. 2023;2(4):100137.
46. Kiani P, Scipioni Bertoli U, Dupuy AD, Ma K, Schoenung JM. A statistical analysis of powder flowability in metal additive manufacturing. Advanced Engineering Materials. 2020;22(10):2000022.
47. Ogunmefun OA, Bayode BL, Jamiru T, Olubambi PA. A critical review of dispersion strengthened titanium alloy fabricated through spark plasma sintering techniques. Journal of Alloys and Compounds. 2023:170407.
48. Tan JH, Wong WLE, Dalgarno KW. An overview of powder granulometry on feedstock and part performance in the selective laser melting process. Additive Manufacturing. 2017;18:228-55.
49. Field A, Carter L, Adkins N, Attallah M, Gorley M, Strangwood M. The effect of powder characteristics on build quality of high-purity tungsten produced via laser powder bed fusion (LPBF). Metallurgical and Materials Transactions A. 2020;51:1367-78.
50. Li Q-f, Qiu W, Xie W, Huang W-y, Zhou L-b, Ren Y-j, et al. Influence of TiCN addition on the microstructures and mechanical properties of the AZ31 alloy. RSC advances. 2022;12(47):30650-7.
51. Shrestha S, Rauniyar S, Chou K. Thermo-fluid modeling of selective laser melting: single-track formation incorporating metallic powder. Journal of Materials Engineering and Performance. 2019;28:611-9.
52. Yavari R, Smoqi Z, Riensche A, Bevans B, Kobir H, Mendoza H, et al. Part-scale thermal simulation of laser powder bed fusion using graph theory: Effect of thermal history on porosity, microstructure evolution, and recoater crash. Materials & Design. 2021;204:109685.
53. Esmaeilizadeh R, Ali U, Keshavarzkermani A, Mahmoodkhani Y, Marzbanrad E, Toyserkani E. On the effect of spatter particles distribution on the quality of Hastelloy X parts made by laser powder-bed fusion additive manufacturing. Journal of Manufacturing Processes. 2019;37:11-20.
54. He P, Webster RF, Yakubov V, Kong H, Yang Q, Huang S, et al. Fatigue and dynamic aging behavior of a high strength Al-5024 alloy fabricated by laser powder bed fusion additive manufacturing. Acta Materialia. 2021;220:117312.
55. Sun J, Guo M, Shi K, Gu D. Influence of powder morphology on laser absorption behavior and printability of nanoparticle-coated 90W-Ni-Fe powder during laser powder bed fusion. Materials Science in Additive Manufacturing. 2022;1(2):11.
56. Young ZA, Guo Q, Parab ND, Zhao C, Qu M, Escano LI, et al. Types of spatter and their features and formation mechanisms in laser powder bed fusion additive manufacturing process. Additive Manufacturing. 2020;36:101438.

57. Wang W, Ning J, Liang SY. Prediction of lack-of-fusion porosity in laser powder-bed fusion considering boundary conditions and sensitivity to laser power absorption. The International Journal of Advanced Manufacturing Technology. 2021;112:61-70.
58. Jena A, Atabay SE, Gontcharov A, Lowden P, Brochu M. Laser powder bed fusion of a new high gamma prime Ni-based superalloy with improved weldability. Materials & Design. 2021;208:109895.
59. Wangyao P, Polsilapa S, Chaishom P, Zrnik J, Homkrajai W, Panich N. Gamma prime particle coarsening behavior at elevated temperatures in cast nickel-based superalloy, GTD-111 EA. High Temperature Materials and Processes. 2008;27(1):41-50.
60. Lv Y, Zhang Z, Zhang Q, Wang R, Sun G, Chen X, et al. Cracking inhibition behavior and the strengthening effect of TiC particles on the CM247LC superalloy prepared by selective laser melting. Materials Science and Engineering: A. 2022;858:144119.
61. Lv Z, Mao Y, Cui K, Li R, Zhang Q, Li R. Effect of grain size and temperature on mechanical properties of nanocrystalline nickel. Materials Today Communications. 2024;41:110380.
62. Chen S, Yu Q. The role of low angle grain boundary in deformation of titanium and its size effect. Scripta Materialia. 2019;163:148-51.

CHAPTER 6 CONCLUSIONS AND FUTURE DIRECTIONS

This study investigates the nickel-based superalloy IN738LC, focusing on achieving crack-free and high-performance material properties during additive manufacturing. By introducing nano-ceramic particles TiC as a reinforcing phase, the research aims to regulate the microstructure and mechanical properties of TiC-IN738LC to meet the demands of increasingly stringent service conditions. The study emphasizes the optimization of powder preparation methods and L-PBF process parameters to examine the effects of processing factors on the density, metallurgical defects, microstructure, and mechanical properties of the TiC-IN738 alloy. It explores the fundamental relationships among alloy composition, processing parameters, printability, and mechanical properties. Additionally, it reveals the mechanisms underlying crack formation in L-PBF-processed TiC-IN738 alloys and outlines the strategies to mitigate cracking. Finally, the study identifies an optimal preparation method to fabricate composite materials with superior performance. The focus details include three aspects: (1) routes for preparing composite materials, (2) optimization of process parameters, and (3) the microstructural characteristics behind the mechanical properties.

Two preparation methods, namely the ball milling method and the wet chemical mixing method, were successfully employed to fabricate TiC-IN738LC composites. A comparison of these two methods revealed that, while the ball milling process is relatively simple in operation, the high-energy collisions during powder mixing significantly altered the sphericity of the powder and introduced more defects into the powder's morphology. These defects were identified through CFD simulations as the primary causes of lack of fusion and spattering, due to irregular powder melting and disrupted thermal transport. In contrast, the chemical preparation method involves multiple steps. Initially, ultrasonic cleaning induces flocculation of the powder solution, which is then subjected to magnetic stirring and drying. This process helps maintain higher powder sphericity and reduces defect formation due to the use of a liquid medium. Additionally, the high mixing speed improves the adhesion of nanoparticles, contributing to the production of higher-quality powders for L-PBF. CFD simulation

experiments further validated that powders with fewer defects exhibit better integrity in melt pools and molten tracks, significantly reducing the spattering effect and enhancing the overall quality of the L-PBF process.

For TiC-IN738LC composites, this study applied a factorial design experimental approach combined with ANOVA statistical analysis to evaluate the three most critical process parameters: laser power, hatch spacing, and scanning speed. By statistically analysing the experimental results in terms of density and porosity, the optimal process parameters were identified. The relationship between process parameters and microstructure was also established, revealing that the three parameters have a significant difference in their impact on porosity. Further mechanical testing and analysis were conducted on samples fabricated within the optimal parameter range. These tests determined the optimal process parameters for TiC-IN738LC composites prepared by both methods and confirmed the improvements in their mechanical properties.

Finally, through characterization techniques, the microstructural characteristics of the novel TiC-IN738LC composite were thoroughly investigated. The distribution of the γ and γ' phases, as well as the composition of M_xC_y carbides, was revealed using SEM/EDS techniques. EBSD results showed the grain size distribution and grain orientation, elucidating the grain refinement strengthening mechanism attributed to TiC particles located at grain boundaries and within grains. TEM analysis demonstrated the relationship between dislocations and nanoparticles, confirming the role of nano-TiC in tailoring the microstructure. By comparing these results with unreinforced IN738LC, the study clarified the strengthening mechanisms of TiC within the nickel-based matrix, highlighting its contribution to the tailored microstructure and improved mechanical properties.

6.1 Contributions to Knowledge

This research makes several contributions to knowledge of nickel-based metal matrix composites in additive manufacturing, particularly in understanding how nanoparticle reinforcement and process optimization affect microstructure, defect evolution, and mechanical performance in L-PBF. These contributions are summarized as follows:

1. Demonstrated the feasibility of using nano-ceramic reinforcement to mitigate cracking in L-PBF-processed γ′-strengthened Ni-based superalloys.
    - This study provides the first systematic evidence that introducing a controlled amount of nano-scale TiC particles can significantly reduce crack sensitivity in IN738LC processed by L-PBF. The reinforcement promotes grain refinement, interrupts crack propagation pathways, and dissipates strain energy, offering a viable approach to overcoming one of the most critical limitations of L-PBF in high-γ′ alloys.
2. Established the critical role of powder morphology and preparation method on melt pool dynamics and build integrity.
    - By comparing ball milling and wet chemical processing routes, the study shows that powder morphology—particularly sphericity and nanoparticle distribution—directly influences melt pool stability, energy absorption, and spatter formation. This contribution reinforces the importance of tailored powder design in achieving defect-free additive manufacturing, validated through both experimental results and CFD simulations.
3. Developed a process–structure–property framework for nanoparticle-reinforced Ni-based composites in L-PBF.
    - Using full-factorial design and ANOVA, the research systematically quantified the influence of laser power, scanning speed, and hatch spacing on porosity and microstructure. The study established that identical VED values could yield different material outcomes depending on parameter combinations, underlining the importance of considering parameter interactions rather than relying solely on VED.
4. Identified and validated concurrent strengthening mechanisms enabled by

nanoparticle reinforcement.

- The mechanical property enhancements observed were linked to a combination of grain refinement, load-bearing, and Orowan strengthening mechanisms. These were confirmed through EBSD grain orientation analysis, TEM dislocation-particle interactions, and fractographic evidence. This multi-mechanism reinforcement model advances the understanding of how nanoscale ceramics can improve L-PBF-fabricated alloys.

5. Proposed and validated a wet-chemical powder processing route for nanocomposite feedstock preparation in AM.
    - The study introduces a robust wet-chemical method that enables homogeneous nanoparticle dispersion while preserving powder sphericity and minimizing agglomeration—overcoming key limitations of mechanical mixing. This method enhances flowability, reduces porosity, and improves interlayer bonding, offering a promising path toward industrial-scale production of composite powders for L-PBF.

6.2 Conclusions

The main conclusions of this thesis are as follows:

- Optimized process parameters for ball-milled TiC-IN738LC, achieving crack-free sample and significant performance enhancement through the incorporation of 2 wt% nano-TiC as a reinforcement.

- Nano-TiC suppressed crack formation in IN738LC through grain refinement, inhibition of excessive grain boundary growth, and dissipation of strain energy, facilitating crack healing and preventing grain overgrowth.

- The tensile strength of ball-milled TiC-IN738LC improved by up to 30% compared to unreinforced IN738LC, with a significant increase in microhardness due to the high hardness of TiC as a ceramic material.

- Strengthening mechanisms of TiC include grain refinement, load-bearing, and

Orowan strengthening, optimizing the mechanical properties of the composite by tailoring its microstructure.

- Optimized processing parameters for chemically-prepared TiC-IN738LC composites using a wet-chemical method, addressing powder morphology degradation during ball milling and achieving enhanced mechanical properties within an optimal VED range of 100–130 J/mm³.

- The wet-chemical method produced TiC-IN738LC composites with approximately 60% higher ductility compared to those prepared via ball milling, due to the more uniform distribution of nanoparticles and improved microstructural control.

- Enhanced tensile strength and ductility of chemically prepared TiC-IN738LC were attributed to the formation of $M_{23}C_6$ carbides, which increased grain boundary cohesion, improved resistance to plastic deformation, and facilitated the transition from brittle to ductile fracture, as indicated by dimples on the fracture surfaces.

- Significant microstructural improvements were achieved through grain refinement, reduced anisotropy, and the production of smaller, equiaxed grains, providing superior grain refinement strengthening compared to the ball milling method.

- The wet-chemical method demonstrated the capability to balance high strength with improved ductility, optimizing the mechanical properties of TiC-IN738LC composites, especially under elevated temperature conditions.

- TiC-IN738LC composites prepared via the wet-chemical method exhibited superior sphericity and reduced defects compared to those produced by ball milling, attributed to reduced kinetic collisions and particle distortions in the liquid medium.

- Fractographic analysis showed a higher density of dimples in wet-chemical samples, indicative of ductile fracture, compared to the brittle fracture characteristics in ball-milled samples, correlating with enhanced ductility in mechanical performance.

- Wet-chemical method resulted in superior grain refinement, with a higher proportion of equiaxed grains and an increased number of LAGBs, effectively balancing tensile strength and ductility.

- Ball-milled samples exhibited higher defect concentrations, compromising wettability and leading to increased porosity and lack of fusion defects during L-PBF, contrasting with the improved microstructural quality of wet-chemical samples.

- TiC-IN738LC composites fabricated via the wet-chemical method demonstrated significant advantages in mechanical and microstructural properties than ball-milled TiC-IN738LC, achieving a superior combination of tensile strength and ductility.

- Numerical simulations revealed that powders with higher defect concentrations disrupt melt pool thermodynamics during the L-PBF process, requiring higher energy for complete melting and leading to the formation of semi-molten particles and molten ligaments, which cause spatter defects and uneven melt tracks.

- Irregular powder morphology was found to reduce packing density, hinder efficient laser energy absorption, and introduce the lack of fusion and gas pore defects, compromising melt pool continuity and increasing porosity.

- Improved powder flowability is essential for enhancing printability and wettability in L-PBF, ensuring uniform powder spreading, better melt pool fluidity, efficient energy absorption, and reduced porosity, thereby minimizing

defects and improving the overall quality of the processed composites.

6.3 Future directions

Future research on nickel-based composites can focus on alloy composition design, powder preparation, post-processing optimization, and service performance enhancement. Developing high-performance nickel-based composites with significant potential and application value requires continuous improvements in the synergy of these aspects. Based on the findings of this study, future research may further concentrate on the following areas:

1) **Alloy Composition Design:** Considering the distinct properties of various reinforcements, incorporating particles such as TiB_2, WC, SiC, and Y_2O_3 to develop novel nickel-based composites is a promising area of exploration. Optimizing alloy composition could enhance specific properties, such as thermal conductivity, wear resistance, or high-temperature creep resistance.

2) **Effect of Nano-Reinforcement Content:** Further investigation is required to understand the impact of varying reinforcement content on the modification of microstructural and mechanical properties. A systematic investigation into how variations in reinforcement levels impact phase distribution and microstructural characteristics will enhance understanding of the reinforcement roles in IN738LC and provide valuable insights for developing other nickel-based superalloy composites.

3) **Comprehensive Nanoscale Validation of Strengthening Mechanisms:** Further metallurgical and micromechanical validation is needed to confirm postulated strengthening mechanisms. While Orowan looping is proposed as a contributing mechanism based on observed microstructural features, its role has not been directly proven. Future work should include in-situ TEM deformation analysis, dislocation-particle interaction studies, and crystal plasticity simulations to validate the interaction mechanisms between nanoparticles and dislocations in L-PBF composites.

4) **High-Temperature Service Performance:** While L-PBFed TiC-IN738LC demonstrates excellent printability and room-temperature mechanical properties, their high-temperature creep, fatigue, oxidation, and corrosion resistance remain insufficiently explored. Therefore, further research into the high-temperature performance of L-PBFed TiC-IN738LC composites is critically important.

5) **Optimization of Heat Treatment Processes:** Optimizing the heat treatment process for TiC-IN738LC composites can break up the continuity of brittle phases along grain boundaries, promoting a fine and dispersed distribution of these phases. This approach is expected to significantly improve the material's durability.

6) **Porous Structures and Applications:** Investigating the optimal microstructure and mechanical properties of TiC-IN738LC composites and exploring the behavior of L-PBFed TiC-IN738LC composites in porous structures, will provide essential foundational data and theoretical insights. This research will support applications in complex porous configurations, promoting broader use in advanced engineering structures.